Doctoral Dissertation
Doctoral Program in Chemical Engineering (38th Cycle)

Valorisation of biomass-derived wastewaters via aqueous phase reforming for energy recovery: a multi-level performance assessment

Giulia Farnocchia

* * * * * *

Supervisors

Prof. Raffaele Pirone, Supervisor
Prof. Samir Bensaid, Co-supervisor
Dr. Giuseppe Pipitone, Co-supervisor

Politecnico di Torino
October 31st, 2025

I hereby declare that the contents and organisation of this dissertation constitute my own original work and does not compromise in any way the rights of third parties, including those relating to the security of personal data. Furthermore, I declare that I have used *Generative AI tools exclusively for editorial support, such as grammar correction, translations, paraphrasing suggestions, or improving readability.*

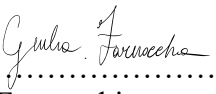

.....

Giulia Farnocchia

Turin, October 31st, 2025

Summary

With global energy demand reaching 620 EJ and 53.2 Gt CO2eq. emissions in 2024, 74.5% of which is attributed to the use of fossil fuels, the need to accelerate the shift toward renewable energy systems is more urgent than ever. In this context, biorefinery technologies, particularly aqueous phase reforming (APR), offer a promising route for producing H_2 from biomass-derived wastewaters, contributing to energy recovery strategies. APR is a thermo-catalytic process for converting oxygenated hydrocarbon into a H_2-rich gas mixture, under moderate temperatures (200–270 °C) and pressures (15–60 bar). However, the industrial application of wastewater-based APR remains limited by catalyst deactivation and economic challenges due to a relatively low technology readiness level and the limited scalability to different wastewaters. Experimental tests were performed on selected feedstocks of interest from both a compositional and a national strategic perspective, specifically pulp and paper (P&P) mill effluents and winery wastewaters (WWW). These results were combined with techno-economic (TEA), energy sustainability (ESA), and life-cycle assessments (LCA), aiming to bridge the gap between lab-scale results and process upscale for industry, outlining key technical, economic, and environmental challenges. Experimental results revealed that while P&P effluents exhibited low reactivity due to their dominance of poorly reformable acids and low pH, WWW showed strong potential as an APR feedstock, since over 70 wt.% of total organic carbon was ethanol. Therefore, a deep investigation of ethanol APR performances in varying operating conditions was carried out. Ethanol conversion reached 100% at 270 °C within 1 hour, compared to only 60% at 230 °C, with 250 °C providing the best trade-off between conversion and H_2 productivity. Among the commercial catalysts, Ru/Al2O3 showed higher conversion and H_2 productivity than Pt/Al2O3, although Pt offered slightly better H_2 selectivity. To reduce noble metal content, a 2 wt.% Ru/CeO2 catalyst was synthesized via exsolution, a novelty in the field of APR. While exsolution was successfully obtained, its APR performance remained modest, likely due to limited surface area and large particle size. Further tests with exsolved Ru- and Fe-based catalysts supported on yttria–zirconia revealed that the bimetallic 2 wt.% Ru–1 wt.% Fe system delivered the highest H_2 productivity, suggesting a beneficial Ru–

Fe synergy and confirming the potential for reduced noble metal use without sacrificing activity.

Building upon these findings, process-scale simulations were developed for an industrial facility treating 2.5 m^3/h of WWW through two configurations: Scenario 1 (S1) for CHP generation, and Scenario 2 (S2) for H_2 purification and recovery. Energetic analyses confirmed that both systems were energetically self-sufficient, with Energy Sustainability Index (ESI) values above 1, indicating positive net energy generation. A similar trend was observed for the EROI, with values of 1.57 for S1 and of 2.71 for S2, further confirming long-term energy feasibility. Since both ESI and EROI remain only slightly above unity, this highlights a limited operational margin; consequently, system sustainability relies heavily on efficient heat recovery and stable reaction performance to maintain the overall energy balance.

The minimum selling prices (MSPs) were 0.86 USD/kWh for S1 and 15.5 USD/kg H_2 for S2, both above current market levels, mainly due to the high capital costs of the APR reactor, CHP, and PSA units, but demonstrating to be completely energy self-sufficient. Cost-reduction strategies showed counterintuitive insights: increasing ethanol conversion to 95% raised the MSP for electricity by 7% due to higher heat demand but lowered the MSP for H_2 by 21% (to 12.3 USD/kg H_2) thanks to improved H_2 yields. Further decreases could be achieved by integrating additional ethanol-rich wastewaters from other processes, strengthening overall economic viability and the role of APR within wastewater valorisation frameworks. No financial subsidies from the Italian government were considered.

The LCA confirmed competitive results, with GWP reductions of 80% for S1 compared to most European electricity mixes and 79% for S2 relative to conventional steam methane reforming. When compared with renewable technologies, the GWP values for S1 and S2 were comparable with photovoltaic and electrolysis powered by solar energy respectively, with platinum usage accounting for up to 70% of total GWP. This underscores the necessity for efficient recovery of noble metal catalysts or the transition toward non-critical metals.

Overall, this work shows that APR can be integrated into large-scale wastewater treatment, achieving up to 99% COD removal while recovering renewable energy. It outlines a model for APR-based biorefineries that unite wastewater purification and green energy production, in line with the circular economy goals and contributing to UN SDGs 6 (clean water and sanitation) and 7 (affordable and clean energy).

Acknowledgments

The doctoral thesis was written at the conclusion of the PhD program funded under the PNRR, Mission 4, Component 1 “Strengthening the provision of education services: from nursery schools to universities” - Investment 4.1 “Expansion of the number of PhD programs and innovative PhD programs for public administration and cultural heritage,” through Ministerial Decree No. 351 of April 9, 2022.

Table of contents

List of Tables

List of Figures

Chapter 1 Introduction

1.1 The European role in the energy transition

According to the United Nations, the world's population has increased from 5.7 billion in 1995 to 8.2 billion to 2024 [1]. Population growth has been one of several factors contributing to the rise in global primary energy demand, alongside economic growth and increases in per-capita energy use. The primary energy demand rose from 369 EJ in 1990 to about 590 EJ in 2017, an almost 60% increase in less than 30 years [2], hitting a record of 620 EJ in 2023 [3]. Projections of the International Energy Agency (IEA) for 2040 confirm that this trend will continue, driven by population growth, urbanization, and economic development in emerging regions [4]. Given the strong link between global energy demand and reliance on fossil fuels, CO_2 emissions have increased by approximately 75% since 1990. According to the IPCC Sixth Assessment Report (AR6), global CO_2 emissions from fossil fuel combustion and industrial processes reached approximately 38 Gt CO_2 in 2019 [5]. More recent inventories indicate that global emissions continued to increase after 2019. In particular, data from the Joint Research Centre (JRC) database of the European Commission show that total greenhouse gas emissions (GHG) reached a new record of 53.2 Gt CO_2-eq in 2024, with fossil fuels combustion accounting for about 74.5% of total GHG emissions, while the remaining share is attributable to methane, nitrous oxide, and fluorinated gases [6]. Furthermore, the IEA examined how population growth, primary energy demand, and CO_2 emissions may evolve trough the period 2023–2050, as illustrated in Figure 1. This projected co-evolution differs from historical trends, where global population growth has generally been slower than the increase in energy demand [7]. In recent years, however, growth in energy demand has shown signs of moderation, driven primarily by improvements in energy efficiency and by the emerging electrified technologies [4]. It should be noted that these projections do not explicitly account for the rapid expansion of artificial intelligence–related technologies and data centres, which could exert additional upward pressure on future energy demand if not accompanied by further efficiency gains and appropriate policy measures.

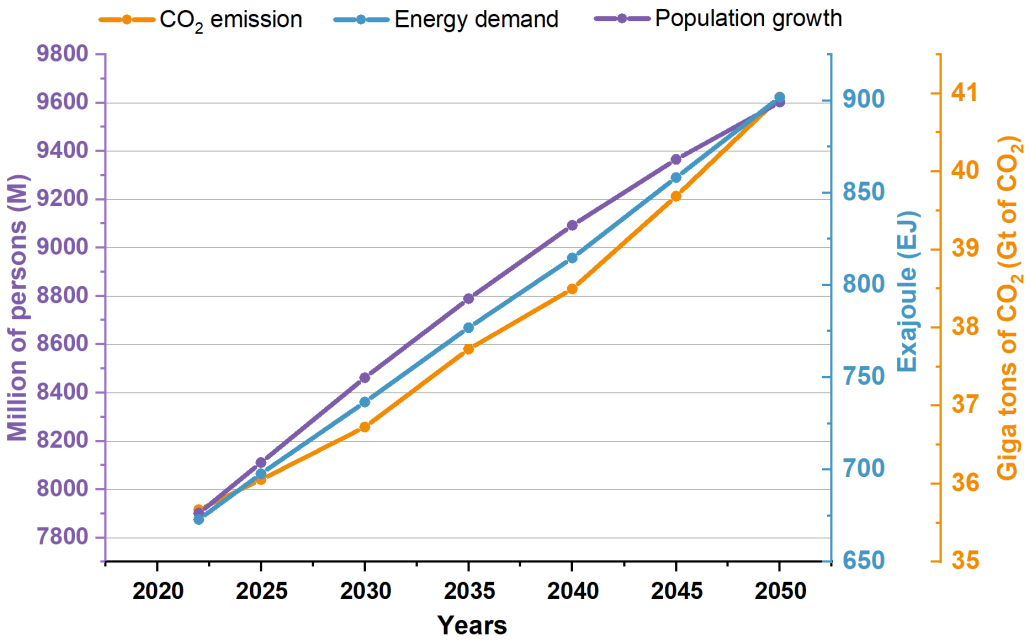

Figure 1. Projected global trends in population growth, primary energy demand, and CO_2 emissions from 2023 to 2050. Population (purple line) is expressed in millions of persons; energy demand (blue line) in exajoule (EJ); and CO_2 emissions (orange line) in giga tons. Data source: IEA, World Energy Outlook 2023 report [4].

Nevertheless, global CO_2 emissions remain on an upward trajectory. Considering this situation, the European Union (EU) has implemented a range of policies to support the energy transition while reducing environmental harm [7]. Established under Directive 2003/87/EC, a key milestone was the launch of the EU Emissions Trading System (EU ETS) in 2005 [8]. This initiative introduced a binding cap on CO_2 emissions from energy production, forming one of the EU's foundational climate strategies. This directive was followed by two more directives: the Renewable Energy Directive (RED I, Directive 2009/28/EC), which set renewable energy targets for 2020 [9], and the Energy Efficiency Directive (EED, Directive 2012/27/EU), which imposed minimum national targets to achieve the EU's 2020 goals and introduced energy performance labelling schemes such as the EU Ecolabel [10]. Thereafter, in 2019, the European Green Deal established the objective of climate neutrality by 2050 through the European Climate Law, providing funding mechanisms for a transition towards a clean energy economy [11]. In 2021, the European Commission introduced the Fit for 55 package, a set of legislative proposals intended to bring EU policies in line with the 2030 goal of cutting greenhouse gas emissions by at least 55% from the 1990 levels [12]. Moreover, the Russian invasion of Ukraine in 2022 exposed Europe's dependence on imported fossil fuels, as Russian gas alone had covered nearly 40% of the EU-27 supply the year before [13]. The combined effect of sanctions and market disruptions generated significant price volatility and compelled a rapid reorientation of European energy policy. In response, the REPowerEU plan put energy security ahead of climate targets, diverging from the Fit for 55 package [14]. Within this broader European framework for accelerating the energy transition, significant public investments have been mobilised to support research and innovation in sustainable energy technologies. In particular, the NextGenarationEU initiative, implemented at national level through the Italian National Recovery and Resilience Plan (PNRR), aims to foster decarbonisation, circular economy strategies, and the development of clean energy systems [15], [16]. In this context, the present PhD research is funded under MUR Ministerial Decree No. 351, which

supports doctoral programmes aligned with PNRR priorities, and specifically addresses the catalytic production of hydrogen from waste-derived feedstocks, contributing to the advancement of integrated waste-to-energy and hydrogen technologies.

1.2 Europe energy mix and hydrogen as a key vector for decarbonization

While global emissions reached their record in 2023, Europe has slowed its growth, with emissions declining by nearly 9% that year (around 220 Mt), despite modest GDP growth (0.7%) [17], differing from global trends (Figure 2).

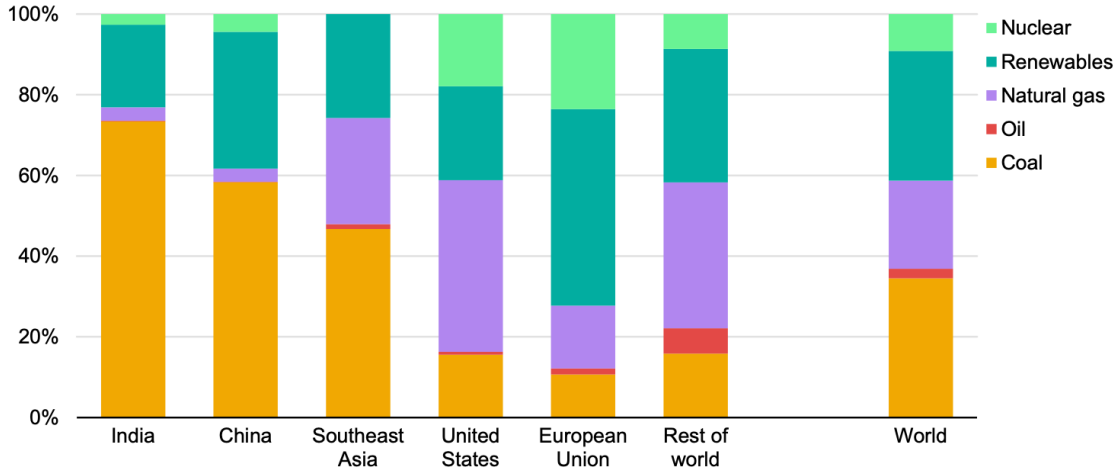

Figure 2: Electricity generation mix by source in selected regions in 2024. Shares are expressed as percentages of total generation. Source: IEA, Global Energy Review 2025.

This reduction was the result of structural changes in energy sectors and industry. Renewables provided about half of the decline, contributed around 48% of electricity generation in 2024, complemented by nuclear power at roughly 23%, while natural gas and coal dropped to 16% and 11%, respectively [3].
Although this overall trend, significant differences also exist within Europe itself (Figure 3) [18].

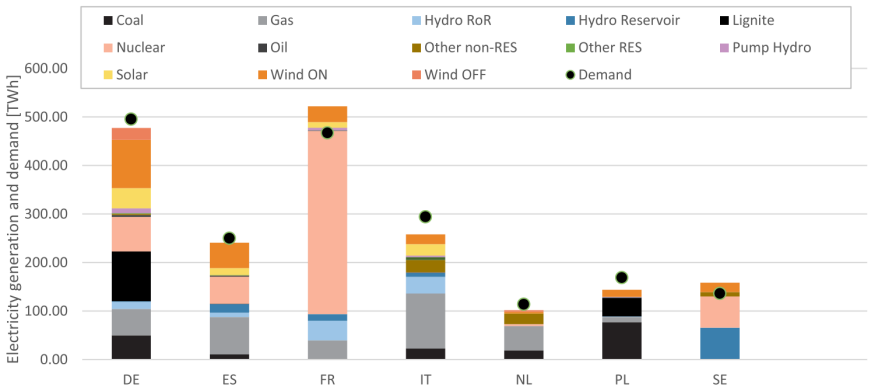

Figure 3: Electricity generation and demand by source in selected EU countries (2019). Source: [18].

In particular, Italy offers a notable case: in 2023, its electricity supply remained heavily dependent on natural gas (38.4%) and oil (37.0%). In contrast, renewables such as hydro (2.7%), biofuels and waste (10.7%), along with wind and solar, accounted for a much smaller share compared with the EU average [3,19]. This stands in sharp contrast to countries like France and Spain, where nuclear and wind power make up a far larger share of the mix (see Figure 3). Although, Italy's electricity mix remains anchored to natural gas, the rapid expansion of photovoltaic capacity is gradually increasing. Similarly, the current drop in EU emissions reflects the rapid uptake of five key technologies: solar PV, wind, nuclear, electric vehicles, and heat pumps, which together avoided over 10% of energy-related CO_2 between 2019 and 2024 without which emissions would have risen at a rate nearly three times higher [3]. In parallel with the expansion of renewable electricity generation, industrial decarbonization efforts increasingly point to the need for integrating additional energy carriers, among which H_2 is gaining remarkable importance [3]. Global H_2 demand has been steadily increasing, confirming its growing relevance in the future energy mix. As shown in Figure 4, most global H_2 output still originates from fossil fuels, primarily natural gas through steam methane reforming (SMR) and coal gasification, while electrolysis contributes only a very limited portion, remaining below 1 Mt H_2 per year, representing less than 1 % of total global production [20].

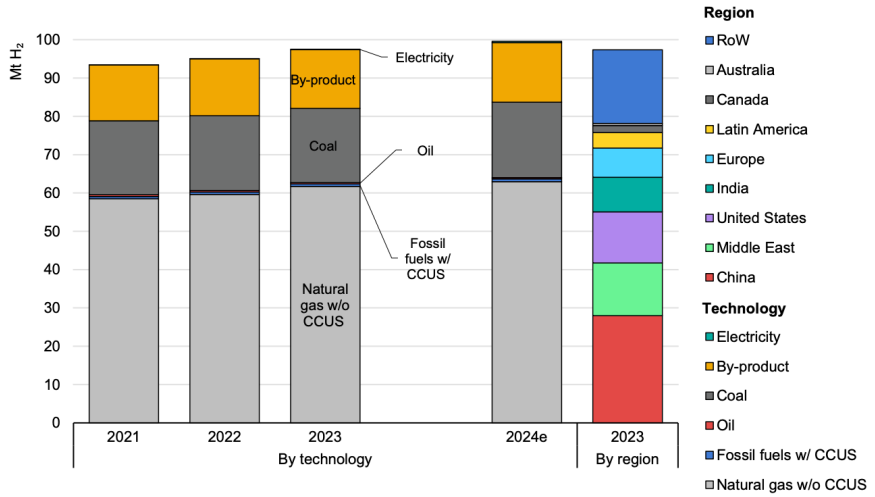

Figure 4: Global H_2 production by technology and region (2021–2023). Source: IEA, Global H_2 Review 2024, CC BY 4.0 [20].

This imbalance reflects the still-dominant role of conventional methods, especially in China, which accounts for nearly one-third of global H_2 output and relies heavily on coal-based processes. For this, H_2 today is more a *climate problem* than a climate solution, accounting for more than 0.9 Gt CO_2/y of emissions associated with fossil-based H_2 production, as defined in the IEA Global Hydrogen Review [20].
Looking ahead, global H_2 demand is projected to exceed 500 Mt by 2050, nearly a fourfold increase compared with 2020 levels, driven by the rapid expansion of renewable-powered electrolysis and carbon capture, utilization, and storage (CCUS) technologies, as foreseen in the IEA Net Zero Emissions scenario [21]. Despite these goals, progress remains limited. Economically, H_2 production still faces a wide cost gap between conventional and low-carbon pathways. In fact, today H_2 produced via SMR currently costs between 0.8 and 5.7 USD /kg H_2, depending on gas prices and carbon-capture configuration [20]. In contrast, green H_2 generated through electrolysis remains significantly more expensive, with price ranges varying between 4 and 13 USD /kg H_2, depending on electricity costs,

electrolyser efficiency, and plant utilization rate [22]. The present cost discrepancy stresses the need to diversify decarbonisation approaches beyond electrolysis and explore cost reduction strategies, such as the integration of biorefineries solutions, based on waste-based feedstocks.

1.3 The biorefinery concept

The goal of biorefineries is to convert different biomass wastes, such as forestry residues, agro-industrial by-products, organic municipal waste, algae and wastewaters into various energy carriers, chemicals and materials. The basic principle is to treat waste as a resource to minimize waste generation and reduce reliance on fossil fuels [23]. The processes inside a biorefinery can be classified into two main groups: biochemical and thermochemical [24] (Table 1).

Table 1:Main biomass conversion technologies with their advantages and disadvantages [25].

Technology	Pros	Cons	Ref
	Thermochemical conversion		
Pyrolysis	Carbon-negative potential, high conversion efficiency; enables full utilization of biomass	Lower net energy output; slower production rate; may cause air pollution	[26]
Gasification	Partial oxidation yields, syngas usable as biofuel; low emissions and operating cost	Tar formation can block fuel lines and filters	[27]
Liquefaction	Broad feedstock range; easy transport; no drying needs	Comparatively high cost; thermal degradation and catalyst deactivation can occur; challenges in scale-up and product separation	[28]
Combustion	Mature technology with scalable applications; heat recovery potentials, volume reduction	Formation of harmful by-products and ash deposition; costly emission control and maintenance	[29]
	Physical conversion		
Mechanical extraction	Inexpensive; no solvent separation; no hazardous reagents; simple operation	Low yield and high labour demand	[30]
Briquetting of biomass	Easier storage and transport; suitable for furnaces; high burning efficiency	High installation cost; large space needed; requires advanced drying/crushing equipment	[31]
	Chemical conversion		

Hydrolysis	Mild reaction conditions; high sugar yield at low temperature	Corrosive environment; high cost; environmental issues due to acid usage	[32]
Solvent extraction (i.e. DES)	Efficient lignin and hemicellulose removal; low toxicity; biodegradable and recyclable;	High viscosity; energy-intensive recovery; limited scalability; possible loss of performance on reuse	[33]
Supercritical conversion of biomass	No solvent residue; very efficient and fast extraction	Expensive installation; high energy demand; needs high pressure operation	[34]
	Biological conversion		
Anaerobic digestion	Low emissions; high-quality products; eco-friendly	Requires pre-treatment; high operational cost; slow reaction rate; limited large-scale application	[35]
Fermentation	Controlled process; high and fast yield; energy-efficient	Scale-up difficulties; heat generation; contamination risk	[36]
Enzymatic conversion	Few by-products; mild conditions; high selectivity	Requires pre-treatment; high risk of deactivation; enzyme cost	[37]

Examples of biochemical processes are fermentation, enzymatic hydrolysis and anaerobic digestion. They are preferred over thermochemical processes because they operate under milder conditions and typically offer high selectivity, which makes them particularly suitable for producing targeted products such as bioethanol or biogas or a high-value specialty product. Their main limitations are longer reaction rates, the high sensitivity to inhibitory compounds, such as polyphenols, heavy metals and salts and therefore the need for relatively clean or pretreated feedstocks [25].

By contrast, thermochemical technologies, such as gasification, pyrolysis hydrothermal liquefaction, and reforming are more versatile toward complex feedstocks, provide faster conversion rates and better suited for large-scale energy carrier generation. Nevertheless, they are energy intensive, requiring elevated pressure and temperatures, often above 200-400 °C, and typically produce complex multiphase effluents (gas, aqueous and solid residues) that require separate treatments, making their downstream processes challenging. These two approaches can also be integrated in order to maximize their efficiencies. However, a key limitation in both is their incomplete organic conversion, which often leads to the formation of undesired by-products [27], [28], [29]. As an example, hydrothermal and fermentation processes often leave behind an aqueous phase containing unconverted carbon. Rather than being discarded, this residual fraction has the potential to be recovered and even repurposed. One promising route is to recover and repurpose these waste streams using a thermo-catalytic process termed aqueous phase reforming (APR), which operates under mild conditions to convert dissolved

oxygenates into H_2-rich gas, offering a dual benefit: reducing carbon waste and generating renewable H_2. The next section explores this process in more detail.

1.4 Aqueous phase reforming

APR was first introduced by Dumesic and co-workers in the early 2000s as a thermo-catalytic process to convert oxygenated hydrocarbons derived from biomass into H_2 and alkanes under liquid-phase conditions [38]. APR was presented as a milder process, which could operate between 200–270 °C and moderate pressures (15–60 bar) [39].

1.4.1 Thermodynamics of APR

APR emerged as a potential technology for converting biomass-derived oxygenated hydrocarbons into a H_2-rich gas phase, according to the following generic stoichiometry (1):

$$C_nH_{2y}O_n + nH_2O \leftrightarrow nCO_2 + (y+n)H_2 \quad (1)$$

The former reaction is the result of the combination of two main different phenomena: the reforming of the oxygenated substrate (2), where C–C and C–H bonds are broken to produce CO and H_2, and the water–gas shift (WGS, (3)), in which CO reacts with H_2O to form CO_2 and additional H_2, which under APR conditions is a three phases reaction, occurring at the interphase between liquid (water), gas (CO) and the solid (catalyst) [40].

$$C_nH_{2y}O_n \leftrightarrow nCO + H_2 \quad (2)$$

$$CO + H_2O \leftrightarrow CO_2 + H_2 \quad (3)$$

In particular, Equation (2) corresponds to the reforming of oxygenated hydrocarbons with a C:O atomic ratio of 1:1, typical of molecules such as methanol, ethylene glycol, or glycerol [41]. From a thermodynamic point of view, the APR becomes favorable at temperatures above 230 °C for small alcohols and polyols, compared to alkanes, which require much higher temperatures.
For this, APR offers two main advantages. Firstly, compared to conventional steam reforming (SR), APR takes place in the liquid phase. This represents a significant benefit in terms of energy demand. Indeed, APR feedstocks are generally dilute aqueous solutions of alcohols, polyols, or oxygenated sugars, which avoids the vaporization enthalpy required for SR, since that process occurs above 800 °C (Figure 5) [17], [40]. Moreover, in contrast to SR, under APR conditions the thermodynamics of the WGS reaction is also favoured ($\Delta G^o < 0$), as shown in Figure 5,b. This differs from SR, where a separate reactor operating at lower temperatures is needed after the reforming step to enable the WGS reaction.

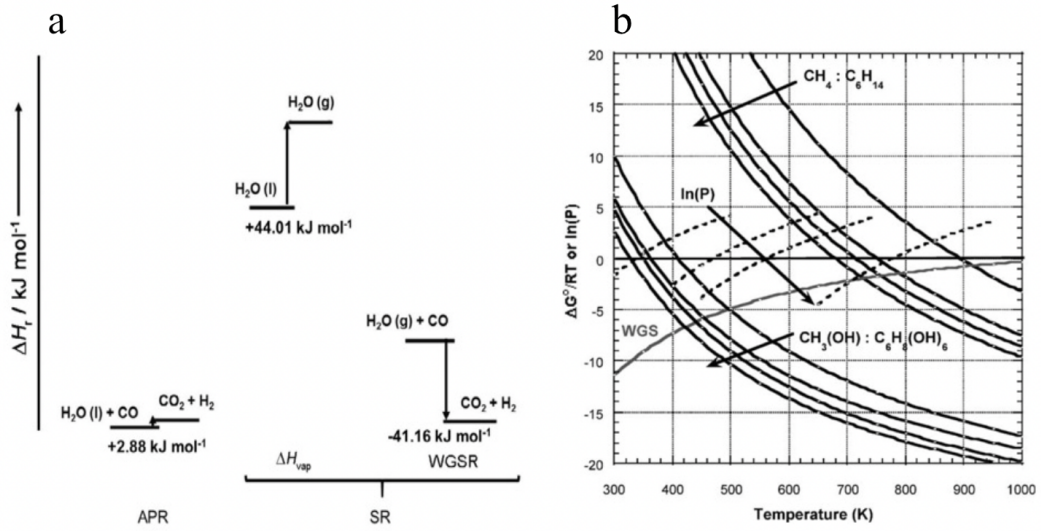

Figure 5: Graphical representation of the enthalpy difference (ΔH°) in APR and SR for the WGS reaction (a) [40] and Gibbs free energy (ΔG°/RT, b) variation diagram for key reactions in APR: methane and alkanes formation (e.g., C_6H_{14} in figure) becomes thermodynamically favorable (ΔG° < 0) only above ~730 K, the oxygenated hydrocarbons reforming (e.g., CH_3OH in figure), together with the WGS reaction, are already favorable under typical APR conditions (473–550 K) [39].

Ripken et al. [40] investigated the thermodynamics of several model compounds, such as ethylene glycol, glycerol, and xylitol, demonstrating that both the reforming and the WGS reactions are endothermic at ambient temperature and pressure (ΔH > 0), as confirmed also by other works [42]. However, despite their positive enthalpy, the Gibbs free energy becomes negative above approximately 40 °C due to the strong positive entropy contribution. The entropy gain, arising from the formation of gaseous products (H_2 and CO_2) from liquid-phase reactants, drives the overall process to become exergonic (ΔG < 0). Consequently, the WGS reaction remains strongly favoured at low and moderate temperatures, with ΔG° reaching highly negative values below 500 K, precisely within the operational range of APR. On this basis, APR is an attractive technology that produces a gas stream rich in H_2 and CO_2, with only limited (or inexistent) CO content, a mixture with potential applications in fuel cells [43].
Connected to the thermodynamics, in APR a critical issue is the selectivity toward H_2, which is often hindered by the competing reaction of methanation [39] [44]. In particular, it has been demonstrated that methane can be formed in APR through CO and CO_2 methanation (Eq. (4) and (5)) and by C-O bond cleavage, but also through C–C bond cracking of the carbon backbone, followed by hydrogenation of a methyl group, as for the case of ethanol [45].

$$CO + 3H_2 \leftrightarrow CH_4 + H_2O \quad (4)$$

$$CO_2 + 4H_2 \leftrightarrow CH_4 + 2H_2O \quad (5)$$

In particular, it was demonstrated that methanation was reduced at high temperature with ethylene glycol [46], [47], whereas an opposite trend was observed with glycerol [44]. Specifically, different molecular structures can lead to distinct reaction mechanisms. In both cases, however, pressures higher than the water

saturation pressure promoted methanation over H_2 formation. This points to a broader concept: APR performance can vary not only with operating conditions but also with the nature of the catalyst and of the feedstock. These aspects will be discussed in the following paragraphs.

1.4.2 APR main reaction mechanisms

The molecule can interact either with the support or with the metal [48]. Figure 6 illustrates the main reaction pathways that oxygenated hydrocarbons, such as polyols can undergo. When the substrate interacts with the support, a dehydration reaction occurs, followed by hydrogenation, which consumes H_2 atoms and reduces the overall H_2 yield. When the substrate interacts with the metal active site, the first step is dehydrogenation, followed by two main reaction pathways [38]:

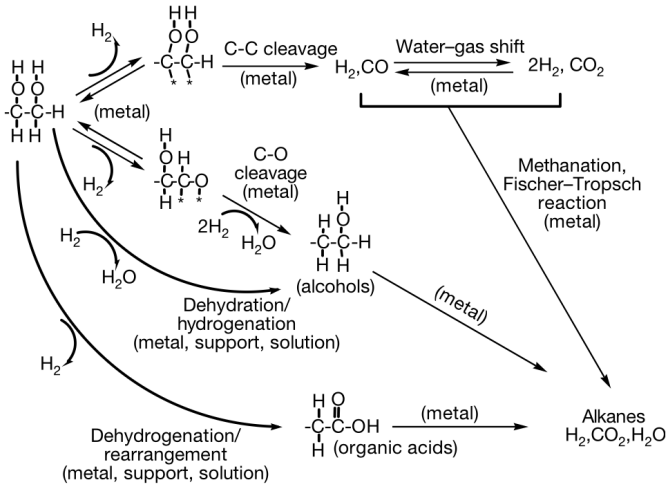

Figure 6: Schematic representation of the main reaction pathways occurring during APR, including the preferential C–C bond cleavage forming H_2 and CO that undergo the WGS reaction, as well as C–O bond cleavage, dehydrogenation, and hydrogenation steps leading to alkanes. Parallel methanation and Fischer–Tropsch reactions can also yield alkanes and other hydrocarbons [38].

i) The C–O bond cleavage pathway, which is not desirable, as it consumes H_2 molecules and leads to the formation of alkanes trough dehydrogenation reactions reducing H_2 content.

ii) The C–C bond cleavage pathway, which by contrasted is preferred, since it generates additional H_2 and CO. Under APR conditions, the WGS reaction converts CO and H_2O into CO_2, further boosting H_2 production. In the case of Pt, it has been demonstrated that C–C bond cleavage is favoured because Pt–C bonds are more stable than Pt–O bonds, leading adsorbed species to preferentially bind to the catalyst surface through Pt–C interactions [38].

The second one is the preferred pathway to maximize H_2 production through APR, but other reactions can also occur. In particular, CO can further react with H_2 leading to CH_4 and alkene formation, reducing H_2 productivity. Also, dehydrogenation reactions can lead to the formation of organic acids, which

could limit the reaction forward as in the case of acetic acid and propionic acid [49,50], or further be rearranged, ending in alkene formation from that part of the starting molecule with carbon backbones that are not directly bonded to oxygen atoms. Additionally, as seen before, at lower temperature (500 K), CH_4 formation from H_2 and CO/CO_2 is strongly favoured ($K \sim 10^9$) [39].

1.4.3 Effect of reaction conditions

APR reaction mechanisms are highly influenced by the operating conditions, such as substrate concentration, temperature, pressure relative to water saturation (P/P_{sat}), the catalyst involved and the reactor used.

1.4.3.1 Effect of feed concentration

APR is generally considered a process suitable for dilute streams, as noted in the previous paragraph. When feedstock concentrations are increased from 1 to 10 wt.%, higher amounts of liquid co-products are typically formed, resulting in lower H_2 and overall gas yields. This trend was clearly demonstrated in a systematic study on oxygenated hydrocarbons derived from hydrothermal liquefaction (HTL) water [51]. In the work, the carbon concentration was varied from 0.3 to 1.8 wt.%. For ethanol, the carbon-to-gas conversion decreased from 70% to 51%, while the H_2 yield dropped from 24% to 17%. A similar effect was observed when ethanol was included in a synthetic mixture together with acetic acid and glycolic acid [52]. Diluted feedstocks are generally preferred in APR, especially when the goal is to maximize H_2 production. However, most studies investigate feedstock concentrations ranging between 1 and 10 wt.%. As concentration increases, process efficiency tends to decrease, but the same happens at the opposite extreme. When the feed is too diluted, a large amount of energy is required to heat the excess water, while the H_2 produced per volume of treated water reduces drastically. As a result, the process approaches an unfavourable energy balance, where the heat demand may exceed the energy recovered from gas production.

1.4.3.2 Effect of feed nature

The effect of temperature on the thermodynamics of APR was discussed previously. In general, the prevalence of C–C bond cleavage over C–O bond cleavage depends on the nature of the feed and the catalyst [53], and it would be limiting to assume the dominance of one pathway over the other based solely on temperature. Since the C-C bond requires higher energy than the C-O bond cleavage, investigate the optimal operating conditions and catalysts properties is crucial to favour C-C pathways, thus maximizing H_2 production. It has been demonstrated that the balance between these two pathways is highly substrate dependent. For instance, R. Alcalá et al. demonstrated that at higher temperatures, C–C bond cleavage dominates ethanol APR over Pt-based catalysts [54].
Differences among substrates were highlighted also in the work of Dumesic et al., where shorter oxygenates, such as methanol achieved higher H_2 selectivity compared to glucose or sorbitol at higher temperatures, as illustrated in Figure 7 [39].

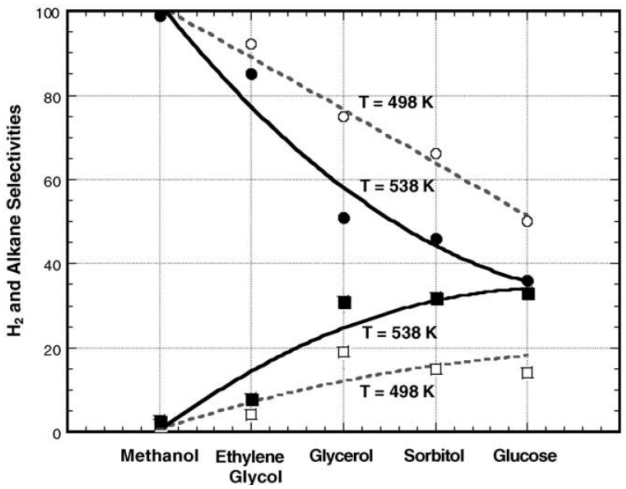

Figure 7: H_2 (circles) and alkane (squares) selectivity obtained from the aqueous-phase reforming of 1 wt.% oxygenated hydrocarbons over a 3 wt.% Pt/Al2O3 catalyst are shown. Data collected at 498 K are represented as empty symbols with dashed lines, while those at 538 K are shown as filled symbols with solid lines [39].

1.4.3.3 Effect of reaction pressure

System pressure plays a crucial role in APR as it dictates whether the reaction medium remains in the liquid phase, thereby avoiding the costly vaporization step. Typically, APR operates under pressures just enough above the saturation temperature (P_{sat}) of water to ensure the system to remain in liquid form throughout the process [39]. In fact, when the system pressure corresponds to the P_{sat} , two phases coexist. At this point, it becomes much harder to control and maintain the temperature, since the two phases exhibit different heat transfer coefficients and, consequently, local temperature differences can generate. Moreover, at this condition, the energy duty required by the APR reactor is the highest, as heat is no longer supplied only for liquid heating but also for the latent heat associated with the phase change. For instance, at 270 °C and the corresponding P_{sat}, the enthalpy of the saturated liquid is 1184 kJ/kg, while an additional 1605 kJ/kg must be provided to evaporate the same mass of water, according to the thermodynamic properties of water under saturated conditions [55].

However, the relationship between pressure and product distribution is non-linear. Experimental studies on butanol APR demonstrated that H_2 and CO_2 selectivity increased with pressure up to the bubble-point, after which further pressure rise caused a decline in gas yields due to suppression of volatile product desorption and enhanced solubility of gases in the liquid phase [56]. Similarly, in glycerol APR, moderate pressures (30–40 bar) favoured higher H_2 yields, whereas excessively high pressures reduced overall conversion and shifted selectivity towards liquid-phase products [57]. From a thermodynamic standpoint, elevated pressures stabilize the liquid phase but also increase the propensity for methanation, particularly when the H_2 partial pressure is high, thus potentially lowering net H_2 selectivity [41,43].

In summary, optimal APR operation is achieved by maintaining the system slightly above the water P_{sat}, providing the best compromise between substrate conversion and H_2 selectivity, particularly when the main interest lies in establishing APR as a viable route for sustainable H_2 production.

1.4.3.4 Catalyst effect

The choice of catalyst is arguably the most critical factor governing activity, selectivity, and stability in APR [48]. Noble metals, particularly platinum (Pt) supported on oxides such as Al_2O_3, SiO_2, or carbon was widely investigated in literature due to its good H_2 production activity in APR. In fact, Pt promotes both C–C bond cleavage and the WGS reaction while minimizing unwanted methanation [58]. Although Pt offers high H_2 selectivity and low CO production, its high cost has encouraged the search for more cost-effective alternatives (30.7 USD/g) [59]. Among these, ruthenium (Ru) price is about half that of platinum (14.1 USD/g) [59], Although it is still considered a precious metal, Ru has gained considerable attention due to its strong activity in C–C bond cleavage. Studies on Ru/C and Ru/Al_2O_3 catalysts showed that Ru promotes deep reforming of polyols, achieving high H_2 productivity. However, at high H_2 concentration, Ru is known also for catalysing methanation reactions, which could increase CH_4 formation at the expense of H_2 selectivity. [41,47]. Figure 8 reports the tendency of the most investigated metals for C-C bond cleavage, WGS and methanation reactions.

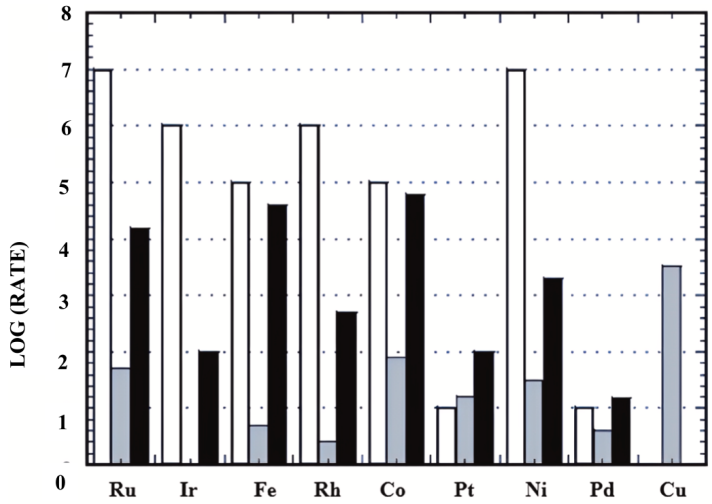

Figure 8: Comparative frequency of C–C breaking bond reactions (white), WGS reaction (grey), and methanation process (black) for various metal [60].

Among the non-noble substitutes, nickel-based catalysts have been deeply investigated. When promoted with basic oxides such as Ca, Mg, or Ce, Ni catalysts exhibit improved dispersion, reduced sintering, and enhanced tolerance to carbon deposition [42]. Although their intrinsic activity is lower than Pt [61], Ni catalysts can achieve competitive H_2 yields under optimized conditions, especially when operated at higher temperatures or with appropriate supports [56]. Bimetallic systems, such as Pt–Re and Pt–Sn, bridge the gap by tuning selectivity between gaseous and liquid products, combining the reforming efficiency of Pt with modifiers that suppress hydrogenolysis [62]. More recently, Ru–Pt catalysts have also been shown to exhibit synergistic behaviour, where Ru promotes C–C bond cleavage and Pt enhance WGS activity while suppressing methanation, resulting in higher H_2 production rates compared to their monometallic counterparts [63]. The selection of catalyst support is also a crucial factor in APR. Reducible oxides such as CeO_2 and ZrO_2 have been shown to enhance oxygen mobility and promote the WGS reaction. In particular, oxygen vacancies facilitate WGS by activating water molecules: firstly, H_2 dissociates, and the resulting oxygen species react with earlier formed CO to produce CO_2, thereby promoting the WGS pathway [60]. It was also

demonstrated that using a CeO_2 support reduces the methanation activity of Ni compared to an Al_2O_3 support [64]. It has been shown that acidic supports like Al_2O_3 may favour dehydration reactions, lead to coke formation and exhibit low stability at high temperatures [65], [53], [43]. Furthermore, a recent finding indicates that Ni catalysts supported on Al–Ca mixed oxides can deliver high H_2 yields and improved stability, highlighting the need to fine-tune support acidity and basicity to manage side reactions effectively [42]. Although Pt remains the reference catalyst, systems based on Ru and Ni offer promising routes to reduce costs and improve the scalability of APR for renewable H_2 production.
Despite significant advances in the performance of catalysts, APR remains strongly affected by deactivation phenomena. The most common issues reported in literature include metal sintering, leaching under hydrothermal conditions, and carbonaceous fouling from phenolic oligomers and heavy oxygenates [66]. Promising strategies to mitigate these effects are the pretreatment of feedstocks (e.g., phenolic extraction, adsorption) and the use of basic or reducible supports to suppress coke and alloying or bimetallic formulations capable of stabilizing active sites [48]. Moreover, catalyst stability is closely tied to the preparation method, suggesting that innovative synthesis approaches may offer a pathway to prolong activity and resistance to harsh APR conditions.

1.4.3.5 Synthesis methods effect

The synthesis route strongly determines the physicochemical properties of APR catalysts, including metal dispersion, particle size, reducibility, and support–metal interactions, all of which ultimately influence catalytic activity, selectivity, and stability [48]. Conventional preparation techniques such as impregnation, co-precipitation, and deposition–precipitation remain the most widely employed due to their simplicity and scalability [67]. However, recent research has highlighted that advanced methods, such as colloidal synthesis, sol–immobilization, and sono-chemical techniques, can offer finer control over active phase morphology. For instance, Callison et al. showed that different Pt nanoparticles sizes supported on Al_2O_3 showed size-dependent selectivity in glycerol APR: larger particles (~3.5 nm) favoured liquid products such as 1,2-propanediol, while smaller particles (~2.2 nm) promoted H_2 formation, pointing out a significant correlation between nanoparticle size and reaction pathway [68]. Similarly, Hakim et al. compared deposition–precipitation and impregnation methods for Ni–Ce–Cu catalysts supported on hydroxyapatite and demonstrated that the former produced improved metal distribution and higher surface areas, which in this case improved H_2 yields [67]. Sono-chemical synthesis has also emerged as a powerful tool: Ni–Mo/γ-Al_2O_3 catalysts prepared under optimized ultrasound irradiation exhibited enhanced physical characteristics (i.e., surface area, pore volume and size) and yielded higher selectivity toward 1,3-propanediol from glycerol [69], while Mo-promoted Ni/CeO_2 prepared via ultrasonic cavitation showed reduced particle agglomeration and improved H_2 productivity [70]. Together, these examples demonstrate again that results are system-specific and that tailoring synthesis methods is possible to mitigate deactivation phenomena such as sintering and coke formation but also to tune product distribution between H_2 and liquid co-products. Therefore, rational catalyst preparation emerges as a crucial design parameter for optimizing APR performance.

1.4.3.6 Reactor design effect

Over the years, a variety of reactor designs have been employed for APR, reflecting the gradual evolution from fundamental studies to applied process development. Stirred batch reactors are the most widely used at the laboratory scale from the early studies, since they allow for preliminary screening of catalysts and evaluation of the kinetics aspects under controlled conditions. Batch systems are limited in assessing long-term catalyst stability and they do not replicate the continuous nature of industrial effluents [71]. For this fixed-bed tubular reactors have become the best choice since they operate continuously, ensuring complete catalyst wetting good temperature control, good for scaled up studies. However, they may suffer from mass transfer limitations when large catalyst particles are used. For instance, D'Angelo et al. reported strong intraparticle diffusion resistance in fixed-bed APR with pellets of around 1.5 mm diameter, whereas adopting a wash-coated microchannel reactor overcame this limitation and improved H_2 selectivity through more efficient mass transfer [72]. Nijhuis and co-workers further demonstrated that operating a Pt–Ru wash-coated microchannel reactor under two-phase flow regime with H_2 stripping increased sorbitol conversion and boosted H_2 selectivity by up to 30% compared to conventional reactors [71]. Such designs belong to the broader class of intensified reactors, which have been explored to overcome heat and mass transfer limitations. Besides microchannels, membrane reactors have also been tested, enabling simultaneous reforming and selective H_2 separation, which doubled H_2 recovery compared to conventional systems [73]. Structured reactors, including foams and monoliths, are also gaining attention for their ability to enhance radial heat and mass transfer in three-phase APR systems [43]. Overall, batch reactors remain essential for early-stage catalyst testing, while fixed-bed systems dominate subsequent studies under continuous, industrially relevant conditions. Emerging intensified reactors represent the next step, enabling optimization strategies that can accelerate the scale-up of APR toward more efficient H_2 production.

1.5 Potential wastewater streams for APR application

Building upon the understanding of APR fundamentals, recent research has increasingly focused on the applicability of the process to real aqueous effluents, since wastewaters are often diluted streams and their waste nature would provide cost reduction strategies for H_2 production and energy recovery. In this work, APR has been explored as a dual-function process capable of reducing both the organic content of wastewater and to convert residual carbon into H_2-rich gas phase. Furthermore, the growing studies on biorefinery effluents and agro-industrial side streams have boosted the interest in identifying industrial wastewaters as suitable feedstocks to accelerate APR development towards industrial scale [74].

The suitability of a given effluent largely depends on the concentration and composition of dissolved organic content. Wastewaters rich in short-chain alcohols (methanol, ethanol, butanol) [75–77], polyols (glycerol, sorbitol, xylitol) [78–80] and volatile fatty acids (lactic, glycolic acids) [51] are particularly attractive because these compounds are known to undergo efficient C–C and C–O bond cleavage under APR conditions, producing H_2 -rich gas mixtures [81]. From a broader biorefinery perspective, aqueous fractions from lignocellulosic biomass conversion processes, such as HTL [82,83], Fischer–Tropsch synthesis [84], and pyrolysis [85,86], biodiesel production [78], as well as from food-processing industries including breweries [87], cheese whey [88], fruit juices [89] and starch-

based processes [90], have also been evaluated. Other promising effluents include those from biogas slurry [91], sewage sludge [92], which may contain constituents of the lignocellulosic fraction, such as xylitol, glucose, fructose, and sucrose [93] [80,94,95]. Our research group have deeply investigated APR from the water fraction of HTL process [51,66,82,96,97] because this aqueous phase, although often considered a low-value by-product, actually contains a significant share of the feedstock carbon (28–45 wt.% of the initial carbon ends up dissolved in this stream) [51]. For instance, Panisko et al. characterized the wastewater from the HTL of corn stover and loblolly pine residues, reporting the presence of low-molecular-weight organic acids (glycolic, acetic, formic, propionic), simple alcohols such as methanol and ethanol, along with minor amounts of ketones and phenolic compounds [98]. Recently, Pola et al. characterized the aqueous fraction obtained from the HTL of Kraft black liquor, an alkaline stream rich in hemicellulose and lignin residues from the pulp and paper (P&P) process. They reported a total organic carbon (TOC) of about 30 g/L, with major constituents including organic acids (formic, acetic, glycolic, lactic), simple alcohols (methanol, ethanol), and a notable fraction of phenolic compounds such as catechol [99]. While organic acids and alcohols are valuable substrates for APR, phenolics can act as catalyst poisons, making their selective removal a key step prior to further valorisation by APR. Building on the literature knowledge of the best-performing model compounds in APR, this know-how serves to explore the wide range of potential industrial wastewaters available with a more practical approach, contributing to bridging the gap that still exists between APR research and its industrial application. In particular, two types of wastewaters were selected and further investigated in the present work: those from the P&P mill industry and from wineries.

1.5.1 P&P wastewater potential

The P&P industry is one of the largest industrial users of water and ranks third worldwide in wastewater generation, after the primary metals and chemical industries [100]. Every year, more than 400 million tons of paper and cardboard are manufactured globally, with Italy contributing nearly 9 million tons on its own [101]. Because of this, the industry is under growing pressure to reduce its water footprint and lessen the environmental impact of its wastewater. P&P wastewaters are highly variable, as their composition depends on the production stage, such as wood chipping, pulping, bleaching, or papermaking, and on whether virgin or recycled fibers are used (Figure 9).

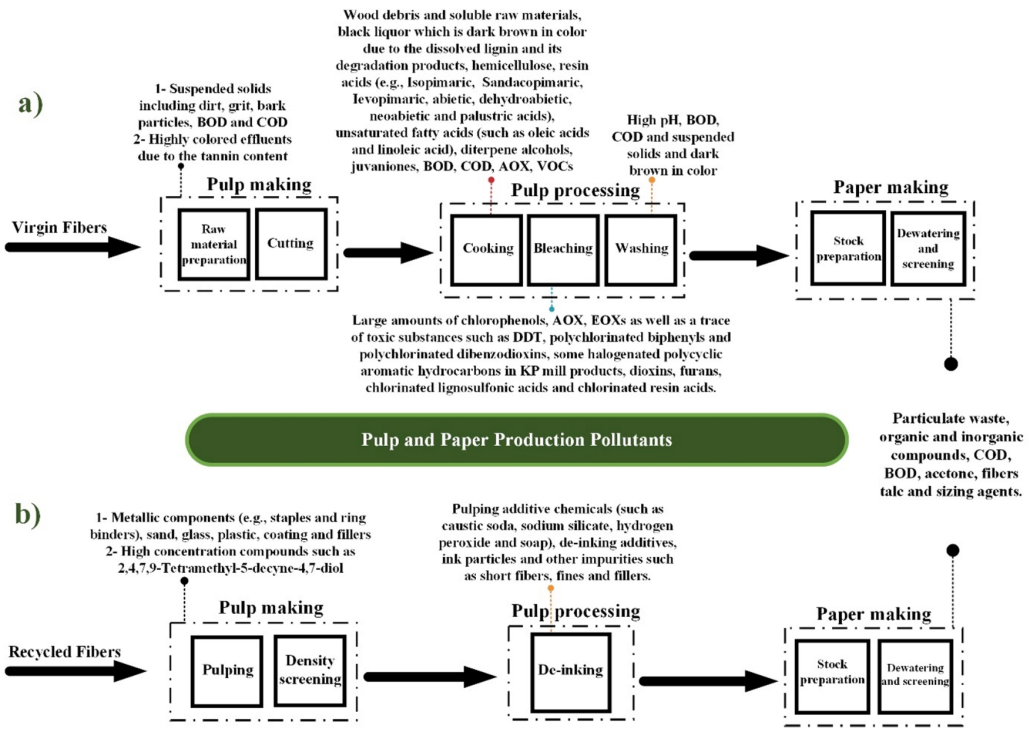

Figure 9. A simplified scheme of P&P production cycle from virgin (a) and recycled (b) fibers and their main waste streams. Taken form [102].

P&P wastewaters represent as promising feedstock for APR application, based on the assumption that during the different processing stages, a portion of the cellulose and hemicellulose fractions may hydrolyse and release dissolved sugars into the effluent. The role of biomass derived sugars in APR has been extensively investigated [79,94]. It has been shown that simple sugars like glucose can achieve H_2 selectivity of up to 46% at 95% glucose conversion when using Pt-based catalysts [80]. Ru-based catalysts have been shown to be active in the pretreatment of biomass-derived sugars, such as glucose and maltose, converting them into their corresponding sugar alcohols (e.g., sorbitol and maltitol, respectively) [103,104]. Furthermore, bimetallic catalysts combining Pt and Ru have demonstrated complementary activity, outperforming their monometallic counterparts in terms of H_2 yield when working with starch-based wastewaters. In particular, PtRu/C achieved one of the highest reported H_2 yields, reaching approximately 51 mmol H_2/g TOC [90]. P&P wastewater could therefore serve as potential APR feedstock. Conventionally P&P wastewaters undergo physical, chemical, and biological treatment methods, but they often fail to effectively remove pollutants while recovering the carbon content for energetic valorisation [105]. Biological treatments remain the most common approach, typically combining aerobic and anaerobic stages, and achieving COD removal efficiencies between 75% and 90%. Before performing biological treatments, several pretreatment steps such as coagulation, flocculation, and sedimentation are usually employed in order to eliminate any suspended solids and to improve the downstream performance. In recent years, advanced oxidation processes (AOPs) and membrane filtration systems have emerged as promising alternatives, since they have shown to be capable of reaching COD removal efficiencies up to 99%. However, large-scale adoption remains limited by their relatively high energy demands and high capital costs [102]. This opens the door to alternative technologies such as APR, which could both reduce COD by converting residual sugars and polyols in their P&P

waste streams and recover energy in the form of valuable gases that can be used on-site or sold externally.

1.5.2 Winery wastewaters potential

Several studies have highlighted that wastewaters from wineries could serve as potential feedstocks for energetic valorisation strategies, as they contain compounds that are not fully oxidized and thus retain significant chemical energy [70], [107]. An innovative approach involves exploiting bioethanol from winery wastewater (WWW) in APR as an approach for energetic valorisation of WWW. Ethanol compared to more complex oxygenates such as glycerol and sorbitol, due to its small size and lower oxygen content reduce the competitive adsorption on the catalyst and condensation products and a reduced tendency to side reactions that lower H_2 selectivity [108]. Moreover, since ethanol has been widely investigated as a model compound, extensive information is already available on its APR performance. In pioneering work, Dumesic and co-workers investigated ethanol reforming over Pt-based catalysts such as Pt/SiO_2 and Pt/Al_2O_3, achieving H_2 yields close to the theoretical maximum under optimized conditions [58]. Subsequent studies confirmed that ethanol APR can reach complete conversion depending on the catalyst and operating parameters, with product distributions dominated by H_2 and CH_4, and negligible CO due to the efficient WGS reaction [91], [109]. More recent research has demonstrated that catalyst structure and metal–support interactions strongly influence selectivity: for instance, small Ru particles or Ru–Pt bimetallic systems suppress methanation and enhance H_2 selectivity compared to their monometallic counterparts [110], while PdZn intermetallic catalysts stabilized on carbon supports have shown stable operation with CO-free H_2 production [111]. Moreover, high availability of bioethanol in several industrial effluents such as winery, brewery, and distillery wastewaters, makes it a particularly attractive substrate for APR, offering the combined benefits of H_2 production and wastewater remediation.

In 2021, global wine production was estimated at approximately 25 billion liters [112]. Considering that WWW generation ranges from 1 to 4 litre per litre of wine, this corresponds to an average of ~62.5 billion litres of WWW produced worldwide in the same year [106]. WWW is characterized by high COD values, ranging from 800 to 300,000 mg O_2/L [113], with ethanol alone contributing up to 70 wt.% of the TOC. Other typical components include organic acids (acetic and tartaric acids), soluble sugars (glucose, fructose), polyphenolic compounds (tannins, lignin derivatives) and inorganic salts [113]. Conventionally, in Italy the management of winery by-products and wastewater is regulated by national legislation (Law 238/2016) [114], which requires the delivery of grape marc (vinacce) and grape lees (fecce) to authorized distilleries, unless they are directed to approved alternative processes for energy recovery (e.g., biogas generation, combustion). In distilleries, the ethanol contained in WWW is recovered and purified into alcoholic beverages such as grappa and brandy, while the residual effluent is typically treated through biological processes [115]. However, ethanol concentration in WWW is highly variable depending on the processing stage, winery size, and product diversity [106], which complicates recovery through distillation [116]. Furthermore, distilleries themselves are not environmentally neutral: the production of 100 L of

pure alcohol has been estimated to release approximately 900 kg of CO_2-equivalent emissions [117].
Alternative biological treatments for WWW include constructed wetlands and microbial fuel cells (MFCs). Wetlands can achieve up to 88% COD removal, while MFCs reach around 42% but also enable limited energy recovery [118]. Conventional activated sludge processes, more widely used, typically achieve 80–97% COD removal [119,120], yet they often fail to meet stringent discharge limits and lack in recover energy strategies. In addition, they require long retention times and large storage volumes, which reduce process efficiency [121]. This context highlights the potential of APR, as it could simultaneously address COD removal and generate a H_2 -rich gas, thus coupling wastewater treatment with renewable energy production. It can also be considered in combination with existing biological processes, as demonstrated in recent studies. In particular, Bu et al. showed that combining biogas slurry (BS), the liquid fraction obtained from distiller grain anaerobic digestion, with APR using a MOF-based catalyst resulted in an improved COD removal efficiency of 86% and additional energy recovery, producing over 10 mL H_2 within 6-hour reaction time (2.17 mL H_2 per mL of BS fed) [91].

1.6 Research gap in APR development at industrial level

Many of the studies available in the literature are based on synthetic wastewater streams, formulated to mimic the composition of real effluents. This approach is often adopted because working with real wastewaters is highly challenging: while these high-strength effluents are rich in organics well-suited for APR, they also frequently contain inhibitory compounds such as inorganic salts and phenolics [66], [74], [83]. Current research is therefore increasingly oriented towards evaluating the effect of such minor constituents on APR performance, with a particular focus on catalyst stability and deactivation phenomena.
It has been demonstrated that residual waters from lignin-rich HTL contain mainly organic acids and phenolics. While these species can be partially converted to H_2 by APR, the presence of phenolics compounds was identified as a major cause of catalyst deactivation [83]. Follow-up studies revealed that pretreatments, such as the selective extraction of phenolics, can significantly enhance reforming efficiency and prolong catalyst lifetime [82,122]. Other studies have investigated the APR of phenolic compounds, demonstrating its limited feasibility due to low H_2 yields[43].
Beyond pretreatment, the design of the catalyst can also play an important role towards preventing catalyst deactivation. Catalysts that have been tailored with a controlled pore size distribution could provide a several advantages: small pores would allow access to small, light oxygenates, such as APR substrates, while larger molecules, which are sterically hindering and that are primarily responsible for deactivation (such as lignin-derived oligomers or phenolics) would be blocked. Another way is related to novel synthesis strategies that have been developed to enhance catalyst resistance to sintering and leaching. An example is the use of exsolution techniques, where active nanoparticles are partially embedded into the support lattice. This approach has been shown to improve metal anchoring and enhance redox stability [107], [123]. For example, Huang et al. demonstrated that Ni exsolved from perovskite oxides significantly enhanced both CO conversion and H_2 yield in the WGS reaction, while maintaining superior long-term stability compared to conventional catalysts [124]. Therefore, this approach could be exploited to potentially reduce deactivation phenomena in APR. Despite these

advances, the majority of APR research remains confined to laboratory scale, with only a few studies progressing to pilot demonstration and none yet reaching full industrial implementation [49]. This limited progress is partly due to the reluctance of industry to consider APR at large scale, given the persisting uncertainties surrounding catalyst deactivation and stability with real streams. To accelerate this transition, it is essential to integrate techno-economic analysis (TEA), energy assessments, and life cycle assessment (LCA) into process development. These methodologies have the potential not only evaluate the feasibility of APR at industrial scale and to identify its role within broader biorefinery and wastewater valorisation strategies but may also serve as a powerful tool to support the decision making toward industrial scale-up by providing robust, quantitative insights into performance, sustainability, and economic viability. The research group performed a detailed conceptual design and TEA of a coupled HTL–APR system for lignocellulosic residues, showing that the integration could supply over 100% of the H_2 required for biocrude upgrading while achieving competitive H_2 costs of around 1.5 €/kg compared with electrolysis [97]. Complementarily, it was evaluated the use of in situ H_2 from glycerol APR to produce sustainable aviation fuel (SAF), combining TEA with a LCA analysis. Their results demonstrated that APR integration reduced the minimum fuel selling price by 17% and lowered the greenhouse gas footprint by ~54% relative to conventional fossil-based H_2 supply [125]. This study is a practical demonstration which highlight the potential role of APR in the bioeconomy as a pathway to valorise aqueous organic wastes into H_2 and other valuable gases.

1.7 Aim of the thesis

The present work aims to investigate the feasibility of APR as a valorisation strategy for biomass-derived wastewaters using a multi-level performance assessment. Since the major challenges in APR development lie in its implementation at industrial scale, identifying real waste streams as viable feedstocks was a crucial first step. This approach could significantly accelerate the integration of the technology into existing systems while offering potential economic and environmental benefits in line with circular economy principles. With this in mind, and considering that small alcohols, polyols, and sugar alcohols were identified as the most suitable APR compounds, two industrial wastewaters were selected accordingly: 1) the P&P wastewater was selected for its potential content of dissolved sugars or remaining from cellulose processing, with cellulose being a well-known and explored APR substrate [126,127], 2) winery wastewaters were chosen for their residual ethanol content, a small alcohol which was already presented earlier for its favorable reforming activity.
Subsequently to their supply, their chemical composition was characterized and their APR performance evaluated. Even though APR has been substantially studied, several questions regarding the effects of operating conditions on catalytic performance and product distribution remain. For this reason, this thesis includes also an investigation of the major model compound, ethanol, varying reaction parameters to investigate their influence on APR efficiency and H_2 selectivity. Furthermore, since catalyst selection represents another critical aspect, an initial screening of commercially available and literature-established catalysts was conducted, followed by the introduction and evaluation of a newly synthesized

catalyst prepared via exsolution, which to the best of my knowledge, had never been applied to APR before.

While previous studies have explored the efficiency of APR using a range of feedstocks, moving from controlled lab conditions to full-scale industrial applications demands more than just a proof of concept. For this, a detailed process design based on the development of a suitable wastewater treatment facility based on APR for energy recovery, combined with realistic performance data (with the aim of industrial applicability) scaled from tests performed in a continuous reactor, is mandatory. In this thesis, the technology was investigated to assess its ability to deliver two different renewable energy outputs: electricity and hydrogen. The energetic performance of the process was then evaluated over both short-term operational cycles and long-term deployment through an energy sustainability assessment (ESA), as previously explained for evaluating similar studies [128].

To integrate the analysis of the scaled process's energy performance, a TEA was carried out to estimate cost expectations and identify development limitations for potential optimization strategies. Finally, to complete the study and given the growing importance of sustainability in industrial processes, an LCA was also conducted to understand its broader environmental impact, from resource input to emissions and waste. The environmental performance, based on global warming potential (GWP) impacts, was then compared with both conventional and emerging energy recovery routes that produce comparable energy vectors. The combination of these multi-level performance analyses aligns with the overall aim of this thesis to contribute to the development of APR toward a practical reality, in line with the need for innovative biorefinery processes that not only produce renewable energy but also promote clean water supply, as strongly recommended by the sustainable development goals.

Chapter 2. Material and methods

2.1 Experimental methodology

2.1.1 Wastewaters characterization

A comprehensive investigation was conducted on the collected wastewater samples to assess their chemical composition and to define suitable disposal and valorisation strategies. This process also involved direct consultations with wastewater producers. In particular, WWW exhibited a high variability in composition, reflecting the specific production methods adopted by each winery. For this reason, several assumptions were necessary to simplify the analysis. To validate these assumptions, a dedicated survey was developed, and its main findings are presented in Table 2.

Table 2. Summary of the main findings and assumptions adopted in this study, derived from the survey on operational parameters and management practices for winery wastewater, based on data collected from Frescobaldi and other representative Italian wineries.

Parameter	Value	Notes
Ethanol concentration (wt.%)	5	Based on Frescobaldi winery wastewater, a large winery
Operation period (months)	8	Depends on the dimension of the winery, for large wineries up to 8 months
Winery wastewater sent to distilleries (%)	60	For the production of alcoholic beverages (such as grappa, spirits, and brandy)
Winery wastewater sent for tartaric acid recovery (%)	20	Tartaric acid is the most abundant acid in wine and is used to measure acidity levels
Winery wastewater reused internally (%)	20	Reused for irrigation or as amendment when in a more solid form
Wine lees waste (%)	30-50	Up to 50% of winery wastewater can consist of wine lees
Cost of winery wastewater treatment (€/m^3)	< 1	Wastewater treatment is the responsibility of the winery, but distilleries pay for the collected wastewater

For the wastewater characterization, five real industrial effluents were obtained from different production sectors through direct coordination with companies willing to provide representative samples for research purposes. Two industries belonged to the P&P sector. Burgo Group supplied four distinct wastewater streams from virgin cellulose fibre processing processes (R1, R2, R3, and R4), while Pro-Gest S.p.A. provided a fifth effluent (R5) derived from a recycled cellulose fibre.

A third collaboration was also established with a Tuscan winery (Frescobaldi, Florence, Italy) from which a sample of real winery wastewater was received.
The organic composition of the liquid fraction was characterised using high-performance liquid chromatography (HPLC, Prominence Shimadzu, Kyoto, Japan) equipped with a refractive index detector (RID-10A, Shimadzu, Kyoto, Japan) and a 300 mm × 7.8 mm ROA-Organic Acid H^+ (8%) column (Rezex Phenomenex, Torrance, USA). The mobile phase consisted of 5 mM H_2SO_4 in water, operated at a flow rate of 0.7 mL/min and a column temperature of 50 °C. To complement the investigation of the organic composition the liquid phase was also analysed using gas chromatography–mass spectrometry (GC-MS, 7890A GC coupled with 5975C MS, Agilent Technologies, Santa Clara, USA) equipped with a DB-5 ms column (30 m × 0.25 mm × 0.25 μm). Samples were derivatized with methyl chloroformate (MCF) following the procedure described by Tito et al. [96] and developed by Madsen et al. [97]. The injector was operated with helium as carrier gas at a constant flow of 0.8 mL/min, and the oven program consisted of 40 °C (1 min), ramped at 5 °C/min to 300 °C, with a final hold of 5 min. The TOC was measured using a TOC-VCSH analyser (Shimadzu, Kyoto, Japan) equipped with a non-dispersive infrared detector. Thermogravimetric analysis (TGA) was performed on the solid content collected from the centrifugation of R5 wastewater sample using a TG 209 F1 Libra® (NETZSCH GmbH, Selb, Germany). Approximately 0.01 g of sample was analysed using a heating rate of 10 °C/min over a temperature range of 25–900 °C under a nitrogen flow of 60 mL/min. The quantification of total sulfur (S_{tot}), calcium (Ca^{2+}), magnesium (Mg^{2+}), and potassium (K^+) was performed using inductively coupled plasma mass spectrometry (ICP-MS, iCAP Q, Thermo Scientific, Waltham, USA). Nitrate (NO_3^-), orthophosphate (PO_4^{3-}), and COD were quantified using HACH LANGE cuvette tests (Hach GmbH, Düsseldorf, Germany) and a DR5000 spectrophotometer (Hach, Germany). Nitrates and orthophosphate were determined using LCK340 and LCK350, respectively, while COD was measured with the LK514 cuvette test. Inorganic anions (chlorides: Cl^-, sulfates: SO_4^{2-}, nitrates: NO_3^-) for the P&P wastewater were analysed using an ion chromatography (Thermo Scientific, Waltham, USA) equipped with an ADRS 600 suppressor (4 mm), a conductivity detector, and an IonPac AS11-HC-4 μm column (4 × 250 mm, Thermo Fisher, USA). The eluent was composed of 30 mM KOH, operating isostatically at a flow rate of 1.5 mL/min with a column temperature of 30 °C. The total polyphenol content of the winery wastewater sample was quantified using the Folin–Ciocalteu colorimetric method (ISO 14502-1:2005) as described by Fraterrigo et al. in [129].

2.1.2 Catalytic tests

The APR tests were initially performed in batch mode to investigate the influence of operating parameters and feed composition on H_2 production. Experiments were conducted in a 300 mL Parr (4561) mini bench-top reactor equipped with a digital pressure transducer and magnetic stirring (380 rpm) to avoid external mass-transfer limitations. The reactor was loaded with 75 g of aqueous solution containing ethanol or real wastewater feeds. The mixture was purged with nitrogen to remove air and then pressurized to the desired initial pressure (2–6 bar), such that the final operating pressure resulted from the sum of the temperature-dependent saturation pressure and the initially applied N_2 pressure. Tests were carried out at temperatures ranging from 230 to 270 ºC and ethanol concentrations between 1 and 5 wt.%, using

100gr of Pt and Ru based catalysts. In particular, Pt/C and Pt/Al_2O_3, were tested alongside Ru/C, Ru/Al_2O_3, Ru-ex/CeO_2. The reaction time was varied between 0 and 6 hours, with continuous temperature monitoring until steady-state conditions were reached. Additional APR experiments were carried out in a smaller 70 mL batch reactor to assess the performance of novel catalysts (Ru/CeO_2, $Y_2Ru_{0.1}Fe_{0.1}Zr_{1.8}O_7$, $Ru_{0.2}Y_2Zr_{1.8}O_7$ and $Y_2Zr_{1.8}Fe_{0.2}O_7$). A solution of 1 wt.% of ethanol in 30 mL was prepared with a 40 mg of catalyst. The desire initial pressure was set at 5 bar as for described above and the APR reaction was performed at 3 different temperatures (230, 250 and 270 ºC). The smaller reactor setup enabled an efficient screening of their catalytic behaviour while minimizing material consumption and maintaining similar reaction environments.

Once the reaction time was reached, the system was cooled to room temperature before opening. The gas phase was first analysed using a micro–gas chromatograph (Micro-GC, SRA Instruments, Milan, Italy) equipped with a thermal conductivity detector (TCD). The system was composed of two columns: a Molsieve 5A column (100 °C) that used argon as the carrier gas for the analysis of H_2, O_2, N_2, CH_4, and CO, and a PoraPLOT U column (85 °C) that used helium as the carrier gas for the analysis of CO_2, C_2H_6, C_2H_4, and C_3H_8. The injection temperature was set at 100 °C. The inlet pressure was set at 2.1 bar. Gaseous components were quantified by external calibration using certified standard gas mixtures and linear regression, with N_2 employed as an inert tracer to determine the total gas formed from the initial headspace pressure via a molar balance. Subsequently, the liquid phase was collected and filtered prior to TOC analysis and HPLC analysis of the organic compounds, as described in the previous paragraph.

Following the batch experiments, continuous reactor tests were designed to simulate the steady-state operation of an upscaled industrial process. The catalytic tests were carried out using a PID Microactivity-Efficient MME61020 reactor (PID Eng&Tech) operating under continuous-flow conditions. The setup consisted of a tubular stainless steel SS316 reactor (with an internal diameter of 9.1 mm and a length of 305 mm) housed in an isothermal furnace and equipped with a high-pressure gas–liquid separator, a condenser maintained at 5 °C, a pump to carry out the liquid stream and a flow controllers for feed and pressure regulation. APR experiments were conducted at 270°C, using a liquid feed rate of 0.6 $mL \cdot min^{-1}$, a system pressure of 60 bar, a residence time of 3.3 minutes and a catalyst mass of 1 g (WHSV = 1.8 h^{-1}). The input feed consisted of a 5 wt.% ethanol aqueous solution. After reaching the target temperature, the reactor was left to stabilize for approximately 30 minutes to ensure steady-state conditions, after which gas and liquid samples were periodically collected and analysed, following the same procedures described previously for the batch tests.

The performance of the catalysts in the ethanol APR was evaluated through the following indicators as reported below:

The ethanol conversion (%) expresses the fraction of ethanol converted during the reaction, calculated as the ratio between the reacted and the initial moles of ethanol (6):

$$Conversion_{ethanol}\ (\%) = 100 \times \frac{mol_{in}ethanol - mol_{final}ethanol}{mol_{in}ethanol} \qquad (6)$$

i) The carbon-to-gas conversion (C to G, %) quantifies the fraction of carbon atoms from the feedstock converted into gaseous species and is defined as:

$$C\ to\ G\ (\%) = 100 \times \frac{mol_{fin} C_{gas}}{mol_{in} C_{ethanol}} \quad (7)$$

ii) The stochiometric H_2 yield (Y_{H2}, %) measures the efficiency of converting the reactant into a desired product and here it is expressed as:

$$Y_{H_2}\ (\%) = 100 \times \frac{mol\ H_2}{mol_{in}\ ethanol} \quad (8)$$

iii) The APR H_2 selectivity (APR–S_{H2}, %) indicates the deviation of the experimental H_2/CO_2 molar ratio from the theoretical stoichiometric value expected for the reforming of ethanol, as follow:

$$APR - S_{H_2}\ (\%) = 100 \times \frac{\frac{molH_{2(observed)}}{molCO_{2(observed)}}}{\frac{molH_{2(theretical)}}{molCO_{2(theretical)}}} \quad (9)$$

iv) The H_2 productivity is expressed as the ratio between the moles of H_2 produced in the gas phase and the initial moles of carbon fed to the reactor:

$$H_2\ productivity = \frac{mmolH_2}{mol_{in} C_{ethanol}} \quad (10)$$

v) Finally, the H_2 production normalized to nominal Ru loading (mmol H_2/gRu) was calculated to evaluate the intrinsic catalytic activity, accounting for differences in the amount of active metal in each formulation:

$$Normalized\ H_2\ production = \frac{mmolH_2}{gRu} \quad (11)$$

2.1.3 Catalyst synthesis

The Ru/CeO_2 exsolved catalyst was synthesized through a modified Pechini method, originally introduced by Pechini (1967) as a polymerizable complex route for the preparation of mixed metal oxides with high homogeneity and controlled stoichiometry [130]. This approach relies on the formation of metal–organic chelates between dissolved metal cations and hydroxycarboxylic acids, followed by polyesterification with a polyalcohol, promoting the development of a polymeric network that ensures atomic-scale mixing of the precursors.
In the present synthesis, the method was adapted using oxalic acid as the chelating and precipitating agent and ethanol as the solvent and polyalcohol medium.
In order to obtained a final mass of catalyst of 1.5g, the following two precursor solutions were prepared separately:

(i) an oxalate solution, obtained by dissolving 1.983 g of *oxalic acid monohydrate* in 16 mL of ethanol;
(ii) a metal precursor solution, prepared by dissolving 3.709 g of *cerium(III) nitrate hexahydrate* ($Ce(NO_3)_3 \cdot 6H_2O$) and 6.294 g of *ruthenium nitrosyl nitrate* in 88 mL of ethanol under continuous stirring until complete dissolution.
Once both solutions were homogeneous, the oxalate solution was added dropwise to the Ce–Ru precursor mixture under vigorous stirring. The system rapidly increased in viscosity as metal oxalate complexes formed (Figure 10). The resulting gel-like suspension was aged under stirring for 2 h to promote the coordination equilibrium between the mixed metal ions and oxalate ligands, forming a mixed-metal oxalate gel.
The reaction mechanism is schematically represented in Figure 10. Oxalic acid initially coordinates with metal cations (M^{n+}) to form a metallic oxalate complex, as shown in the first reaction. Subsequently, ethanol reacts with the oxalate groups to generate ester linkages through partial esterification, as illustrated in the second reaction, promoting mild polymeric cross-linking within the gel matrix:

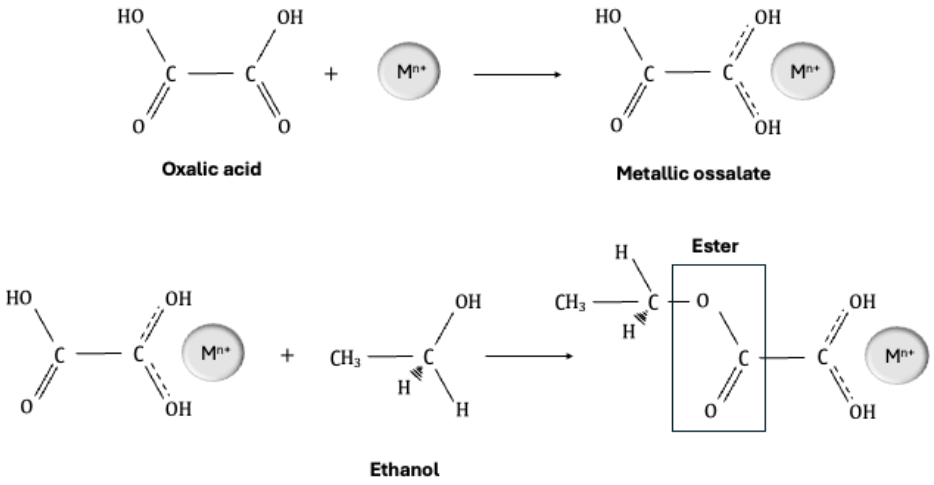

Figure 10 Diagram showing the reaction pathway in the modified Pechini oxalate method. Oxalic acid first binds with metal ions (M^{n+}), forming oxalate complexes. These then react with ethanol, leading to partial ester formation and the development of a polymeric gel network. This step promotes an even distribution of cations before calcination (adapted from [131]).

After ageing, the gel was centrifuged at 4000 rpm for 15 minutes at 15 °C. The supernatant was discarded, and the gel was dried at 80 °C for 12/20 hours under loosely covered aluminium foil. The resulted solid was finely ground and subsequently calcined in air in subsequent 2 steps, each of 4h (450 ºC and 550 ºC) at 5 °C/min heating and cooling rate to decompose organic residues. Prior to obtaining the final exsolved catalyst, several trial-and-error experiments were carried out to identify the optimal combination of the variables reported in Table 3.

Table 3. Variable parameters explored during the exsolution synthesis.

Parameter	Levels investigated	Notes
Ru loading (wt.%)	2, 5	Nominal metal loading
Calcination temperature (°C)	450, 500, 550, 600, 700, 800	Air atmosphere
Exsolution temperature (°C)	300, 500, 600, 750, 900	Reduction under 5 wt. % H_2 flow
Exsolution time (h)	4, 8, 10	Reduction dwell time

The final material was ground again to ensure homogeneity before structural characterization by XRD.
Once no RuO_2 phases were detected by XRD analysis, the reduction/exsolution step was carried out in a tubular furnace at 750 °C, using a heating and cooling rate of 5 °C/min and a 4 h isothermal hold under a 5 vol.% H_2 atmosphere. The occurrence of Ru nanoparticle exsolution was subsequently verified by TEM imaging.
The Ru/CeO_2 impregnated catalyst, as well as the Ru–Fe exsolved, Ru-exsolved, and Fe-exsolved catalysts, were synthesized following the procedures described by Rizzetto et al. [132] and Skinner et al. [133], respectively, within the framework of two distinctive research activities. These catalysts were provided for testing in the APR of ethanol under the experimental conditions and reactor setup previously described.

2.1.4 Catalysts characterization

Transmission electron microscopy (TEM) analysis was carried out to study the shape and particle size of the catalysts. All samples were subjected to TEM using a TALOS F200X transmission electron microscopy system with a LaB6 source at an acceleration voltage of 200 kV. Small amounts of synthetic ruthenium-based catalysts were dropped onto a Cu-grid TEM grid (300 mesh size) that had been covered in a lacy carbon layer to create the TEM samples. Using a CMOS camera attached to the transmission electron microscope, pictures of the catalysts surfaces were taken. In particular, the particle size distribution was determined using ImageJ software (https://imagej.net/) by assuming a spherical geometry for the nanoparticles. A total of 100–150 well-resolved particles were analysed to generate the statistical distribution, and the most frequently observed particle diameter was taken as the average size.
N_2 Physisorption Analyses were conducted to evaluate the textural properties of the catalysts, namely their surface area and pore structure. Measurements were performed using a Micromeritics TriStar ASAP 3020 analyzer. Prior to analysis, the samples were degassed in flowing nitrogen at 200 °C for 2 h in a Micromeritics FlowPrep 060 unit to remove moisture and adsorbed species. N_2 adsorption–

desorption isotherms were then recorded at liquid nitrogen temperature (−196 °C). The specific surface area was determined using the Brunauer–Emmett–Teller (BET) method [134,135], while the pore size distribution was obtained from the desorption branch of the isotherm according to the Barrett–Joyner–Halenda (BJH) model [136].

Powder X-ray diffraction (PXRD) analyses were carried out on a PANalytical Empyrean diffractometer operating at 40 kV and 40 mA, using Cu Kα radiation (λ = 1.5406 Å). Diffraction patterns were collected in the 2θ range of 20–80° with a step size of 0.026° in a continuous scan mode. Ru/CeO_2 catalysts samples were analysed after the following sequential thermal treatments: calcination at 450 °C for 4 h, re-calcination at 550 °C for 4 h, before and after the reduction at 750 °C for 4 h. Before analysis, each sample was finely ground and spread on a zero-background silicon holder. Phase identification was performed using HighScore Plus (Malvern PANalytical) and the ICDD PDF-4+ database.

To investigate the reducibility of the $Ru–ex/CeO_2$ catalyst and to determine the optimal reduction temperature, a H_2/Temperature-Programmed Reduction (H_2-TPR) analysis was conducted. Approximately 27 mg of sample calcinated at 800 ºC for 10h were pretreated under a helium flow of 40 cm^3/min at 300 °C for 30 min (heating rate: 10 °C/min), followed by cooling to 50 °C under the same atmosphere. The reduction profile was then recorded by introducing a 5 vol.% H_2/Ar gas mixture (20 cm^3/min) while heating from 50 °C to 900 °C at a rate of 10 °C/min, with an isothermal hold of 10 min at the final temperature.

2.2 Model Development and evaluation framework

2.2.1 Process design and simulation

A further step was taken by adopting a comprehensive approach in which the experimental results were used to simulate and scale the process up to an industrial level. The modelled process was then integrated into a broader evaluation framework, where its energetic, economic, and environmental performance was assessed to identify the potential and limitations of APR applied to ethanol-rich wastewaters, such as those from winery effluents.

The results of the experimental activities, which provided quantitative data on feedstock composition, APR performance, and product distribution, were used as input parameters for simulating the APR process at an industrial scale.

The process simulations were carried out using a simulation software: Aspen Plus® V14.0.1 (AspenONE Performance Engineering, Burlington, USA). The reference treatment capacity was set to 2.5 m^3/h of ethanol-rich wastewater, which is representative of a medium-to-large winery operating continuously over eight months a year. The thermodynamic framework employed combined the Peng–Robinson (PR) equation of state and the Non-Random Two-Liquid (NRTL) model to accurately describe the vapor–liquid equilibria and reaction system behaviour.

Two energy recovery configurations were modelled:

- Scenario 1 (S1): The gaseous products are utilized in a cogeneration unit, providing both the thermal and electrical energy required to sustain plant operation. Any surplus electricity is exported to the grid and sold.
- Scenario 2 (S2): H_2 is separated from the gas products and purified through pressure swing adsorption (PSA) for external commercialization, while the remaining combustible gas fraction is employed in cogeneration to satisfy the plant's internal energy requirements. Any excess electricity generated is also sold externally.

Both scenarios S1 and S2 share the same upstream configuration consisting of a wastewater storage tank, clarification steps and feed preheating units. The APR reactor, for both scenarios, was modelled as an isothermal plug-flow system operating at 270 °C and 80 bar (representative of the experimental setups discussed previously). Derived from the observed laboratory data, ethanol conversion was set to 75%. The downstream sections were separately designed to reflect the different energy recovery pathways i.e. electricity production and H_2 production for S1 and S2 respectively. The net mass and energy balances derived from the simulations provided the basis for subsequent ESA, TEA, and LCA described in the following sections. Finally, sensitivity analyses were performed to evaluate additional process optimization strategies, such as increasing the ethanol conversion efficiency from 75% up to 95%. Additional modifications to the plant configuration were also tested where additional flash and compression stages were integrated in order to improve heat recovery and wastewater treatment efficiency.

2.2.2 Energy Sustainability Analysis (ESA)

The ESA is a methodology developed to evaluate the overall energy efficiency and sustainability of the APR process applied to ethanol-rich wastewaters as the winery wastewater [128]. ESA is particularly suited for emerging and low-TRL technologies, when data are incomplete, uncertain, or not fully industrial. Mass and energy balances were obtained from process simulations and extrapolated to assess the energy performance of both scenarios. In particular, an overview of the main process energy flows is reported in Figure 11:

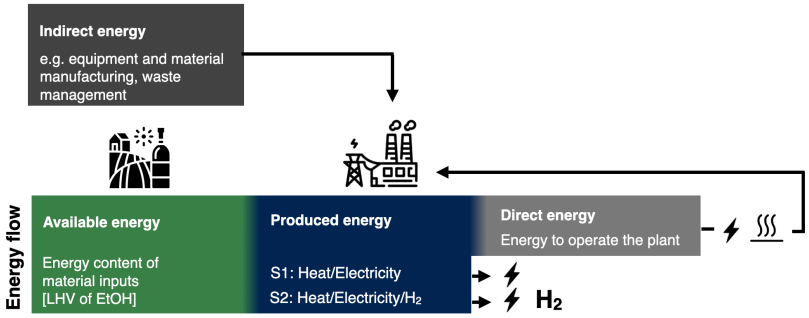

Figure 11. Sketch of the main energy flows participating in the APR process. The input available energy (ethanol content in winery wastewater) is the same for both S1 and S2. In S1, heat and electricity are cogenerated, where the surplus electricity is sold. In S2, H_2 is recovered and sold first, while residual energy helps in supporting the plant's cogeneration unit. Leftover electricity is also sold.

The main energy flows considered in the analysis are defined as follows:

- Available energy ($E_{\_available}$, MJ): Represents the total energy content present in the process feedstock. In this case, the only energy source is ethanol, and its lower heating value (LHV) was used to quantify the input energy. Although not directly included in the ESA calculations, $E_{\_available}$ was reported as a reference baseline for both scenarios.
- Produced energy ($E_{\_produced}$, MJ): Corresponds to the gross energy generated by the process. For S1, it refers to the sum of thermal and electrical outputs produced from cogeneration, similarly for S2, where in addition to the cogeneration outputs, it also accounts for the chemical energy (LHV) of the H_2 recovered by the PSA unit. Internal heat recovery was accounted for as useful energy production while reducing $E_{\_direct}$, ensuring consistency and avoiding double counting.
- Direct energy ($E_{\_direct}$, MJ): Includes the energy directly required to operate the plant, such as the thermal duty of the APR reactor and heat exchangers, and the electricity consumed by pumps and compressors.
- Indirect energy ($E_{\_indirect}$, MJ): Refers to the primary energy embodied in the process infrastructure and supporting activities, including the supply of catalyst precursors, equipment manufacturing, and waste treatment.

All energy flows were normalized to one hour of plant operation and expressed in MJ. The ESA employed two key performance indicators: the Energy Sustainability Index (ESI), the Energy Return on Investment (EROI) and the Energy Payback Time (EPT) [137]. The ESI provides an indicator of the short-term energy self-sufficiency of the system and was calculated according to Equation (12):

$$ESI = \frac{E_{produced}}{E_{direct}} \quad (12)$$

An ESI greater than 1 indicates a self-sustaining system in which the energy produced exceeds the operational energy demands.
The EROI, in contrast, assesses the long-term energy sustainability of the technology by including indirect energy contributions related to construction, maintenance, and material inputs. It is defined as:

$$EROI = \frac{E_{produced} - E_{direct}}{2 * (E_{indirect})} \quad (13)$$

Indirect energy demand was estimated using the Cumulative Energy Demand (CED) indicator derived from life cycle inventory data obtained through the ecoinvent database, following the LCA-based approach described by Ruggeri et al. [138]. The CED includes upstream energy requirements associated with the production of materials, catalysts, and auxiliary inputs and it is expressed as $MJ_{eq.}$. Auxiliary services include maintenance activities, infrastructure-related energy

inputs, logistics, utilities, and operational support services that are typically not fully captured in process-based inventories but contribute to the long-term energetic requirements of the plant. In accordance with the ESA methodology, the aggregated indirect energy term was conservatively multiplied by a factor of two to account for additional life-cycle contributions that are often highly uncertain or incompletely captured in process-based inventories, such as plant construction, decommissioning, maintenance, and infrastructure renewal. This conservative correction aims to ensure long-term technological "vitality", i.e. the ability of the system to energetically sustain both its operation and its eventual replacement at the end of its lifetime. The factor-of-two correction represents a conservative assumption and does not correspond to a calibrated parameter, as the objective of the EROI calculation was not to optimize its numerical value but rather to avoid a potential underestimation of indirect energy demands.

To complement the EROI, the EPT was also evaluated. EPT represents the time required for the net energy produced by the system to compensate for the cumulative indirect energy investment. Following the ESA methodology, it was calculated as:

$$EPT = \frac{E_{indirect}}{\frac{E_{net}}{n}} \quad (14)$$

where $E_{net} = E_{produced} - E_{direct}$, and n is the assumed plant lifetime (20 years in this work). Under these assumptions, EPT can be expressed as the inverse of the EROI scaled by the plant lifetime. A low EPT value indicates that the cumulative indirect energy investment associated with materials, construction, and auxiliary services is recovered over a relatively short operational period, suggesting that the system can sustain long-term operation from an energetic standpoint. Together with EROI, EPT provides a complementary perspective: while EROI expresses the magnitude of net energy gain, EPT translates this information into a time-based indicator, facilitating interpretation of long-term energetic viability.

2.2.3 Techno-Economic Assessment (TEA)

The TEA was conducted following the methodology proposed by Towler and Sinnott [139], widely applied in the evaluation of industrial and catalytic processes, including glycerol and sorbitol APR [140,141]. The economic assumptions were based on the European context, integrating country-specific data where available. Specifically, labour costs were derived from the Italian metalworking industry collective agreement, wastewater treatment costs were taken from a Spanish case study, and interest rates were based on values provided by the European Central Bank. All costs were updated to 2024 monetary values and are reported in USD2024 (hereafter referred to as USD).

The total cost of production (TCOP, USD/y) was estimated as the sum of variable, fixed, and annualized capital costs according to (15).

$$TCOP = VCOP + FCOP + ACC \quad (15)$$

where VCOP represents variable cost of production, FCOP fixed costs of production, and ACC the annualized capital charge. VCOP includes costs that depend on the annual plant production rate. In particular, two different COD treatment costs were considered, since the organic content of the wastewater stream determines the applicable treatment cost. For wastewater with COD > 500 ppm, a dedicated treatment facility was assumed, with an average cost of approximately USD 1.05 per kg of COD removed [142]. For wastewater with COD < 500 ppm, streams can be discharged into public sewage systems in accordance with Italian Legislative Decree 152/2006 [143] and the EU Urban Wastewater Treatment Directive [144], a significantly lower treatment cost of USD 0.53/m^3 was adopted, based on European municipal wastewater data from Jaén, Spain [145]. Catalyst costs were estimated assuming the use of 5 wt.% Pt/C with a one-month lifetime, after which the catalyst were replaced with a 99% recycling efficiency. Consequently, only 1 wt.% of fresh catalyst replacement per month was considered as VCOP, representing a conservative assumption compared to similar TEA studies, which often neglect catalyst costs or assume longer lifespans [141,146]. The detailed cost parameters adopted for the TEA analysis are summarized in Table 4.

Table 4. Cost parameters and unit costs adopted for the TEA analysis, including raw materials, operating, and capital-related costs (VCOP, FCOP, and ACC).

Category	Parameter	Value	Unit	Reference
Raw materials (VCOP)	Fresh Pt	30.70	USD/g	[59]
	Fresh activated carbon	2.75	USD/kg	[147]
	Solids transport	0.02*	USD/kg	[148]
	COD treatment > 500 ppm	1.05	USD/kg	[142]
	COD treatment < 500 ppm	0.53	USD/m^3	[145]
Fixed operation costs (FCOP)	Labor	24 588.0	USD/year/shift position	[149]
	Supervision	25.0	% labor	[139]
	Maintenance	4.0	% ISBL	[139]
	Insurance	1.5	% ISBL + OSBL	[139]
	Overhead charges	50.0	% labor + supervision	[139]
	Land rent	1.5	% ISBL + OSBL	[139]
Economic parameters in ACC	ISBL	-	-	[139,150]
	OSBL	40.0	% ISBL	[139]
	Engineering cost	25.0	% ISBL + OSBL	[139]
	Contingency	10.0	% ISBL + OSBL	[139]
	CRF	6.5	%	[139]
	Plant life	20.0	years	assumed
	Nominal interest rate	3.4	%	[151]
	Inflation	0.7	%	[152]
	Real interest rate	2.6	%	calculated

* Assumptions: 50 km distance with a 2000 kg capacity diesel truck, diesel efficiency: 3.5 km/L, driver wage of 20 USD/h.

FCOP (USD/y) represents costs that are independent of plant capacity and are typically estimated as fixed percentages, based on factors such as the process's technological maturity, degree of innovation, and the overall uncertainty associated with the technology [139]. These include expenses such as supervision, maintenance, insurance, overhead, and land rent, as summarized in Table 4. The ACC (USD/y) term represents the portion of the fixed capital investment (FCI) distributed over the plant's operational life, as calculated by Equation (16):

$$\text{ACC} = \text{FCI} \times \text{CRF} \tag{16}$$

The FCI comprises four major components: *(i)* inside battery limits (ISBL), the cost of all the process equipment and their installation costs; *(ii)* outside battery limits (OSBL), the costs related to additional infrastructure and supporting facilities required for the plant construction; *(iii)* engineering costs, the expenses associated with project design and consulting services; *(iv)* contingency costs, to cover unforeseen expenses typically associated with first-time plant construction.
The CRF term annualizes the FCI over the expected plant lifetime (n, years) at a discount rate (i, %), as expressed in Equation (17):

$$CRF = \frac{i\,(1+i)^n}{(1+i)^n - 1} \tag{17}$$

The discount rate (i) accounts for the real interest rate, corrected for inflation (approximately 0.7%/year) [152]. All economic assumptions used for VCOP, FCOP, and ACC calculations are reported in Table 4.
ISBL cost estimation was primarily based on two reference databases: the CCUS database [150] and the Towler and Sinnott database, whereas the costs of the combined heat and power (CHP) system and the APR reactor were obtained from literature sources [153,154]. Depending on data availability, equipment purchase costs were estimated using one of the following equations [139], [150]:

$$C_{eq.} = a + (b * S^n) \tag{18}$$

$$C_{eq.} = C_{min} + (\frac{S}{S_{min}})^n \tag{19}$$

where a and b are empirical cost constants, S represents the equipment size or capacity (e.g., flow rate, power, or volume), n is the scaling exponent, and C_{min} is the cost at the reference size S_{min}. Each equipment cost was estimated based on its corresponding technical specification (S) and scaled to the actual size or capacity required for the plant, as determined from the scaled-up process simulations. All equipment used in the simulation was considered in the TEA. The list of equipment, including specifications and reference size parameters used for scale-up, is reported in Table 16 (common equipment among scenarios) and Table 19 (scenario-specific

equipment). Once the purchase costs of each equipment were calculated, four correction factors were subsequently applied to obtain bare module costs, which integrate cost related to installation, material used, and pressure to sustained, along with an update to the 2024 Chemical Engineering Plant Cost Index (CEPCI) [153,154]. The cost factors are reported in Table 5, whereas purchased and final costs values for each equipment are listed in Table 21.

Table 5. Cost factors adopted for the calculation of the final equipment costs.

Cost factors	Values	Notes	References
Installation factors	2 - 7	Depending on the equipment complexity	[155]
Material factor	1.3	Stainless steel	[139]
Pressure factor	1 - 1.2	1: 1-5 atm 1.1: 6-25 atm 1.2: 25-100 atm	[155]
Chemical Engineering Plant Cost Index (CEPCI)	798	All costs were updated to 2024 values*	[154]

* Historical CEPCI values considered were 509.7 (2007), 567 (2013), 797 (202320), and 798 (2024).

Economic performance was evaluated by calculating the minimum selling price (MSP) of the final product: Electricity (USD/kWh) for S1, H_2 (USD/kg H_2) for S2. The MSP was obtained as the ratio between the annualized total cost of production (TCOP, USD/y) and the corresponding annual production of electricity or H_2. In particular, in S2, the revenue generated from the sale of surplus electricity produced by the PSA tail gas cogeneration was subtract from the total annual costs, assuming a market price of USD 0.36/kWh. This value lies within the range reported for Italy during the 2022–2023 period, between non-household electricity prices (approximately 0.35 – 0.29 €/kWh) and household electricity prices (approximately 0.36–0.39 €/kWh) [156]. Given the energy crisis and the high volatility of electricity prices, the value of USD 0.36/kWh, converted from euros to US dollars to ensure consistency with the economic analysis currency, was adopted as a representative intermediate and conservative estimate of potential electricity market prices. Recovered thermal energy was not assigned an economic value, as it is fully reused within the process to meet internal heat demands and is therefore not exported as a saleable product.

2.2.4 Life Cycle Assessment (LCA)

An LCA was conducted to evaluate the environmental impacts associated with applying APR to ethanol-rich winery wastewaters (WWW). This assessment aimed at quantifying the environmental performance of the simulated process under the two distinct configurations (S1 and S2), and to benchmark the results against conventional and most emerging technologies which are nowadays employed for

the production of electricity and H_2. In the first scenario (S1), the cogenerated electricity was benchmarked to the electricity produced using European national electricity mixes and main renewable sources, including photovoltaic, geothermal, and hydropower systems. In the second scenario (S2), the H_2 produced was compared against conventional production routes such as SMR but also with less established technologies such as water electrolysis fed by renewable sources. While comparisons with fossil-based systems provide a reference to current dominant production routes, the inclusion of renewable technologies enables a more balanced evaluation of GWP performance, given that APR relies on a waste-derived, biogenic feedstock rather than primary fossil resources. The LCA followed the principles and framework established by the ISO 14040 and 14044 standards [157,158]. The system boundaries encompassed all relevant stages from cradle-to-grave, including *(i)* raw material supply and plant construction *(ii)* the operative phase, for which data from process simulations were employed, and *(iii)* the end-of-life stage, covering equipment decommissioning and material disposal or recovery (Figure 12).

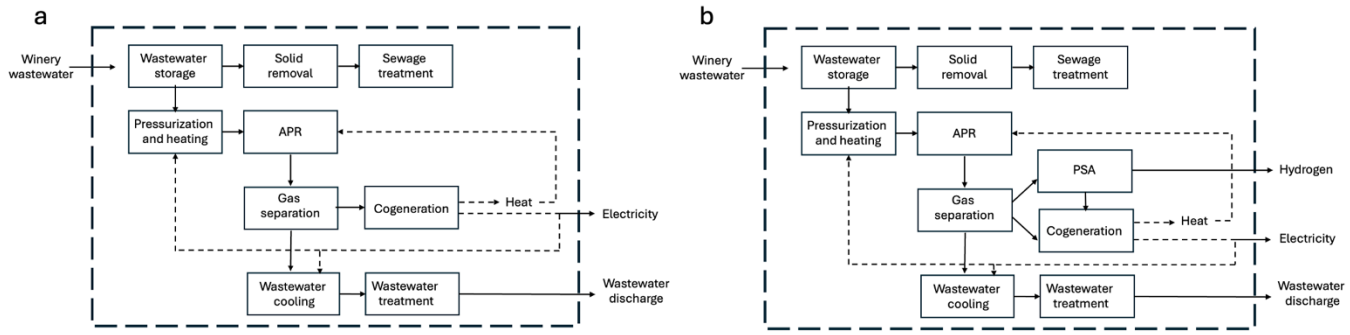

Figure 12 System boundaries considered for the life cycle assessment (LCA) of the APR process for winery wastewaters valorisation for Scenario 1 (a) and Scenario 2 (b).

In order to model the impact of plant buildup, the proxy dataset *"chemical plant construction, organics unit"* from the ecoinvent database was adopted. A pro-rata approach was applied to account for the different functional outputs of the two scenarios. For S2, the construction share was allocated based on a reference process which already available in the database (*steam reforming*), which produces the same energy vector output (H_2). Consequently, the proportion was performed per kilogram of H_2 produced (functional unit: 1 kg H_2). In contrast, for S1, the output product was electricity. Since no analogous proxy dataset for an electricity-producing process was available, the allocation of the plant construction impacts were indirectly related to the treated wastewater volume, using a proportional scaling between the reference flow adopted for S2 (0.36 m^3) and the one corresponding to S1 (1.29×10^{-2} m^3). This proportional method enabled the distribution of the *proxy* construction share within S1 while maintaining consistency with the modelling approach used for S2. Overall, this procedure ensured methodological comparability between scenarios while reflecting their distinct functional units and outputs: electricity in S1 and H_2 in S2. Specific assumptions and estimates are reported in Table 6.

Table 6. Assumptions and estimates used to pro-rate the plant construction quota for the LCA model, using the "chemical plant construction, organic" proxy from ecoinvent 3.9.1. Scaling is based on kg of H_2 in S2 first, while the quota for S1 was calculated based on the treated wastewaters volumes in S2 compared to the S1.

Aspect	Scenario 1	Scenario 2
Proxy used per FU (unit)	2.01 E-11	5.30 E-10
Assumption basis	Proportional to the wastewater entering in S2	Proportional to proxy plant capacity (steam reforming)
Methodology for estimation	Pro-rated based on wastewater volume (m^3)	Pro-rated based on same functional unit as the proxy (1kg of H_2)
Scaled wastewater volume (m^3)	1.29 x 10^{-2}	0.36

The background data were sourced from the *ecoinvent v3.9.1* database (*cut-off* system model) [159], while the analysis was implemented in Python using the *Brightway2* framework via the *Activity Browser* interface, chosen for its flexibility and open-source accessibility [160].

The life cycle impact assessment (LCIA) was performed following the Environmental Footprint (EF) v3.1 no LT method, focusing primarily on the global warming potential (GWP100) impact category. Both direct and indirect CO_2 emissions were considered, with characterization factors of +1 for fossil CO_2 and 0 for non-fossil sources. This treatment represents a simplifying assumption whereby biogenic CO_2 emissions are considered carbon-neutral over the short carbon cycle, as they are assumed to be balanced by prior CO_2 uptake during biomass growth. Table 7 summarizes the main methodological steps adopted in this study.

Table 7. Summary of the cornerstones for the present LCA study

LCA Step	Details
Step I Goal and scope definition	Evaluate the environmental footprint of ethanol APR from WWW for electricity (S1) and/or H_2 (S2) production through attributional LCA Benchmarking against alternative technologies Functional units (FUs): 1 kWh of electricity (S1), 1 kg H_2 (S2) Boundaries of analysis: cradle-to-grave approach, including raw material extraction, end-of-life treatment of the infrastructure and of the WWW
Step II Inventory analysis	Foreground: based on data provided from the (upscaled) process simulations, basic equipment sizing for materials Background: *ecoinvent 3.9.1*, system model: *cutoff* Calculation implementation: python *brightway2* framework in *Activity Browser*
Step III Impact assessment	Selected indicators from Environmental Footprint (EF) methodology v3.1 no LT were used for impact assessment, GWP100 (with +1/0 CFs for fossil/non fossil carbon), and total aggregated single score impact (i.e., through EF normalization)
Step IV Interpretation	Compare the LCA results for each scenario and benchmark against alternative technologies producing the same energy vectors

*Italics are used only for proper nouns such as software and database names.

Although scenarios S1 and S2 are defined by different functional units, both represent alternative pathways for energy production. The EF single-score approach was therefore applied to provide a preliminary, integrated comparison of their overall environmental performance on a common energy basis (1kg H_2= 33kWh), accounting simultaneously for all impact categories and reflecting the specific design and operational characteristics of each scenario [161]. To enable energy-based comparability, the H_2 production in S2 was converted into its energy equivalent using the LHV of H_2. The single-score results were obtained by normalizing all midpoint impact categories with global normalization factors as proposed by Crenna et al. in [162] and subsequently applying the weighting factors described by Sala et al. in [163] for the EF v3.1 no LT method. The impact categories used to calculate the single score are the following: acidification, climate change (GWP100), freshwater ecotoxicity, particulate matter formation (human health), freshwater eutrophication, marine eutrophication, terrestrial eutrophication, human toxicity (carcinogenic), human toxicity (non-carcinogenic), ionising radiation (human health), land use, ozone depletion, photochemical oxidant formation (human health), energy resource depletion (fossil fuels), material resource depletion (metals and minerals), and water use. The resulting aggregated score represents the overall environmental burden of each configuration, allowing a direct comparison between the two scenarios in terms of their relative overall sustainability performance. No losses associated with the conversion of H_2 to electricity were included.

Chapter 3. Evaluating wastewaters potentials as APR feedstocks

3.1 Pulp & Paper industry wastewater

P&P is considered a water intensive industry, generating 10 to 300 m^3 of water per ton of product produced, with high strength wastewater, with high-strength effluents mainly arising from debarking, pulping, bleaching, and papermaking operations [101]. COD content can vary from hundreds to over 12.000 mgO_2/L [164] depending on the mill size, the paper making method and the different process stage at which the wastewater is generated [165] (Figure 13).

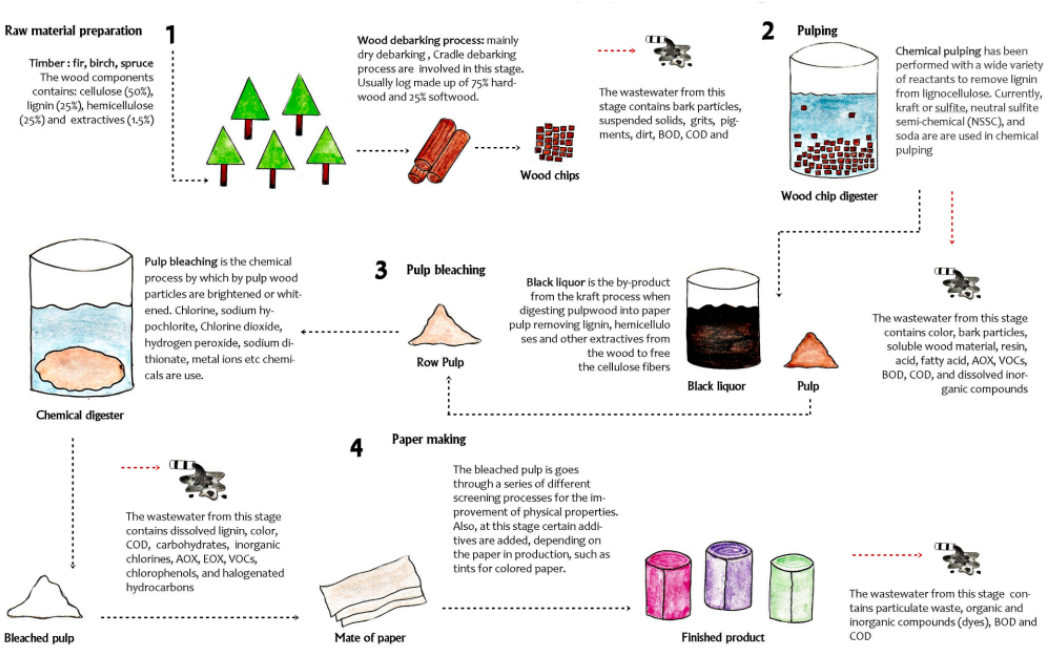

Figure 13. Schematic illustration of the main waste generation stages in the papermaking process. The diagram outlines four key steps, raw material preparation, pulping, pulp bleaching, and paper making, highlighting the sources and composition of wastewater streams produced at each stage, including suspended solids, lignin, organic compounds, and various chemical residues [166].

In particular, P&P wastewaters were collected from 2 Italian industries: Burgo Group S.p.A., a leading Italian producer of virgin paper with reported sales of 2.34 million tonnes in 2022 and Pro-Gest S.p.A., one of the largest players in Europe in the recycling and packaging sector, recovers 1.5 million tonnes of paper annually while manufacturing 1.3 million tonnes of new paper. Both industries were selected for their reputation and strong commitment to sustainable and environmentally focused industrial models [159], [167]. In particular, four samples (R1–R4) were provided by Burgo Group, and the fifth (R5) by Pro-Gest. R1 originates from the paper-making section, where fibers and fillers are removed by a flotation unit (around stage 4, Figure 13). R2 represent a mix of different streams generating from

the pulp bleaching stage, containing brownish water rich in lignosulfonates and residual bleaching chemicals (stage 3). R3 consists of stripped condensates generated during black liquor evaporation and steam stripping, containing light organic compounds and traces of sulfur species (stage 2-3). R4 represents unstripped condensates from the same evaporation system, showing higher levels of volatile organics and sulfides before stripping (stage 2-3). R5 instead come from the last stage but starting from recycled cellulose fibers (stage 3 from Figure 9 b). Their main physicochemical properties and liquid compositions have been measured and are shown in Table 8, illustrating differences in COD, TOC, pH, and low-molecular-weight organics.

Table 8: Main composition of the five P&P wastewaters collected: R1-R4 from Burgo Group and R5 from Pro Gest Group.

Waste stream	pH	COD ($mg\ O_2\ L^{-1}$)	TOC ($mg\ C\ L^{-1}$)	SS (%wt C)	Main liquid compounds (HPLC)
R1 – virgin fiber	7	150–200	630	n.d.	Hydroxy acetone (HA), acetic acid, propionic acid
R2 – virgin fiber	4.5	750–1200	750	n.d.	Glycerol, acetic acid, propionic acid, ethanol
R3 – virgin fiber	3	900–1000	>1700	n.d.	HA, acetic acid and propionic acid in traces
R4 – virgin fiber	2	900–1000	1700	n.d.	Glycerol, acetic acid and propionic acid in traces
R5 – recycled fiber	6	900–1000	1300–1500	8%	HA, acetic and propionic acid, ethanol, glycerol, sugar traces

The reported ranges reflect the potential temporal variability of the samples provided by the company, and all laboratory data fell within these ranges. SS stays for suspended solids.

COD values were the most variable potentially due to the combined effects of residual organic compound deposition and residual microbial activity.
The different wastewaters were treated trough APR, with the potential to both wastewater treatment and H_2 production. The five samples were tested at 270 °C using a Pt supported on activated carbon, selected due to the high abundance of organic acids detected in their composition Table 8. The carbon-to-gas (C to G) conversion and H_2 productivity results are shown in Figure 14.

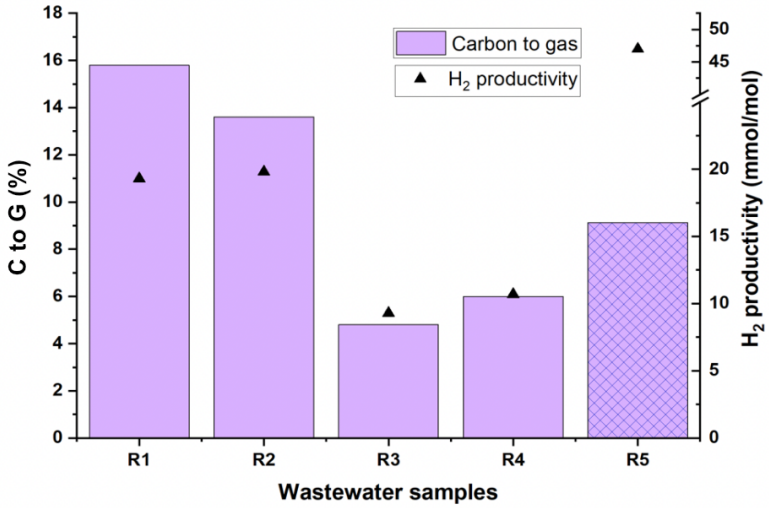

Figure 14. Carbon-to-gas conversion (bars, left axis) and H_2 productivity (triangles, right axis) for the five tested P&P wastewater samples (R1–R5). R5 is shown with a cross-hatched shading to distinguish it from the virgin fibre wastewater (R4), while R5 originates from recycled paper processing.

Notably, samples R1 and R2 achieved the highest C to G conversion despite exhibiting the highest COD and TOC levels. This trend contrasts with previous studies, which reported higher APR performance for more diluted streams. In particular, Luo et al. showed that increasing the glycerol concentration in the feedstock from 5 wt.% to 10 wt.% reduced the H_2 yield and C to G conversion by 37% and 44%, respectively, at 220 °C using Pt/Al_2O_3 [168].

Several factors may contribute to the observed results. Among which the presence of inorganic salts, suggested by observing the HPLC chromatograms of the five wastewater streams reported in Figure 15. A distinct positive peak appearing at approximately 6 min of retention time was detected in all wastewater samples except R1. This signal can be associated with the presence of inorganic salts dissociated in solution [169], which are well known to promote catalyst deactivation by accelerating surface poisoning [51].

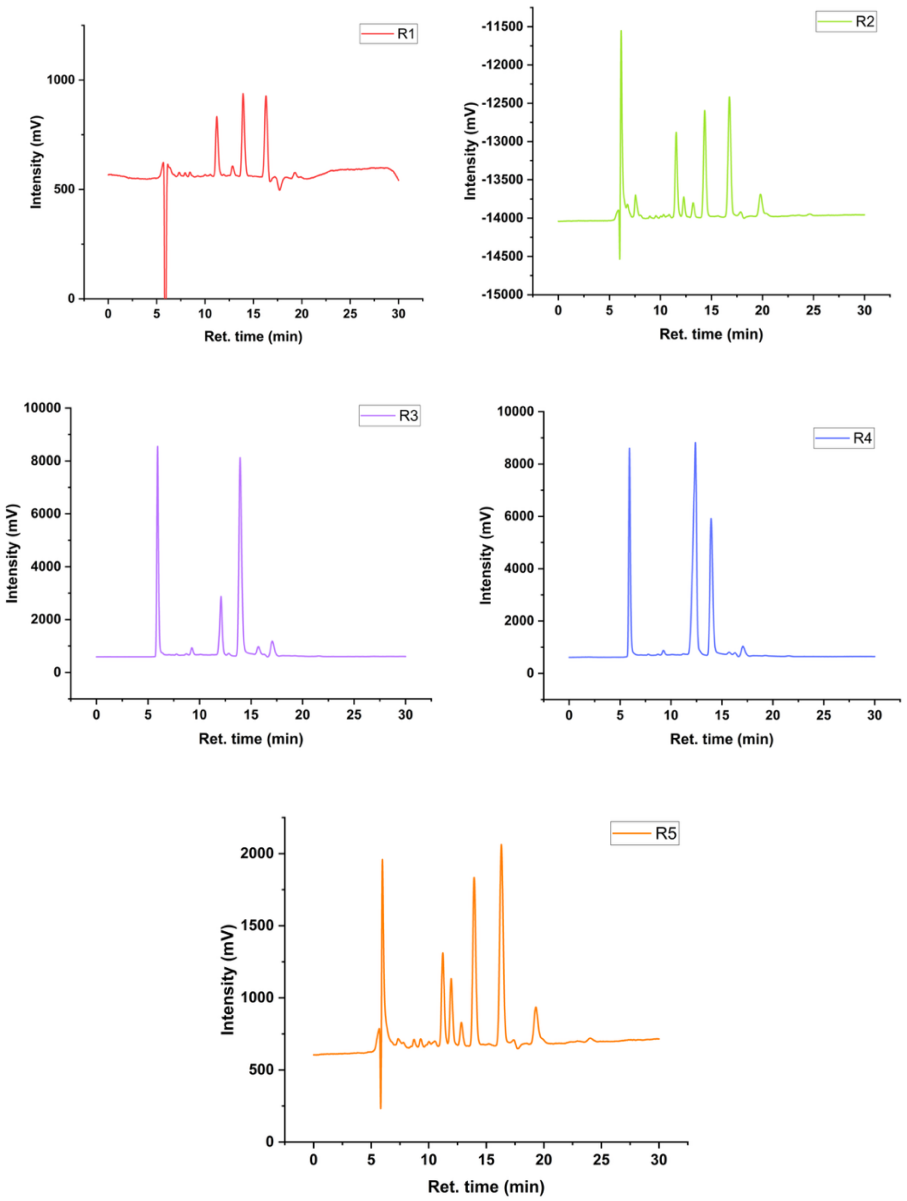

Figure 15. HPLC chromatograms of the five P&P wastewater samples (R1–R5), showing the main organic compounds detected in each stream.

In particular, the anionic composition of each stream was measured, and the main anionic species are summarized in Table 9.

Table 9. Anionic composition of the analysed wastewater samples. Concentrations of the main inorganic anions: chlorides (Cl^-), nitrites (NO_2^-), and sulphates (SO_4^{2-}) expressed in mg/L. n.d. indicates "not detected."

Sample	Chlorides – Cl^- (mg/L)	Nitrite - NO_2^- (mg/L)	Sulfates – SO_4^{2-} (mg/L)
R1	54	3	146
R2	68	2	238
R3	n.d.	n.d.	349
R4	n.d.	n.d.	1010
R5	221	n.d.	87

In addition, the pH decreased strongly from 7 to 2 passing from R1 to R4 (Table 8). Such low pH can promote humin formation in the presence of sugar fragments, typically eluting between 3 and 7 min, as observed in R2, R3, and R4 [170]. Both inorganic salts and humin formation have been reported as contributors to catalyst deactivation [98], which could explain the reduced C to G conversion and lower H_2 productivity observed in this experiment.
A further liquid fraction analysis revealed that major oxygenates such as acetic acid, propionic acid, persisted after 1 hour of APR in R1 and R2. Instead, R3 and R4 did not show any significant changes between pre- and post-APR chromatograms. However, gas compositions in R1–R4 were dominated by CO_2, with H_2 yields of only ~10–15 vol%, indicating that decomposition reactions were more significant than selective reforming. In contrast, the recycled fiber wastewater (R5) showed higher H_2 productivity (46 $mmolH_2/molC_{in}$) and higher C to G conversion.
Further characterization tests were then performed on the R5 wastewater. This sample was the only one found to contain SS, accounting for 8 wt.% of the total carbon. In particular, the liquid fraction exhibited a very low carbon content (~0.1 wt.%), whereas the solid fraction contained ~43 wt.% carbon. TGA of the solids revealed that only ~20% was of organic origin, while the remainder consisted of inorganic material (Figure 16), which could be residual fillers widely used in the last step of the papermaking, such as kaolin clay, TiO_2, and calcium carbonate ($CaCO_3$) [165].

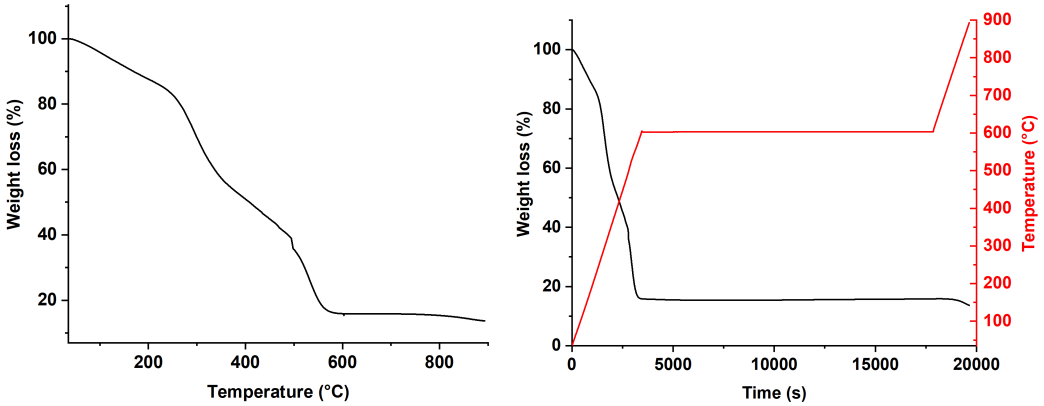

Figure 16. Thermogravimetric analysis of the suspended solids collected from the centrifugated R5 wastewater sample over a temperature range of 25 to 900°C (right) and over time (left).

HPLC analysis of the liquid fraction revealed hydroxy acetone (HA), acetic acid, propionic acid, ethanol and glycerol as the main constituents (see Table 8 above).
In particular, after 2 h of reaction with R5, ethanol and glycerol underwent reforming with conversion rates of 11% and 100%, respectively, while acetic acid showed a slight increase attributed to ethanol reforming, and the other compounds remained unchanged (Figure 17).

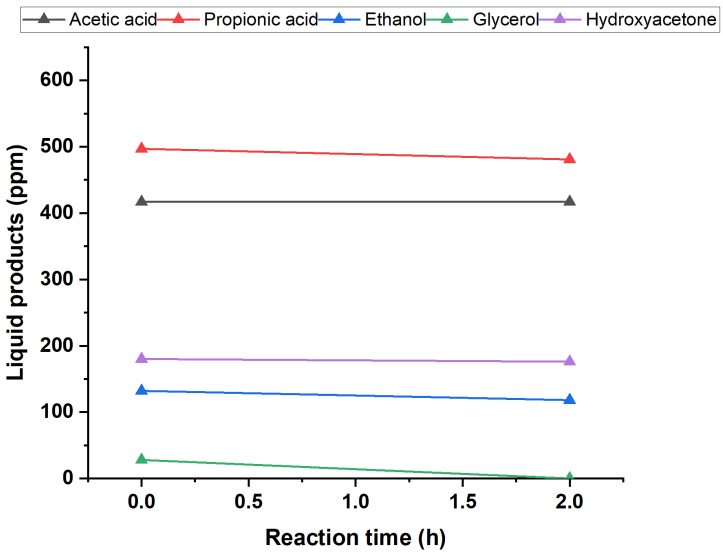

Figure 17. Concentration profiles of ethanol, acetic acid, and propionic acid during APR of the R5 wastewater liquid fraction at 270 °C over Pt/C.

This confirmed the high reforming activity of glycerol under APR conditions, which is well-documented in the literature [78,171], [80]. In contrast, organic acids such as acetic and propionic acid are much less reactive under APR conditions especially when in mixtures, which explains the absence of significant changes in their concentrations. However, ethanol also did not undergo efficient reforming, likely due to catalyst deactivation phenomena that limited its conversion. The hypothesis of rapid catalyst deactivation is further supported by the formation of solid residues at the end of the APR test. These deposits can again be attributed to humin formation, as traces of sugars were detected in the feed. Dilution tests were performed to mitigate this phenomenon, and while humin formation decreased, process efficiency was also reduced. Specifically, the thermal energy required to heat the wastewater from 250 to 270 °C at 60 bar was estimated at ~88 kJ/L, whereas the maximum recoverable gas-phase energy after 1 h of APR was only ~3 kJ/L, leaving little room for optimization. Although some observations may indicate catalyst deactivation, this aspect was not investigated, as it was beyond the scope of this preliminary study. Catalyst stability is typically assessed by comparing the physicochemical properties of fresh and spent materials, including changes in surface area, pore structure, and active sites. Microscopic techniques such as SEM and TEM can further reveal surface deposits, while comparative activity tests using a reference substrate allow evaluation of performance loss. However, these analyses were not conducted in this work. Nonetheless, they are essential for assessing long-term catalyst stability and should be addressed for scale-up studies.

Overall, these findings suggest that the composition of R5 wastewater, along with the other P&P streams are not particularly favorable for APR. Although R5 exhibited the highest H_2 productivity on a molar carbon basis, this result must be interpreted in light of the low carbon content and limited removal of organic compounds from the liquid fraction, as many species remained even after the reaction. In fact, complete ethanol reforming would require prior removal of acetic and propionic acids, whose presence inhibits ethanol conversion. Although ethanol, as a small alcohol, has high potential for H_2 production via APR, the low ethanol (130 ppm) and glycerol (28ppm) content in this stream further reduces its suitability. For this reason, R5 was not pursued for further investigation, and

attention was instead directed toward other wastewater streams with compositions inherently more promising for valorisation through APR.

3.2 Winery wastewater as a source of bioethanol

The winery sector represents Italy's leading agricultural commodity. In 2023, the country produced 38.3 MhL of wine, accounting for about 15% of global production. In the same year, Italy was also reported as the world's top exporter by volume (21.4 MhL) and second by value (€7.7 bn, after France), generating a total turnover of €11.8 bn [112]. Despite its economic relevance, winemaking is unfortunately associated with several environmental challenges: it has a significant water footprint which generates multiple waste streams, making their efficient management a priority. Figure 18 provides a schematic representation of the main production stages and the associated side streams.

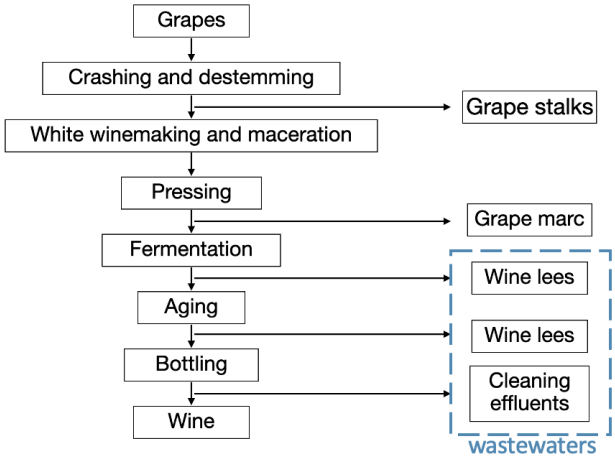

Figure 18: Main winemaking steps and the corresponding residues generated at each stage of the process. Modified from [172].

A quantification of winery by-products based on the grape input shows that grape marc represents the largest fraction, accounting for about 44 % of the total residues, followed by wine lees at 30 % and grape stalks at 26 %, whereas cleaning effluents depends on operational practises (equipment washing, tank cleaning). On average, for every hL of wine produced, approximately 18 kg of grape marc, 6 kg of wine lees, and 4 kg of grape stalks are produced. At the national scale, the 2016 Italian harvest generated roughly 927 kt of grape marc, 309 kt of wine lees, and 206 kt of grape stalks, with corresponding carbon footprints of 834 kt CO_2-eq., 278 kt CO_2-eq., and 185 kt CO_2-eq., respectively for their management [173]. At the national scale, the management of winery by-products is regulated under Italian legislation, which requires these residues to be removed from wineries within a fixed timeframe and directed to controlled recovery or disposal routes[143]. The carbon footprints reported for the 2016 Italian harvest correspond to the conventional management of winery by-products, which primarily involved regulated disposal and low-value recovery routes such as controlled distillation, agronomic reuse, and waste treatment, including associated emissions from transport, storage, and processing.

These streams nonetheless retain a high organic and energy content, indicating that alternative valorisation pathways such as APR could reduce management-related emissions while enabling energy recovery from residues otherwise treated as waste.
For the purposes of this work, we focus on the last two categories of winery wastewater: wine lees and cleaning effluents (WWW), which represent the liquid fractions, in contrast to grape marc, which is the main solid residue. Moreover, several energy valorisation strategies have already been explored for grape marc, a solid-rich stream that is less suitable as an APR feedstock. In contrast, WWW is characterized by high variability, depending on winery practices and the type of wine produced.
Subsequently, a Tuscan winery (Frescobaldi), which has been producing wine in the region since the early 14th century, was contacted to provide real wine lees sample. The liquid fraction was characterized as reported in Section 2.1. Table 10 reports the main organic compounds identified, with ethanol representing over the 70% of the carbon content of the stream, in line with literature data [174], [119], [175].

Table 10: Main winery wastewater organic and inorganic components detected in the wine lees sample.

Parameter	Value	Unit
Total organic carbon (TOC)	70.200	mgC/L
Ethanol	50.650	mgC/L
Glucose	3.400	mg/L
Fructose	950	mg/L
Acetic acid	620	mg/L
Nitrates (NO^{3-})	220	mg/L
Phosphates (PO^{4-})	150	mg/L
Ca^{2+}	17	mg/L
Stot	1700	mg/L
Mg^{2+}	190	mg/L
K^{+}	1.000	mg/L
Total phenols	2	mg/L
Suspended solids (SS)*	1	wt. %

*Suspended solid content was calculated as an average value from literature data [120], [176]

The HPLC analysis was able to identify the 75% of the total carbon, of which 71% was ethanol, while the remaining 4% was attributed to acetic acid, glucose, and fructose, as illustrated in Figure 19.

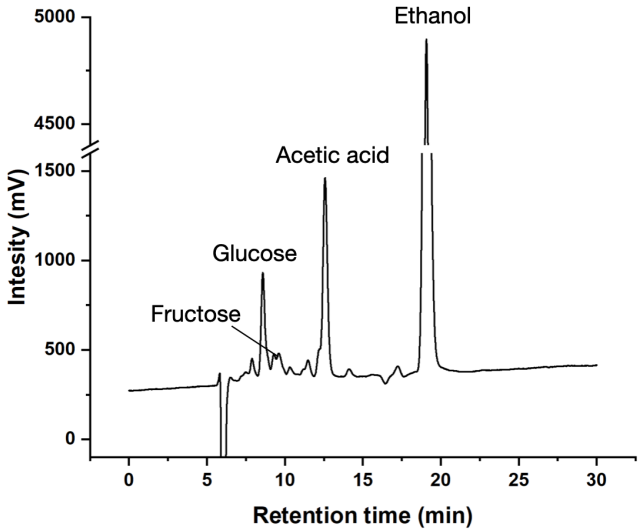

Figure 19. HPLC chromatogram of the winery wastewater sample showing the main organic compounds identified (fructose, glucose, acetic acid, and ethanol).

In order to investigate the 25% missing carbon content in the liquid fraction of the collected winery wastewaters, we performed a complementary analysis. To determine the remaining fraction, GC–MS analyses were performed after extraction according to the protocol reported in Section 2.1, enabling the identification of additional compounds not detected by HPLC Table 11.

Table 11. Main compounds identified via GC–MS, listed in order of abundance.

Compound
L-proline
D-proline
Ethanol diacetate
1-propanol 2-(2-hydroxypropoxy)
Butanedioc acid
Ethanol 2-(2-methoxyethoxy)
2-oxazolidone

A cleaning effluent from a local winery was also collected to evaluate its suitability as an APR feedstock, with particular attention to its composition in relation to APR performance. As expected, this effluent was much less concentrated than the wine lees wastewater, with a TOC value of 200 ppm, indicating a very dilute stream. The HPLC chromatogram revealed just three main peaks, identified as acetic acid, acetaldehyde, and ethanol in order of abundance. Together, these compounds accounted for only ~50% of the total carbon content.

A series of APR tests were carried out using both the wine lees wastewater and the cleaning effluent. Starting for the latter, two catalysts were tested: Ru/Al_2O_3 and Pt/Al_2O_3, both of which are widely used in literature and are recognized for provide good APR performances [43], [53]. Figure 20 reports the HPLC chromatograms of the feed (blue) and the post-APR liquid (orange) after 2 h of reaction at 230 °C with both catalysts.

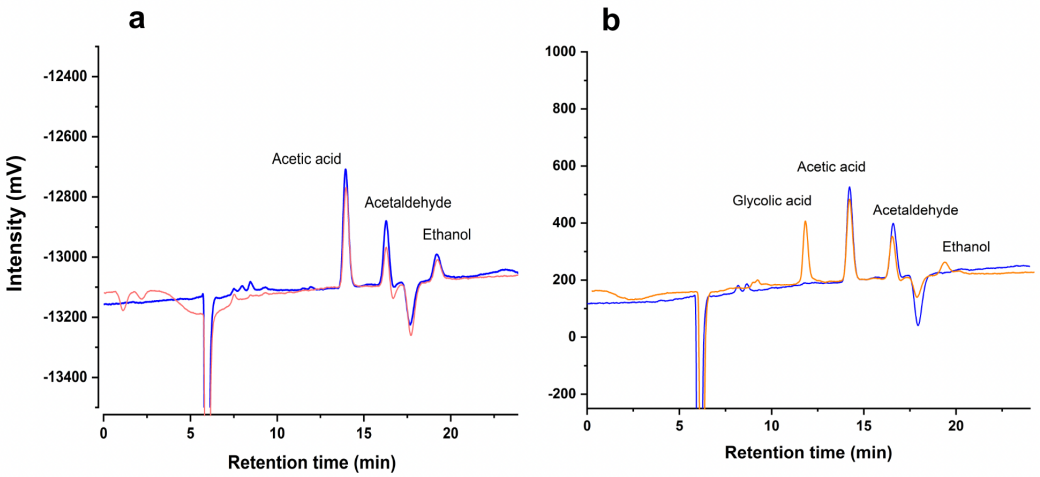

Figure 20. HPLC chromatograms of the cleaning effluent before APR (blue) and after 2 h of reaction at 230 °C (orange) using (A) Ru/Al_2O_3 and (B) Pt/Al_2O_3 catalysts.

For Ru/Al_2O_3 (Figure 20,a), a clear reduction in the intensity of the three main components was observed, with conversion rates of 23%, 37%, and 18% for acetic acid, acetaldehyde, and ethanol, respectively. For Pt/Al_2O_3 (Figure 20,b), however, the conversion of the three components could not be reliably calculated due to the appearance of an additional peak at ~11–12 min, which was not previously identified in the winery cleaning effluent. This peak may indicate a possible contamination, potentially originating from a vial previously exposed to glycolic acid, which elutes in the same retention time window. This is further supported by the unexpected absence of ethanol in the feed (blue chromatogram) and the appearance of its peak only in the post-APR liquid (orange chromatogram). Since glycolic acid APR is known to produce ethanol as a liquid by-product [52], this further strengthens the assumption of glycolic acid contamination.

In addition, the instability of the cleaning effluent during storage must also be considered, particularly regarding the ethanol fraction. A possible explanation is biological contamination, as residual microorganisms from the fermentative processes of the biomass may have remained active in the stream. Microscopic inspection indeed confirmed the presence of microbial presence.

Although a direct comparison of liquid-phase conversion was not possible between the two catalysts, the gas analysis showed that Ru/Al_2O_3 produced 2 mmol of H_2, compared to only 0.1 mmol with Pt/Al_2O_3. Combined with the low TOC and the relatively high proportion of acetic acid, a known recalcitrant compound in APR due to its strong adsorption on active sites without further conversion, these findings indicate that this effluent is not a promising feedstock for APR.

Given these limitations, subsequent experiments focused on the wine lees wastewater, which was tested without dilution at 250 °C and 270 °C for 2 h using the Ru/Al_2O_3 catalyst (Figure 21). The Ru-based catalyst was chosen due to the high ethanol content in this stream and previous evidence [24,44,58] showing that Ru exhibits superior APR performance with alcohols, whereas Pt is more effective with organic acids.

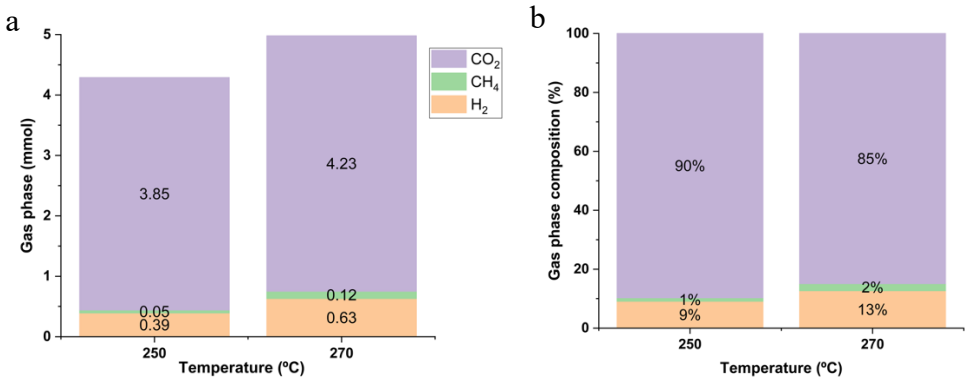

Figure 21. Gas-phase composition obtained from APR of winery wastewater at 250 °C and 270 °C, with the absolute gas production expressed in mmol of CO_2, CH_4, and H_2 (a) and their relative gas composition expressed as percentage contribution to the gas phase (b).

At 270 ºC temperature, H_2 content in the gas phase increased by 60%, while CO_2 increased only by 9%. Under these conditions, 0.63 mmol of H_2 were produced within 2 h of reaction, corresponding to a productivity of 63 mmol/g_{cat}·h. When compared with literature data on ethanol APR using similar ethanol concentrations and Ru-based catalysts, our result was approximately half of the value reported under controlled and simplified reaction environments [109]. Several factors may explain this difference. First, the real wastewater stream is a complex mixture of compounds rather than a pure ethanol solution. In particular, the presence of acetic acid could negatively affect H_2 productivity due to competitive adsorption on the active Ru sites. This effect has been demonstrated in several studies [49,52], where the strong binding of acetic acid to the catalyst surface inhibits or slows down the conversion of other compounds. However, Nozawa et al. [109] previously showed that, with Ru-based catalysts, ethanol reforming is not strongly suppressed by the presence of acetic acid, suggesting that ethanol has a stronger affinity for the active sites and its reforming if favoured over the acetic acid one. Another potential hindering factor could be the insoluble solids, observed at the end of the reaction in the liquid fraction, which was attributed to the formation of humins. This is consistent with literature reports, where sugars undergo dehydration to 5-HMF followed by condensation into polymeric humins under typical APR conditions [88]. These results suggest that humin formation could be the responsible for the lower H_2 productivity observed with the real wastewater feedstock.

To mitigate this effect, the wastewater was diluted first to 1:2 and then to 1:3 in order to reduce the initial sugar concentration, following strategies reported in the literature, where humin formation becomes negligible if the sugar-derived carbon content remains below 0.3 wt.% C [52].

A noticeable reduction of solids was observed already at the 1:2 dilution, with a further slight decrease at 1:3, although they did not completely disappear. However, APR performance in terms of H_2 productivity remained unchanged at all dilution levels. The main effect was instead observed in the gas composition: H_2 increased from 12 to 27 vol.% when moving from the undiluted sample to the 1:3 dilution, while CO_2 decreased from 85 to 70 vol.% Figure 22. It should be noted that this increase in H_2 vol.% does not reflect an increase in the absolute amount of H_2 produced, which instead does not change much, but rather results from the reduced formation of CO_2, which alters the relative composition of the gas phase.

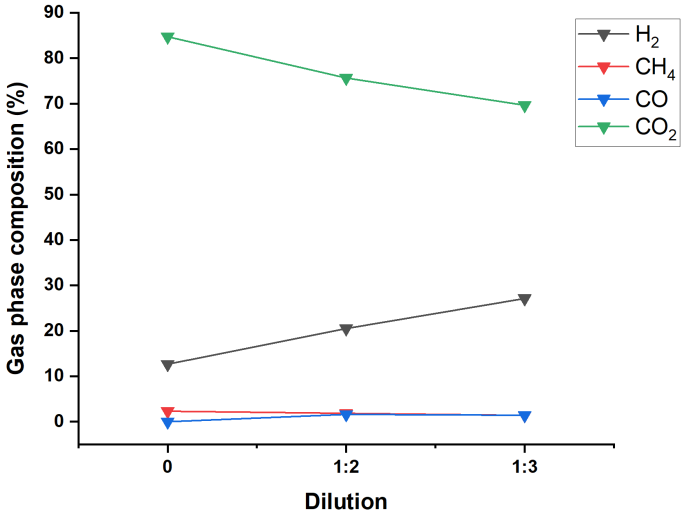

Figure 22. Effect of sample dilution on the gas-phase composition after 2-hour APR tests at 270°C with 5wt.% Ru/Al_2O_3.

The predominance of CO_2 in the gas phase suggests that sugar degradation pathways are favoured over complete reforming, as also reported in previous studies [79]. These findings indicate that reforming is only partially occurring although H_2 is the second most abundant gaseous product in all tests, no significant increase in H_2 productivity was observed with higher dilution. This points to the possible involvement of catalyst deactivation phenomena that may inhibit further H_2 generation. As previously reported, sugar reforming can promote the formation of organic deposits that reduce catalyst activity. In addition, aromatic compounds are widely recognized as among the most problematic species for APR catalysts, although their effect is concentration dependent. Indeed, it has been demonstrated that when the aromatic content is below 0.1–0.3 wt.% C, deactivation phenomena are negligible [51]. In our case, the phenol content of the as-is sample was measured to be 2 ppm, well below this critical threshold. Nevertheless, further dilution of the wastewater would compromise the energetic feasibility of the process, as it would increase water demand and consequently heating requirements. Under the tested conditions, the H_2 yield, assuming ethanol as the sole carbon source, was only 0.1% respect to the theoretical ethanol APR yield, in which one mole of ethanol can generate at best six moles of H_2. No further dilution was applied, since preliminary calculations showed that diluting further to 1:4, even though at most a tenfold increase in H_2 yield (10%) could be achieved, the H_2 produced would still not compensate for the energy required to heat the additional water from 250 to 270 °C, even when accounting for heat recovery by recirculation.

The main energy drivers of this evaluation are summarized in Table 12. For the 1:4 dilution case, 1 kg of feedstock contained 2.4 wt.% ethanol. Assuming ethanol APR occurred with a 10% H_2 yield, the energy produced in the form of H_2 would be 76.4 kJ/kg, compared to a total heat demand of 88 kJ/kg, leading to a net negative energy balance of –11.6 kJ/kg.

Table 12. Main energy parameters estimated for the APR of winery wastewater at 1:4 dilution, assuming ethanol as the only carbon source, a 10% H_2 yield and the resulting net energy balance.

Parameter	Value	Unit
APR feedstock dilution	1:4	-
Water heat demand (250→270ºC)	88.0	kJ/kg
EtOH concentration	2.4	wt. %
H_2 theoretical production (10% H_2 yield)	0.6	g/kg
H_2 energy content (LHV)	120	kJ/kg
Energy theoretically produced	76.4	kJ/kg
Net energy	-11.6	kJ/kg

Since the complexity of the real stream makes it difficult to assess APR performance, and given that ethanol is its main component, ethanol APR will be studied separately under controlled conditions. This simplified system served as a model compound to first establish a solid understanding of ethanol APR under different operating conditions. Once a clear understanding of the compound's behaviour in APR is achieved, it will then be used as a basis to evaluate the real potential of developing a comprehensive scheme for winery wastewater valorisation through APR.

Previous studies have investigated the APR of ethanol; however, these works are typically limited to specific catalysts, reactor configurations, or narrowly defined operating conditions. Most literature reports focus on optimizing performance under a given set of conditions rather than providing a systematic evaluation of how APR behaviour evolves as key operating parameters are varied. In contrast, the present work adopts a parametric approach, in which temperature, pressure, ethanol concentration and catalyst type are independently varied to obtain a broader and more comparative understanding of ethanol APR performance.

Chapter 4. Experimental investigation of ethanol APR

This chapter aims to expand both our knowledge and that of the broader literature on ethanol APR by investigating how operating conditions affect process performance, with the goal of identifying optimal parameters to maximize H_2 yield and carbon conversion efficiency. Ultimately, this work contributes to the broader objective of bridging the gap toward real-world application of APR as a viable solution for the treatment of ethanol-rich wastewaters, enabling both carbon reduction and renewable energy recovery.

4.1 Ethanol aqueous phase reforming

APR of ethanol has attracted considerable attention, as ethanol is easy to handle, readily transported, and, being a small alcohol, well suited to this process [177]. While ethanol does not have the ideal C:O atomic ratio of 1:1 generally considered favorable for APR, the oxygen atoms directly bonded to carbon weaken the C–C bonds and help facilitate reforming reactions [81]. Despite its 2:1 C:O ratio, ethanol still holds strong potential for H_2 production, with a theoretical yield of up to 6 mol of H_2 per mol of ethanol, according to the following stoichiometric equation (20):

$$CH_3CH_2OH + 3H_2O \rightarrow 6H_2 + 2CO_2 \quad (20)$$

It has been shown that the choice of active metal significantly influences both H_2 productivity and the overall reaction stoichiometry, thereby affecting the resulting gas composition. In particular, previous studies [109,178] have identified two main pathways for ethanol APR Figure 23.

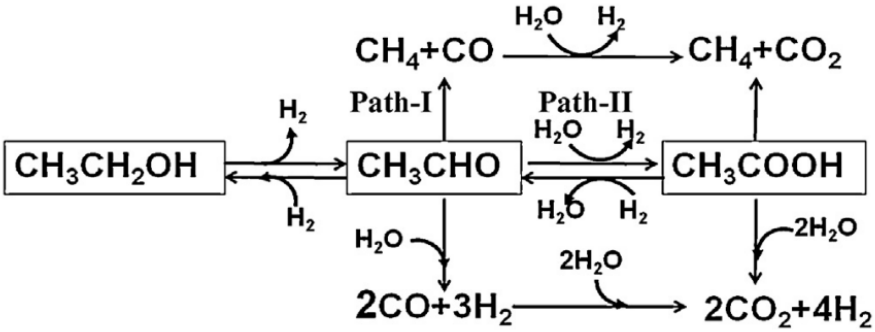

Figure 23. Reaction pathways proposed for ethanol aqueous-phase reforming, highlighting two main pathways: Path I proceed through acetaldehyde formation and subsequent decomposition in methane and CO, while Path II involves further oxidation to acetic acid. Reactions such as methanation also contribute to the overall product distribution [109].

Path-I proceeds through acetaldehyde formation, followed by its decomposition into methane and CO, the latter being further converted via the WGS reaction to

produce H_2 and CO_2, resulting in a gas phase enriched in H_2, CO_2, and CH_4. Path-II, instead, involves the oxidation of acetaldehyde to acetic acid, in parallel with the release of one mole of H_2. Acetic acid can then undergo reforming and potentially generating additional H_2, leading to a gas phase dominated by H_2 and CO_2. Alongside these, side reactions such as methanation of CO/CO_2, Fischer–Tropsch, and dehydration reactions can contribute to the overall product distribution. In particular, Arcalá et al. demonstrated through density functional theory (DFT) analysis that C–C bond cleavage must occur faster than C–O bond cleavage, since the energy change is lower for the former (4 kJ/mol) compared to the latter (42 kJ/mol) on a Pt-based catalyst [54]. However, by changing the type of catalyst, the activity for C–C bond cleavage changed accordingly, as shown by Davda et al. [39]. To investigate these trends, two of the most widely studied metals were selected for comparative testing.

4.2 Catalyst screening

Aware that Ru is the most frequently adopted active phase for alcohol reforming due to its high C–C bond cleavage activity [109], we aimed to verify and compare its performance against Pt, which is known for high H_2 selectivity but lower C–C cleavage efficiency [63]. To this end, ethanol APR tests were performed using Pt- and Ru-based catalysts. Since the support plays a decisive role in catalytic performance, two different supports were also selected: the activated carbon, chosen for its very high surface area, inert character, and hydrothermal stability under APR conditions , and the Al_2O_3, selected for its well-established role in promoting WGS activity due to its relative basicity and for enabling high metal dispersion, which leads to small particle sizes that are known to favour APR performance [75,179]. Since Ru is the most frequently adopted active phase for alcohol reforming due to its high C–C bond cleavage activity [109], we aimed to verify and compare its performance against Pt, which is known for high H_2 selectivity but lower C–C cleavage efficiency [63]. To this end, ethanol APR tests were performed using Pt- and Ru-based catalysts. Since the support plays a decisive role in catalytic performance, two different supports were also selected: the activated carbon, chosen for its very high surface area, inert character, and hydrothermal stability under APR conditions , and the Al_2O_3, selected for its well-established role in promoting WGS activity and for enabling high metal dispersion, which leads to small particle sizes that are known to favour APR performance [75,179]. In Figure 24, the ethanol conversions and carbon to gas (C to G) are observed with each catalyst are reported.

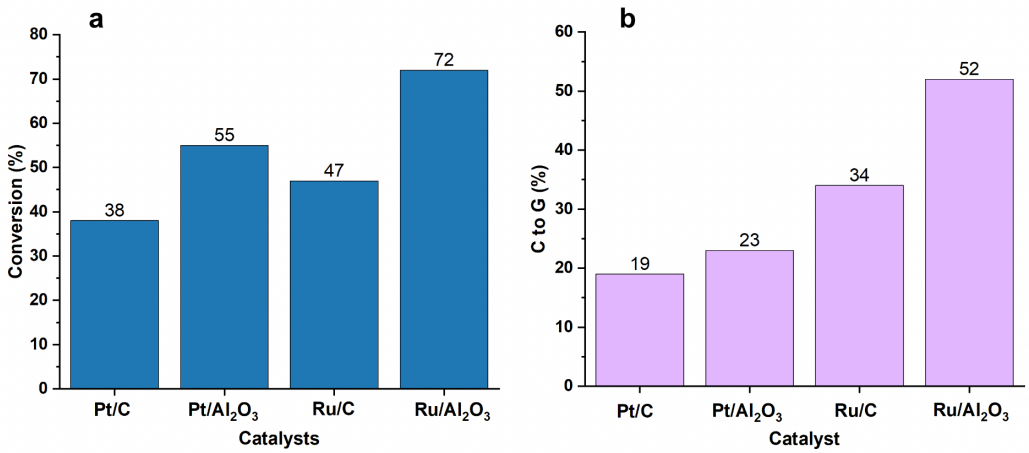

Figure 24. Ethanol APR conversion (a) and carbon to gas (b) over Pt- and Ru-based catalysts supported on carbon and Al_2O_3. Reactions were performed at 230 °C and 2 bar with 0.8 wt. % ethanol solution (75 mL) and 0.2 g catalyst, after 2 h of reaction.

In particular, Ru/Al_2O_3 exhibited the highest ethanol conversion and C to G ratio among all catalysts, followed by Pt/Al_2O_3 for ethanol conversion and Ru/C for C to G. These results suggest that Al_2O_3 could contribute positively to ethanol conversion. In particular, unlike activated carbon, alumina provides weak acidic sites that can help stabilize the active metal phase, enhancing its dispersion and thereby increasing the number of accessible active sites available for reforming [53]. Regarding C to G performance, Ru-based catalysts outperformed Pt-based ones, confirming the superior reforming activity of Ru with small alcohols.
Liquid-phase analysis revealed that Ru-based catalysts produced only trace amounts of acetic acid, up to 0.1 mmol with Ru/Al_2O_3, as a by-product. In contrast, Pt-based catalysts left higher concentrations of oxygenates in the liquid phase, with Pt/Al_2O_3 generating up to 1.6 mmol of acetic acid and 0.1 mmol of acetaldehyde. The gas-phase composition is reported in Figure 25, expressed in mmol of each detected gas, together with the corresponding H_2 productivity for each catalyst.

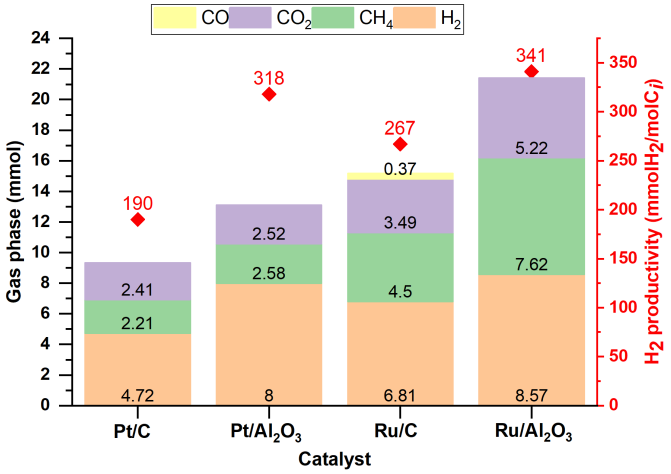

Figure 25. Gas phase products (CO, CO_2, CH_4, H_2) obtained after APR tests over Pt/C, Pt/Al_2O_3, Ru/C, and Ru/Al_2O_3 catalysts. Bars represent the amounts of each gas (mmol), while red rhombus indicate the corresponding H_2 productivity (mmol H_2/mol C_i).

It is worth noting that Ru/Al_2O_3 exhibited the highest H_2 productivity among the tested catalysts, with 8.57 mmol of H_2 produced after 2 h of reaction, compared to

8.0, 6.8, and 4.7 mmol for Pt/Al_2O_3, Ru/C, and Pt/C, respectively. Ru/C was the only catalyst to generate detectable traces of CO.
When the gas products are expressed in terms of volume percentage, however, a different picture emerges. As shown in Figure 26 (a), Pt/Al_2O_3 was the only catalyst in which H_2 accounted for more than half of the gas phase, reaching 61%, while the remaining fraction consisted primarily of CO_2 and CH_4. In contrast, the gas composition for Ru/Al_2O_3 consisted of only 40% H_2, 36% CH_4 and 24% CO_2.
These results have a direct impact on APR H_2 selectivity (Figure 26, b), which is defined as the ratio between H_2 and CO_2 relative to the theoretical stoichiometry of ethanol reforming as in equation (20). The theoretical ratio of H_2/CO_2 for ethanol is 3; thus, lower experimental values indicate that reactions are deviating from the ideal pathway, likely due to side reactions such as methanation. In particular, for every mole of methane formed, four moles of H_2 are theoretically lost from the reforming balance.

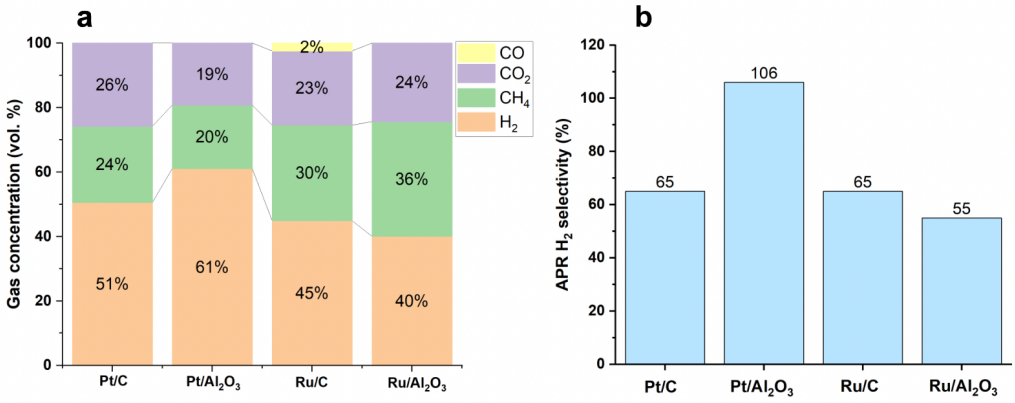

Figure 26 Gas phase composition (CO, CO_2, CH_4, H_2) expressed in percentage after APR tests over Pt/C, Pt/Al_2O_3, Ru/C, and Ru/Al_2O_3 catalysts (a) and APR H_2 selectivity (%) for the same catalysts (b).

The APR H_2 selectivity exceeding 100% for Pt/Al_2O_3 can be explained by the occurrence of parallel reaction pathways which lead to H_2 production in addition to the theoretical ethanol reforming, according to the C-C bond cleavage pathway followed by WGS (see Figure 23). This is supported by the presence of CH_4, which represents ~20% of the gas phase, and by the accumulation of acetic acid in the liquid phase. As illustrated in Figure 23, acetic acid formation proceeds via acetaldehyde dehydrogenation, a reaction that simultaneously produces one mole of H_2. This additional H_2 source leads to a H_2:CO_2 ratio different from the theoretical value predicted for ethanol reforming (i.e., 3:1). Consequently, the observed APR H_2 selectivity reflects the relative contributions of competing pathways, each characterized by a distinct stoichiometry.
These results highlight a trade-off between H_2 selectivity and overall carbon removal to and from the gas phase. While Pt/Al_2O_3 achieved the highest H_2 selectivity (106%), the lower C to G conversion may be representative of a larger fraction of carbon remaining in the liquid phase. Instead, Ru/Al_2O_3 maximized carbon conversion to the gas phase, which is better suited for wastewater treatment applications since the removal of dissolved carbon is the primary objective. The use of carbon supports, however, resulted in lower ethanol conversion. Due to their essentially neutral surface, carbon materials provide limited interaction with the

reactants, which could reduce their ability to promote ethanol reforming. For this reason, they were not considered for further investigation.
Although, Ru is still a noble metal, Ru/Al_2O_3 was selected over Pt for the next tests, due to its lower cost (30.7$/g for Pt, 14.1$/g for Ru) [59] and its higher ethanol conversion and ability to reduce the carbon content in the liquid especially with small alcohols. Moreover, in the long-term perspective of industrial application, even a reduction of approximately 50% in catalyst cost can represent a significant advantage for process feasibility.

4.3 Impact of temperature on ethanol APR

Three different temperatures were investigated (230, 250, and 270 °C) to evaluate the influence of temperature on ethanol APR over Ru/Al_2O_3, with the dual aim of assessing the effect on ethanol conversion and on the distribution of gas products, particularly H_2, over time. For each condition, duplicate tests were performed to ensure reproducibility and pressure was kept constant between tests, 3 bar above P_{sat}.
As shown in Figure 27 ethanol conversion increased markedly with temperature and reaction time. At 270 °C, complete ethanol conversion was achieved within 1 h, whereas at 250 °C full conversion required approximately 3 h. In contrast, at 230 °C requires over 6 h of reaction to reach complete conversion, suggesting a potential kinetic limitation at lower temperature.

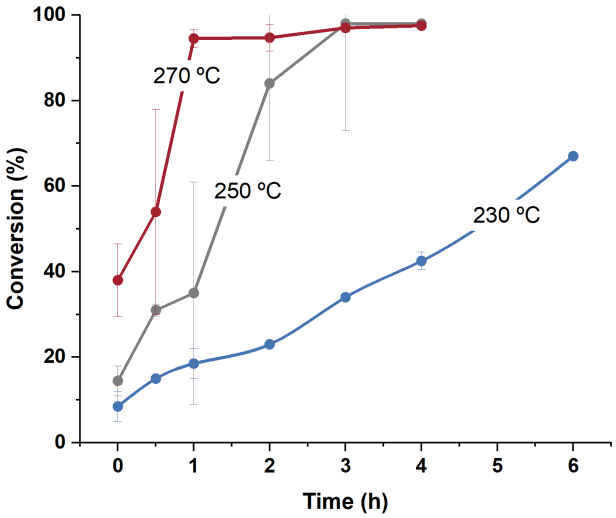

Figure 27 Ethanol conversion as a function of reaction time during APR experiments at 230, 250, and 270 °C. Error bars represent the standard deviation from duplicate measurements.

These results indicate that higher temperatures accelerate ethanol reforming and favour rapid removal of the carbon from the liquid phase. Beyond conversion, however, temperature seems not to affect the product distribution. In fact, the relative percentages of the gaseous species vary mainly with reaction time, as shown in Figure 28, while no additional gas-phase species detected. This suggests that the same reaction pathways occur throughout the investigated conditions; however, from a kinetic standpoint, their relative rates change over time. In particular, at short reaction times, H_2-producing pathways (such as reforming and the WGS) prevail, whereas at longer times H_2-consuming reactions dominate.

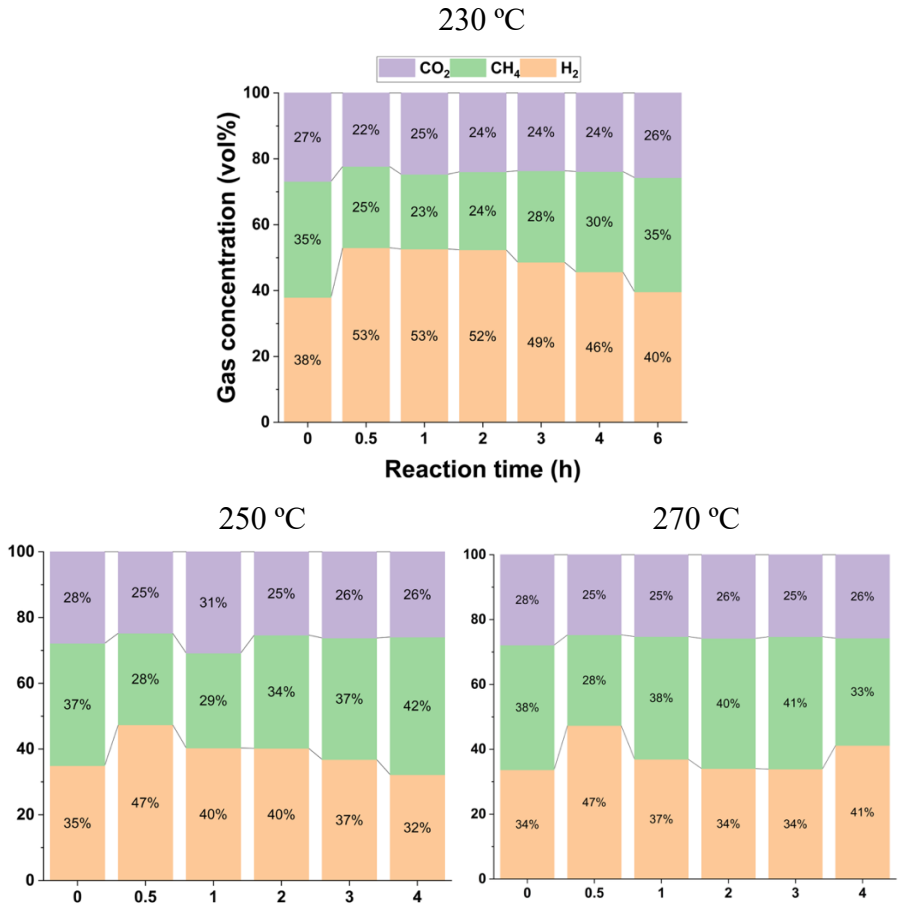

Figure 28 Evolution of gas concentration on a vol basis during APR at 230, 250, and 270 °C as a function of reaction time.

In particular, the main difference is observed at 230 °C, where H_2 remains the dominant product throughout the experiment (40–53 vol.%), with CH_4 and CO_2 contributing in comparable amounts. Although conversion is relatively slow at this temperature, this suggests that the gas composition remains stable over time and that the most affected performance parameter is H_2 selectivity, which is, in fact, the highest at 230 °C, reaching 79% after 30 minutes of reaction time and then stabilizing at around 70% on average (Figure 29, a).

At 250 °C a more significant gas concentration change can be observed, H_2 concentration gradually decreases from ~47 to 32 vol.%, while CH_4 increases from 28 to 42 vol.%, while the concentration of CO_2 remains almost constant (~25–30 vol.%). Similarly, at 270 °C, the relative amount of CH_4 progressively increases up to ~41 vol.% while H_2 stabilizes in the 34–41 vol.% range. These results indicate that, as temperature increases, ethanol conversion raises, but side reactions such as methanation gain importance, leading to higher CH_4 yields at the expense of theoretical APR H_2 selectivity.

This trend provides further insight into the interplay between thermodynamics and kinetics. Although methanation is an exothermic reaction and is therefore thermodynamically favoured at lower temperatures, the experimental results show that H_2 yield increases with temperature, indicating kinetically controlled behaviour. At higher temperatures, the enhanced reforming and WGS rates lead to increased H_2 production and accumulation in the gas phase. This higher H_2 partial pressure kinetically promotes H_2-consuming reactions, such as methanation, which

become increasingly competitive with reforming pathways. As a result, part of the produced hydrogen is converted into CH_4, reducing the net H_2 yield and affecting selectivity, as observed in Figure 29.

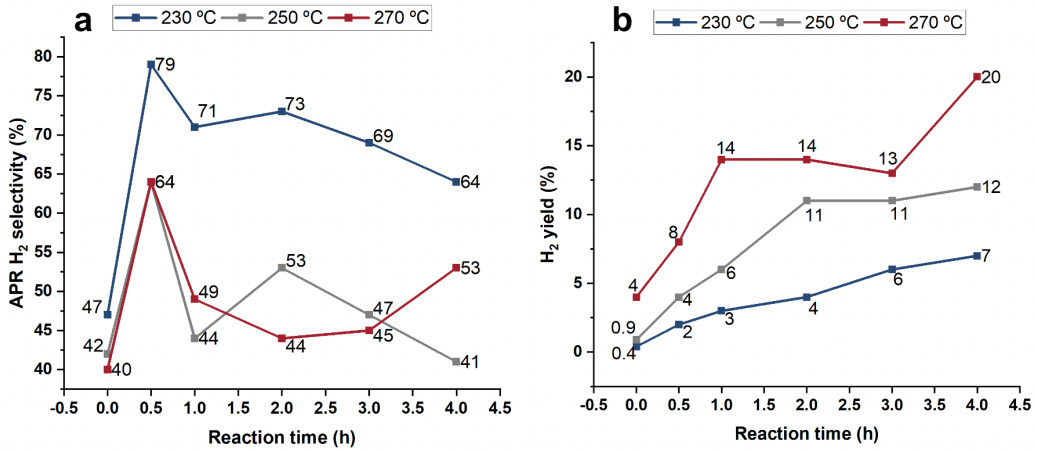

Figure 29. Evolution of APR H_2 selectivity (a) and H_2 yield (b) as a function of reaction time at 230, 250, and 270 °C.

Interestingly, all three temperatures exhibit a distinct peak in H_2 selectivity at around 30 minutes of reaction time, reaching 1.89, 4.25, and 7.83 mmol of H_2 at 230, 250, and 270 °C, respectively. These values correspond to H_2 yields of 2%, 4%, and 8% relative to the theoretical ethanol APR stoichiometry, before declining or stabilizing at longer reaction times. This suggests that initially, around 30 minutes after the system reaches the operating temperature, the reaction follows the theoretical stoichiometry toward H_2 formation, while, as H_2 begins to accumulate, secondary reactions progressively prevail, consuming the H_2 just produced.

Looking at the bigger picture, even though the gas-phase product distribution is not strongly affected at higher temperatures, the overall H_2 yield exhibits a more pronounced temperature influence, with higher operating temperatures leading to increased H_2 production per carbon content present in the feed (Figure 29, b).
Overall, these results confirm that higher temperatures accelerate ethanol conversion but also intensify secondary reactions, particularly methanation, which competes with H_2 formation and reduces H_2 selectivity. A clear trade-off emerges: at 230 °C, gas mixtures remain H_2-rich but conversion is slow; at 270 °C, conversion is rapid but H_2 selectivity drops markedly. The intermediate case (250 °C) offers a more favorable balance, with sufficiently high conversion while H_2 still represents a significant share of the gas phase, with a reduce heat requirement compared to 270 ºC.

4.4 Ethanol concentration effect

To further investigate ethanol reforming under conditions representative of winery wastewaters, experiments were conducted by varying the ethanol concentration between 1 and 5 wt.%, consistent with the typical range found in such effluents.
Firstly, ethanol conversion, H_2 yield, C to G conversion, and APR H_2 selectivity were evaluated for three different ethanol concentrations (1, 2.5, and 5 wt.%) at 270 °C over reaction time and results are shown in Figure 30.

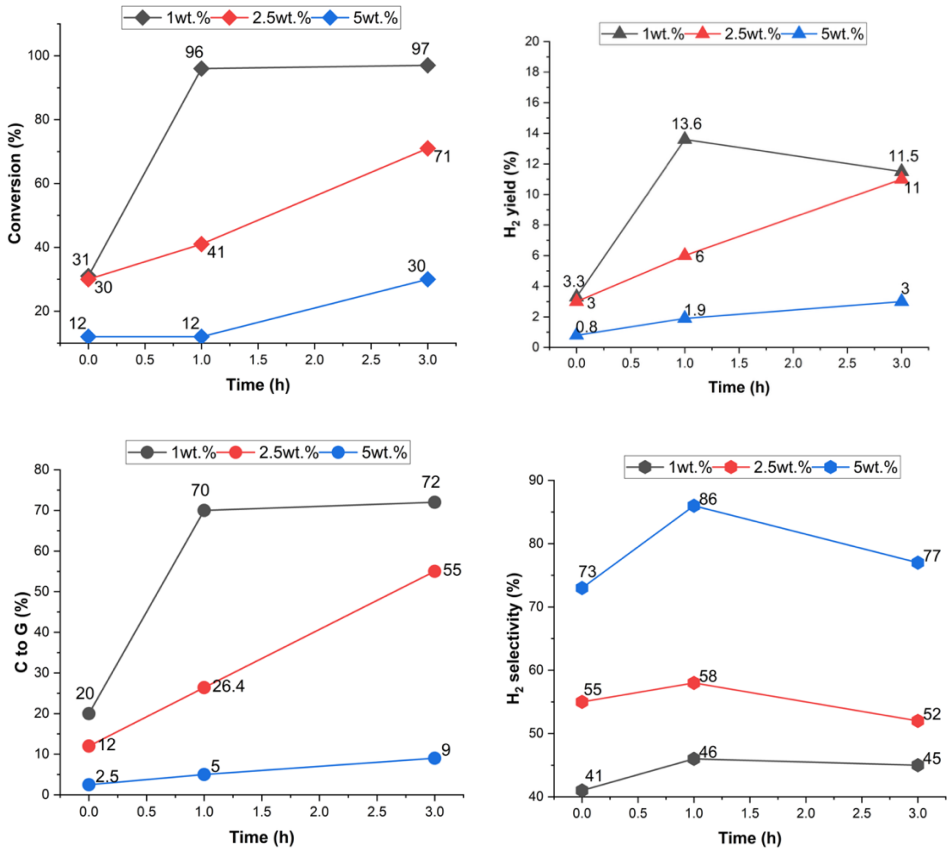

Figure 30. Ethanol APR performance at 270 °C for different feed concentrations (1, 2.5, and 5 wt.% ethanol solution) over time. The graphs report: ethanol conversion (%), H_2 yield (%), carbon-to-gas (C to G, %) conversion, and APR H_2 selectivity (%).

At the lowest ethanol concentration (1 wt.%), nearly complete conversion (~96%) was reached after 1 h reaction, accompanied by the highest H_2 yield (~14%) and C to G ratio (~70%). These results alone suggest that the ethanol conversion and removal from the liquid is more efficient for more diluted feeds, probably due to a better interaction between the catalyst surface and reactant molecules. At higher substrate concentrations mass transfer limitation phenomena can arise due to the increased viscosity of the liquid and reduced diffusivity hinder both the diffusion of reactants toward active sites and the removal of products from the catalyst surface, thereby lowering the overall reaction rate, as previously observed in similar studies [79] [47]. At higher ethanol concentrations (2.5 wt.% and 5 wt.%), despite ethanol conversion and C to G ratio being lower, the APR H_2 selectivity increases substantially, reaching its maximum at 5 wt.% (~80%). This suggests that, despite the slower conversion rate, the reaction pathway more closely follows the theoretical APR stoichiometry, with reduced occurrence of side reactions such as methanation. To further clarify these trends, the gas-phase distribution was analysed over time (Figure 31).

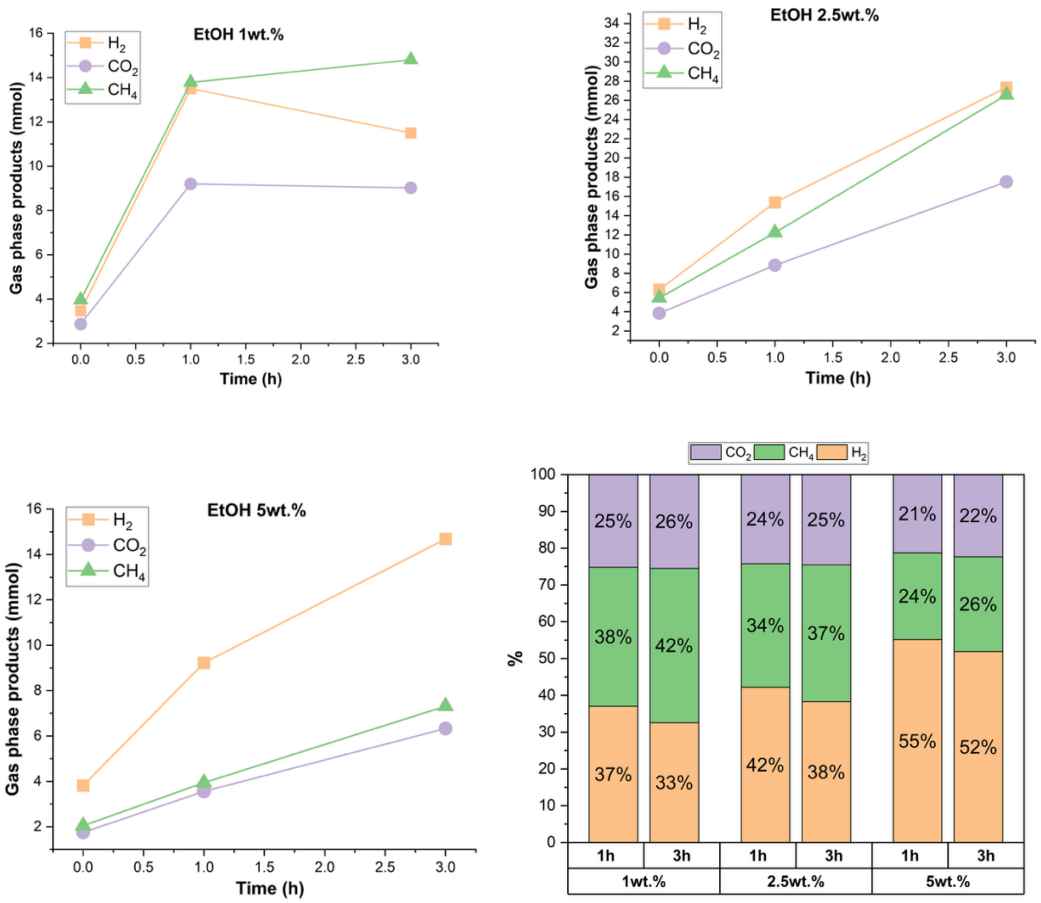

Figure 31. Gas-phase products obtained during ethanol APR at 270 °C for different ethanol feed concentrations (1, 2.5, and 5 wt.%) over time. The graphs report the evolution of H_2, CO_2, and CH_4 formation in mmol after 1 h and 3 h of reaction, and the corresponding gas-phase distribution in percentage by volume.

The evolution of gas production over time reveals different trends depending on ethanol concentration. At the lowest concentration (1 wt.%), H_2 production reached its maximum of ~14mmol after 1 hour and then decreased, accompanied by a parallel rise in CH_4, surpassing H_2. This trend combined with the almost complete ethanol conversion observed under these conditions, suggests that once ethanol stop to be converted and H_2 accumulate in the gas environment, secondary reactions may become dominant, such as methanation reactions. In contrast, for the more concentrated ethanol solutions (2.5 and 5 wt.%), both H_2 and CH_4 production continued to increase with reaction time. For the 2.5 wt.% case, H_2 and CH_4 exhibited comparable increasing rates, while for 5 wt.% the increase in CH_4 was lower. The gas-phase distribution (Figure 31, bottom right) shows that H_2 represents the largest share of gaseous products for 5 wt.% feed, followed by 2.5 and 1 wt.%. However, the higher reforming performance observed al higher concentration is only apparent, since it must be interpreted considering the much lower overall ethanol conversion achieved at 5 wt.%, only about 30% after 3 hours, which in fact translates into a maximum C to G ratio of merely 9%.

Interestingly, using more diluted feeds leads to faster conversion and more effective carbon removal, even when the gas mixture contains higher levels of CH_4. This is especially relevant in real-world waste treatment, where the feed compositions is usually far from the ideal stoichiometry required for APR. In these cases, producing a gas stream that includes H_2 along with other combustible gases such as CH_4 and CO could be directly used as a fuel source. Therefore, for continuous or semi-

continuous APR processes, shorter residence times may be preferred for dilute feeds to maximize H_2 productivity and liquid carbon removal, while longer operation could be more suitable for concentrated feeds, enhancing H_2 selectivity. This versatility strengthens the potential of APR for valorising diverse wastewaters, from brewery wastewater (COD ≈ 1500 mg/L) [87] to sewage or domestic wastewater (COD = 600–900 mg/L) [180] and aqueous fractions of lignocellulosic pyrolysis bio-oils (≈ 1 wt% organics) [86] by generating usable fuel gases while achieving efficient carbon abatement in the liquid phase.

4.5 Pressure effect

The effect of the initial system pressure on ethanol APR performance was investigated by comparing standard conditions (Std, 3 bar as initial pressure) with experiments performed at 2.5 times higher initial pressure (2.5P). As shown in Figure 32, ethanol conversion was nearly unaffected by the increase in pressure, reaching about 96–97% after 1 h for both conditions, and remaining stable thereafter. However, significant differences emerged in H_2 yield and selectivity.

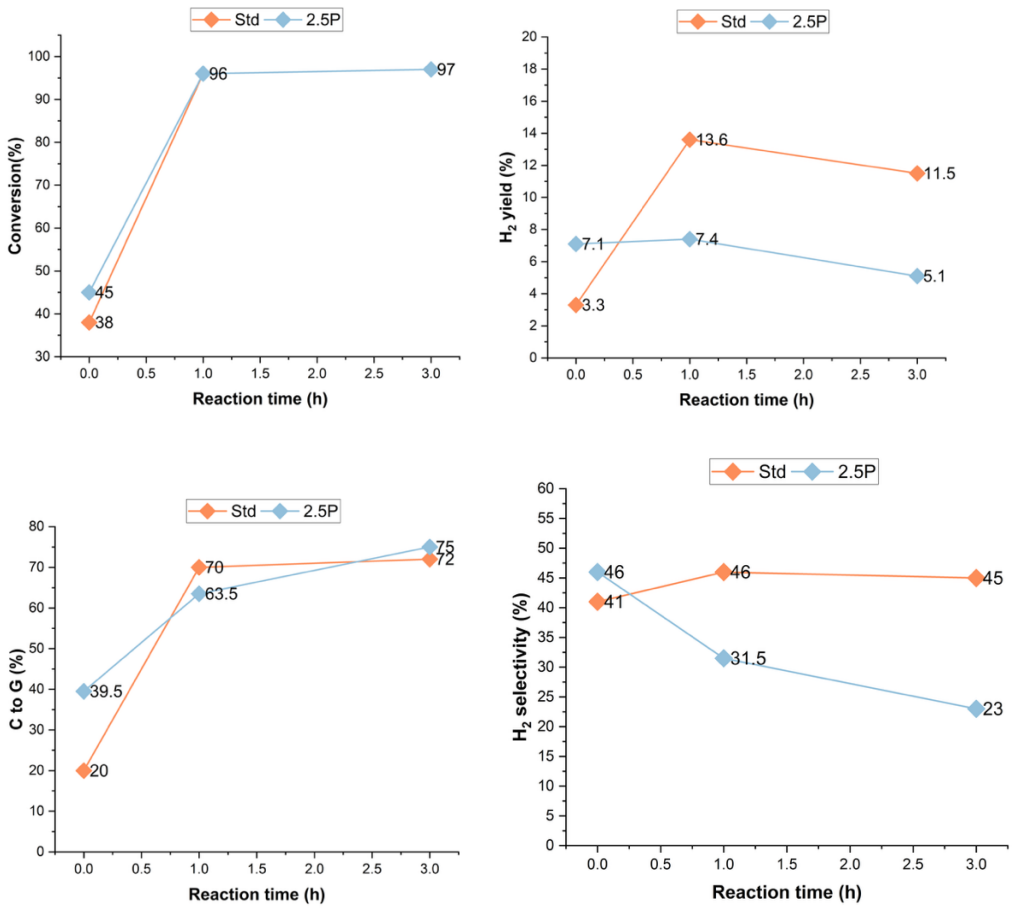

Figure 32. Comparison between standard conditions (Std) and the 2.5 times higher pressure than std conditions vs. ethanol conversion, H_2 yield, carbon-to-gas (C-to-G) conversion, and H_2 selectivity as a function of reaction time.

With standard pressure conditions, the H_2 yield peaked at 13.6% after 1 h. A decrease in H_2 yield can then be observed after a few hours (11.5% after 3 h). In contrast, the 2.5P condition showed substantially lower H_2 yields, with H_2 yields at around 7.4% after one 1 h, declining to a yield of 5.1% after 3 h. This decrease can be attributed to thermodynamic and kinetic constraints associated with high-pressure operation. Higher pressure thermodynamically disfavours overall gasification by shifting reforming equilibria toward the liquid phase. In addition, elevated pressure promotes H_2-consuming reactions such as methanation, which are favoured by a reduction in the total number of gas moles. As a result, H_2 produced via reforming and the WGS is increasingly consumed, leading to lower net H_2 yield and selectivity [47].

The C to G followed a similar trend, confirming the proposed theory of pressure having a negative correlation with respect to gas formation. While both conditions showed comparable results after 3 h (~72–75%), the gas formation rate was considerably slower under 2.5P, especially during the first hour. Furthermore, the APR's H_2 selectivity was observed to decrease significantly as pressure was increased, dropping from 46% under standard conditions to only 23% at 3 h in the 2.5P case. This suggests that elevated pressures not only suppress reforming and WGS reactions, but also promote secondary pathways such as methanation and CO_2 hydrogenation. This, in turn, leads to increased CH_4 formation at the expense of lower H_2 yields. This behaviour is further confirmed by the gas-phase composition results reported in Figure 33. Under standard pressure (Std), the gas evolution trends mirror those observed for conversion and H_2 yield, with H_2 and methane showing comparable formation rates after 1 h, while CO_2 remains relatively stable. However, at higher initial pressure (2.5P), a clear suppression of H_2 production is evident, with H_2 decreasing over time, whereas CH_4 continuously increases, becoming the dominant gas-phase component after 3 h (Figure 33).

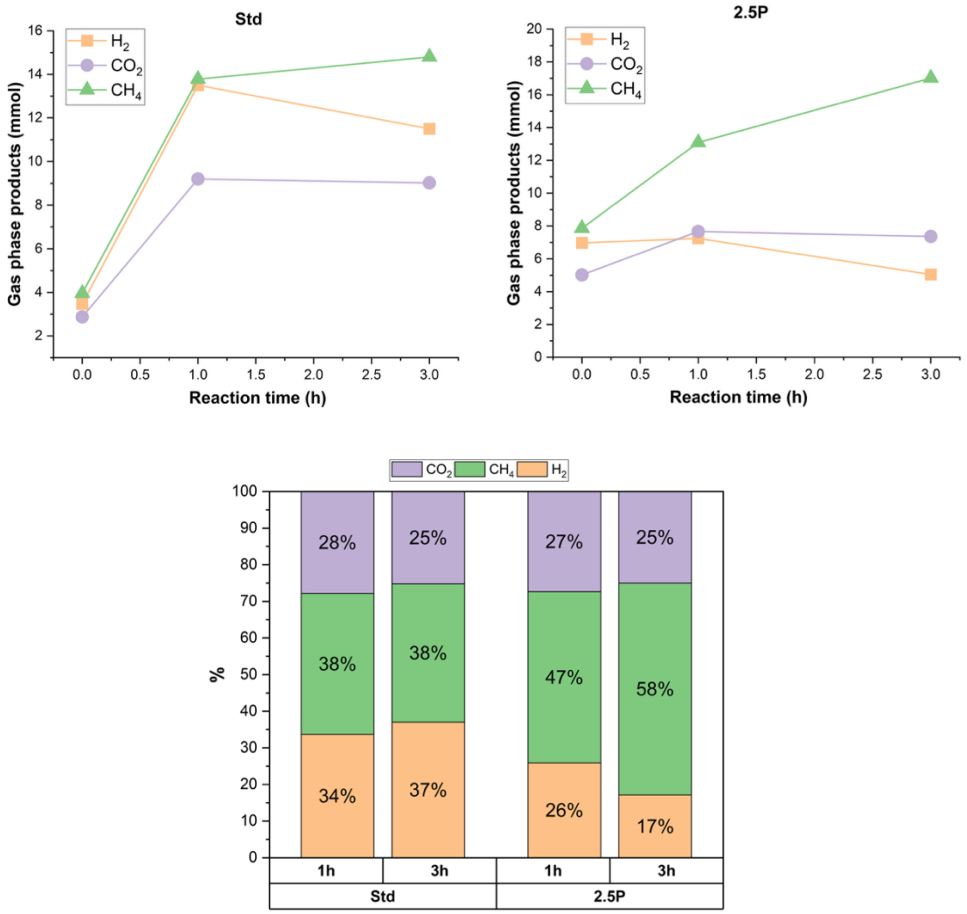

Figure 33. Gas-phase composition and product distribution obtained during APR at the standard (Std) and higher pressure (2.5P) conditions. The upper plots show the evolution of individual gas components (H_2, CO_2, CH) as a function of reaction time. The lower stacked bars display H_2, CO_2 and CH_4 relative volumetric percentages after 1 h and 3 h of reaction.

The gas composition profiles showed in the lower portion of Figure 33 further reinforces this interpretation, since the H_2 share can be observed to be lower in the 2.5P condition, dropping from 26% to 17% between 1 h and 3 h, while methane increases from 47% to 58%. Under standard conditions, instead, the gas phase shows higher H_2 concentrations (34–37%) with more balanced CO_2 and CH_4 contributions over the same time period.

These findings suggest that the APR reaction pathways are strongly influenced when operating at initial pressures 4.5 times higher than the P_{sat} (since at standard pressure the system is already about 2 bar above the P_{sat}), both from a kinetic and thermodynamic standpoint. While the total carbon conversion remains comparable after long reaction times, H_2 productivity and selectivity are substantially reduced, emphasizing the importance of maintaining moderate or standard pressure conditions to favour reforming and WGS reactions over methanation.

4.6 Effect of the support

With the aim of broadening knowledge on ethanol reforming, the strategy was to investigate innovative and relatively abundant materials for application in APR, with the goal of advancing the technology beyond laboratory boundaries toward real-world application. The design criteria addressed two aspects: on one hand, to explore novel materials such as Ru supported on CeO_2 in the ethanol APR reaction, and on the other, to enhance process profitability either by reducing noble metals content or by increasing catalyst stability, thereby minimizing activity loss and frequent replacement.

For this purpose, CeO_2 was selected as a potential substitute for Al_2O_3. Previous studies had shown that Pt- or Ni-doped CeO_2 outperformed Al_2O_3-based catalysts by more than 30-fold [181], [182]. Moreover, Al_2O_3 suffers from limited thermal and hydrothermal stability, leading to surface area loss even within typical APR operating conditions, making it less suitable for prospective industrial applications [47]. Ceria is among the most abundant rare-earth oxides, and its exceptional catalytic activity is linked to the Ce^{3+}/Ce^{4+} redox couple, which provides remarkable oxygen mobility and generates oxygen vacancies known to enhance activity, particularly in WGS reactions [183]. DFT studies, for instance, have demonstrated that higher oxygen vacancy concentrations lower the activation energy for water splitting [184]. In addition, Ru was selected as the active metal at a reduced loading (2 wt.%), compared to a conventional 5 wt.% Ru/Al_2O_3 benchmark. Given Ru/CeO_2's previously demonstrated superiority over Ru/Al_2O_3 in similar reactions, its potential in ethanol APR was explored [185].

Catalytic tests performed with 2 wt.% Ru/CeO_2 at 250 °C using a 1 wt.% ethanol solution for 1 h reaction time, showed that, when normalized to the nominal Ru content, the catalyst showed slightly lower ethanol conversion, and H_2 productivity compared to the commercial counterpart (Table 13).

Table 13. Physicochemical properties and catalytic performances of Ru-based catalysts supported on Al_2O_3 and CeO_2.

Catalyst	Support	Ru loading (wt. %)	Surface area (m^2/g)	Pore volume (cm^3/g)	Average pore width (nm)	Particle size (nm)	EtOH conversion rate (mol/g_{Ru})	H_2 productivity ($mmolH_2/g_{Ru}$)
Ru/Al_2O_3	Al_2O_3	5	114	0.26	9.0	5.2 ± 2.5	1.7	554
Ru/CeO_2	CeO_2	2	89	0.20	0.9	-	1.3	443

The Ru loading (%) refers to the nominal value. Physicochemical properties were determined from nitrogen adsorption–desorption isotherms collected at −196 °C. The specific surface area was calculated from the monolayer capacity obtained by applying the BET model to the adsorption branch of the nitrogen isotherm. The total pore volume was estimated from nitrogen uptake at high relative pressures, and the average pore width was calculated from the BET surface area and total pore volume.

These results can be rationalized by considering the physical properties of the two catalysts, particularly pore size and surface area. In the case of CeO_2, the support exhibits predominantly microporous structures (<2 nm), which are generally less favorable for catalytic applications compared to mesoporous supports (2–50 nm), such as alumina [186]. Additionally, assuming a comparable Ru particle size

distribution, Ru/CeO_2 exhibits a 21% lower surface area than Ru/Al_2O_3. However, TEM analysis did not clearly show Ru nanoparticles on Ru/CeO_2. Instead, EDX elemental mapping revealed a non-uniform Ru distribution, with particles accumulating in localized regions of the support rather than being evenly dispersed (Figure 34). This prevented any reliable estimation of particle size and dispersion, so catalytic performance is reported on a per-gram-of-nominal Ru content in the catalyst rather than normalized to the actual Ru exposed content accounting for its real distribution on the support.

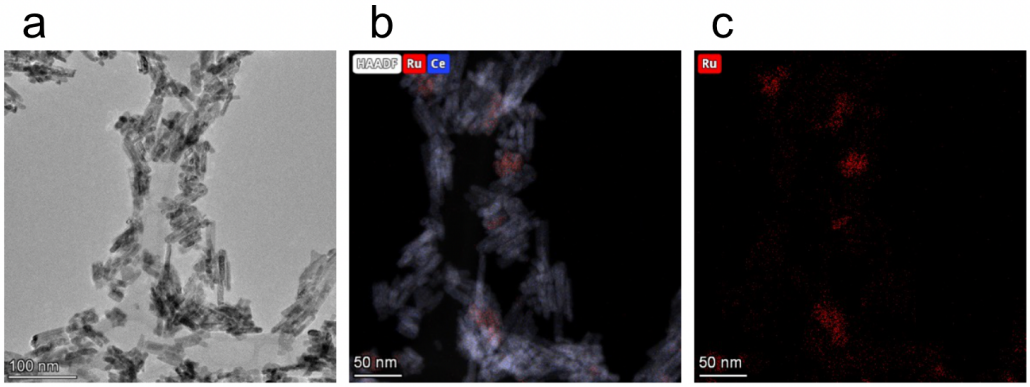

Figure 34. (a) TEM image of the Ru/CeO_2 impregnated catalyst showing the particular rod-like nanostructured morphology of the support. (b) HAADF-STEM image with EDX elemental mapping highlighting the distribution of Ru (red) and Ce (blue). (c) EDX map of Ru, confirming the heterogenous dispersion of ruthenium species across the support.

In contrast, this was feasible for the commercial catalyst, which exhibited a much more homogeneous nanoparticle distribution and particle size observed at the HAADF-STEM images (Figure 35).

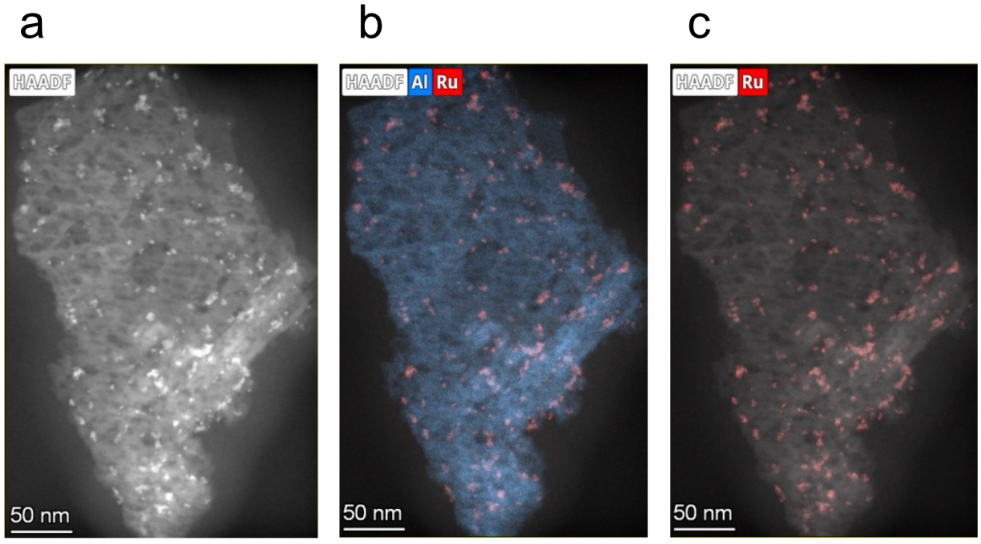

Figure 35. (a) HAADF image of the commercial Ru/Al_2O_3 catalyst particles, (b) the EDX overlay mapping showing Al (blue) and (c) Ru distribution (red) highlighting the homogeneous dispersion of Ru nanoparticles across the Al_2O_3 support.

Particle size distribution was manually determined by analysing over 150 particles from multiple TEM images of the same sample. The commercial catalyst exhibited

an average particle diameter of 5.3 ± 2.3 nm, where the majority of particles had a diameter of 4–5 nm. The particle size distribution follows a gaussian behaviour, with a smaller fraction of particles with a diameter of 2–4 nm, and another small fraction with particles of 6–8 nm in diameter. A small fraction of agglomerates was also identified (diameter greater than 12 nm, Figure 36).

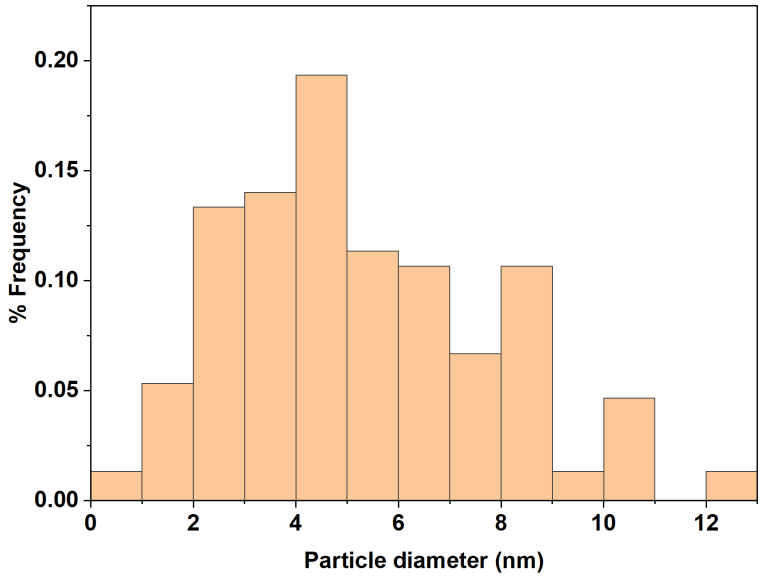

Figure 36. Particle size distribution of the commercial catalyst obtained from TEM measurements (150 particles). The average particle diameter was calculated as 5.3 nm.

EDX elemental analysis further enabled the determination of local mass concentrations of the elements in the sample. For Ru/Al_2O_3, the Ru loading was found to vary between 2 and 11 wt.%, with an average value higher than the nominal 5%. Such variability could have affected the observed APR performances, since the catalytic response is influenced by particles with different local loadings, and the results may strongly depend on which regions of the catalyst surface were predominantly engaged during the tests. From the TEM images it was also possible to estimate the metal distribution accounting to 20% according to the methodology explained in the Section 2.1 (catalyst characterization).

The two supports exhibit distinct chemical properties: alumina is characterized primarily by weak acidic sites, whereas CeO_2 is dominated by basic sites. While basicity is generally known to promote the WGS reaction by facilitating water activation, this effect was not evident here [185]. At comparable Ru loading, the CeO_2-supported catalyst displayed ~20% lower H_2 productivity than its Al_2O_3 counterpart (Figure 37).

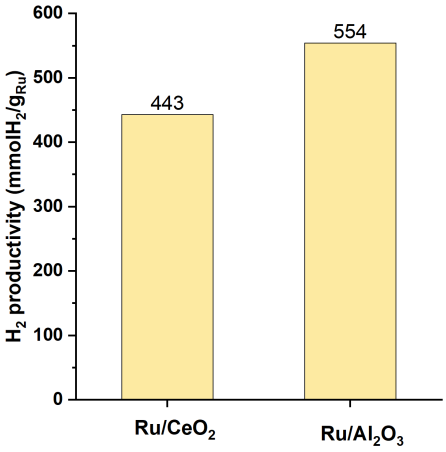

Figure 37. H_2 productivity performance normalized on the nominal amount of Ru from Ru/CeO_2 and Ru/Al_2O_3 catalysts at 250ºC for 1h reaction time.

This discrepancy can instead be attributed to morphological and physical differences between the supports, particularly in terms of pore size and surface area. The ~20% reduced surface area of CeO_2 catalyst could potentially be the responsible for the lower H_2 productivity, suggesting that the commercial catalysts is not the just more active but that the higher H_2 produced per unit of carbon in the feedstock can be largely attributed to the higher available surface area. These findings highlight the critical influence of synthesis method on support properties, which in turn directly affect catalytic performance.

4.7 Effect of exsolution

Exsolution is here explored as a novel synthesis route for APR applications, building on the documented exsolution properties of CeO_2 [187] and the promising stability enhancements reported for exsolved catalysts [170], [188]. This aspect is particularly relevant in view of future applications to real wastewater streams, where harsh conditions, such as high salinity, variable pH, or the presence of inhibitory organics, can strongly affect catalyst performance.
A 2 wt.% Ru-ex/CeO_2 catalyst was synthesized trough co-precipitation followed by an exsolution step according to the procedure detailed in Section 2.1 (catalysts synthesis). Several combinations of Ru loading, calcination, reduction temperatures and time were tested (Table 3), before obtaining a pure fluorite phase characteristic of CeO_2 [189]. In particular, two calcination steps were required: the first at 450 °C for 4 h and the second at 550 °C for 4 h, followed by a reduction step at 750 °C for 4 h. A TPR-H_2 analysis was also performed to define the appropriate reduction temperature for the exsolution and calcination steps, ensuring complete reduction of Ru species, which occurred already below 300 ºC (Figure 38).

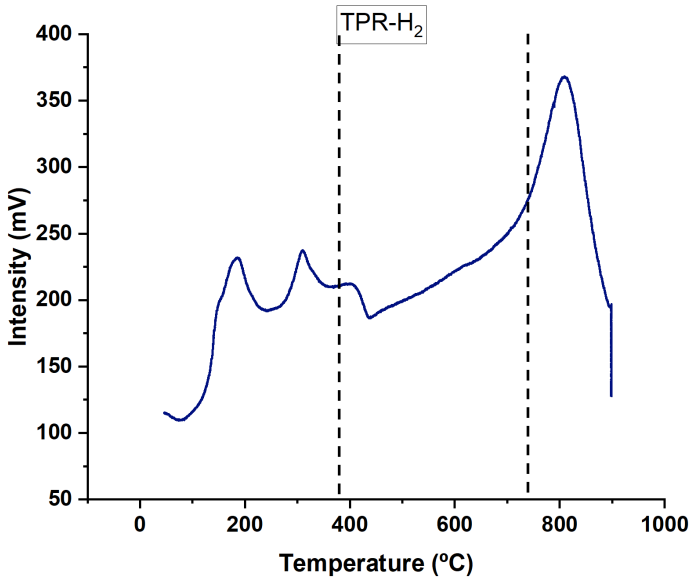

Figure 38. H_2-temperature programmed reduction (TPR) profile of the synthesized 2 wt.% Ru/CeO_2 catalyst, highlighting three main reduction regions: below 230 °C, between 230–600 °C, and above 600 °C.

Three main reduction regions were identified: (i) below 230 °C, associated with the reduction of RuO_x species; (ii) between 230 and 600 °C, corresponding to the reduction of Ce^{4+} to Ce^{3+}; and (iii) above 600 °C, attributed to the reduction of bulk ceria, as previously reported [190].

Although, Naeem et al. showed that higher reduction temperatures increase the extent of Ru nanoparticle exsolved on CeO_2 surfaces, 750 °C was selected as the reduction temperature to balance a good exsolution extent with structural stability, avoiding excessive particle growth and preventing destabilization of the ceria support.

XRD analysis confirmed the formation of a pure fluorite crystal structure, with diffraction patterns showing only the typical CeO_2 reflections and no detectable RuO_2 peaks (Figure 39). This indicates that Ru atoms were incorporated into the CeO_2 lattice without disrupting its fluorite structure. A slight shift of the main peaks toward higher 2θ values was also observed, consistent with lattice contraction due to the smaller atomic radius of Ru compared to Ce, further supporting substitutional incorporation of Ru into the lattice.

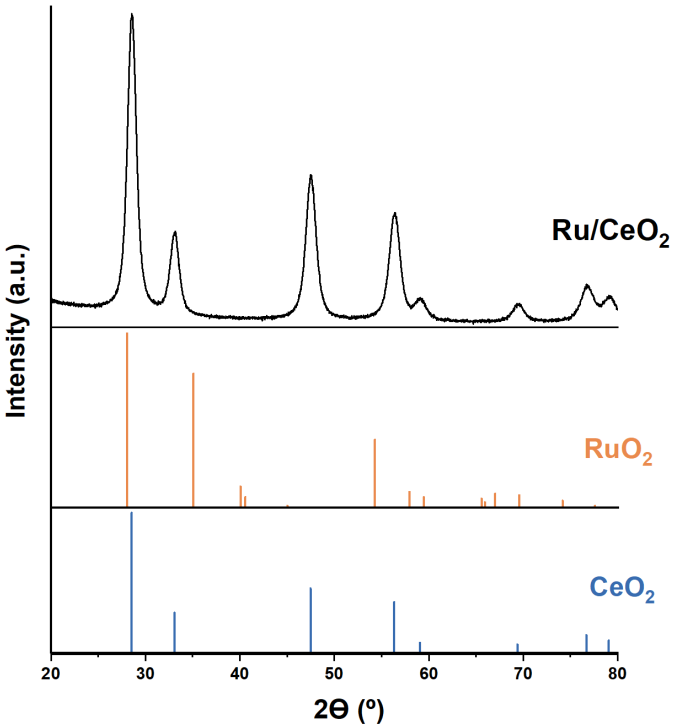

Figure 39. XRD diffraction patterns of CeO_2 and the new synthetized Ru-ex/CeO_2 catalyst. Both samples display the characteristic fluorite crystal structure of CeO_2, with no detectable RuO_2 peaks.

In addition, TEM imaging was performed to verify the presence, size, and distribution of Ru nanoparticles. Representative TEM images from the same sample are shown in Figure 40.

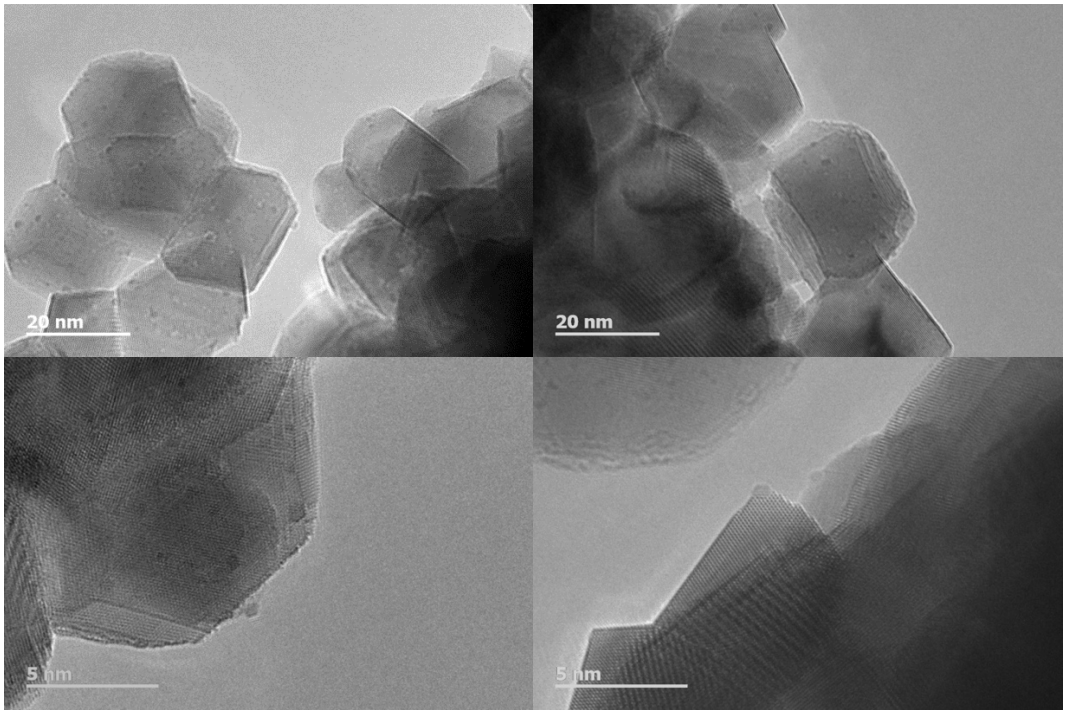

Figure 40. TEM images of the 2 wt.% Ru-ex/CeO_2 catalyst at different magnifications. The images reveal well-defined faceted nanoparticles exhibiting predominantly truncated octahedral and polyhedral morphologies, typical of ceria-based materials. The lattice fringes are clearly visible, confirming the high crystallinity of the CeO_2 support and the preservation of its fluorite structure after synthesis.

It was observed a homogeneous distribution of Ru nanoparticles across the CeO_2 support, without significant nanoparticle agglomeration or big differences in particle sizes. Particle sizes were confirmed to be quite small, with an average diameter size of 1.13±0.5 nm, and its size distribution reported in Figure 41.

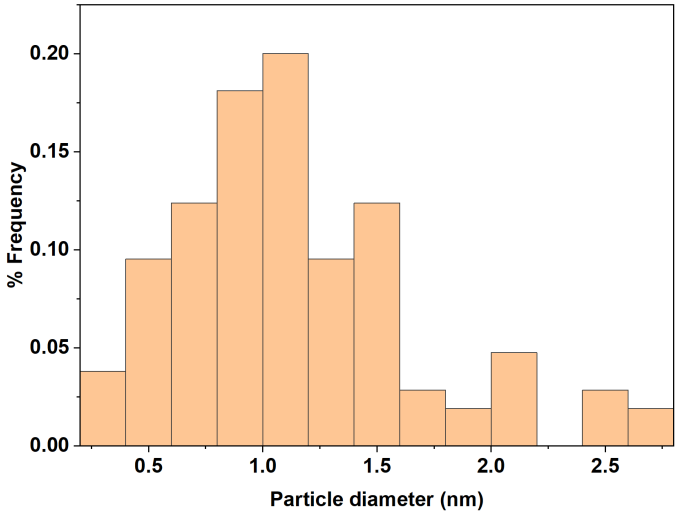

Figure 41. Statistical histogram showing the particle size distribution for 2wt.% Ru/CeO_2. The x-axis reports the particle diameter (nm), while the y-axis shows the relative frequency expressed as percentage. Most particles fall between 0.8 and 1.2 nm in diameter, with a maximum frequency around 1.1 nm.

Regarding the support, CeO_2 grains exhibited a polyhedral morphology characteristic of the fluorite structure, as also reported by Naeem et al. [191], where ceria-based solids showed nanocrystals evolving from irregular polyhedral at lower reduction temperatures to well-defined cubic and truncated-octahedral shapes at higher temperatures. In this case, the grains was approximated to a parallelepiped geometry with well-defined flat facets and sharp edges, showing an average length of 28 nm and a height and width of 22 nm.
The synthesis method strongly influenced the final structure of the catalyst support. As shown in Figure 34 the impregnated catalyst developed a rod-like morphology after calcination at 500 °C for 5 h, whereas the exsolution route, which was based on co-precipitation followed by two calcination steps and a subsequent exsolution, resulted in the nanostructure shown in Figure 40.
This structural change also affected catalytic performance: despite having the same nominal loading of Ru, the exsolved catalyst exhibited significantly lower activity than the impregnated one.
Ethanol APR tests were performed at 250 °C for 1 h using a 1 wt.% ethanol solution, yielding 22% ethanol conversion, with a C to G equalS to 0.1%. The H_2 productivity was significantly lower than that of the impregnated counterpart (44 mmol H_2/gRu vs. 442 mmol H_2/gRu), but the H_2/CO_2 ratio was slightly higher (3.8 vs. 3.3). This ratio indicates a slightly higher APR H_2 selectivity, (128% vs to 109%), suggesting a greater contribution of parallel H_2-producing reactions. However, the lower H_2 productivity observed for the exsolved catalysts could be attributed to their reduced surface area. TEM analysis of the impregnated catalyst revealed less dense regions, likely corresponding to voids or cavity-like structures, which were not evident in the exsolved sample. Consistently, N_2 physisorption measurements showed that the impregnated Ru/CeO_2 exhibited pore volumes within the range typical of mesoporous materials, which are generally preferred for catalytic applications.

Further examination of the gas phase showed that H_2 was the dominant product (67–69%), followed by CO_2, with CH_4 in the 10–15% range. These values are comparable to those of the Ru/CeO_2 impregnated catalyst, although the consistently high H_2 fraction remains noteworthy. The stability of the exsolved catalyst was further assessed by extending the reaction time up to 3 h (Figure 42).

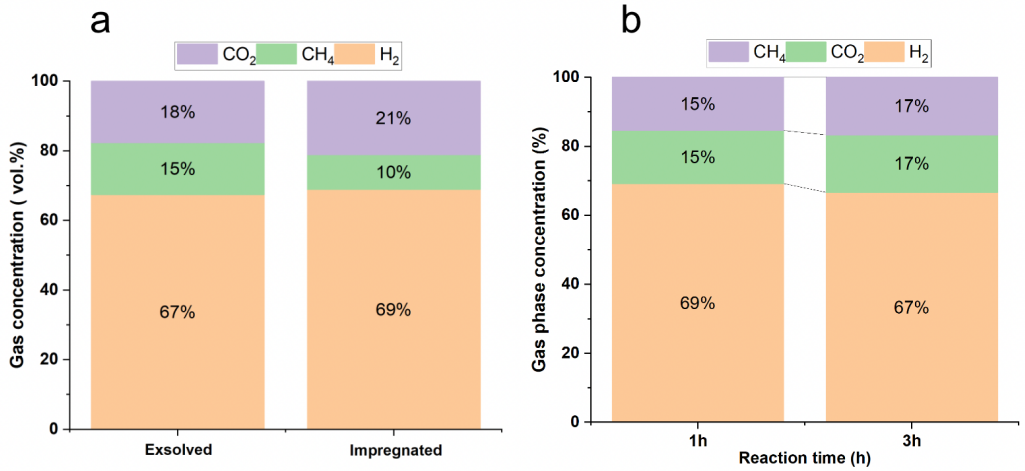

Figure 42. Gas-phase composition from APR tests over Ru/CeO_2 catalysts: (a) comparison of exsolved and impregnated samples after 1 h, and (b) exsolved catalyst after 1 and 3 h reaction time.

No significant shifts in gas composition were observed, in contrast to the commercial Ru/Al_2O_3 catalyst, where prolonged reaction times typically resulted in an increased CH_4 fraction. These results suggest that the exsolved catalyst could provide improved long-term stability in APR performance compared with the commercial counterpart, particularly in terms of H_2 selectivity, as its H_2 fraction remained consistently higher than that of Ru/Al_2O_3, which never exceeded 47% at 250 °C. However, its overall H_2 productivity is still about seven times lower than that of the commercial catalyst, indicating that further investigations are needed to improve its activity. Possible strategies for improvement of performance include testing higher exsolution temperatures to increase the amount of exposed Ru nanoparticles and, consequently, enhance catalytic performance, while maintaining the stability advantage of the exsolved system.

Regarding the liquid fraction analysis, both acetic acid and acetaldehyde were detected. For both the impregnated and exsolved catalysts, around 2% of the initial ethanol was converted to acetaldehyde and less than 1% to acetic acid, with no significant differences observed between the two catalysts in this respect.

Although the exsolved sample exhibited smaller particle sizes, which are typically associated with enhanced H_2 productivity, the exsolved catalyst showed lower activity compared to its impregnated counterpart. This discrepancy can likely be attributed to its reduced surface area, as indicated by BET analysis and supported by TEM observations suggesting lower porosity. In particular the exsolved catalysts exhibit a 2.9 m^3/g surface area, almost 30 times lower than its impregnated counterpart (Table 13), which instead the h2 productivity resulted only 10 times lower than the impregnated. This suggests that the exsolved catalyst could potentially outperform the impregnated one if a higher surface area were achieved. Such improvement could be tailored by adjusting synthesis parameters, for instance by lowering the calcination temperature, since it's well known that higher calcination temperatures cause particle growth in ceria, leading to a reduced surface area [189].

4.7.1 Effect of exsolution with bimetallic and no-noble metals

Given the strong tendency of fluorite structures to undergo exsolution, a modified fluorite-based support was tested in collaboration with the Department of Materials Engineering at Imperial College London. Three exsolved catalysts were synthesized following methodology previously developed [133]: using a $Y_2Zr_2O_7$ support reduced at 1100 °C for 6 h. A 4 wt.% Ru-exsolved catalyst was selected to evaluate the effect of higher Ru loading, while a bimetallic Ru–Fe catalyst (2 wt.% Ru, 1 wt.% Fe) was included to investigate potential synergies, as Fe has previously been shown to enhance catalytic activity in other systems. For instance, the review of Joshi and Vaidya reported that Fe addition to noble and transition metals (Pt–Fe, Ni–Fe, Ru–Fe) consistently enhanced H_2 selectivity by promoting the WGS step and suppressing methanation [43]. Similarly, Coronado et al. highlighted that Fe-containing bimetallic catalysts improved durability and H_2 productivity compared to monometallic systems, owing to the synergistic balance between C–C bond cleavage activity of noble metals and the WGS activity promoted by Fe redox cycling ($Fe^{2+} \leftrightarrow Fe^{3+}$) [47]. Finally, a third catalyst with Fe-only (2 wt.% Fe) was prepared to assess the feasibility of fully replacing noble metals. The inclusion of Fe was also motivated by its reported activity in phenol oxidation, which is particularly relevant for potential APR applications to winery wastewaters, known to contain phenolic compound [99]. The major characteristic of these catalysts are reported in Table 14.

Table 14. physiochemical characteristics of the exsolved catalysts.

Sample identification	Catalyst atomic formula	Metal loading (wt. %)	Surface area (m^2/g)	Average Ru particle size (nm)
RuYZr	$Y_2Zr_{1.8}Ru_{0.2}O_7$	4	7.2	2.3
Ru-FeYZr	$Y_2Zr_{1.8}Ru_{0.1}Fe_{0.1}O_7$	2 (Ru) 1(Fe)	4.0	3.4
FeYZr	$Y_2Zr_{1.8}Fe_{0.2}O_7$	2	2.8	126.7

TEM images of the three samples, in their as-synthesized form and after the exsolution step, are shown below (Figure 43). The appearance of nanoparticles on the catalyst surface is evident only after the exsolution treatment.

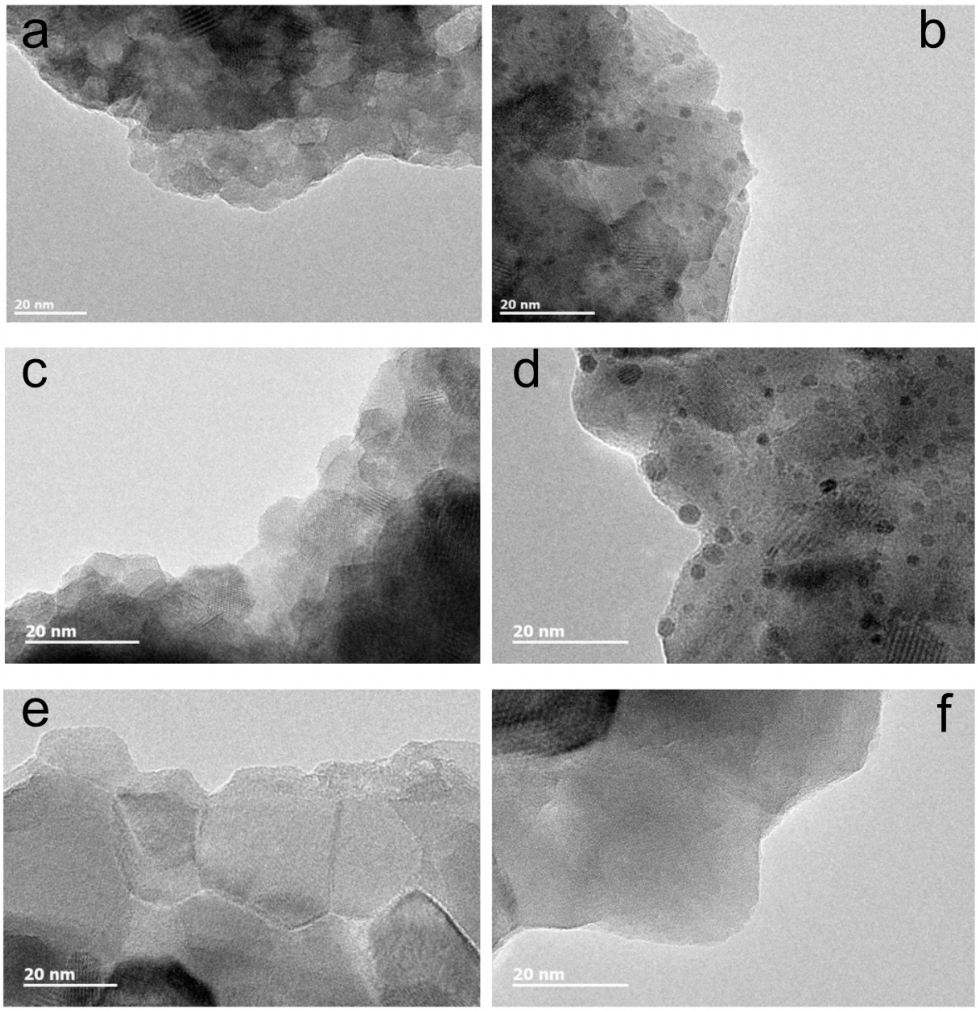

Figure 43. TEM images of the three catalysts: Ru-exsolved, Ru–Fe exsolved, and Fe-exsolved in their as-synthesized state (a, c, e) and after the exsolution step (b, d, f). Nanoparticles are visible on the catalyst surface only after the exsolution treatment, confirming the formation of exsolved Ru/Fe nanoparticles.

From the TEM images, the particle size distributions of each sample were estimated. Based on measurements of more than 100 particles, the average particle sizes for the Ru-, Ru–Fe-, and Fe-exsolved nanoparticles were 2.3 ± 0.7 nm, 3.4 ± 0.9 nm, and 127 ± 33 nm, respectively. The corresponding particle size distributions are reported in Figure 44.

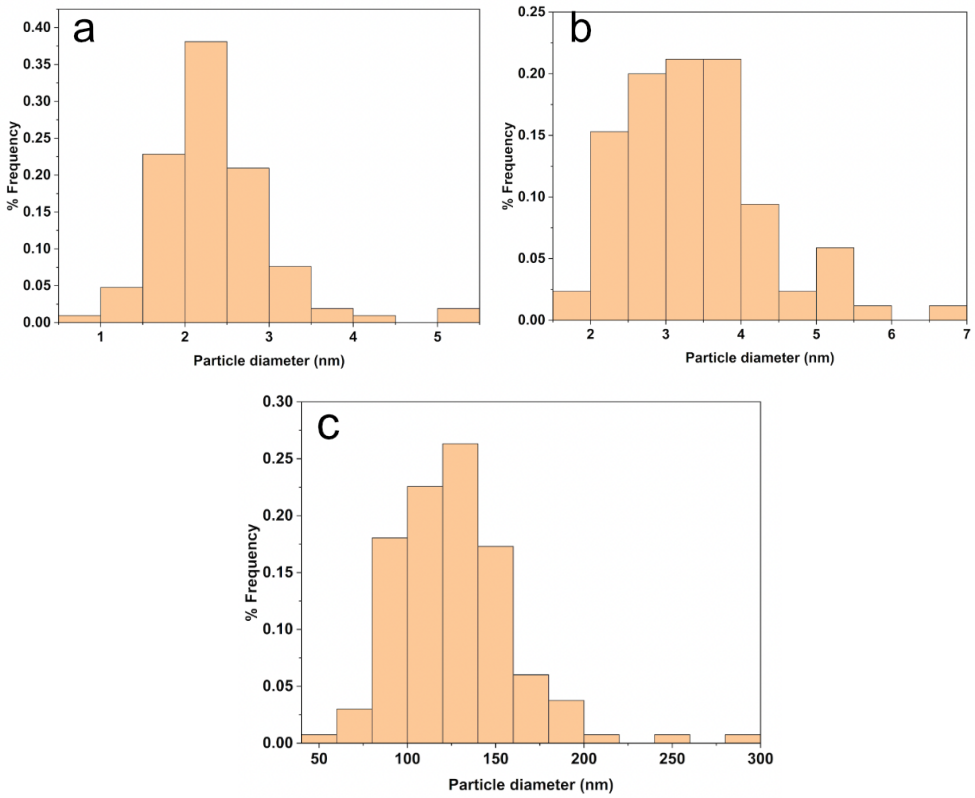

Figure 44. Particle size distribution histograms of the exsolved nanoparticles obtained from TEM image analysis. (a) Ru-exsolved catalyst, (b) Ru–Fe-exsolved catalyst, and (c) Fe-exsolved catalyst. Average particle diameters were 2.3 ± 0.7 nm, 3.4 ± 0.9 nm, and 126.7 ± 33 nm, respectively. Each distribution was determined from measurements of more than 100 individual particles.

TEM analysis was also performed on both the as-synthesized and exsolved catalysts to complement the SEM characterization and to better visualize surface morphological changes associated with the exsolution process (Figure 45). Before reduction, all samples showed a relatively smooth and compact surface with well-defined grains. This property is characteristic of dense perovskite structures (A, B, D, E, G). After the exsolution treatment (C, F, H, I), clear morphological differences could be observed. In the Ru- and Ru–Fe-containing samples, the exsolved nanoparticles were less apparent on the surface, consistent with the acquired TEM images that only showed very small metallic nanoparticles (below 5 nm).. However, the surface roughness was increased noticeably compared to the as-synthesized state, suggesting nanoparticle emergence and partial restructuring of the perovskite surface. In contrast, for the Fe-only catalyst (I), larger spherical nanoparticles were clearly visible and uniformly distributed across the perovskite surface.

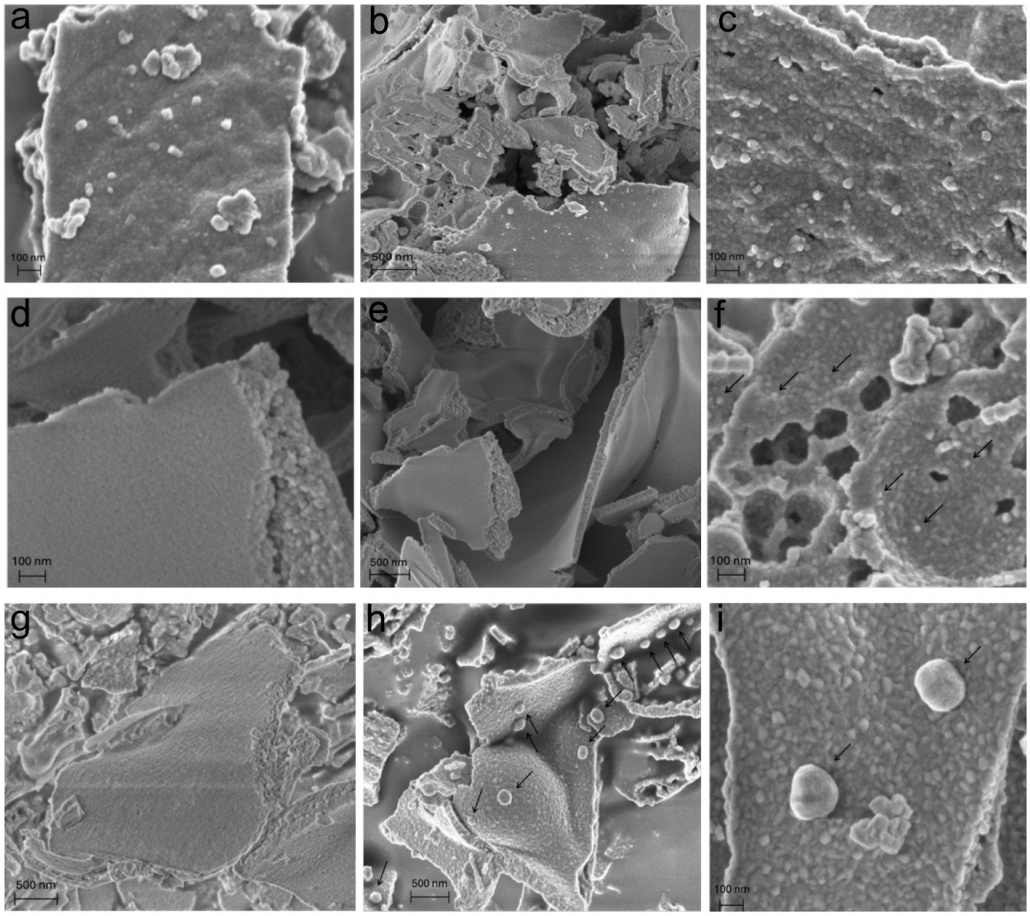

Figure 45. SEM images of the catalysts in their as-synthesized state (a, b, d, e, g) and after the exsolution step (c, f, h, i). Images were recorded at 2.00 kV, WD = 5.1 mm, with an InLens detector at 100k× magnification. (a - c) Ru-exsolved, (d - f) Ru–Fe exsolved, and (g - i) Fe-exsolved.

APR tests were carried out at 250 °C for the three catalysts. The H_2 yields, carbon-to-gas conversion, and APR H_2 selectivity after 1 h of reaction with a 1 wt.% ethanol solution are reported in Figure 46.

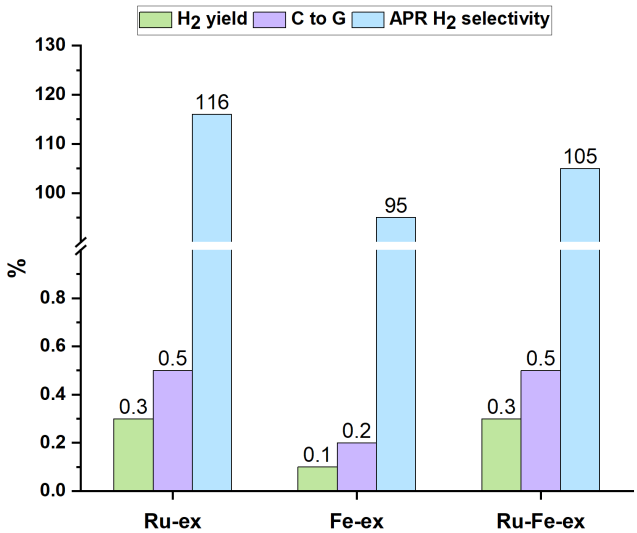

Figure 46. Performance of the exsolved catalysts in ethanol APR at 250 °C for 1 h with a 1 wt.% ethanol solution. Reported are H_2 yield (green), carbon-to-gas conversion (violet), and APR H_2 selectivity (blue).

The Fe-only catalyst exhibited the lowest performance compared to its Ru- and Ru–Fe-based counterparts. Interestingly, both Ru- and Ru–Fe-exsolved catalysts achieved H_2 selectivity values exceeding 100%, indicating the occurrence of parallel H_2-producing reactions beyond the theoretical ethanol APR pathway.
After the APR tests, the three catalysts were re-examined by TEM to verify whether the reforming conditions had affected their morphology or stability. No significant changes in particle distribution or size were observed. TEM images, HAADF-STEM, and elemental mapping of the catalysts after APR are reported in Figure 47.

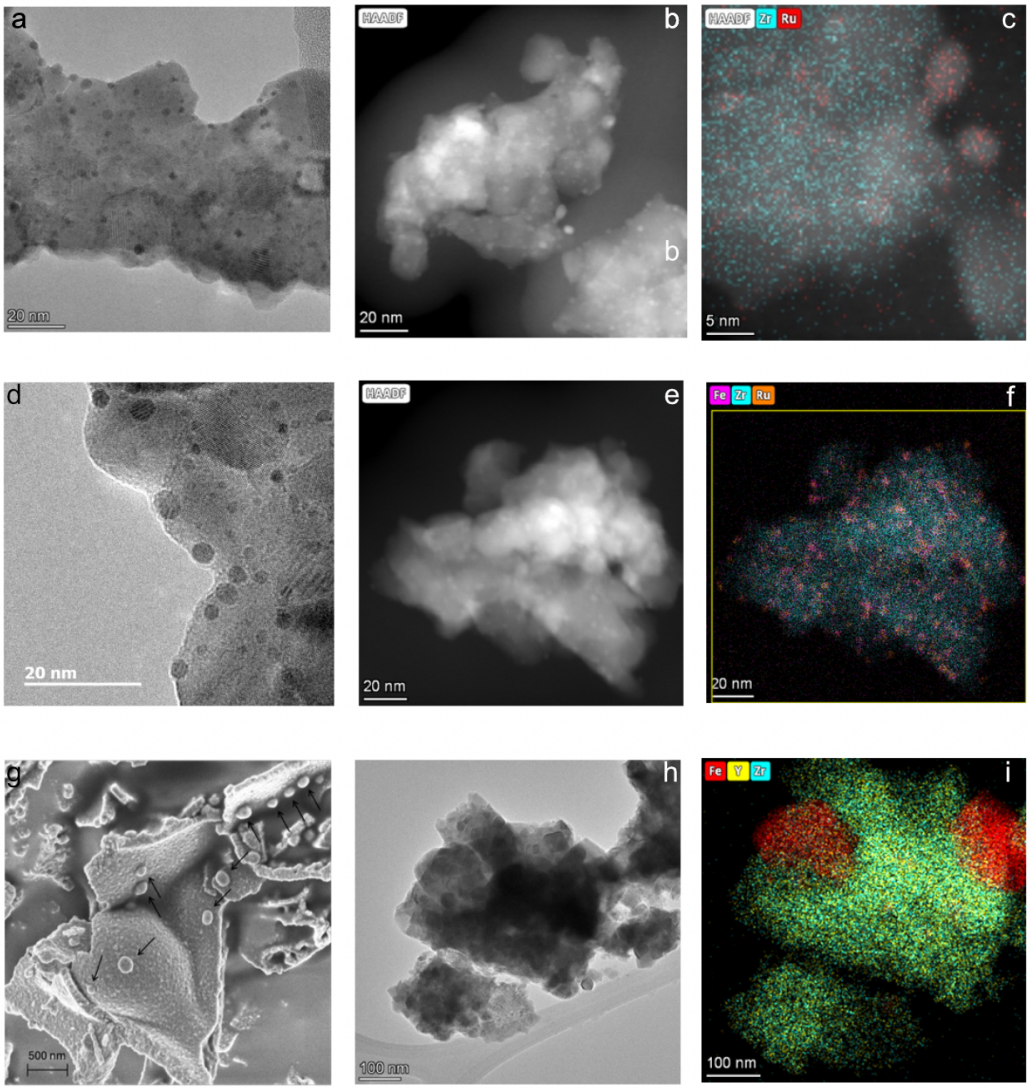

Figure 47. TEM, HAADF-STEM, and EDX elemental mapping of the exsolved catalysts. (a–c) Ru-exsolved sample: (a) TEM micrograph, (b) HAADF-STEM image, and (c) EDX elemental mapping showing Ru distribution (red) over the support. (d–f) Ru–Fe-exsolved sample: (d) TEM micrograph, (e) HAADF-STEM image, and (f) EDX elemental mapping showing Ru (orange) and Fe (pink) distribution within the support matrix. (g–i) Fe-exsolved sample: (g) TEM micrograph, (h) HAADF-STEM image, and (i) EDX elemental mapping with Fe (red) on the support.

The gas and liquid phases of the two best-performing catalysts (Ru–Fe and Ru-exsolved) are reported in Table 15, with no significant differences in their gas and liquid composition. In the liquid phase, the main compound detected was acetaldehyde, accounting for about 2% of the initial ethanol carbon for both

catalysts, while acetic acid was present in smaller amounts. In the gas phase, H_2 represented 61% and 66% of the total volume for Ru–Fe and Ru-exsolved, respectively, followed by CH_4 (20% and 15%) and CO_2 (the remaining fraction). The H_2/CO_2 ratios were 3.2 for Ru–Fe and 3.5 for Ru-exsolved, indicating that both catalysts promoted comparable reaction pathways. However, when normalizing H_2 production to the nominal Ru content (mmol H_2 per gram of Ru), the results diverge: the Ru–Fe catalyst, with only 2 wt.% Ru, achieved 118 mmol H_2/gRu, whereas the Ru-exsolved catalyst, containing 4 wt.% Ru, reached 73 mmol H_2/gRu.

Table 15. Gas and liquid phase composition after 1 h of APR reaction at 250 °C with 1 wt.% ethanol solution for Ru-exsolved and Ru–Fe-exsolved catalysts. Reported values include H_2, CH_4, and CO_2 production (mmol), H_2/CO_2 ratio, H_2 productivity normalized to nominal Ru content (mmol H_2/gRu), and liquid products acetaldehyde (AcH) and acetic acid (AcOH).

	Gas phase (mmol)					Liquid phase (mmol)	
Catalyst	H_2	CH_4	CO_2	H_2/CO_2	mmolH_2/grRu	AcOH	AcH
Ru-ex	0.124	0.028	0.035	3.5	73	36	295
Ru-Fe-ex	0.103	0.033	0.032	3.2	118	57	310

This indicates that the Ru–Fe catalyst is more efficient, despite the Ru-exsolved catalyst exhibiting smaller particle sizes, which are generally expected to enhance H_2 productivity. The improved performance of Ru–Fe could be attributed to the synergistic role of Fe, which may promote the WGS reaction, boosting H_2 productivity. Both catalysts were further tested at 270 ºC to evaluate whether Ru activity in ethanol APR could be enhanced at higher temperature. A 2.5- and 3-fold increase in H_2 production was recorded for Ru–Fe and Ru-exsolved, respectively (Figure 48).

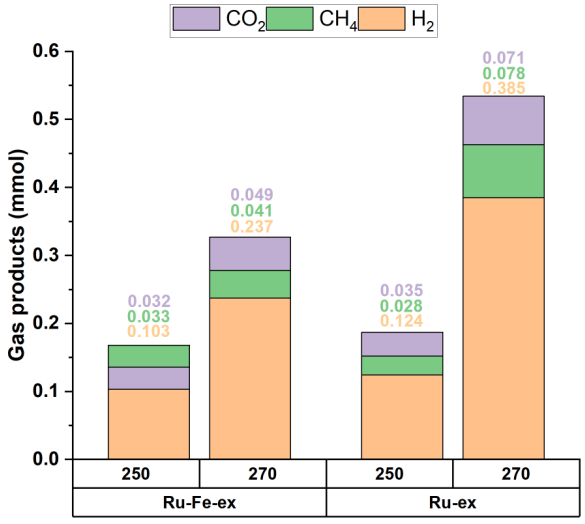

Figure 48. Gas-phase products (H_2, CO_2, and CH_4, in mmol) obtained from Ru–Fe exsolved and Ru-exsolved catalysts at 250 °C and 270 °C after 1 h of reaction with a 1 wt.% ethanol solution.

However, while the H_2/CO_2 ratio remained higher for Ru-exsolved (5.4 vs 4.8), CH_4 production increased 2.8-fold, reaching ~15% of the gas phase. In contrast, CH_4 formation in the Ru–Fe catalyst only increased 1.24-fold, representing just

13% of the gas phase, with CO_2 accounting for another 15%. Interestingly, both catalysts reached a H_2 fraction of ~72% in the gas phase, but in the Ru–Fe sample the increase in H_2 was more pronounced relative to CH_2, whereas in Ru-exsolved both rose in parallel.
Normalizing the data to the nominal Ru loading, the contrast between the two systems could be confirmed. The Ru–Fe catalyst achieved a productivity of 275 mmol H_2 /g_{Ru}, while the Ru-exsolved catalyst reached 222 mmol H_2 /g_{Ru}. This demonstrates that Ru–Fe outperformed Ru-exsolved, highlighting the potential of bimetallic exsolution as a mean to reduce noble metal content while maintaining or even enhancing H_2 productivity.
To further validate these findings and evaluate the effect of reaction time on the APR performance of the exsolved catalysts, both systems were tested at extended reaction times of 3 h and 5 h, with particular attention to gas products, H_2 productivity normalized to Ru content, and C to G conversion. As shown in Figure 49 A, gas-phase products after 1 h and 3 h of reaction reveal an overall increase in H_2 for both catalysts. However, the Ru–Fe catalyst exhibited a significantly higher improvement, about 91% compared to only 31% for the Ru-exsolved catalyst. Correspondingly, the H_2 productivity normalized to the nominal Ru content reached 521 mmol H_2/gRu for Ru–Fe and 294 mmol H_2/gRu for Ru-exsolved (Figure 49 B). Furthermore, the carbon-to-gas conversion increased by a factor of 2.5 for Ru–Fe, whereas only a 16% increase was observed for Ru-exsolved.

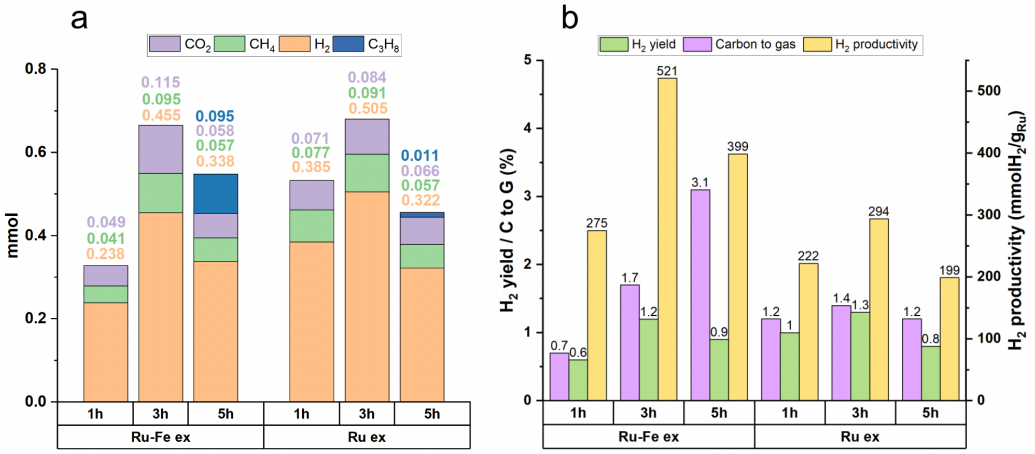

Figure 49. Gas phase products (H_2, CH_4, CO_2 and C_3H_8 in mmol) obtained from Ru–Fe exsolved and Ru-exsolved catalysts at 250 °C under different reaction times (1, 3 and 5 h, a) with 1 wt.% ethanol solution and corresponding H_2 production in mmol H_2/gRu together with C to G and H_2 yields (b)..

The situation changed to some extent at a longer reaction time of 5 h. In particular, the carbon-to-gas ratio increased by 82% for the Ru–Fe catalyst, while it decreased by 14% for the Ru-exsolved sample. Regarding H_2 productivity normalized per gram of Ru, a decrease was observed for both catalysts. This decrease was more pronounced for Ru-ex (−32%) compared to Ru–Fe (−23%). Nevertheless, the H_2 productivity remained higher for the Ru–Fe catalyst, further confirming the better performance of the bimetallic exsolved system.
The increase in carbon-to-gas ratio for Ru–Fe can be attributed to the formation of a fourth gaseous product, propane (C_3H_8), accounting for 17% of the gas-phase composition compared to only 2% in the Ru-ex catalyst. This result indicates that competitive reactions to reforming gain relevance after 5 h of reaction, decreasing H_2 production by approximately four moles for every mole of propane formed.

Depending on the application context, these results could still be relevant for energy valorisation purposes, where the primary objective is to reduce the carbon content of the liquid stream while generating a combustible gas mixture from ethanol-rich wastewaters. Conversely, from an industrial standpoint, particularly when targeting H_2 production, these findings suggest that the optimal residence time should not exceed 3 hours to maximize H_2 yield under continuous operation. Further tests could assess a 4 h reaction time to better understand when propane formation begins and to evaluate whether higher hydrogen production can be achieved.

Chapter 5: Scale up of ethanol APR to the real case scenario of a winery

5.1 Continuous reactor experimental data

In the perspective of scaling up the reaction to an industrial level, ethanol APR was carried out in a continuous-flow reactor to mimic the operation of an industrial process. A 5 wt.% ethanol aqueous solution was selected as feed, as ethanol concentrations in wine less wastewater typically vary between 1 and 10 wt.% depending on the specific wine production stage. Therefore, 5 wt.% was considered a representative intermediate value, corresponding to a realistic average concentration that would result from the collection and storage of mixed winery wastewater streams. Moreover, higher ethanol concentrations have previously been shown to be less favorable for APR performance (see previous chapter); thus, the chosen concentration represents a conservative case, since lower ethanol contents generally yield higher H_2 productivity. The reaction temperature was set at 270 °C to ensure high ethanol conversion, a pressure of 60 bar, a flow rate of 0.6 mL/min and 1 g of 5 wt.% Pt/C catalyst were selected. Pt/C was chosen for its well-established performance in the APR of model wastewater systems. This catalyst has shown superior activity in the reforming of synthetic domestic sewage [180] and, given that the characterized winery wastewater also contained acetic acid as a minor compound, Pt was preferred over Ru due to its higher activity toward carboxylic acid reforming reported in literature [53]. Furthermore, the reaction stoichiometry observed over Pt/C was easily approximated to a realistic overall reaction, described as:

$$CH_3CH_2OH + H_2O \rightarrow 2H_2 + CH_4 + CO_2 \quad (21)$$

The ethanol conversion trend and gas-phase composition observed during the continuous APR test are shown in Figure 50.

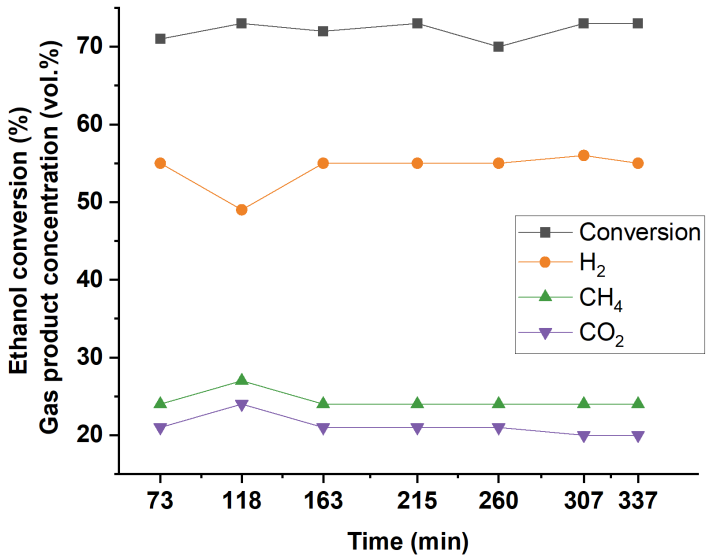

Figure 50. Ethanol conversion and gas-phase products observed APR of ethanol over Pt/C at 270ºC as a function of time of stream. Ethanol conversion is shown in black, while the main gas products: H_2, CH_4, and CO_2 in orange, green and purple respectively.

On average, ethanol APR achieved ~75 % conversion, with H_2, CH_4, and CO_2 concentrations of approximately 55, 25, and 20 vol.%, respectively, confirming stable catalytic behaviour and reproducible gas-phase composition under continuous operation.

5.2 Process design and scaled up

Building upon the experimental results obtained for the continuous ethanol APR, the process was scaled up and modelled to represent the treatment of 2.5 m^3/h of wastewater typically generated by a medium-sized winery. Characterization of the winery wastewater revealed glucose and fructose concentrations below the ~1 wt.% of C threshold previously identified for significant humin formation [88]. Under such dilute conditions, the H_2 contribution from these sugars was negligible compared to that of ethanol and was not expected to influence catalyst stability. Although acetic acid is frequently detected in winery wastewaters, its carbon concentration in the analysed sample was below 1 wt.%. Considering its low concentration and the established evidence that acetic acid behaves as an inert species in APR, without adverse effects on H_2 yield or catalyst durability, it was excluded from the simulation [52].

Consequently, being ethanol the dominant soluble organic source, for the sake of this preliminary assessment, only ethanol APR was considered for the subsequent process modelling and assessments. The scaled-up simulation was designed to adapt to two process configurations differing in the treatment of the gaseous products: S1 for the cogeneration of electricity and heat and S2 for H_2 separation and purification.

The simplified process flow diagrams (PFDs) of these two scenarios are shown in Figure 51 and Figure 52, respectively. These schematics summarize the principal unit operations and energy recovery pathways, providing a conceptual overview

prior to the more detailed Aspen Plus® simulation results presented later in this section.

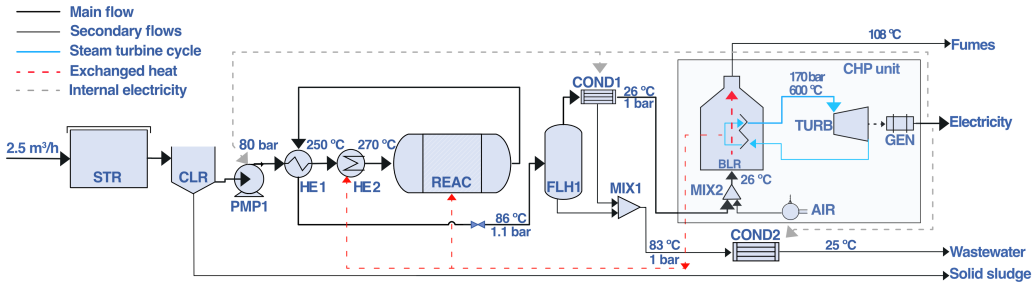

Figure 51. Scenario 1: Process flow diagram for the cogeneration of electricity and heat. Thermal energy, shown in red, is entirely used to meet the plant's internal heat demands, while net electricity, after covering the plant's electrical needs (shown in grey), exits the system. Abbreviation: STR: storage tank. CLR: clarifier. PUMP1: pump1. HE1-HE2: heat exchanger 1–2. REAC: APR reactor. FLH1: flash 1. COND1-COND2: condenser1–2. MIX1-MIX2: mixer1–2. BLR: blower. TURB: turbine. GEN: generator.

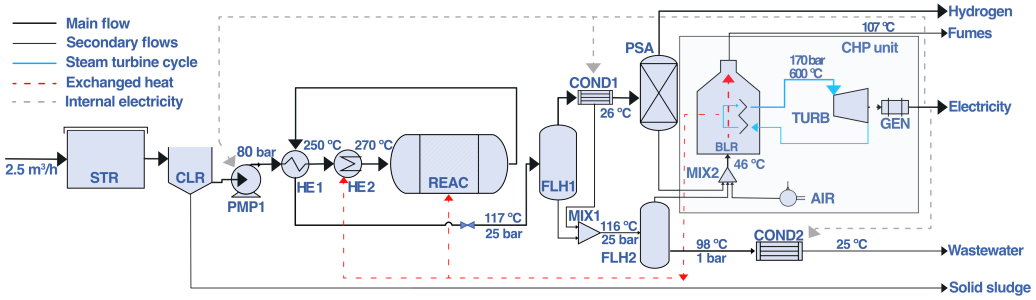

Figure 52. Scenario 2: Process flow diagram for H_2 separation and purification. Heat integration (red dashed lines) and internal electricity use (grey dashed lines) are illustrated. Thermal energy is entirely used to meet the plant's heating demands, while the net electricity, after covering internal requirements, is exported for external sale. Abbreviation: STR: storage tank. CLR: clarifier. PUMP1: pump1. HE1-HE2: heat exchanger 1–2. REAC: APR reactor. FLH1-FLH2: flash 1–2. COND1-COND2: condenser1–2. MIX1-MIX2: mixer1–2. BLR: blower. TURB: turbine. GEN: generator.

5.2.1 Upstream Configuration

The upstream configuration, common to both scenarios, was designed to handle the winery wastewater stream entering the APR process. A 78 m³ storage tank was sized to guarantee one day of operation plus a 30% safety margin, based on an inlet flow rate of 2.5 m³/h. Following, a clarifier was dimensioned using a conservative surface overflow rate (SOR) of 0.3 m³/h·m, lower than the values typically reported for biologically treated municipal wastewater [192], to enhance the settling of solid particles of various sizes, including leaf residues and other organic degradation products typical of winery wastewater (here referred as solids).

The clarified stream was then pressurized by a high-pressure pump (PMP1) and preheated to APR operating conditions. In particular, the stream was preheated through two successive heat exchangers: HE1, trough which the thermal energy from the APR reactor effluent was recovered to preheat the feed to 250 °C; HE2, which provides the additional duty required to reach the reaction temperature of 270 °C was supplied externally.

The design specifications for the common upstream equipment are summarized in

Table 16, which includes the main operating parameters for the storage tank, clarifier, pump, and heat exchangers.

Table 16 Lists of common upstream equipment for Scenario 1 and Scenario 2, reported with design specifications.

Unit	Sizing Reference	Specification
Storage tank	Volume: 78.0 m^3	One day inflow + 30% of capacity
Clarifier	Flow rate: 2.5 m^3/h	3 h retention time, SOR: 0.3 $m^3/h \cdot m^2$ Volume: 8.0 m^3
High-pressure pump	Power rating: 19.0 kW	Discharge pressure: 5.00 bar Flow rate: 0.7 L/s
Heat exchanger 1 (HE1)	Surface: 13.0 m^2	Shell and tube, net energy exchanged: 741.0 kW U: 1250.0 W/ $m^2 \cdot K$, fouling effect considered
Heat exchanger 2 (HE2)	Surface: 3.0 m^2	Shell and tube, net energy exchanged: 84.0 kW U: 2750.0 $W/m^2 \cdot K$, fouling effect considered
APR reactor	Input flow: 2525.0 kg/h	Volume: 0.14 m^3, 3.3 min retention time Catalyst loading: 70.0 kg , WHSV*= 1.8 h^{-1}

*WHSV was calculated based on the ethanol mass flow rate divided by the mass of catalyst.

5.2.2 The APR reactor

The stoichiometry observed from the experimental bench-scale tests (Equation (20)) was used for subsequent calculations and process simulations. This choice represents a conservative approach compared to performing the analysis based on the theoretical stoichiometry, which assumes the production of 6 mol of H_2 per mol of ethanol converted. Such theoretical yields could potentially be achieved by optimizing various process parameters, including catalyst selection, substrate concentration, reactor configuration, and other operating conditions. Nevertheless, the conservative experimental data were adopted for the large-scale process simulations to obtain more realistic estimates of mass and energy flows. These results were then used to support the energetic, economic, and environmental assessments. The Aspen Plus process simulation flowsheets, along with the corresponding mass flows and operating conditions (pressure and temperature) for each stream, are presented in Figure 53 and
and for Scenarios 1 and Figure 54 and Table 17 and Table 18 for Scenario 2 respectively.

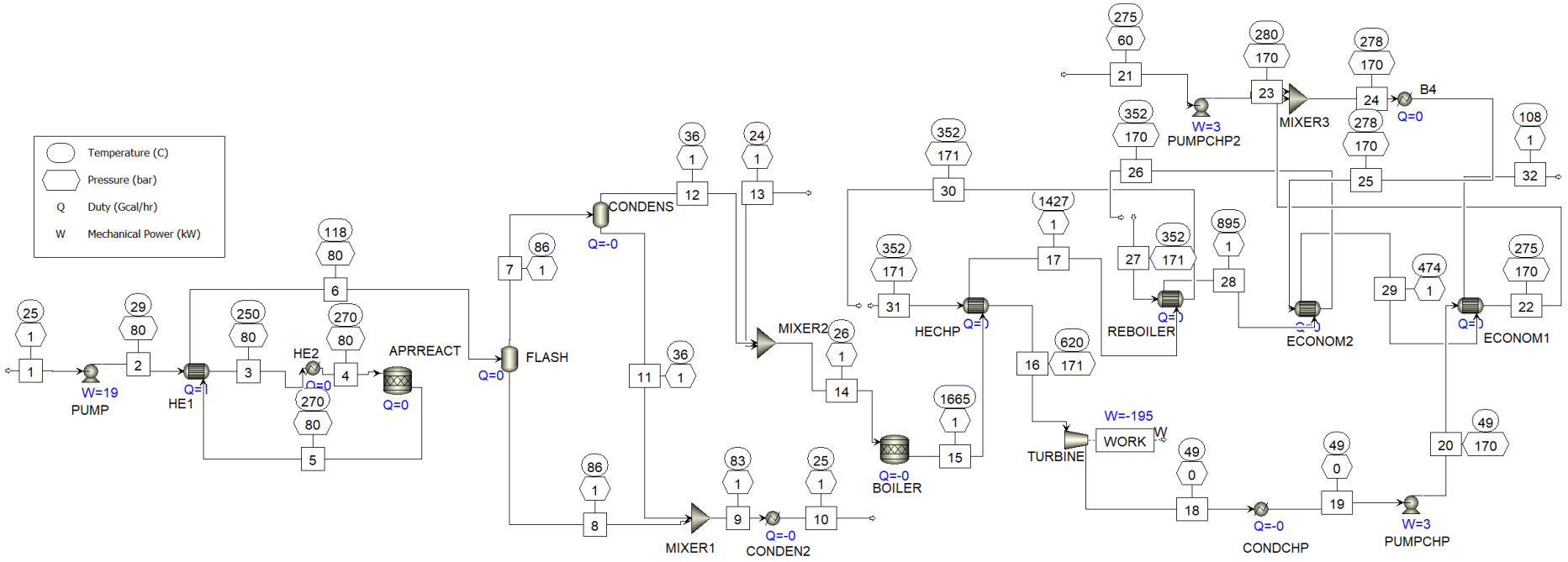

Figure 53. Scenario 1 simulation flowsheet extracted from Aspen plus v14.

Table 17. Aspen Plus simulation stream data for Scenario 1, including mass flow rate (kg/h), temperature (°C), pressure (bar), and phase (liquid, vapor, or mixed).

	1	2	3	4	5	6	7	8	9	10	11	12	13	14	15	16	17	18
Phase	*Liquid Phase*	*Liquid Phase*	*Liquid Phase*	*Liquid Phase*	*Mixed*	*Mixed*	*Vapor Phase*	*Liquid Phase*	*Mixed*	*Mixed*	*Liquid Phase*	*Vapor Phase*	*Vapor Phase*	*Vapor Phase*	*Vapor Phase*	*Vapor Phase*	*Vapor Phase*	*Mixed*
Temperature (ºC)	25	29	250	270	270	117	85	85	82	25	36	36	23.6	26	1665	620	1427	48
Pressure (bar)	1	80.0	80.0	80.0	80.0	80.0	1.1	1.1	1.0	1.0	1.0	1	1.1	1.2	1	170.0	1	0.1
Total mass flow (kg/h)	2526.00	2526.00	2526.00	2526.00	2526.00	2526.00	321.15	2204.85	2355.64	2355.64	150.79	170.36	1230.00	1400.36	1400.36	553.00	1400.36	553.00
Water (kg/h)	2399.70	2399.70	2399.70	2399.70	2362.66	2362.66	158.93	2203.72	2354.19	2354.19	150.46	8.47	0.00	8.47	190.16	553.00	190.16	553.00
ETHANOL (kg/h)	126.30	126.30	126.30	126.30	31.58	31.58	30.47	1.11	1.43	1.43	0.32	30.14	0.00	30.14	0.30	0.00	0.30	0.00
H_2 (kg/h)	0	0.00	0.00	0.00	8.29	8.29	8.29	0.00	0.00	0.00	0.00	8.29	0.00	8.29	0.08	0.00	0.08	0.00
CO_2 (kg/h)	0	0.00	0.00	0.00	90.49	90.49	90.47	0.02	0.02	0.02	0.00	90.47	0.00	90.47	237.07	0.00	237.07	0.00
CH_4 (kg/h)	0	0.00	0.00	0.00	32.99	32.99	32.99	0.00	0.00	0.00	0.00	32.99	0.00	32.99	0.33	0.00	0.33	0.00
O_2 (kg/h)	0	0.00	0.00	0.00	0.00	0.00	0.00	0.00	0.00	0.00	0.00	0.00	258.30	258.30	0.71	0.00	0.71	0.00
N_2 (kg/h)	0	0.00	0.00	0.00	0.00	0.00	0.00	0.00	0.00	0.00	0.00	0.00	971.70	971.70	971.70	0.00	971.70	0.00

Streams	19	20	21	22	23	24	25	26	27	28	29	30	31	32
Phase	*Liquid Phase*	*Liquid Phase*	*Liquid Phase*	*Liquid Phase*	*Liquid Phase*	*Liquid Phase*	*Liquid Phase*	*Liquid Phase*	*Liquid Phase*	*Vapor Phase*	*Vapor Phase*	*Vapor Phase*	*Vapor Phase*	*Vapor Phase*
Temperature (ºC)	48	49	275	275	279	277	277	351	352	895	473	351	352	108
Pressure (bar)	0.1	170	60.0	170	170	170	170	170	170	1	1	170	170	1
Total mass flow (kg/h)	553.00	553.00	729.00	553.00	729.00	1282.00	1282.00	1282.00	1283.00	1400.36	1400.36	1283.00	553.00	1400.36
Water (kg/h)	553.00	553.00	729.00	553.00	729.00	1282.00	1282.00	1282.00	1283.00	190.16	190.16	1283.00	553.00	190.16
ETHANOL (kg/h)	0.00	0.00	0.00	0.00	0.00	0.00	0.00	0.00	0.00	0.30	0.30	0.00	0.00	0.30
H_2 (kg/h)	0.00	0.00	0.00	0.00	0.00	0.00	0.00	0.00	0.00	0.08	0.08	0.00	0.00	0.08
CO_2 (kg/h)	0.00	0.00	0.00	0.00	0.00	0.00	0.00	0.00	0.00	237.07	237.07	0.00	0.00	237.07
CH_4 (kg/h)	0.00	0.00	0.00	0.00	0.00	0.00	0.00	0.00	0.00	0.33	0.33	0.00	0.00	0.33
O_2 (kg/h)	0.00	0.00	0.00	0.00	0.00	0.00	0.00	0.00	0.00	0.71	0.71	0.00	0.00	0.71
N_2 (kg/h)	0.00	0.00	0.00	0.00	0.00	0.00	0.00	0.00	0.00	971.70	971.70	0.00	0.00	971.70

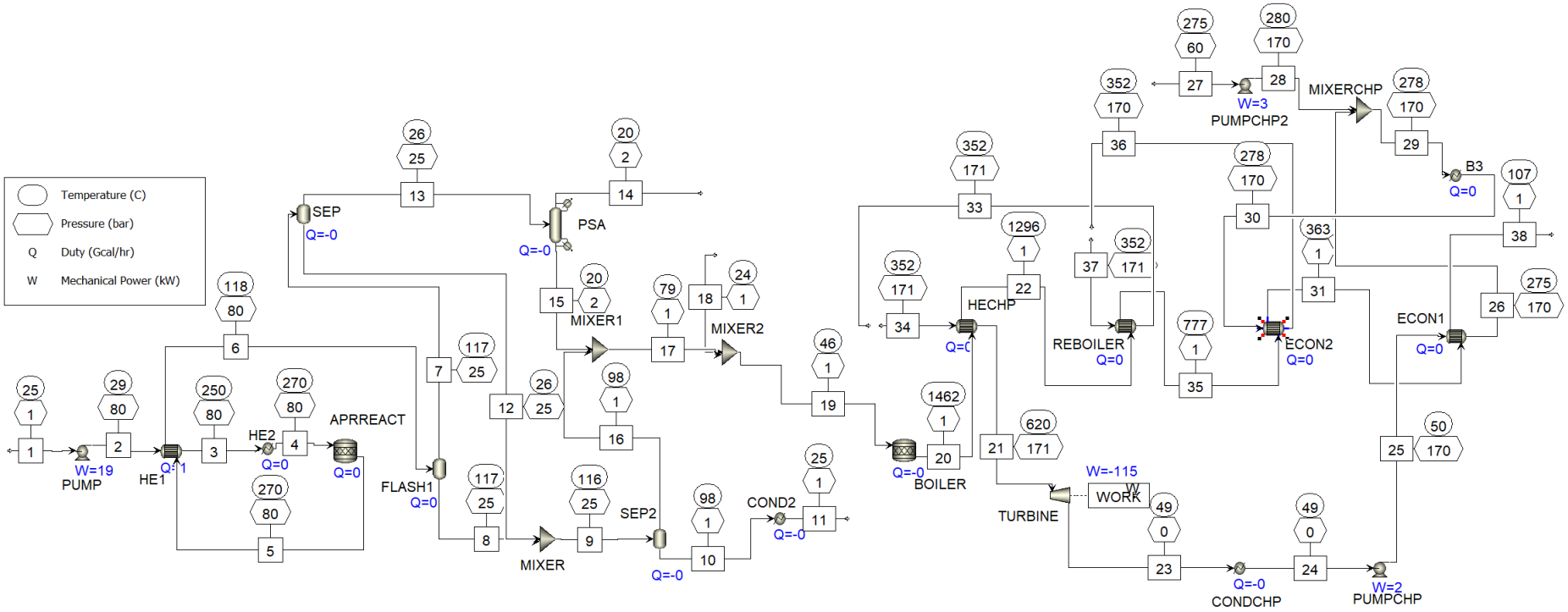

Figure 54. Scenario 2 simulation flowsheet extracted from Aspen plus v14.

Table 18. Aspen Plus simulation stream data for Scenario 2, including mass flow rate (kg/h), temperature (°C), pressure (bar), and phase (liquid, vapor, or mixed).

Stream	1	2	3	4	5	6	7	8	9	10	11	12	13	14
Phase	*Liquid Phase*	*Liquid Phase*	*Liquid Phase*	*Liquid Phase*	*Mixed*	*Mixed*	*Vapor Phase*	*Liquid Phase*	*Mixed*	*Liquid Phase*	*Liquid Phase*	*Liquid Phase*	*Vapor Phase*	*Vapor Phase*
Temperature (ºC)	25	29	250	270	270	117	116	116	115	97	25.0	26.0	26.0	20.0
Pressure (bar)	1	80	80	80	80	80	25	25	25	1	1.5	25.0	25.0	2.0
Total mass flow (kg/h)	2526	2526	2526	2526	2526	2526	158.29	2367.70	2393.89	2294.80	2294.80	26.19	132.11	7.93
WATER (kg/h)	2399.70	2399.70	2399.70	2399.70	2362.65	2362.65	12.64	2350.01	2362.37	2291.70	2291.70	12.35	0.28	0.00
ETHANOL (kg/h)	126.30	126.30	126.30	126.30	31.57	31.57	15.34	16.22	29.70	3.09	3.09	13.48	1.87	0.00
H_2 (kg/h)	0	0	0	0	8.28	8.28	8.28	0.01	0.01	2.62E-07	0.00	0.00	8.28	7.04
CO_2 (kg/h)	0	0	0	0	90.49	90.49	89.16	1.32	1.66	1.53E-03	0.00	0.34	88.82	0.89
CH_4 (kg/h)	0	0	0	0	32.98	32.98	32.86	0.12	0.13	2.55E-05	0.00	0.01	32.85	0.00
O_2 (kg/h)	0	0	0	0	0	0	0	0	0	0	0.00	0.00	0.00	0.00
N_2 (kg/h)	0	0	0	0	0	0	0	0	0	0	0.00	0.00	0.00	0.00

Stream	15	16	17	18	19	20	21	22	23	24	25	26	27	28	29
Phase	*Vapor Phase*	*Vapor Phase*	*Mixed*	*Vapor Phase*	*Mixed*	*Vapor Phase*	*Vapor Phase*	*Vapor Phase*	*Mixed*	*Liquid Phase*	*Liquid Phase*	*Liquid Phase*	*Liquid Phase*	*Liquid Phase*	*Liquid Phase*
Temperature (ºC)	20.0	97.5	79.0	23.6	45.5	1462.0	620.0	1296.3	48.7	48.7	49.8	275.0	275.0	279.5	278.1
Pressure (bar)	2.0	1.0	1.0	1.1	1.0	1.0	170.9	1.0	0.1	0.1	170.0	170.0	60.1	170.0	170.0
Total mass flow (kg/h)	124.18	99.09	223.27	952.00	1175.27	1175.27	327.00	1175.27	327.00	327.00	327.00	327.00	729.00	729.00	1056.00
WATER (kg/h)	0.28	70.67	70.95	0.00	70.95	188.43	327.00	188.43	327.00	327.00	327.00	327.00	729.00	729.00	1056.00
ETHANOL (kg/h)	1.87	26.61	28.48	0.00	28.48	0.28	0.00	0.28	0.00	0.00	0.00	0.00	0.00	0.00	0.00
H_2 (kg/h)	1.24	0.01	1.25	0.00	1.25	0.01	0.00	0.01	0.00	0.00	0.00	0.00	0.00	0.00	0.00
CO_2 (kg/h)	87.94	1.67	89.60	0.00	89.60	233.06	0.00	233.06	0.00	0.00	0.00	0.00	0.00	0.00	0.00
CH_4 (kg/h)	32.85	0.13	32.99	0.00	32.99	0.33	0.00	0.33	0.00	0.00	0.00	0.00	0.00	0.00	0.00
O_2 (kg/h)	0.00	0.00	0.00	199.92	199.92	1.08	0.00	1.08	0.00	0.00	0.00	0.00	0.00	0.00	0.00
N_2 (kg/h)	0.00	0.00	0.00	752.08	752.08	752.08	0.00	752.08	0.00	0.00	0.00	0.00	0.00	0.00	0.00

Stream	30	31	33	34	35	36	37	38
Phase	*Liquid Phase*	*Vapor Phase*	*Vapor Phase*	*Vapor Phase*	*Vapor Phase*	*Liquid Phase*	*Liquid Phase*	*Vapor Phase*
Temperature (ºC)	278.1	363.3	352.0	352.0	777.2	351.6	352.0	106.8
Pressure (bar)	170.0	1.0	170.9	170.9	1.0	170.0	170.9	1.0
Total mass flow (kg/h)	1056.00	1175.27	1056.00	327.00	1175.27	1056.00	1056.00	1175.27
WATER (kg/h)	1056.00	188.43	1056.00	327.00	188.43	1056.00	1056.00	188.43
ETHANOL (kg/h)	0.00	0.28	0.00	0.00	0.28	0.00	0.00	0.28
H_2 (kg/h)	0.00	0.01	0.00	0.00	0.01	0.00	0.00	0.01
CO_2 (kg/h)	0.00	233.06	0.00	0.00	233.06	0.00	0.00	233.06
CH_4 (kg/h)	0.00	0.33	0.00	0.00	0.33	0.00	0.00	0.33
O_2 (kg/h)	0.00	1.08	0.00	0.00	1.08	0.00	0.00	1.08
N_2 (kg/h)	0.00	752.08	0.00	0.00	752.08	0.00	0.00	752.08

The operating pressure adopted for simulating the ethanol APR reaction was determined through sensitivity analyses conducted over a pressure range of 60 to 110 bar, evaluating the corresponding variations in APR duty and steam fraction. The rationale was to identify an optimal balance that, on one hand, ensures a minimum overpressure relative to the vapor pressure at the selected temperature (approximately 55 bar at 270 °C) to maintain the liquid phase, and on the other hand, avoids excessively high pressures that could challenge reactor design constraints and material limitations.
Within the explored range, lower APR pressures were found to increase the overall energy demand, consistent with observations reported in previous studies [44]. This rise in reactor thermal duty is primarily associated with a higher vapor fraction, as illustrated in Figure 55. Reactor duty is controlled mostly by the latent heat of water vapour formation (ΔHvap = 1604.5 kJ/kg H_2O at 55 bar), along with the endothermic nature of the ethanol APR reaction (ΔHrxn = +95.1 kJ/mol EtOH), both contributing to additional heat requirements as the reaction proceeds. Consequently, increasing the reactor pressure reduces the vapor fraction in the outlet stream, thereby lowering the reactor duty since less energy is consumed through vaporization (see Figure 55). Although operating at higher pressures may help to reduce vaporization losses, operating at excessively high pressures showed a decrease in gas productivity and consequently a decrease in overall APR performance[47]. However, the reduction in reactor duty with increasing pressure is much more pronounced than the corresponding decrease in conversion and reforming activity. Simulations results indicated that above a pressure of 80 bar, the vapor fraction dropped below 80% and the APR duty decreased by approximately 72%, after which both trends begin to plateau (as shown in Figure 55). This behaviour suggests the existence of a favorable trade-off between operating pressure and vaporization extent, optimizing process efficiency under high-pressure conditions. Therefore, an operating pressure of 80 bar was selected for the simulations to minimize energy consumption while maintaining satisfactory process performance.

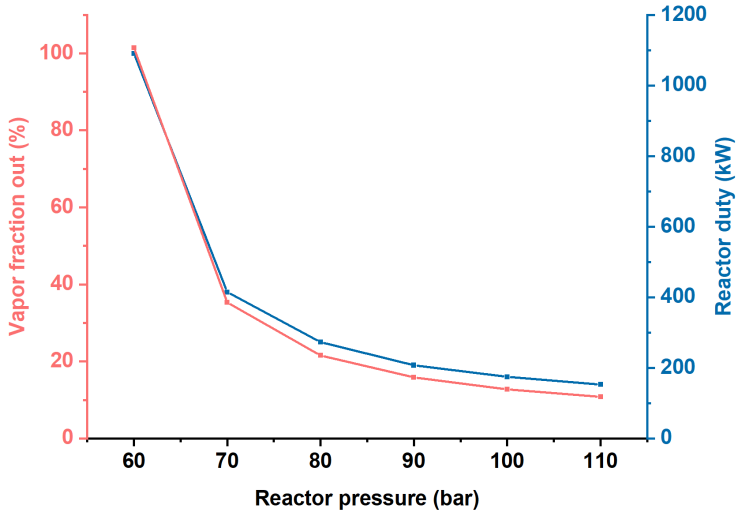

Figure 55. Influence of APR operating pressure on the thermal reactor duty and vapor fraction in the outlet stream.

In addition to sharing the same upstream configuration and core APR reaction section, the downstream phase differs between the two scenarios, with all

equipment designed to maximize the yield of the main products while minimizing the COD, expressed as the residual ethanol content in the liquid phase exiting the process.

5.2.3 Downstream Scenario 1: Electricity production

For S1, the downstream configuration is here described in more detailed: following the APR reactor, the effluent stream was expanded from 80 to 1.1 bar in a flash separation unit (FLH1) to promote phase separation. The resulting temperature decreases from 118 °C to 86 °C facilitated efficient gas–liquid separation.
In accordance with the design guidelines proposed by Towler and Sinnott, the inlet gas velocity was maintained below 30 m/s. Under the simulated operating conditions, a superficial gas velocity of 0.05 m/s was calculated using the gas and liquid densities obtained from the Aspen Plus simulations. A residence time of 10 minutes was chosen to ensure adequate disengagement and complete settling of retained liquid droplets. To satisfy the residence time of 10 minutes, the vessel diameter had to be of 1.3 m [139]. The final flash drum volume was fixed at 0.55 m^3, incorporating a 25% design safety margin above the minimum requirement, as recommended by the manual. The separated gas phase (mainly H_2, CH_4, CO_2) was subsequently cooled to 36 °C in COND1 and mixed with a slightly pressurized (1.1 bar) air stream containing a 10% excess of oxygen relative to the stoichiometric requirement for the complete combustion of the APR gas products. The resulting mixture was assumed to undergo combustion in a boiler under adiabatic conditions, producing a high-temperature flue gas stream at approximately 1665 °C. The flue-gas outlet temperature (approximately 1665 °C) was obtained from the boiler energy balance. An average flue-gas specific heat capacity of 1.5 kJ/kg·K was adopted to estimate the temperature rise associated with the calculated combustion heat release (≈956 kW). This value was selected conservatively, as detailed Aspen Plus simulations of adiabatic combustion without heat recovery predict flue-gas temperatures exceeding 1800 °C, with Cp equal to 1.52 kJ/kg·K while the present approach neglects the heat contribution from water condensation. The resulting temperature is therefore considered conservative and consistent with typical flue-gas temperatures from hydrocarbon combustion [174], [193]. The high-temperature flue gas was utilized for cogeneration through steam production. The selection of a steam Rankine cycle over a gas turbine was motivated by safety and operational robustness. The post-APR gas stream may contain residual H_2 and exhibits variable composition depending on the treated wastewater, which would pose challenges for direct expansion in gas turbines. Moreover, pressure reduction is required for gas–liquid separation downstream of the APR reactor, making direct gas turbine integration impractical. By contrast, the steam cycle operates as a closed loop with water as the working fluid, decoupling electricity generation from gas composition fluctuations and providing a safer and more flexible solution, particularly in view of future scale-up to complex and variable wastewater feedstocks The CHP unit generated a total thermal output of 319 kW and an electrical power of 195 kW. The recovered thermal energy was sufficient to cover:

- the APR reactor duty at 270 °C (235 kW);
- the Feed preheating in the secondary heat exchanger HE2 (84 kW), which raised the feed temperature from 250 to 270 °C;

- Generation of high-pressure steam (HPS) in the Rankine cycle, operating at 170 bar and 620 °C with a flow rate of approximately 550 kg/h.

The generation of HPS is schematically shown in Figure 54, where the flue gas was passed counter-currently through four successive heat exchangers: (I) a superheater, increasing steam temperature from 352 °C to 620 °C; (II) a reboiler, providing the latent heat of vaporization at 170 bar; and (III–IV) two economizers. The first economizer heated liquid water at 170 bar from ambient temperature to 275 °C (729 kg/h stream directed to process units), while the second further raised the temperature of the remaining flow (550 kg/h) from 275 °C to 352 °C.

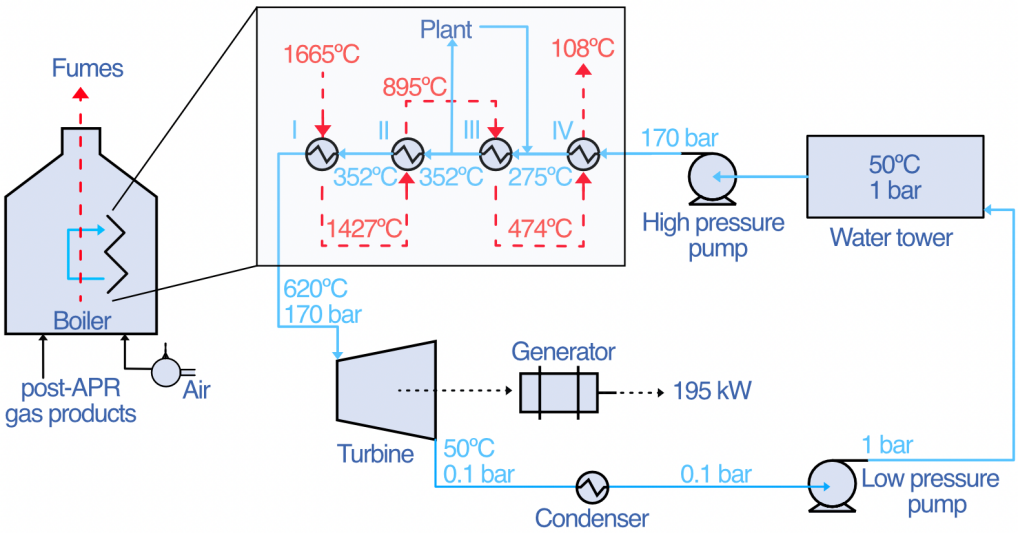

Figure 56. Schematic representation of the combined heat and power unit modelled in Scenario 1. The diagram illustrates how post-APR gas products are burned with air in the boiler, and the heat from the resulting hot flue gases is exchanged with water from the water tower for electricity and heat generation. Four successive heat exchangers (I–IV) provide the heat required to meet plant thermal duties, vaporize the water, and superheat the steam to 620°C at 170 bar for electricity production via the turbine. The reported temperatures and pressures are based on the process simulations.

Splitting the economization stage into two units was adopted as an efficiency-oriented design strategy. Since the reactor operates at 270 °C, a limited temperature approach ($\Delta T \approx 5$ °C) is sufficient to supply the reactor duty and the upstream heat exchanger HE2 (Figures 51–52). Therefore, 57% of steam (729 $kg \cdot h^{-1}$) is withdrawn after the first economizer to cover the plant thermal requirements, avoiding unnecessary heating. Only the remaining 43% (approximately 550 $kg \cdot h^{-1}$), intended for cogeneration, is further heated in the second economizer from 275 to 352 °C before entering the reboiler and superheater. This configuration prevents the entire steam flow from being raised to the saturation temperature at 170 bar, thereby reducing heat losses and improving overall energy efficiency. The high-pressure steam produced in the system was then expanded lowering the pressure to 0.1 bar and generating a gross electrical output of 195 kW, with an isentropic efficiency of 85%. This corresponds to an electrical efficiency of about 20% and an overall Rankine cycle efficiency of 53%. The steam turbine's exhaust gases were released from the system at temperatures between 100 and 110 °C to avoid condensation and related operational issues. After meeting all internal power requirements from pumps and compressors (around 30 kW), the net electric power available for export

to the grid was approximately 165 kW. A simplified process flow diagram for S1 is reported in Figure 51.
In this configuration, the plant effluent requires post-treatment, as the residual COD of 1268 ppm exceeds the discharge limits established by national regulations (500 ppm for sewage systems and 150 ppm for surface waters) [143]. To reduce the COD level below 150 ppm, additional downstream treatment stages would be necessary (see Section 5.4.3).

5.2.4 Downstream Scenario 2: Hydrogen production

For S2, the downstream section was modified to allow for H_2 recovery and purification. After passing through heat exchanger HE1 for heat recovery, the effluent stream was expanded to 25 bar before entering the first flash separator (Flash 1), where the initial gas and liquid separation took place. The gas phase leaving Flash 1, at 117 °C, was then cooled to 26 °C in a condenser (COND1) before entering the PSA unit. The PSA system was modelled to operate at 25 bar and 26 °C, consistent with literature data reporting H_2 purities of up to 99% and recovery efficiencies of approximately 85% for feed streams containing around 10 mol% H_2, which is considered conservative since in the present work the H_2 content is about 50 mol% [194]. This assumption is considered conservative, as in the present work the H_2 content is approximately 50 mol%. From an energy point of view, the PSA energy duty was considered negligible, as the high operating pressure of the APR effluent eliminated the need for additional gas compression, typically the most energy-intensive stage of PSA operation [195].
The liquid stream from Flash 1 was combined with the condensate recovered prior to the PSA unit and directed to a second flash separation unit (FLH2), where the pressure was reduced to 1 bar (see Figure 52). This pressure drop caused the temperature to decrease from 117 °C to 98 °C, enabling the recovery of approximately 89 wt.% of the residual ethanol present in the liquid phase, corresponding to the unconverted fraction from the APR reactor. This secondary separation step effectively reduced the COD of the aqueous stream, which was then cooled to ambient temperature and, depending on the process configuration (as discussed in Sections 5.4.3 configuration effect), either discharged or routed to a wastewater treatment unit.
The gas phase generated from the second flash (FLH2 in Figure 52), together with the PSA off-gas, was directed to the boiler for combined heat and power (CHP) generation. Under the specified operating conditions, the treatment of 2.5 m^3/h of winery wastewater produced a total thermal output of 319 kW and a gross electrical output of 115 kW. Due to the additional H_2 separation step in S2, the overall LHV of the gas stream sent to the CHP system decreased by approximately 26% compared to S1, resulting in a slightly lower flue gas temperature of about 1462 °C. Nevertheless, consistent with the methodology described for S1, the total available thermal energy was fully utilized to meet the internal heat requirements of the process, while approximately 87 kW of net electricity remained available for external export after accounting for internal demands.
The detailed design specifications for the downstream equipment used in both scenarios are summarized in Table 19.

Table 19. Downstream equipment specification for Scenarios 1 and 2, with equipment capacities in bold used for cost estimation.

Equipment	Scenario 1	Scenario 2
Flash 1	P: 1.1 bar Tin: 118 °C Tout: 86 °C Duty: 0 kW RT: 10 min Settling velocity: 0.1 m/s **Vol: 0.55 m^3**	P: 25 bar Tin: 118 °C Tout: 117 °C Duty: 0 kW RT: 10 min Settling velocity: 0.1 m/s **Vol: 0.49 m^3**
Condenser 1	Double pipe Net heat exchanged: 114 kW **Area: 6.08 m^2** U: 1000 W/ m^2 ·K	Double pipe Net heat exchanged: 20 kW **Area: 1.12 m^2** U: 1000 W/ m^2 ·K
PSA	-	P: 25 bar T: 26 °C 99% H_2 purity 85% H_2 recovery 7 kg/h H_2
Flash 2	-	P: 1 bar T: 97.5 °C Duty: −9.15 kW RT: 10 min Settling velocity: 0.1 m/s **Vol: 0.55 m^3**
Condenser 2	Plate and frame Net heat exchanged: 171 kW **Area: 13 m^2** U: 1150 W/ m^2·K	Plate and frame Net heat exchanged: 210 kW **Area: 16 m^2** U: 1150 W/ m^2·K
Air blower	Flow rate: **1230 kg/h** Power rating: 2.8 kW P: 1.1 bar Isentropic compression	Flow rate: **952 kg/h** Power rating: 2.2 kW P: 1.1 bar Isentropic compression
CHP (Boiler + turbine + generator)	Fuel LHV: 956 kW Fumes T: 1665 °C **Electricity capacity: 195 kW** 0.6 wt.% water content ηel: 20% Thermal capacity: 319 kW ηthermic: 33% ηisentropic: 85% ηmechanical: 100% Discharge pressure: 0.1 bar 6% heat loss (LHV)	Fuel LHV: 712 kW Fumes T: 1462 °C **Electricity capacity: 115 kW** 6 wt.% water content ηel: 16% Thermal capacity: 319 kW ηthermic: 44% ηisentropic: 85% ηmechanical: 100% Discharge pressure: 0.1 bar 6% heat loss (LHV)
Pump CHP 1	Discharge pressure: 170 bar ΔP: 110 bar Flow rate: 0.2 L/s **Power rating: 3.4 kW** η: 95%	Discharge pressure: 170 bar ΔP: 110 bar Flow rate: 0.2 L/s **Power rating: 3.4 kW** η: 95%
Pump CHP 2	Discharge pressure: 170 bar ΔP: 171 bar	Discharge pressure: 170 bar ΔP: 171 bar

	Flow rate: 0.15 L/s **Power rating: 2.8 kW** η: 95%	Flow rate: 0.09 L/s **Power rating: 1.9 kW** η: 95%
Economizer CHP 1	Double pipe Net heat exchanged: 170 kW **Area: 1.95 m^2** U: 769 W/ m^2·K	Double pipe Net heat exchanged: 100 kW **Area: 1.82 m^2** U: 769 W/ m^2·K
Economizer CHP 2	Double pipe Net heat exchanged: 215 kW **Area: 0.83 m^2** U: 769 W/ m^2·K	Double pipe Net heat exchanged: 177 kW **Area: 1.10 m^2** U: 769 W/ m^2·K
Reboiler CHP	Double pipe Net heat exchanged: 298 kW **Area: 0.5 m^2** U: 769 W/ m^2·K	Double pipe Net heat exchanged: 244 kW **Area: 0.5 m^2** U: 769 W/ m^2·K
Heater CHP	Double pipe Net heat exchanged: 137 kW **Area: 0.17 m^2** U: 769 W/ m^2·K	Double pipe Net heat exchanged: 82 kW **Area: 0.12 m^2** U: 769 W/ m^2·K
Cooling water	25–40 °C **Total plant flow rate: 36 m^3/h**	25–40 °C **Total plant flow rate: 27 m^3/h**

5.3 Energy Sustainability Assessment (ESA) Results

The energy sustainability of S1 and S2 was evaluated using the ESA methodology described in section 2.2.2. The main energy flows for both configurations, expressed in MJ, along with the corresponding ESI, EROI and EPT values for 75% and 95% ethanol conversion, are summarized in Table 20, together with additional simulations at 95% ethanol conversion (S1–95 and S2–95), where the potential improvement of ethanol conversion would affects the overall energy performance of each scenario.

Table 20. Detailed energy flows included for the ESA evaluation as previously shown in Figure 11.

Scenario	S1	S1–95	S2	S2–95
Ethanol conversion (%)	75	95	75	95
Available energy (MJ)	3384	3384	3384	3384
Produced energy (MJ)	1850	1990	2409	2725
Direct energy (MJ)	1254	1442	1247	1436
Indirect energy (MJ)*	380	346	428	371
Net energy (MJ)	596	549	1162	1288
ESI	1.48	1.38	1.93	1.90
EROI	1.57	1.59	2.71	3.47
EPT (anni)	12.73	12.57	7.38	5.76

* Indirect energy values already include the factor-of-two correction applied in the EROI calculation to account for additional life-cycle contributions, as expressed in Eq. (13).

Starting from the same initial energy content in ethanol, S1 and S2 lead to different energy outputs and energy quality profiles. At 75% ethanol conversion, S2 achieves

a produced energy output of 2409 MJ, representing a 30% increase compared to S1. This difference reflects the distinct thermodynamic efficiencies associated with the energy conversion pathways in each scenario. When ethanol conversion increases to 95%, the energy gap widens slightly, with S2 producing 36% more total energy than S1.

Despite these variations in produced energy, the direct energy requirements for plant operation remain comparable between the two scenarios at equal conversion levels. However, at higher conversion (95%), a 15% increase in direct energy demand is observed for both scenarios. This increases is primarily governed by the intensified extent of the APR reaction, which promotes greater vapor formation (see Section 5.2.2) and consequently increases the thermal duty of the APR reactor.

Conversely, indirect energy demand, which includes contributions from raw material supply, catalyst production, infrastructure construction and dismantling, and waste management, exhibits the opposite trend. Increasing ethanol conversion from 75% to 95% results in a 9% reduction in indirect energy demand for S1 and a 13% reduction for S2.

It should be noted that this decrease does not arise from reduced requirements for catalyst, raw materials, or infrastructure, which are assumed to remain constant across configurations. Instead, the reduction is primarily driven by improved process productivity and enhanced COD removal efficiency, which significantly lowers the energy burden associated with wastewater management. As a result, fixed indirect energy contributions are effectively distributed over a larger amount of useful energy output, leading to a lower indirect energy demand per functional unit. Together with the dominant contribution of platinum catalyst production, waste management remains one of the key drivers of indirect energy investment.

5.3.1 Energy Metrics: ESI and EROI Analysis

All ESI values obtained for the simulated conditions exceed unity, confirming that both configurations are energetically self-sustaining in the short term, i.e., they are capable of meeting their own direct energy requirements while generating a surplus of usable energy. For both S1 and S2, a slight decrease in ESI is observed when increasing the ethanol conversion from 75% to 95%. Although seemingly counterintuitive, this behaviour arises from the higher thermal load of the APR reactor at elevated conversion levels, which reduces the net electrical output from 195 kWh to 182 kWh in S1 and from 115 kWh to 87 kWh in S2. As discussed previously, the thermal duty of the APR reactor directly impacts the electricity exported to the grid; therefore, increased energy requirements lower the net energy produced and, consequently, the ESI. These limited variations in ESI for the improved ethanol conversion scenarios highlight the importance of optimizing APR reactor performance. This could be obtained by optimizing heat recovery and developing catalysts capable of lowering the activation energy of the reforming reactions. Although catalysts do not alter the reaction enthalpy, lowering the activation energy allows the same conversion to be achieved at lower operating temperatures. This reduces the reactor sensible heat demand and, in turn, positively influences the overall process energy balance. From a long-term perspective, the EROI values also confirm a positive energy return for both scenarios, with S2 showing superior energy performances. When the ethanol conversion increases to 95%, S2 achieves an EROI of 3.47, corresponding to an improvement of over 30%,

whereas S1 exhibits no significant variation. The observed differences primarily lie on the quality of the produced energy: in S2, H_2 is credited with its full LHV, whereas in S1, the conversion to electricity unavoidably involves thermodynamic losses. Although both configurations yield similar syngas compositions (mainly H_2 and CH_4), the energy recovery pathway and the downstream configuration determine the differences in net energy return. To complement the EROI analysis, the EPT was evaluated to provide a time-based perspective on long-term energy performance. As reported in Table 20, EPT values range from 5.76 to 12.73 years depending on the scenario and ethanol conversion efficiency. Scenario S1 exhibits the longest payback times, with EPT values of 12.73 years at 75% ethanol conversion and 12.57 years at 95% conversion, reflecting the relatively lower net energy return associated with electricity-only recovery. In contrast, scenario S2 shows substantially shorter EPTs, decreasing from 7.38 years at 75% conversion to 5.76 years at 95% conversion, due to the higher net energy output associated with H_2 recovery. These results confirm that, despite higher indirect energy investments, S2 compensates its embodied energy significantly faster than S1, reinforcing its superior long-term energetic performance. Finally, in line with the EROI results, higher ethanol conversion reduces the EPT mainly in S2, where H_2 recovery enhances net energy returns, while S1 remains largely unaffected due to inherent conversion losses in electricity generation.

5.3.2 Comparison with other hydrogen production technologies

Comparable ESA analyses have been reported for other H_2-producing technologies [196]. For instance, SMR and two-stage anaerobic digestion (TSAD) show ESI values of 3.63 and 3.00, and EROI values of 2.47 and 2.24, respectively. When compared to S2, the ESI is approximately two times lower than SMR and 1.6 times lower than TSAD, however, the EROI of S2 surpasses SMR by 10% and TSAD by 21% (Table 21).

Table 21. Comparison of ESI and EROI values for H_2-producing technologies, including Scenario 2 investigated in this study (APR-S2), steam methane reforming (SMR), and two-stage anaerobic digestion (TSAD).

	APR-S2	SMR	TSAD
ESI	1.93	3.63	3.00
EROI	2.71	2.47	2.24

This finding suggests that, despite higher direct operational energy demands, S2 achieves higher long-term energy performance due to reduced indirect energy demands. Overall, the obtained ESI and EROI metrics, although modest compared to large-scale industrial energy production processes, remain above unity, consistent with other energy recovery systems. These results indicate that the process could, in principle, meet both its direct and indirect energy requirements while generating surplus useful energy for external use. Nevertheless, the proximity of these values to unity reveals the narrow operational margin of the APR system for energy recovery from ethanol-rich wastewaters.

In particular, given EROI values approaching 2, the system demonstrates limited tolerance to inefficiencies or operational deviations. Small variations, such as decreased ethanol conversion, reduced heat recovery efficiency, or increased

auxiliary power demand, could readily drive the EROI below 1, rendering the process energetically unsustainable. Therefore, maintaining precise control of critical process parameters (reactor temperature, pressure, feedstock composition) and ensuring robust heat integration are essential to sustain positive net energy output and guarantee long-term energy sustainability.

5.4 Techno-Economic Assessment (TEA) Results

5.4.1 Minimum Selling Prices

The total capital and operating costs (TCOP) for S1 and S2 were estimated at USD 14.9 M and USD 14.16 M, respectively. When annualized over a 20-year plant lifetime, these correspond to USD 823 k/year for S1 and USD 805 k/year for S2. As shown in Figure 57 and Figure 58, the VCOP represents only about 4% of the annualized TCOP in S1 and approximately 7% in S2.

The dominant VCOP contributor in both scenarios is the COD treatment cost. In S1, this expense amounts to USD 18 k/year, which is over 53% lower than in S2, and accounts for 61% of S1's VCOP. Conversely, in S2, the COD treatment cost increases to USD 38 k/year, representing 77% of VCOP (see Figure 58). The higher COD-related cost in S2 primarily originates from its process configuration. Because the PSA unit operates at 25 bar, the first flash separator experiences a smaller pressure drop than in S1 (approximately 1.1 bar), which limits ethanol recovery to about 50%. In contrast, S1 achieves 98% ethanol recovery in its first flash unit. Consequently, a second flash stage is required in S2 to raise total ethanol recovery to around 90%. Despite this improvement, the liquid effluent from S2 still exhibits a higher residual COD, leading to increased treatment costs and highlighting the strong dependence of COD-related expenses due to incomplete ethanol conversion.

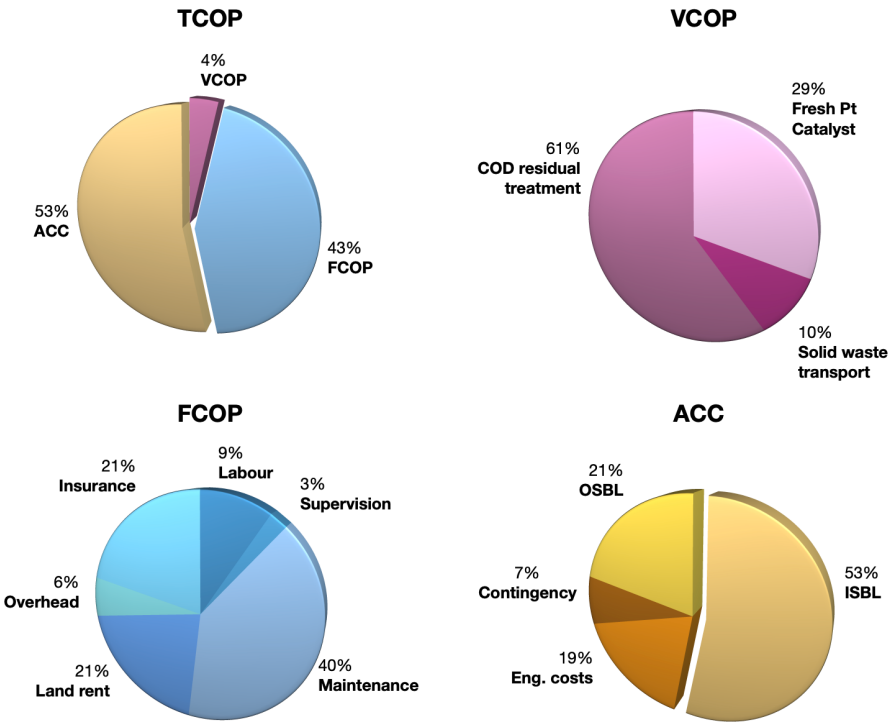

Figure 57. Cost breakdown of the APR-based system under Scenario 1.

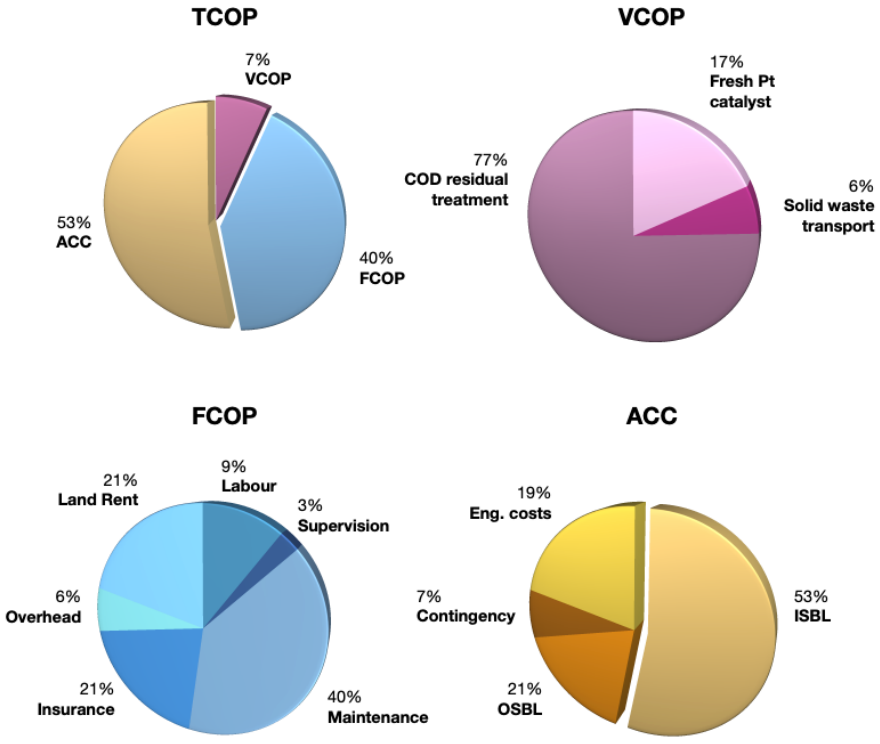

Figure 58. Cost breakdown of the APR-based system under Scenario 2.

Simulating an improvement in APR performance by reaching 95% ethanol conversion in both configurations could lower COD treatment costs by up to 60% as discussed in the following sections. Furthermore, it will be explores how

integrating additional downstream equipment could further reduce COD levels, while also affecting the MSP. Further economic implications of adopting APR as an alternative to conventional wastewater treatment will be investigated, which highlights the potential of the APR process to generate additional economic value via COD removal fees.

Both S1 and S2 exhibit low VCOP due to their self-sufficient operation, which eliminates external utility supply. Additionally, since the feedstock (WWW) is a waste stream, no feedstock cost is considered; the remaining VCOP components are equivalent between the two scenarios.

The FCOP represents 43% and 40% of the annualized TCOP in S1 and S2, respectively. Consistent with findings from similar APR techno-economic analyses on glycerol [146], the largest FCOP contribution arises from equipment maintenance (~40%), followed by land rental and insurance.

Within the ACC, the ISBL component is the dominant contributor in both scenario (Figure 59).

In both S1 and S2, the CHP unit is the single most expensive item, representing 37% of ISBL (USD 1.3 M) in S1 and 27% (USD 901 k) in S2. The higher CHP cost in S1 is directly related to its greater generation capacity requirement, as CHP investment scales with installed electric capacity [197,198].

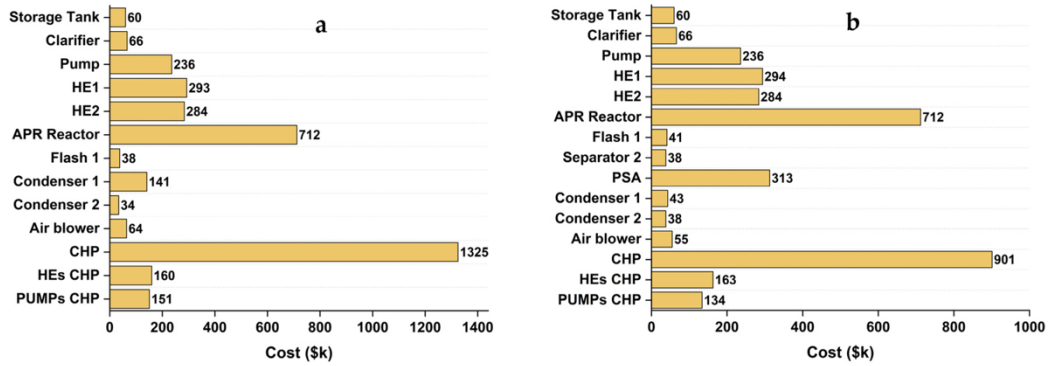

*Figure 59. Breakdown of Inside Battery Limits Costs (ISBL) for the two process configurations: **(a)** S1: electricity production and **(b)** S2: H_2 recovery.*

The APR reactor constitutes the second-largest ISBL element, accounting for 20% of ISBL in S1 and 21% in S2, with comparable absolute costs. The reactor construction material was selected as stainless steel, and the corresponding material correction factor was applied (Table 5). This choice is consistent with previous TEAs of APR systems, and the resulting reactor cost per unit of feed treated aligns with literature-reported values [146].

In S2, the PSA unit represents the third major cost element, contributing 9% of ISBL (USD 313 k/year), while in S1, the heat exchanger HE1 holds this position, accounting for 8% of ISBL. A comprehensive list of all equipment costs, both as-purchased and after correction factor application is reported in Table 22.

Table 22. Purchasing and final installed costs of each equipment item for Scenario 1 and Scenario 2.

Unit of operation	S1		S2		Reference
	purchase cost	final cost	purchase cost	final cost	
Storage tank	$8,400	$59,800	$8,400	$59,800	[50]
Clarifier	$9,200	$65,900	$9,200	$65,900	[62]
Pump	$21,500	$236,100	$21,500	$236,100	[62]
HE1	$25,000	$292,900	$25,000	$294,300	[50]
HE2	$24,200	$283,800	$24,200	$283,800	[50]
APR reactor	$712,300	$712,300	$712,300	$712,300	[64]
Flash 1	$5,600	$37,600	$5,600	$41,400	[62]
Condenser (double pipe)	$14,400	$140,500	$4,000	$38,600	[50]
PSA	–	–	–	$313,000	[51]
Condenser 2 (plate and frame)	$3,500	$33,800	$3,900	$37,800	[50]
Flash 2	–	–	$5,600	$37,600	[62]
Blower	$15,600	$63,800	$13,500	$54,800	[50]
HEs CHP	$284,700	$1,476,000	$196,500	$1,035,400	[50]
Pumps CHP	$13,700	$150,900	$12,200	$134,200	[62]
CHP (boiler + turbine + generator)	$271,000	$1,325,100	$184,300	$901,200	[62]

Considering all cost components, the MSP were estimated at USD 0.86/kWh for electricity production (S1) and USD 15.5/kg H_2 for H_2 production (S2). Both values are significantly higher than current market benchmarks (USD 0.36/kWh for electricity [156] and USD 0.8–12/kg H_2 [20],[199] [22,200]). To identify potential pathways for cost reduction and to better contextualize the comparison with current electricity prices in Italy, an exploratory scenario-based analysis was conducted for both configurations. A set of hypothetical prospective scenarios was defined to assess how selected operating and design choices could influence process economics. Accordingly, three exploratory optimization routes were explored: (i) the effect of increased ethanol conversion to achieve higher yields, (ii) the impact of incorporating additional process units to comply with discharge limits for surface disposal of the residual wastewater after APR, and (iii) the potential reduction in MSPs associated with avoided wastewater treatment costs. The latter is especially relevant, as wastewater treatment represents a service that is normally associated with a cost rather than a revenue stream, and its inclusion highlights the fundamental difference between APR and conventional electricity generation technologies.

5.4.2 Ethanol conversion effect

To investigate how MSP varies, ethanol conversion was increased from 75% to 95% for both scenarios, hereafter referred to as S1–95 and S2–95.
In S1–95, the TCOP showed a modest decrease, from USD 823 k/y to USD 813 k/y, primarily due to lower operating costs associated with the lower COD content left in the output stream, consequently its reduced treatment costs and lower CHP unit cost, which scale proportionally with the amount of electricity generated, which slightly reduced (Figure 60).

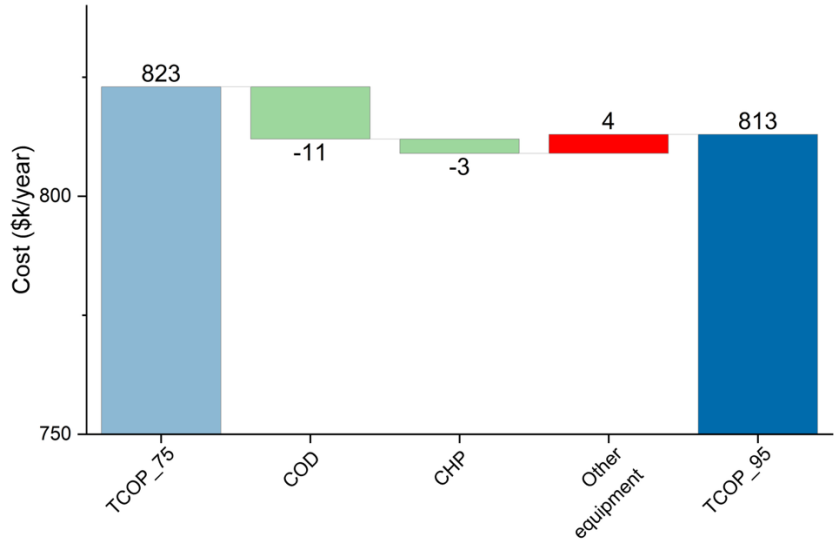

Figure 60 Bridge chart illustrating the variation in TCOP for S1 as ethanol conversion increases from 75% to 95%. The bars represent the annual change in cost ($k/year) for the main cost drivers. Green bars indicate cost reductions: COD treatment and CHP equipment decrease by $11k/y and $3k/y, respectively. However, these savings are partially offset by an increase of $4k/y in other equipment costs (red bar).. As a result, the overall TCOP decreases from $823k/year to $813k/year.

Nevertheless, despite the TCOP reduction, the MSP of electricity increased from USD 0.86 /kWh to USD0.92 /kWh. This represents a key finding of the study, as the seemingly counterintuitive outcome results from the complex interplay of multiple factors: At 95 % ethanol conversion, a greater fraction of the feed is transformed into gaseous products, leading to a 14.5 % increase in the LHV of the gas stream (from 956 kW to 1095 kW) and a higher flue gas flow rate (from 1400 kg/h to 1533 kg/h). The heat recovered from this stream is exploited in the CHP section to generate HPS. However, higher conversion also amplifies the overall endothermic demand of the APR reaction as well as the vaporization effects, thereby increasing the reactor's thermal duty by 22 % (from 235 kW to 287 kW). To satisfy this additional energy requirement, a larger portion of the produced HPS must be redirected to the reactor (848 kg/h versus 729 kg/h), leaving less HPS available for turbine expansion and power generation. Consequently, the net electrical output from the CHP unit drops from 195 kW to 182 kW. Because the MSP is obtained as the ratio between the TCOP and total electricity produced, a relatively small reduction in cost (–1.2 %) combined with a more pronounced drop in energy output (–8 %) yields an overall increase in MSP. The observed rise in MSP at higher conversion mainly stems from the increased reactor duty linked to water vaporization effect. Therefore, operating at higher pressure could help mitigate this effect by limiting the vapor phase fraction, an aspect worth exploring in future optimization studies.

In summary, increasing the ethanol conversion enhances COD removal and the calorific quality of the fuel gas but simultaneously elevates the internal heat demand. This shift in the energy balance ultimately raises the net electricity available and then the production cost.
In S2–95, the effect of increasing ethanol conversion has in contrast a positive effect under an economic perspective. The TCOP decreased by approximately 5 %, from USD805 k/y to USD769 k/y, slightly more than in S1–95, and this translated into a substantial 20 % reduction in the H_2 MSP, which dropped from USD15.5 /kg H_2 to USD12.5 /kg H_2. When compared with H_2 production costs reported for electrolysis-based pathways [199], these values fall within the upper range of literature estimates, suggesting that APR-based hydrogen could become economically competitive under favorable operating conditions such as these, particularly when combined with avoided wastewater treatment costs and when deployed in applications where hydrogen is directly utilized. This improvement derives from both the lower TCOP and a 27 % increase in annual H_2 production (from 40.3 to 51.2 t/y). Within the TCOP, the enhanced COD removal efficiency (from 97.5 % to 99.6 %) plays a crucial role, as COD treatment constitutes a larger portion of the variable operating costs in S2 (see Figure 61). As observed for S1, a higher ethanol conversion entails an increase in reactor heat duty; however, since H_2 is separated in S2, the energy available for electricity generation in the CHP unit is lower, resulting in a reduced net power output (115 kW → 87 kW, –24 %). This in turn slightly decreases CHP-related operating costs, which scale with power generation (Figure 61).

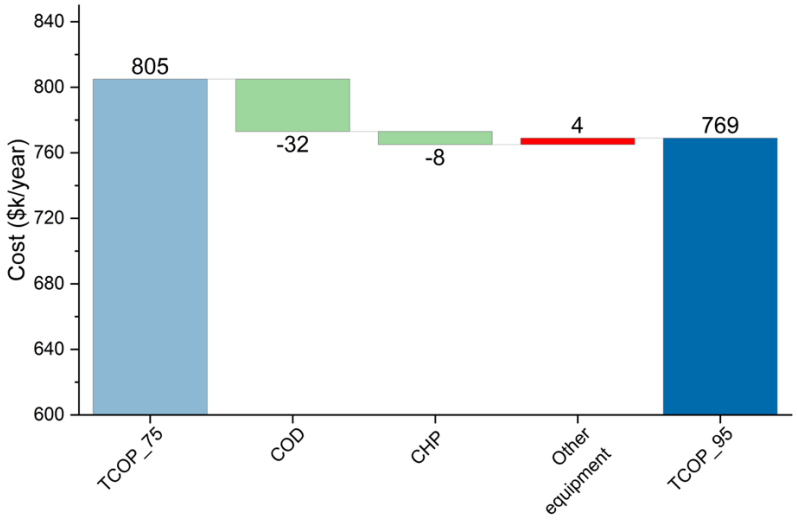

Figure 61. Bridge chart illustrating the variation in TCOP for S2 as ethanol conversion increases from 75% to 95%. The bars represent the annual change in cost ($k/y) for the main cost drivers. Green bars indicate cost reductions: COD treatment and CHP equipment decrease by $11k/y and $3k/y, respectively. However, these savings are partially offset by an increase of $4k/y in other equipment costs (red bar), including the addition of PSA. As a result, the overall TCOP decreases from $805k/y to $769k/y.

Ultimately, the increase in H_2 yield outweighs the loss in electricity revenue, rendering S2 more responsive and economically advantageous under improved APR conversion conditions. A detailed comparison of the corresponding energy flows for both scenarios is summarized in Table 23.

Table 23. Energy balance for S1, S1-95, S2, and S2-95, with focus on those energy flows involved in the increased electricity MSP.

Scenario	Conversion (%)	Product gas heating value (kW)	APR reactor duty (kW)	Other thermal duties (kW)	Plant electricity demand (kW)	Gross electricity (kW)	Exported electricity (kW)
S1	75	956	235	84	29.5	195	166
S1-95	95	1095	287	84	29.6	182	152
S2	75	676*	235	84	27.4	115	88
S2-95	95	712*	287	84	27.5	87	60

Ηoverall=50%, Ηthermal=33%, Ηelectrical(net)=19%

5.4.3 Configuration Effect

Regarding the COD limits for surface discharge, increasing ethanol conversion from 75% to 95% improved the COD removal efficiency from 97.5% to 99.6% in S2 and from 98.0% to 99.9% in S1. Nevertheless, the corresponding COD concentrations, 357 ppm for S2 and 226 ppm for S1, remained above the regulatory discharge limit of 150 ppm for surface waters, indicating that further COD abatement steps were still necessary. To comply with this threshold, a modification of the equipment configuration was evaluated in addition to the optimized ethanol conversion. The modified configurations, referred to as S1–95+ and S2–95+, incorporated an additional flash separation unit in both scenarios, although with different operating specifications tailored to their respective process requirements.
In particular, in the S1–95+ configuration, the COD concentration of the process effluent was further reduced to approximately 105 ppm, thereby allowing direct surface discharge. This improvement resulted from the enhanced ethanol separation efficiency achieved by introducing two flash units. Specifically, Flash 1 was operated at 8 bar, followed by a second flash at 1 bar, whose combination enabled an additional 1% ethanol removal compared to the single-flash configuration.
The resulting MSP of electricity reached USD 0.93/kWh, which is comparable to the value obtained for the single-flash configuration at 95% conversion (S1–95, USD 0.92/kWh). The advantage of producing a treated effluent suitable for direct discharge therefore comes at a moderate economic cost, as the MSP rises from USD 0.86/kWh at 75% ethanol conversion to USD 0.92/kWh at 95% conversion and to to USD 0.93/kWh when an additional flash is introduced. Overall, this demonstrates that while higher conversion enhances COD removal efficiency, it also imposes greater energetic and economic penalties, whereas the addition of an extra flash unit achieves compliance with discharge limits with minimal cost implications.
In the S2+ configuration, the modified setup consisted of an initial gas–liquid separation step operating at 6 bar (compared to the 25 bar of S1), followed by a secondary flash performed at lower temperature before PSA separation, and a compressor addition to restore the gas stream to the required PSA inlet pressure. An additional flash unit operating at atmospheric pressure was subsequently applied to the liquid stream exiting the previous stages, enhancing ethanol recovery and decreasing the final COD concentration to 124 ppm, effectively removing the need for any external wastewater treatment. Under these conditions, the H_2 MSP decreased by 12% (USD12.5 /kgH_2) compared with the base case at 75% conversion (USD15.5 /kg H_2), although it remained approximately 13% higher than in the 95% configuration (USD 13.7/kg H_2). This indicates that the modified configuration in S2 prioritizes COD abatement efficiency over economic

performance, once again highlighting a scenario-specific behaviour in the MSP response. A summary of these results is reported in Table 24.

Table 24. Summary of key techno-economic and environmental indicators across different APR configurations for S1 and S2.

Scenario	Conversion (%)	Turbine (kWh)	APR Revenue (USD0.315/kg_{COD})	COD Removal Efficiency (%)	COD (ppm)	MSP (USD/kWh, USD/kgH_2)
S1	75	195	0	98.8	1268	0.86
S1 *	75	195	629,350	98.8	1268	0.20
S1–95	95	182	0	99.9	226	0.92
S1–95+	95	176	0	100	105	0.93
S2	75	115	0	97.5	2809	15.52
S2 *	75	115	620,988	97.5	2809	4.62
S2–95	95	87	0	99.6	357	12.59
S2–95+	95	94	0	100	124	13.75

5.4.4 Economic Benefits from Avoided Wastewater Treatment Costs

To further explore potential cost reduction strategies, an additional scenario was investigated in which APR is considered not solely as an energy recovery process, but primarily as a wastewater treatment technology capable of replacing conventional COD removal plants. Under this assumption, both scenarios were evaluated in terms of their potential to deliver energy carriers, electricity and H_2 at a competitive price respect to market prices, set at USD 0.20/kWh and USD 4.5/kg H_2.

To achieve these target prices, it was calculated that the facility would need to apply a service fee of USD 0.42 per kg of COD removed, which is still 60% below the average cost associated with traditional wastewater treatment (USD 1.05/kg COD) [142]. According to these assumptions, the APR facility would generate a revenue of approximately USD 629 k/y for S1 and USD 620k/y for S2. These revenues can be deducted directly from the TCOP of each scenario, thereby improving the overall economic balance.

For comparison, if the same quantity of kg of COD removed by APR, accounting to 1.49 kt/year in S1 and 1.48 kt/year in S2, were instead treated through a conventional wastewater treatment plant, the annual treatment costs would reach roughly USD 1.5 M for both cases. Adopting the APR facility instead would result in avoided costs equivalent to approximately 48% of the annual TCOP of the APR-based treatment systems, highlighting the potential economic advantage of implementing APR as a dual-purpose technology for both energy recovery and wastewater treatment.

Furthermore, if the COD service fee were raised to 50% of the conventional treatment cost (USD 0.53/kg COD), the APR process could achieve net-positive operating margins, strengthening its position as a cost-effective and sustainable alternative to conventional wastewater treatment. The configurations denoted as S1* and S2* represent these hypothetical scenarios, where COD abatement revenues are integrated into the cost structure, assuming a service fee of USD 0.42/kg COD removed, as summarized in Table 24 above.

5.4.5 Sensitivity analysis and MSPs variation

A comprehensive sensitivity analysis was carried out on the basic configurations of both scenarios to identify the main cost drivers influencing the MSP and to determine the parameters with the highest potential for improving process competitiveness. The analysis considered variations of ±20% and ±40% in the key techno-economic factors.

For S1, the resulting variations in electricity production costs are illustrated in Figure 62, where the baseline MSP of USD 0.86/kWh, corresponding to the electricity price obtained under the experimental operating conditions, is used as the reference value.

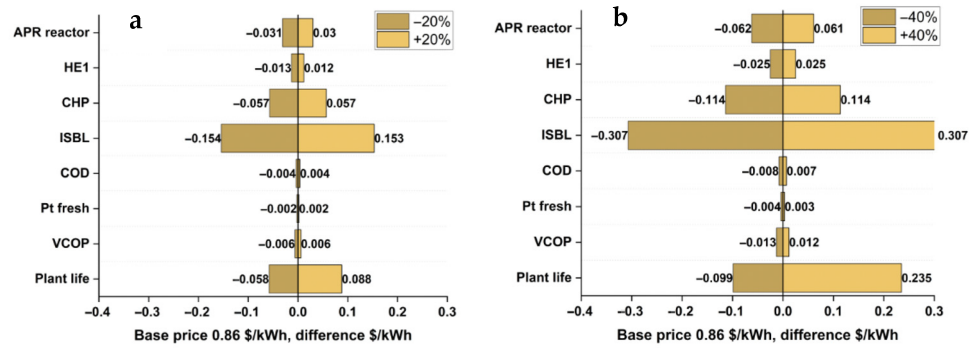

Figure 62 Variation in electricity production cost (USD/kWh) for Scenario 1 obtained from the sensitivity analysis of key techno-economic parameters, considering cost deviations of ±20% (a) and ±40% (b). The baseline electricity price is set at USD 0.86/kWh.

Each bar represents the deviation from this reference value caused by the fluctuation of individual cost parameters, encompassing both capital expenditures (e.g., APR reactor, heat exchanger HE1, CHP unit, and ISBL) and operating expenses (e.g., COD treatment, Pt replacement, and other variable costs), as well as plant lifetime.

An analogous sensitivity analysis was performed for S2, with the results shown in Figure 63, where the reference MSP for H_2 is USD 15.5/kg H_2.

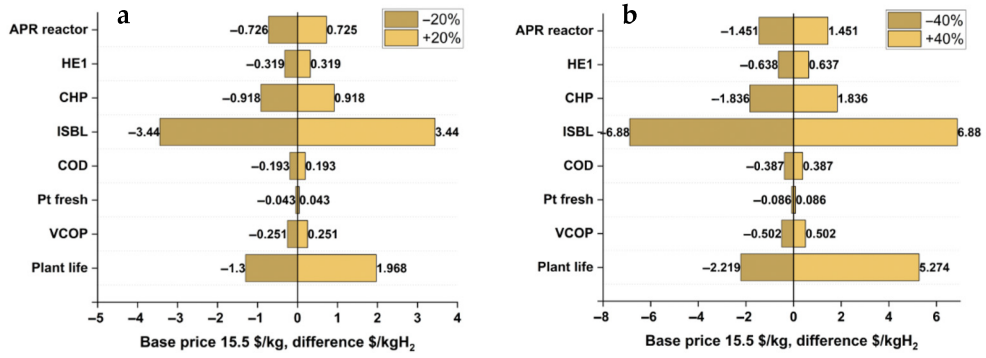

Figure 63. Variation in H_2 production cost (USD/kg) for Scenario 2 obtained from the sensitivity analysis of key techno-economic parameters, considering cost deviations of ±20% (a) and ±40% (b). The baseline H_2 price is set at USD 15/kg.

Not all cost parameters contributed equally to MSP variations. Changes in VCOP produced only marginal effects on both H_2 and electricity prices. In contrast, plant lifetime proved to be one of the most critical factors in both configurations:

extending the operational period by 40% (from 20 to 28 years) could reduce electricity and H_2 MSPs to USD 0.63/kWh and USD 10.2/kg H_2, respectively.
Similarly, capital investment costs, particularly those within the ISBL, exhibited a strong influence on economic performance. Within this category, the APR reactor and CHP unit emerged as the most impactful contributors. As can be inferred from Figure 63, a 40% reduction in the cost of the ISBL equipment could potentially lower the MSP down to USD 0.55/kWh for electricity and USD 8.6/kgH_2 for H_2. Although reducing reactor costs may be difficult or even unfeasible, given their strong dependence on the cost of raw materials required for fabrication at the necessary scale, this finding emphasizes the importance of developing more active catalysts. Catalysts that perform efficiently at shorter residence times can reduce the required reactor volume, which directly influences overall reactor costs. For this reason, advancing catalyst formulations may represents a key research direction for improving the economics of the APR systems. For instance, according to Zhao et al. [201], the use of a bimetallic Ru–Pt catalyst could achieve equivalent ethanol conversion in less than half the time required by monometallic catalysts and therefore potentially reducing the wastewater retention time from 3.3 min to 1.65 min, allowing to halve the reactor volume and further reducing its cost.
The negative effect of catalyst deactivation when treating real wastewaters was also assessed by considering catalyst shorter lifetimes than the one-month period adopted in the baseline economic evaluation. Reducing catalyst life from one month to one week caused a moderate increase in MSP, rising from USD 0.86 to 0.89/kWh in S1 and from USD 15.4 to 16.1/kg H_2 in S2 (i.e., +4.8–5.0%). However, in the one-week replacement case, an additional parallel reactor was included to avoid weekly shutdowns, which would be impractical for continuous industrial operation. This modification, however, led to a substantial MSP increase, reaching USD 1.00/kWh and USD 19.7/kg H_2, equivalent to a 12.8–28.1% rise, as reported in Table 25.

Table 25. Influence of catalyst lifetime on MSP for S1 (USD/kWh) and S2 (USD/kg H_2), compared to the baseline case assuming a one-month catalyst lifespan.

Catalyst lifespan	S1 ($ /kWh)	S2 ($ /kgH_2)
1 month (baseline)	0.86	15.5
2 weeks	0.87	15.7
1 week	0.89	16.1
1 week – 2 APR reactors	1.04	19.7

The influence of the fresh Pt fraction used in catalyst replacement was also evaluated by varying its proportion from 1% (baseline) up to 100%. A strong dependence of the MSP on the fresh Pt loading was observed: at 100% fresh Pt replacement, the MSP increased to USD 1.76/kWh for S1 and USD 36/kg H_2 for S2, representing an approximately twofold rise in both cases (Figure 64).

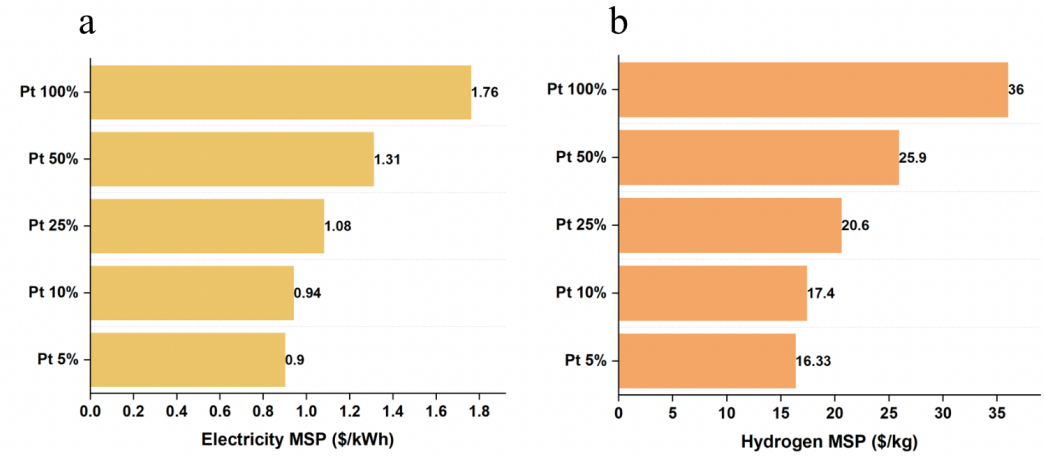

Figure 64. Sensitivity of the MSP for electricity (a) and H_2 (b) to changes in the proportion of fresh Pt added during catalyst replacement relative to the recovered Pt fraction. The reference MSP values correspond to USD 0.86 /kWh for electricity and USD 15.4 /kg H_2, assuming a 1% fresh Pt replacement rate and a catalyst lifetime of one month under standard operating conditions.

The sensitivity analysis also revealed that increasing plant scale could substantially reduce the ISBL cost contribution through economies of scale. Nevertheless, this potential is inherently limited, as the present model already reflects wastewater volumes representative of medium-to-large wineries. A more promising strategy would involve a district-scale approach, where a centralized APR facility processes effluents from multiple producers (e.g., wineries, breweries, and other ethanol-generating industries) [74]. Such an integrated system could justify larger equipment capacities, leading to lower specific capital costs and improved overall economic feasibility, as previously demonstrated in similar studies [97,202].

Finally, the sensitivity analysis also examined the effect of technology novelty by varying the engineering contingency factor, which was set at 10% in this study. Although the APR process has not yet been demonstrated at industrial scale, the technology itself cannot be considered novel, as the system mainly comprises well-established equipment such as heat exchangers and a CHP unit, with no complex distillation steps involved. The only unit that may pose some design challenges is the APR reactor; however, since a continuous plug-flow configuration was adopted in this work, its design remains close to conventional process technologies. For these reasons, the system was not classified as a first-of-a-kind (FOAK) but rather as a non–first-of-a-kind (nFOAK) plant.

To investigate our assumption, a sensitivity analysis was performed by varying the contingency factor between 10% and 40%. The results, summarized in Figure 65, show that for S1, the MSP of electricity increased from USD 0.86/kWh to USD 0.97/kWh, whereas for S2, the H_2 MSP rose from USD 15.5/kgH_2 to USD 17.7/kgH_2, confirming the robustness of the baseline economic assumptions.

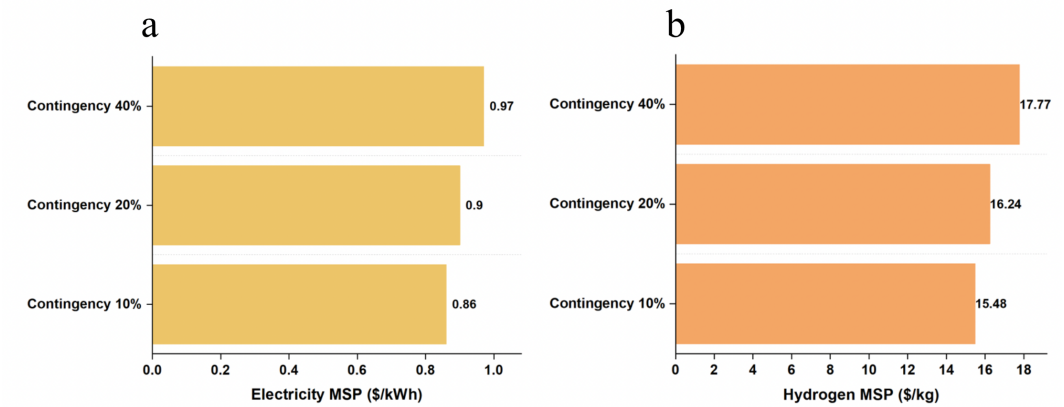

Figure 65. Variation of the MSP for electricity (a) and H_2 (b) as a function of the contingency factor, evaluated within the 10–40% range.

Finally, considering that the investigated APR configuration also serves as a wastewater treatment process, where the equipment is generally simple and contingency factors are typically low, the selection of a 10% contingency is deemed appropriate for this work to ensure a fair and consistent comparison[202], [203].

5.5 Life Cycle Assessment (LCA) Results

The life cycle inventories and datasets adopted for the assessment are provided in Table 26 and

Table 27, for both S1 and S2 scenarios, respectively.

Table 26. LCA dataset modelled for Scenario 1, with 1 kWh of electricity produced as functional unit from WWW APR.

Activity	Electricity production by APR – S1 LCAI				
Function unit	1 kWh of electricity				
Type	Process				
Exchanges					
Activity Name	Amount	Database	Location	Unit	Reference Product
Biosphere					
Carbon dioxide, non-fossil	1.29	biosphere3	air	kg	emission
Nitrogen	5.05	biosphere3	air	kg	resource
Oxygen	1.53	biosphere3	air	kg	resource
Water	0.001	biosphere3	air	m^3	emission
Cooling water	0.187	biosphere3	water	m^3	resource
Technosphere					
market for activated carbon, granular	4.70E-04	ecoinvent cutoff 391	GLO	kg	activated carbon, granular
market for chemical factory, organics no steel	1.87E-11	ecoinvent cutoff 391 (modified)	GLO	unit	chemical factory, organics
market for liquid storage tank, chemicals, organics	8.97E-11	ecoinvent cutoff 391	GLO	unit	liquid storage tank, chemicals, organics
market for spent catalytic converter for cars	-5.00E-04	ecoinvent cutoff 391	GLO	kg	spent catalytic converter for cars
platinum group metal, extraction and refinery operations	2.52E-07	ecoinvent cutoff 391	ZA	kg	platinum
steel production, chromium steel 18/8, hot rolled	7.00E-04	ecoinvent cutoff 391	RER	kg	steel, chromium steel 18/8, hot rolled
transport, freight, lorry, all sizes, EURO4 to generic market for transport, freight, lorry, unspecified	3.35E-03	ecoinvent cutoff 391	RER	ton·km	transport, freight, lorry, unspecified
treatment of automobile catalyst	2.49E-05	ecoinvent cutoff 391	RoW	kg	platinum

treatment of scrap steel, inert material landfill	-7.00E-04	ecoinvent cutoff 391	RoW	kg	scrap steel
treatment of sewage sludge, 70% water, WWT, WW from maize starch production, municipal incineration	-0.132	ecoinvent cutoff 391	GLO	kg	sewage sludge, 70% water, WWT, WW from maize starch production
treatment of wastewater from potato starch production	-0.10	ecoinvent cutoff 391	RoW	m^3	wastewater from potato starch production

Table 27. LCA dataset used to model Scenario 2, with 1 kg H_2 produced as functional unit from WWW APR.

Activity	H_2 production by APR – S2 LCAI				
Function unit	1 kg of H_2				
Type	Process				
Exchanges					
Activity Name	Amount	Database	Location	Unit	Reference Product
Biosphere					
Carbon dioxide, non-fossil	35.10	biosphere3	air	kg	emission
Nitrogen	110.00	biosphere3	air	kg	resource
Oxygen	33.00	biosphere3	air	kg	resource
Water	0.016	biosphere3	air	m^3	emission
Cooling water	5.05	biosphere3	water	m^3	resource
Technosphere					
market for activated carbon, granular	0.01	ecoinvent cutoff 391	GLO	kg	activated carbon, granular
market for chemical factory, organics no steel	5.30E-10	ecoinvent cutoff 391 (modified)	GLO	unit	chemical factory, organics
market for liquid storage tank, chemicals, organics	2.50E-09	ecoinvent cutoff 391	GLO	unit	liquid storage tank, chemicals, organics
market for spent catalytic converter for cars	-0.01	ecoinvent cutoff 391	GLO	kg	spent catalytic converter for cars
platinum group metal, extraction and refinery operations	6.97E-06	ecoinvent cutoff 391	ZA	kg	platinum
steel production, chromium steel 18/8, hot rolled	0.03	ecoinvent cutoff 391	RER	kg	steel, chromium steel 18/8, hot rolled
transport, freight, lorry, all sizes, EURO4 to generic	0.09	ecoinvent cutoff 391	RER	ton·km	transport, freight, lorry, unspecified

market for transport, freight, lorry, unspecified					
treatment of automobile catalyst	6.90E-04	ecoinvent cutoff 391	RoW	kg	platinum
treatment of scrap steel, inert material landfill	-0.03	ecoinvent cutoff 391	RoW	kg	scrap steel
treatment of sewage sludge, 70% water, WWT, WW from maize starch production, municipal incineration	-3.71	ecoinvent cutoff 391	GLO	kg	sewage sludge, 70% water, WWT, WW from maize starch production
treatment of wastewater from potato starch production	-0.19	ecoinvent cutoff 391	RoW	m^3	wastewater from potato starch production

Figure 66 and Figure 67 summarize the resulting carbon footprint (GWP100) values in comparison with selected benchmark technologies for S1 and S2 respectively. The results are expressed in kg CO_2-eq per functional unit, that is, per kWh for S1 and per kg H_2 for S2. To contextualize the environmental performance of the APR process for S1, three reference categories were considered for comparison: (i) the APR scenarios investigated, (ii) national electricity mixes represented by *"market for electricity, medium voltage"* datasets from the background database, reflecting country-specific generation mixes and distribution impacts, and (iii) renewable electricity production in Italy.

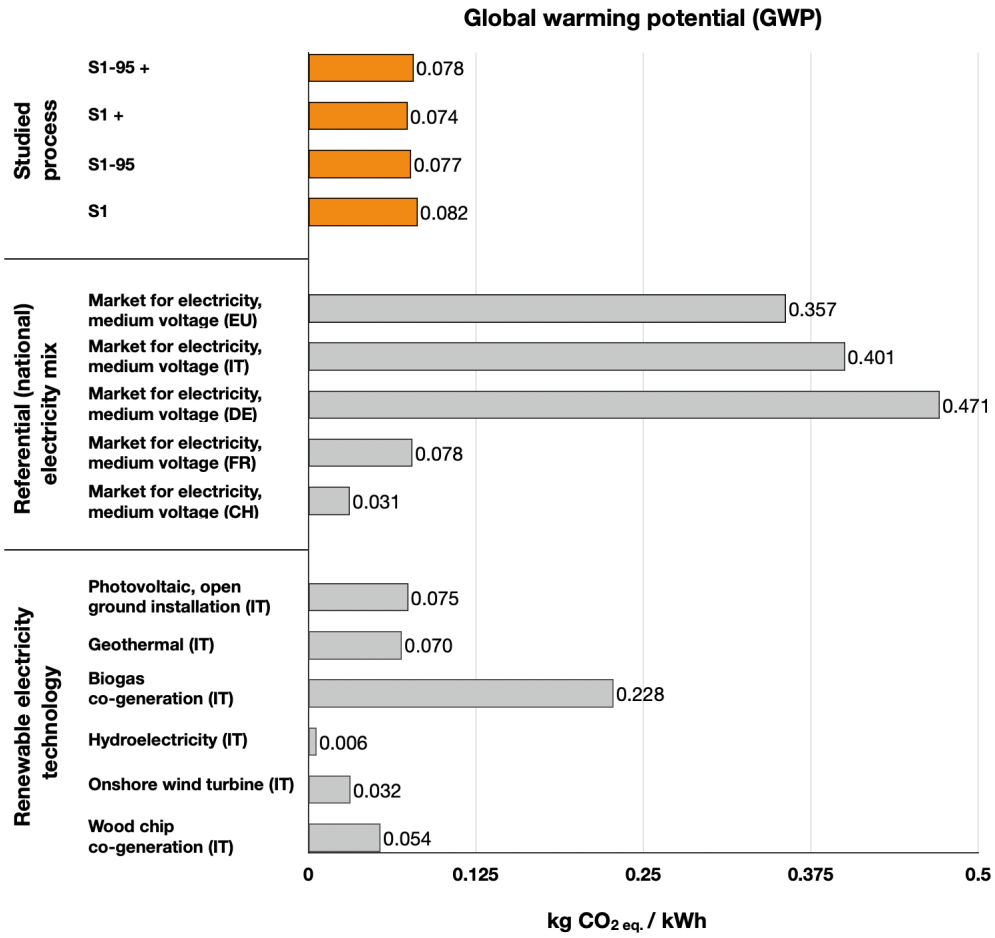

Figure 66. Comparison of APR with alternative technologies for electricity production in terms of GWP (kg CO_2-eq/kWh). Referential nomenclature for APR configurations is reported in Table 26.

The GWP impact of four different APR configurations were evaluated:

1) APR at 75% ethanol conversion and standard configuration (S1)
2) Configuration (1) with an additional flash (S1+)
3) Configuration (1) with an increased ethanol conversion of 95% (S1–95) and
4) Configuration (2) with an increased ethanol conversion of 95% (S1–95+).

Among these, S1+ achieved the lowest GWP, at 0.074 kg CO_2-eq/kWh, followed by S1–95+ with 0.078 kg CO_2-eq/kWh, indicating only a 4% difference. Notably, the configurations exhibiting the lowest GWP values, are precisely those incorporating an additional flash unit, which enhances ethanol separation and thereby reduces the COD of the aqueous output. In particular, the improvement in GWP is primarily driven by the substantial reduction in wastewater-related impacts. The treatment of wastewater from potato starch production shows a 66% decrease, with the corresponding inventory value decreasing from -1.02×10^{-2} to -3.48×10^{-3}. This reduction in COD significantly lowers the associated environmental burden. Conversely, the inclusion of an additional flash unit leads to an increase in steel requirements of approximately 70%. However, this increase has a limited impact on the overall GWP, as the steel demand is amortized over the assumed 20-year plant lifetime. As a result, the benefits associated with reduced COD in the aqueous effluent outweigh the additional material demand, making the COD reduction the

dominant factor contributing to the lower GWP observed in configurations incorporating the flash unit.
When S2 is benchmarked against national electricity mixes, the best-performing APR configuration showed a 4.8-, 5.4-, and 6.3-fold lower GWP than the average electricity generation in Europe, Italy, and Germany, respectively. At the same time, these configurations had comparable GWP to the French electricity mix and 2.3-fold higher than that of Switzerland. These differences stem primarily from France's strong reliance on nuclear power (~67%) and Switzerland's predominance of renewable electricity sources, accounting for about 98% of the national mix, mainly hydropower (~60%), nuclear energy (~30%), and bioenergy (~8%). Both countries' energy profiles substantially reduce CO_2 emissions compared with other national grids [204,205].
In fact, when compared to renewable electricity technologies in Italy, APR shows a similar GWP to photovoltaic electricity (0.075 kg CO_2-eq/kWh) and performs three times better than biogas cogeneration (0.228 kg CO_2-eq/kWh). Nevertheless, it remains less favorable than hydroelectricity, wind power, and wood chip cogeneration, which exhibit lower GWP values.
For S2, three technology categories were analysed as well: (i) the studied APR configurations, (ii) conventional H_2 production pathways, and (iii) renewable H_2 technologies via water electrolysis, including proton exchange membrane (PEM) and solid oxide electrolysis cell (SOEC) systems under various electricity supply conditions (Figure 67).

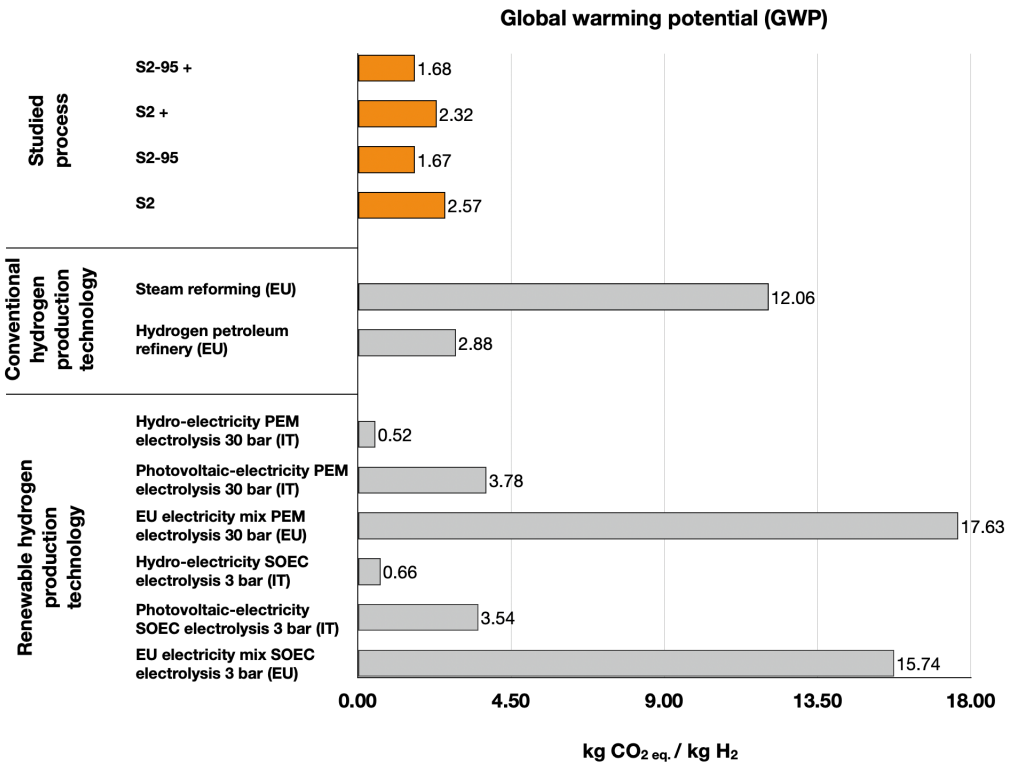

Figure 67. Comparison of APR with alternative technologies for H_2 production on GWP (kg CO_2-eq/kg H_2). Referential nomenclature for APR configurations is reported in

Table 27.

Among the APR cases, the lowest GWP corresponded to S2–95 (95% ethanol conversion) with 1.67 kg CO_2-eq/kg H_2, closely followed by S2–95+ (additional flash and compressor) at 1.68 kg CO_2-eq/kg H_2, while S2 (75% conversion) yielded the highest GWP of 2.57 kg CO_2-eq/kg H_2. Compared to conventional fossil-based H_2 routes, the best-performing APR configuration achieved a 7.2-fold lower GWP than SMR (12.06 kg CO_2-eq/kg H_2) and 1.7-fold lower than petroleum refined H_2 (2.88 kg CO_2-eq/kg H_2). These strong differences could be partially attributed to the fact that winery wastewater feedstocks carries no upstream emissions (impacts are allocated to the primary wine product), whereas fossil-based processes such as SMR and H_2 cracking include extraction, processing, and transport impacts.
Compared to H_2 produced using renewable sources, APR exhibits a 3.2-fold higher GWP than PEM electrolysis powered by hydroelectricity (0.52 kg CO_2-eq/kg H_2) and 2.5-fold higher than SOEC electrolysis under the same power source (0.66 kg CO_2-eq/kg H_2). However, APR performs substantially better than electrolysis powered by photovoltaic electricity (3.54–3.78 kg CO_2-eq/kg H_2) and dramatically outperforms EU grid-powered electrolysis (15.74–17.63 kg CO_2-eq/kg H_2), achieving a 9.4 to 10.6-fold reduction. These comparisons highlight the strong dependence of electrolysis-based H_2 GWP on electricity source, as reflected also in national contexts, e.g., Switzerland, where >90% of electricity derives from nuclear and renewable sources, shows GWP values over two times lower than Italy, where renewables account for only ~40% of the energy mix [205]. Similar findings have been reported in prior studies [206].
Overall, S1 achieves an approximately 80% reduction in emissions compared with the Italian electricity mix, while S2 achieves around 79% compared with SMR, highlighting the advantages of adopting APR as an energy recovery strategy from a GWP standpoint. The low GWP arises mainly from the lack of external electricity or heat demand i.e. self-sufficiency of APR, and the use of a waste feedstock, which further minimizes environmental burdens with biogenic CO_2 emissions compared to fossil-based.

5.5.1 Avoided GWP Impacts Relative to Conventional Pathways

To explicitly address a common counterfactual scenario encountered when comparing different technologies, a comparison was performed between the APR system and a conventional wastewater management pathway combined with grid-based electricity production for scenario S1, while steam methane reforming was considered as the conventional H_2 production alternative for scenario S2.
For the case of S1, results originally expressed per unit of energy were converted to a treatment-based functional unit. Based on the treated wastewater volume associated with 1 kWh of electricity production (0.012951 m^3/kWh), the APR system treats 77.21 kWh-equivalent per m^3 of wastewater. This corresponds to a GWP of 6.4 kg CO_2-eq. per m^3 treated for APR.
In the absence of APR, the equivalent service would be provided through (i) conventional treatment of 1 m^3 of wastewater and (ii) production of 77.21 kWh of electricity from the Italian grid. As a proxy for conventional treatment, the ecoinvent process *treatment of wastewater from vegetable oil refinery* was selected, as it is characterised by a higher organic carbon load (approximately 10 kg C/m^3) and therefore better reflects the high-strength nature of the wastewater treated by APR (≈20 kg C/m^3). For the Italian grid, the proxy *market for electricity production*

in Italy was used. Using these datasets, the GWP associated with conventional wastewater treatment amounts to 21 kg CO_2-eq. per m^3, while electricity generation from the Italian grid contributes an additional 31.27 kg CO_2-eq. per m^3.
As a result, the total GWP of the "no-APR" reference case reaches 52.27 kg CO_2-eq. per m^3 treated, as it accounts for both conventional wastewater treatment and grid-based electricity production required to deliver an equivalent service.
When the two systems are compared on an equivalent service basis, APR achieves an overall GWP reduction of approximately 88% relative to the conventional wastewater treatment plus grid electricity baseline. Although the APR system exhibits higher impacts when considered solely as a wastewater treatment technology (6.4 versus 21 kg CO_2-eq. per m^3), the inclusion of energy recovery fundamentally alters the environmental balance. In particular, the dominant contribution to the climate-change performance of APR arises from the substitution of grid electricity, whose avoided emissions largely outweigh the impacts associated with wastewater treatment.
For scenario S2, the APR system produces 1 kg of H_2 while simultaneously treating 0.36 m^3 of wastewater, resulting in a GWP of 2.57 kg CO_2-eq. per kg H_2.
In the absence of APR, the equivalent service would require (i) H_2 production via SMR and (ii) conventional treatment of 0.36 m^3 of wastewater. Using SMR as the reference H_2 production technology (12 kg CO_2-eq. per kg H_2) and the same wastewater treatment proxy adopted for S1 (21 kg CO_2-eq. per m^3), the wastewater treatment contribution amounts to 7.56 kg CO_2-eq. Consequently, the total GWP of the "no-APR" reference case reaches 19.56 kg CO_2-eq. per kg H_2.
When compared on an equivalent service basis, the APR system achieves an overall GWP reduction of approximately 87% relative to the conventional SMR plus wastewater treatment baseline, highlighting the combined benefit of resource recovery and avoided conventional H_2 production.
These results confirm that APR should be interpreted primarily as a waste-to-energy pathway rather than as a conventional end-of-pipe wastewater treatment solution.
Moreover, these outputs could be integrated into the TEA, as the reduced GWP and the associated avoided externalities can be monetised and accounted for within the cost structure. This integration has the potential to enhance the overall value proposition of the APR system through mechanisms such as carbon credits, water quality trading schemes, reduced wastewater discharge fees, and targeted environmental subsidies.

5.5.2 Contribution and Sensitivity Analyses

A process contribution analysis was conducted to identify the main GWP drivers for the 75% ethanol conversion standard configurations using a 0.001% cut-off threshold. Results are shown in Figure 68.

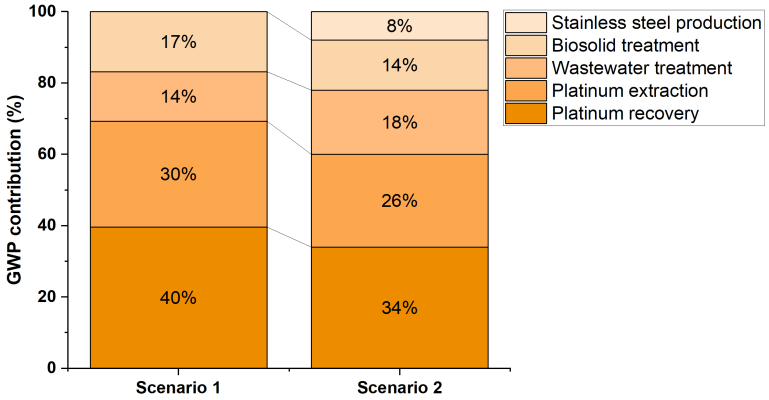

Figure 68. Main contributors to GWP impact categories for S1 and S2.

The combined platinum recovery and extraction stages dominate the total GWP, accounting for 70% in S1 and 60% in S2. Even though 99% catalyst recovery was assumed, the remaining 1% of fresh platinum contributes 30% and 26% of total GWP, respectively. If all platinum were sourced from primary materials, GWP would increase 28-fold in S1 and 33-fold in S2, confirming the substantial environmental burden associated with platinum production and the critical importance of efficient recovery strategies. Considering platinum's classification as a critical raw material (CRM) by the EU by 2011, developing sustainable recovery routes or alternative catalysts is essential [207].
Since the catalyst accounts for more than half of total GWP, a sensitivity analysis was performed varying catalyst replacement rate (catalyst lifespan), fresh Pt content, and Ni substitution to Pt. Catalyst lifetime was tested down to one week, simulating possible deactivation under real wastewater conditions, which necessitated a parallel APR reactor and caused a threefold GWP increase for both S1 and S2 (Table 28).

Table 28. Impact of catalyst lifespan on the global warming potential (GWP, $kgCO_2$ eq) for Scenario 1 (S1) and Scenario 2 (S2), respect to standard scenarios (0.08$kgCO_2$-eq. per S1 and 2.57$kgCO_2$-eq. for S2).

Catalyst lifespan	S1 ($kgCO_2$-eq /kWh)	S2 ($kgCO_2$-eq//kgH_2)
1 month (baseline)	0.08	2.57
2 weeks	0.13	3.92
1 week	0.23	6.80
1 week – 2 APR reactors	0.23	6.82

Whereas, increasing the fraction of fresh Pt from 5% to 100% sharply raised GWP to 2.18 kg CO_2-eq/kWh (S1) and 60.55 kg CO_2-eq/kg H_2 (S2) (Table 29). Nevertheless, 95–99% Pt recovery remains feasible, as confirmed by other APR studies [141], [97].

Table 29. Impact of fresh platinum content in the catalysts on the global warming potential (GWP, $kgCO_2$-eq) for Scenario 1 (S1) and Scenario 2 (S2), respect to standard scenarios (0.08$kgCO_2$-eq. per S1 and 2.57$kgCO_2$-eq. for S2).

Pt wt.%	S1 ($kgCO_2$-eq/kWh)	S2 ($kgCO_2$-eq /kgH_2)
5	0.16	4.84
10	0.27	7.80
25	0.59	16.67
50	1.12	31.55
100	2.18	60.55

While the possibility of reducing GWP through the substitution of Pt with a less environmentally impactful metal, such as nickel (Ni), which has been widely investigated as a non-precious alternative [208] ,[59] has been explored, since current data indicate that, per gram of metal extracted, Ni exhibits a much lower environmental impact than Pt (Table 30).

Table 30. Global warming potential (GWP) of platinum and nickel production, expressed per functional unit (1 kg) and based on cradle-to-gate system boundaries, including the extraction and the refining processes. Data taken from the ecoinvent 391 database.

Metal	Function unit (FU)	GWP ($kgCO_2$-eq/FU)	System boundary
Platinum	1 kg	86213	Cradle-to-gate
Nickel	1 kg	35	Cradle-to-gate

Given the lower GWP associated with the production of 1 kg of Ni compared to Pt, a sensitivity analysis was conducted to assess the effect of substituting Pt with Ni as the catalytic metal. The results are reported in Table 31. In this analysis, the substitution was carried out while maintaining the same atomic ratio and assuming comparable APR performance. No recovery of the spent catalyst was considered, as comprehensive LCAs for Ni-based systems remain limited, hindering fair benchmarking.

Table 31. Global warming potential (GWP) per functional unit (FU) for Scenarios 1 (S1: $kgCO_2$-eq./kWh) and 2 (S2: $kgCO_2$-eq./kgH_2) using 100% fresh Pt- and Ni-based catalysts

Scenario	Catalyst	GWP ($kgCO_2$-eq./FU)
S1	100% fresh Pt	2.18
S1	100% fresh Ni*	0.03
S2	100% fresh Pt	60.55
S2	100% fresh Ni*	1.07

*Here, the comparison is based on an atomic mass equivalence with respect to Pt.

However, to provide an order of magnitude estimate of the potential impact on GWP, a worst-case scenario was evaluated in which 100% of the catalyst metal was replaced with fresh Ni at each substitution cycle. Under this assumption, the GWP decreased by approximately 72-fold in S1 and 56-fold in S2, confirming Ni's strong potential for further reducing the GWP of the APR process. Nevertheless, additional studies and reliable data on Ni recovery strategies, associated costs, and environmental impacts are required to enable a more accurate comparison between the two catalytic systems.

Furthermore, other significant contributors to the GWP are the environmental impacts associated with wastewater and biosolid waste treatments, whose impacts scale proportionally with their respective volumes. This underscores the need for efficient COD reduction technologies to minimize these contributions and contain the overall GWP for the APR technology. In S1-95+, with a 95% ethanol conversion configuration with an additional flash unit eliminated the need for wastewater treatment, resulting in a 40% reduction in total GWP.

In S2 instead, material-related impacts were visible, with stainless steel contributing 8% of the total GWP, primarily due to the increased equipment requirements associated with such configurations.

Finally, a Monte Carlo simulation assessed the robustness of GWP to inventory uncertainties. In particular 2 cases are reported: the standard case with 75% ethanol conversion and 1% fresh Pt and the 100% Ni substitution case, for both scenario (Figure 69).

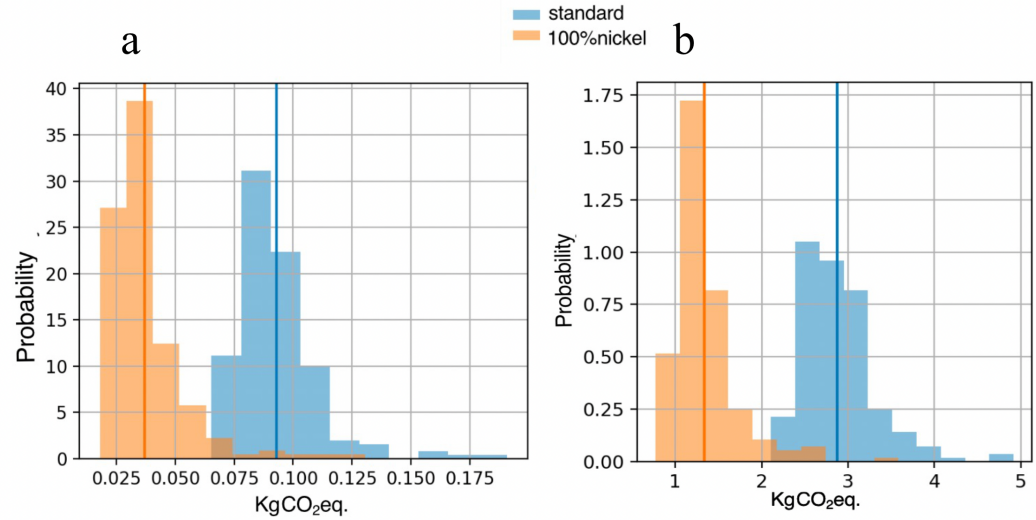

Figure 69. Monte Carlo simulation results for the global warming potential (GWP) considering ±10% standard deviation on all life cycle inventory parameters: (a) S1 and (b) for (b) S2, GWP expressed in kg CO_2-eq./kWh in blue for the standard case (1%freshPt, 75% ethanol conversion), in orange for the 100% Nickel substitution case. Each histogram shows the probability distribution of results from 200 iterations, with the vertical line indicating the mean value.

Although a normal distribution (±10%) was assigned to foreground inventory parameters, the resulting GWP distributions exhibit a clear right-tailed shape. This behaviour is expected, as uncertainty propagation also includes background processes taken from the ecoinvent database, for which uncertainty is commonly represented by log-normal distributions. As a result, the combined effect of foreground and background uncertainties leads to non-normal output distributions, as observed in the Monte Carlo results. Assuming normal distributions with ±10% standard deviation for all parameters, results showed distinct GWP probability distributions with mean values of ~0.094 kg CO_2-eq/kWh (standard case) and ~0.039 kg CO_2-eq/kWh (100% Ni) for S1, and ~2.86 vs. 1.07 kg CO_2-eq/kg H_2 for S2. The clearly separated distributions confirm that GWP reductions from Ni substitution remain robust to uncertainty.

Although GWP100 provides a key metric, it is not sufficient to capture trade-offs among other environmental categories. Therefore, the Environmental Footprint (EF) aggregated indicator was employed to integrate multiple midpoint impact categories into a single weighted score, enabling a more comprehensive evaluation of environmental performance beyond climate change alone. Based on energy-normalized results (per kWh), as described in Section 2.2.4, scenario S1 yielded an EF single score of 1.68×10^{-5}, corresponding to an overall environmental burden approximately 12% higher than that of S2, which exhibited a single score of 1.49×10^{-5}. These single-score results should be interpreted as a preliminary indication rather than as a definitive assessment, as the aggregation procedure was not the primary focus of this study. Nevertheless, they highlight the importance of considering multiple environmental dimensions simultaneously, since focusing exclusively on climate change metrics may obscure relevant trade-offs across other impact categories. This is evident when comparing the results at the level of climate change alone. When normalized on an energy-content basis without accounting for

end-use conversion efficiencies, that is, comparing electricity directly with H_2 using its LHV, the GWP of S2 is only about 6% lower than that of S1. This relatively small difference arises because the electricity-based scenario already incorporates conversion efficiencies associated with electricity generation (see Section 5.4.2), whereas H_2 is evaluated solely on the basis of its chemical energy content and has not yet undergone conversion to electricity. As a result, this comparison should be regarded as indicative and technology-agnostic, rather than representative of final delivered electricity. In contrast, the EF single-score analysis reveals a more pronounced difference between the two scenarios, with the relative gap approximately doubling compared to the GWP-only comparison. This outcome indicates that impact categories other than climate change play a significant role in determining the overall environmental performance of the system and may substantially influence conclusions drawn from a sustainability assessment.

Further insight is obtained for instance, by comparing scenario S1 with the photovoltaic reference on a 1 kWh functional unit basis. While S1 exhibits a GWP comparable to photovoltaics (0.082 versus 0.075 kg CO_2-eq./kWh), several other impact categories, such as land use, freshwater ecotoxicity (both inorganic and organic), fossil energy resource depletion, freshwater eutrophication, human toxicity (carcinogenic and non-carcinogenic), and ozone depletion, show lower values for S1 as shown in the heat map of Figure 70.

This difference is likely attributable to the higher material and chemical intensity associated with photovoltaic system manufacturing. Although photovoltaic electricity benefits from high operational efficiency and low operational emissions, the upstream production of materials and components contributes significantly to non-climate-related environmental burdens.

Overall, these results demonstrate that while climate change remains a key indicator especially when energy producing technologies are evaluated, but a broader multi-impact perspective is essential to capture the full environmental implications of competing energy technologies. The preliminary EF single-score analysis combine with a heat map thus provides valuable insight into potential trade-offs and identifies impact categories that warrant further, more detailed investigation in future work.

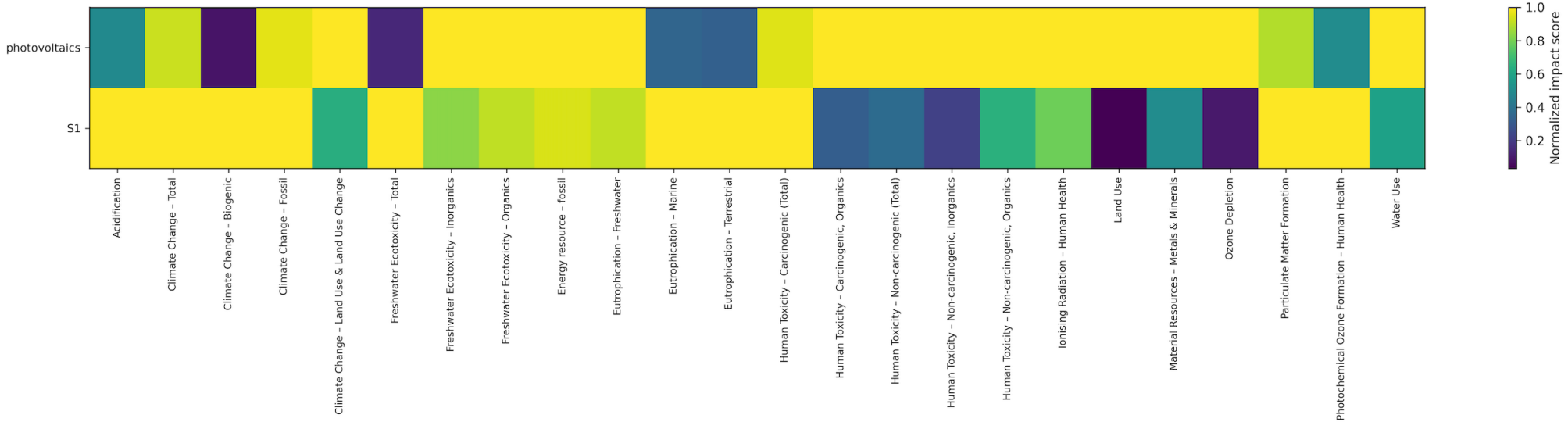

Figure 70. Heat map of normalized Environmental Footprint (EF v3.0, no long-term emissions) midpoint impact results for the photovoltaic reference and scenario S1. Darker colours indicate higher normalized environmental impacts, allowing a rapid visual comparison across impact categories and highlighting trade-offs between the two configurations.

Chapter 6. Conclusion

This thesis investigated the multi-dimensional feasibility of APR as an integrated waste valorisation and energy recovery pathway for biomass-derived wastewaters, with particular focus on the ethanol-rich effluents generated in the winemaking industry. Two complementary approaches were combined: (i) laboratory-scale experimentation to evaluate catalytic performance and identify optimal operating conditions, and (ii) process modelling and scale-up to assess the feasibility of implementing APR at industrial level under realistic conditions.

In the experimental section, two industrial wastewaters were first screened as potential APR feedstocks. Catalytic tests demonstrated that the complex composition of real wastewaters may hinder APR performance due to the presence of inhibitory species such as salts, humins, and organic acids. For this reason, pretreatment strategies such as adsorption, coprecipitation, or solvent extraction were considered to enhance the efficiency of the process and reduce catalyst inhibition. Future work should focus at investigate in depth these counteractive strategies in order to close the gap between laboratory APR data and real industrial applications. Among the investigated streams, P&P wastewater showed a lower COD and a composition dominated by short-chain carboxylic acids, which are poorly reactive under APR conditions. Conversely, winery wastewater, which are characterized by a variable ethanol content dependent on production stage and winemaking method, exhibited a high potential as a feedstock for APR. Consequently, ethanol APR was selected for further investigation as a representative model system.

Experimental results confirmed that temperature, pressure, and substrate concentration have a strong influence on APR conversion efficiency and selectivity. As a matter of fact, ethanol conversion at 270 °C was completed within one hour, while only 60 % was converted after six hours at 230 °C. However, the increase in temperature also lead to a decrease in H_2 selectivity, suggesting a concomitance in parallel methanation and dehydration reactions. For this reason, a temperature of 250 °C was identified as a compromise between ethanol conversion and H_2 selectivity. Another interesting finding focused on investigating the effect of APR efficiency at higher operating pressures and higher ethanol concentrations. The results suggest that higher pressures and higher ethanol concentrations decrease the overall conversion efficiency, shifting the gas composition toward the formation of CH_4. Catalyst screening was also performed and showed promising results: the commercial Ru/Al_2O_3 catalyst achieved higher ethanol conversion and carbon-to-gas yield than its Pt counterpart, although the latter maintained greater H_2 selectivity. Based on these findings, Ru-based catalysts were prioritized for COD abatement, emphasizing total carbon recovery over selective H_2 production. To further explore the possibility of reducing reliance on precious metals for catalytic synthesis, exsolution as a novel synthesis route was also explored. Here, a 2 wt.% Ru–Fe bimetallic catalyst supported on modified yttria-zirconia demonstrated particularly promising performance compared with a 4 wt.% Ru reference catalyst, confirming that partial substitution of Ru with a non-noble promoter can maintain or even enhance productivity.

In the second part of this work, the scaling up of ethanol APR to an industrially relevant case was evaluated. Process simulations were developed to represent the treatment of a 2.5 m^3/h input stream of winery wastewaters through two configurations: S1, based on CHP generation for electricity production, and S2, focused on H_2 purification and recovery. Both were assessed through ESA, TEA, and LCA to provide an integrated evaluation of their energetic, economic, and environmental performance.

Energetic analyses confirmed that both S1 and S2 are self-sustaining, producing more energy than required for their operation. S2 achieved a superior long-term energy performance, particularly at the optimized 95 % ethanol conversion, where higher H_2 recovery improved the EROI from 2.7 to 3.5. However, the TEA showed that MSPs remain higher than current market values, with ~0.86 USD /kWh for electricity production in S1 and ~15.5 USD kg/H_2 for H_2 production in S2. These higher MSPs are linked the high capital costs of the APR reactor and CHP unit in S1, and the PSA unit in S2. Since both systems were energetically self-sufficient, variable costs represented the smallest share of total costs. A sensitivity analysis showed that increasing ethanol conversion enhanced H_2 productivity but also raised the reactor thermal duty by ~22 %, leading to greater vaporization effects and a 7 % increase in electricity MSP for S1. Conversely, S2 benefited from a 20 % decrease in H_2 MSP under the same conditions. To reduce the MSP to near-market price, a service fee for COD removal at competitive rates with conventional wastewater treatment was suggested.

From an environmental perspective, it should be noted that the LCA results presented in this work are subject to limitations related to model representativity and data availability. Due to the absence of fully representative, site-specific life cycle inventories for APR-based wastewater treatment systems, several assumptions and proxy datasets from the ecoinvent database were adopted, particularly for wastewater treatment and background processes. While these choices are consistent with state-of-the-art LCA practice, they introduce uncertainty and should be considered when interpreting the absolute results

The LCA study showed that APR achieves substantially lower GWP than fossil-based technologies, with up to 80 % lower emissions compared with SMR for H_2 and to 5-fold lower than the Italian electricity mix for power generation. Nevertheless, the catalyst dominated total GWP, mainly due to Pt extraction and recovery, accounting for over 60 % of the total impact. Further sensitivity analysis revealed that extending catalyst lifetime or substituting Pt with Ni could reduce GWP by up to 70-fold. Importantly, the sensitivity analysis indicates that limited catalyst lifetime or low reusability could substantially increase GWP, underscoring that the environmental competitiveness of APR critically depends on durable catalyst performance and efficient metal recovery under realistic wastewater operating conditions. Overall, while the present analysis does not yet provide a definitive picture of the environmental performance of APR, it demonstrates that APR has the potential to be environmentally competitive when compared with non-renewable conventional technologies for electricity and H_2 production. Further works are required to ensure catalyst stability and recyclability, as well as to assess the environmental and economic trade-offs associated with treating real wastewaters, which contain a broader range of organic and inorganic species beyond ethanol and may necessitate additional purification or pretreatment steps.

Taken together, the experimental and modelling results indicate that ethanol-rich winery wastewater represents a particularly attractive niche for APR, where treatment and valorisation can be pursued simultaneously. While further work is

required to resolve uncertainties linked to real-matrix complexity and catalyst durability, the present thesis provides the foundations for rational development: it quantifies operating windows, highlights the conversion–selectivity tensions that shape product value, and demonstrates that energetically self-sustaining configurations are attainable at industrial scale. If future research delivers catalysts that remain active, selective, and recoverable under real wastewater conditions, APR could become a cornerstone technology for turning biomass-derived effluents into measurable climate and resource gains.

References

[1] United Nation. World Population Prospects 2024: Summary of Results. 2024.
[2] Ahmad T, Zhang D. A critical review of comparative global historical energy consumption and future demand: The story told so far. Energy Reports 2020;6:1973–91. https://doi.org/10.1016/j.egyr.2020.07.020.
[3] International Energy Agency IEA. Global Energy Review 2025. 2025.
[4] International Energy Agency IEA. World Energy Outlook 2023 2023.
[5] Calvin K, Dasgupta D, Krinner G, Mukherji A, Thorne PW, Trisos C, et al. Synthesis Report (SYR) of the IPCC Sixth Assessment Report (AR6). 2023. https://doi.org/10.59327/IPCC/AR6-9789291691647.
[6] Crippa M, Guizzardi D, Pagani F, Banja M,, Muntean M et al. GHG emissions of all world countries. 2025. https://doi.org/10.2760/5917997.
[7] Gryparis E, Rzeszutko M, Papadopoulos P, Manousakis N, Psomopoulos CS. Correlation analysis of population, energy consumption and overshoot day global trends. Discover Sustainability 2025;6. https://doi.org/10.1007/s43621-025-02088-7.
[8] European Parliament and Council of the European Union. Directive 2003/87/EC of the European Parliament. Official Journal of the European Union 2003:32–46.
[9] European Parliament and Council of the European Union. Directive 2009/28/EC on the promotion of the use of energy from renewable sources. Official Journal of the European Union 2009:16–62.
[10] European Parliament and Council of the European Union. Directive 2012/27/EU on energy efficiency. Official Journal of the European Union 2012:1–56.
[11] European Commission. The European Green Deal. Brussels: 2019.
[12] European Commission. Fit for 55': delivering the EU's 2030 Climate Target on the way to climate neutrality. 2021.
[13] Brożyna J, Lu J, Strielkowski W. Is European current climate regulation strategy feasible? A comparative analysis of "Fit for 55" green transition package for V4 and LEU4. Energy Strategy Reviews 2025;61:101843. https://doi.org/10.1016/J.ESR.2025.101843.
[14] Desogus E, Grosso D, Bompard E, Lo Russo S. Modelling the geopolitical impact on risk assessment of energy supply system: The case of Italian crude oil supply. Energy 2023;284:128578. https://doi.org/10.1016/J.ENERGY.2023.128578
[15] European Commission. Europe's moment: Repair and Prepare for the Next Generation. Brussels: 2020.
[16] Presidenza del Consiglio dei Ministri. Piano Nazionale di Ripresa e Resilienza (PNRR). Rome, Italy: 2021.
[17] Tracking climate pledges: can the Global Stocktake be a landmark moment for energy sector ambition? Analysis - IEA n.d. https://www.iea.org/commentaries/tracking-climate-pledges-can-the-global-stocktake-be-a-landmark-moment-for-energy-sector-ambition (accessed September 1, 2025).
[18] Prina MG, Barchi G, Osti S, Moser D. Optimal future energy mix assessment considering the risk of supply for seven European countries in 2030 and 2050. E-Prime - Advances in Electrical Engineering, Electronics and Energy 2023;5:100179. https://doi.org/10.1016/J.PRIME.2023.100179.
[19] International Energy Agency IEA. Italy - Countries & Regions - IEA 2023. https://www.iea.org/countries/italy/energy-mix (accessed September 2, 2025).
[20] International Energy Agency IEA. Global Hydrogen Review 2024. 2024.
[21] Nnabuife SG, Oko E, Kuang B, Bello A, Onwualu AP, Oyagha S, et al. The prospects of hydrogen in achieving net zero emissions by 2050: A critical review.

Sustainable Chemistry for Climate Action 2023;2. https://doi.org/10.1016/j.scca.2023.100024.
[22] Jeje SO, Marazani T, Obiko JO, Shongwe MB. Advancing the hydrogen production economy: A comprehensive review of technologies, sustainability, and future prospects. Int J Hydrogen Energy 2024;78:642–61. https://doi.org/10.1016/j.ijhydene.2024.06.344.
[23] Conteratto C, Artuzo FD, Benedetti Santos OI, Talamini E. Biorefinery: A comprehensive concept for the sociotechnical transition toward bioeconomy. Renewable and Sustainable Energy Reviews 2021;151. https://doi.org/10.1016/j.rser.2021.111527.
[24] Zhang K. A Review of Biomass Energy: Comparison of Utilization Methods and Future Prospects. E3S Web of Conferences, vol. 606, EDP Sciences; 2025. https://doi.org/10.1051/e3sconf/202560605007.
[25] Aryanfar Y, Castellanos HG, Hammoodi KA, Farifteh M, Keçebaş A, Ghasemlou SM, et al. Cleaner and sustainable circular economy approaches for bio-based product recovery from industrial effluents in a biorefinery. Environ Prog Sustain Energy 2024;43. https://doi.org/10.1002/ep.14483.
[26] Li T, Su J, Wang C, Watanabe A, Teramae N, Ohtani H, et al. Advances in the development and application of analytical pyrolysis in biomass research: A review. Energy Convers Manag 2022;271. https://doi.org/10.1016/J.ENCONMAN.2022.116302.
[27] Jin CL, Wu ZM, Wang SW, Cai ZQ, Chen T, Farahani MR, et al. Economic assessment of biomass gasification and pyrolysis: A review. Energy Sources, Part B: Economics, Planning and Policy 2017;12:1030–5. https://doi.org/10.1080/15567249.2017.1358309.
[28] Qiu B, Tao X, Wang Y, Zhang D, Chu H. Hydrothermal liquefaction for producing liquid fuels and chemicals from biomass-derived platform compounds: a review. Environ Chem Lett 2025;23:81–115. https://doi.org/10.1007/S10311-024-01791-7/TABLES/2.
[29] Luan J, Wang Q, Shao D, Cui B, Han P, He Q. Research progress on influencing factors and control methods of slagging in biomass combustion. Front Energy Res 2025;13:1634354. https://doi.org/10.3389/FENRG.2025.1634354/BIBTEX.
[30] Yate A V., Narváez PC, Orjuela A, Hernández A, Acevedo H. A systematic evaluation of the mechanical extraction of Jatropha curcas L. oil for biofuels production. Food and Bioproducts Processing 2020;122:72–81. https://doi.org/10.1016/J.FBP.2020.04.001.
[31] Nagarajan J, Prakash L. Preparation and characterization of biomass briquettes using sugarcane bagasse, corncob and rice husk. Mater Today Proc 2021;47:4194–8. https://doi.org/10.1016/J.MATPR.2021.04.457.
[32] Srivastava RK, Nedungadi SV, Akhtar N, Sarangi PK, Subudhi S, Shadangi KP, et al. Effective hydrolysis for waste plant biomass impacts sustainable fuel and reduced air pollution generation: A comprehensive review. Science of the Total Environment 2023;859. https://doi.org/10.1016/j.scitotenv.2022.160260.
[33] Hussain M, Ashraf HT, Vasudev V, Yasin S, Jamil MI, Saleem M, et al. Deep eutectic solvents in biomass pretreatment for green approach: a comprehensive review. Polymer Bulletin 2025;82:10513–52. https://doi.org/10.1007/S00289-025-05955-5/FIGURES/8.
[34] Preetam A, Jadhao PR, Naik SN, Pant KK, Kumar V. Supercritical fluid technology - an eco-friendly approach for resource recovery from e-waste and plastic waste: A review. Sep Purif Technol 2023;304:122314. https://doi.org/10.1016/J.SEPPUR.2022.122314.
[35] Grigorescu A, Lincaru C, Dincer H, Sahil S, Nanda S. Process Intensification of Anaerobic Digestion of Biowastes for Improved Biomethane Production: A Review. Sustainability 2025, Vol 17, Page 6553 2025;17:6553. https://doi.org/10.3390/SU17146553.

[36] Malik K, Sharma P, Yang Y, Zhang P, Zhang L, Xing X, et al. Lignocellulosic biomass for bioethanol: Insight into the advanced pretreatment and fermentation approaches. Ind Crops Prod 2022;188:115569. https://doi.org/10.1016/J.INDCROP.2022.115569.
[37] Tao J, Song S, Qu C. Recent Progress on Conversion of Lignocellulosic Biomass by MOF-Immobilized Enzyme. Polymers 2024, Vol 16, Page 1010 2024;16:1010. https://doi.org/10.3390/POLYM16071010.
[38] Cortright RD, Davda RR, Dumesic JA. Hydrogen from catalytic reforming of biomass-derived hydrocarbons in liquid water. Nature 2002;418:964–7. https://doi.org/10.1038/nature01009.
[39] Davda RR, Shabaker JW, Huber GW, Cortright RD, Dumesic JA. A review of catalytic issues and process conditions for renewable hydrogen and alkanes by aqueous-phase reforming of oxygenated hydrocarbons over supported metal catalysts. Appl Catal B 2005;56:171–86. https://doi.org/10.1016/j.apcatb.2004.04.027.
[40] Ripken RM, Meuldijk J, Gardeniers JGE, Le Gac S. Influence of the Water Phase State on the Thermodynamics of Aqueous-Phase Reforming for Hydrogen Production. ChemSusChem 2017;10:4909–13. https://doi.org/10.1002/cssc.201700189.
[41] Xu C, Paone E, Rodríguez-Padrón D, Luque R, Mauriello F. Reductive catalytic routes towards sustainable production of hydrogen, fuels and chemicals from biomass derived polyols. Renewable and Sustainable Energy Reviews 2020;127. https://doi.org/10.1016/j.rser.2020.109852.
[42] Raso R, Abad E, García L, Ruiz J, Oliva M, Arauzo J. Renewable Hydrogen Production by Aqueous Phase Reforming of Pure/Refined Crude Glycerol over Ni/Al-Ca Catalysts. Molecules 2023;28. https://doi.org/10.3390/molecules28186695.
[43] Joshi AN, Vaidya PD. Recent studies on aqueous-phase reforming: Catalysts, reactors, hybrid processes and techno-economic analysis. Int J Hydrogen Energy 2024;49:117–37. https://doi.org/10.1016/j.ijhydene.2023.06.314.
[44] Seretis A, Tsiakaras P. A thermodynamic analysis of hydrogen production via aqueous phase reforming of glycerol. Fuel Processing Technology 2015;134:107–15. https://doi.org/10.1016/j.fuproc.2015.01.021.
[45] Roy B, Martinez U, Loganathan K, Datye AK, Leclerc CA. Effect of preparation methods on the performance of Ni/Al 2O 3 catalysts for aqueous-phase reforming of ethanol: Part I-catalytic activity. Int J Hydrogen Energy 2012;37:8143–53. https://doi.org/10.1016/j.ijhydene.2012.02.056
[46] Xie J, Su D, Yin X, Wu C, Zhu J. Thermodynamic analysis of aqueous phase reforming of three model compounds in bio-oil for hydrogen production. Int J Hydrogen Energy 2011;36:15561–72. https://doi.org/10.1016/j.ijhydene.2011.08.103.
[47] Coronado I, Stekrova M, Reinikainen M, Simell P, Lefferts L, Lehtonen J. A review of catalytic aqueous-phase reforming of oxygenated hydrocarbons derived from biorefinery water fractions. Int J Hydrogen Energy 2016;41:11003–32. https://doi.org/10.1016/j.ijhydene.2016.05.032.
[48] Pipitone G, Zoppi G, Pirone R, Bensaid S. A critical review on catalyst design for aqueous phase reforming. Int J Hydrogen Energy 2022;47:151–80. https://doi.org/10.1016/j.ijhydene.2021.09.206.
[49] Zoppi G, Pipitone G, Gruber H, Weber G, Reichhold A, Pirone R, et al. Aqueous phase reforming of pilot-scale Fischer-Tropsch water effluent for sustainable hydrogen production. Catal Today 2021;367:239–47. https://doi.org/10.1016/j.cattod.2020.04.024.
[50] Pipitone G, Hensley AJR, Omoniyi A, Zoppi G, Pirone R, Bensaid S. Unravelling competitive adsorption phenomena in the aqueous phase reforming of carboxylic acids on Pt catalysts: An experimental and theoretical study. Chemical Engineering Journal 2024;482. https://doi.org/10.1016/j.cej.2024.148902.

[51] Pipitone G, Zoppi G, Bocchini S, Rizzo AM, Chiaramonti D, Pirone R, et al. Aqueous phase reforming of the residual waters derived from lignin-rich hydrothermal liquefaction: investigation of representative organic compounds and actual biorefinery streams. Catal Today 2020;345:237–50. https://doi.org/10.1016/j.cattod.2019.09.040.
[52] Pipitone G, Zoppi G, Ansaloni S, Bocchini S, Deorsola FA, Pirone R, et al. Towards the sustainable hydrogen production by catalytic conversion of C-laden biorefinery aqueous streams. Chemical Engineering Journal 2019;377. https://doi.org/10.1016/j.cej.2018.12.137.
[53] Pipitone G, Zoppi G, Pirone R, Bensaid S. A critical review on catalyst design for aqueous phase reforming. Int J Hydrogen Energy 2022;47:151–80. https://doi.org/10.1016/j.ijhydene.2021.09.206.
[54] Alcalá R, Mavrikakis M, Dumesic JA. DFT studies for cleavage of C-C and C-O bonds in surface species derived from ethanol on Pt(111). J Catal 2003;218:178–90. https://doi.org/10.1016/S0021-9517(03)00090-3.
[55] F.Cavani, G. Centi, M. Di Serio, I. Rossetti, A. Salvini, G. Strukul. Fondamenti di chimica industriale. 2022.
[56] Roy B, Sullivan H, Leclerc CA. Effect of variable conditions on steam reforming and aqueous phase reforming of n-butanol over Ni/CeO2 and Ni/Al2O 3 catalysts. J Power Sources 2014;267:280–7. https://doi.org/10.1016/j.jpowsour.2014.05.090.
[57] Seretis A, Tsiakaras P. Aqueous phase reforming (APR) of glycerol over platinum supported on Al2O3 catalyst. Renew Energy 2016;85:1116–26. https://doi.org/10.1016/j.renene.2015.07.068.
[58] Gursahani KI, Alcalá R, Cortright RD, Dumesic JA. Reaction kinetics measurements and analysis of reaction pathways for conversions of acetic acid, ethanol, and ethyl acetate over silica-supported Pt. vol. 222. 2001.
[59] U.S. Geological Survey (USGS). Mineral Commodity Summaries 2025. Reston, VA: 2025.
[60] Liew WM, Ainirazali N. Cutting-edge innovations in bio-alcohol reforming: Pioneering pathways to high-purity hydrogen: A review. Energy Convers Manag 2025;326. https://doi.org/10.1016/j.enconman.2024.119463.
[61] Alessio HJ, Pestana GL, Comelli RA, Grau JM. Hydrogen production via aqueous phase reforming of glycerol over Ni-Co/γ-Al2O3 catalysts: Effect of support modification with lanthanides and alkaline earth metals. Fuel 2026;404. https://doi.org/10.1016/j.fuel.2025.136217.
[62] Li X, Zhang L, Wang S, Wu Y. Recent Advances in Aqueous-Phase Catalytic Conversions of Biomass Platform Chemicals Over Heterogeneous Catalysts. Front Chem 2020;7. https://doi.org/10.3389/fchem.2019.00948.
[63] Zhao Z, Zhang L, Tan Q, Yang F, Faria J, Resasco D. Synergistic bimetallic Ru–Pt catalysts for the low-temperature aqueous phase reforming of ethanol. AIChE Journal 2019;65:151–60. https://doi.org/10.1002/aic.16430.
[64] Rui N, Zhang X, Zhang F, Liu Z, Cao X, Xie Z, et al. Highly active Ni/CeO2 catalyst for CO2 methanation: Preparation and characterization. Appl Catal B 2021;282:119581. https://doi.org/10.1016/J.APCATB.2020.119581.
[65] Chen L, Zhu Y, Zheng H, Zhang C, Zhang B, Li Y. Aqueous-phase hydrodeoxygenation of carboxylic acids to alcohols or alkanes over supported Ru catalysts. J Mol Catal A Chem 2011;351:217–27. https://doi.org/10.1016/j.molcata.2011.10.015.
[66] Zoppi G, Pipitone G, Galletti C, Rizzo AM, Chiaramonti D, Pirone R, et al. Aqueous phase reforming of lignin-rich hydrothermal liquefaction by-products: A study on catalyst deactivation. Catal Today 2021;365:206–13. https://doi.org/10.1016/j.cattod.2020.08.013.
[67] Hakim L, Husin H, Sari R, Dewi R, Meriatna. Characteristic of hydroxyapatite-supported Ni, Ce, Cu catalyst prepared by deposition-precipitation and impregnation method for glycerolaqueous phase reforming process. Rasayan

Journal of Chemistry 2020;13:99–104.
https://doi.org/10.31788/RJC.2020.1315267.
[68] Callison J, Subramanian ND, Rogers SM, Chutia A, Gianolio D, Catlow CRA, et al. Directed aqueous-phase reforming of glycerol through tailored platinum nanoparticles. Appl Catal B 2018;238:618–28.
https://doi.org/10.1016/j.apcatb.2018.07.008.
[69] Sing Yu FW, Ameen M, Aqsha A, Izham M, Azizan MT, Sher F. Effects of ultrasound irradiations time over Ni–Mo/γ-Al2O3 catalyst synthesis for 1,3 – Propanediol selectively via aqueous phase reforming of glycerol. Case Studies in Chemical and Environmental Engineering 2021;3.
https://doi.org/10.1016/j.cscee.2021.100096.
[70] Md Radzi MR, Mohd Yusoff MH. Mo-Promoted Ni/CeO2 Synthesized via Sonochemical Method as Potential Catalyst in Aqueous Phase Reforming of Glycerol for Production of 1,3-Propanediol. AIP Conf Proc, vol. 2610, American Institute of Physics Inc.; 2022. https://doi.org/10.1063/5.0099593.
[71] Neira Dangelo MF, Schouten JC, Van Der Schaaf J, Nijhuis TA. Three-phase reactor model for the aqueous phase reforming of ethylene glycol. Ind Eng Chem Res 2014;53:13892–902. https://doi.org/10.1021/ie5007382.
[72] Neira D'Angelo MF, Ordomsky V, Van Der Schaaf J, Schouten JC, Nijhuis TA. Aqueous phase reforming in a microchannel reactor: The effect of mass transfer on hydrogen selectivity. Catal Sci Technol 2013;3:2834–42.
https://doi.org/10.1039/c3cy00577a.
[73] Vaidya PD, Lopez-Sanchez JA. Review of Hydrogen Production by Catalytic Aqueous-Phase Reforming. ChemistrySelect 2017;2:6563–76.
https://doi.org/10.1002/slct.201700905.
[74] Zoppi G, Pipitone G, Pirone R, Bensaid S. Aqueous phase reforming process for the valorization of wastewater streams: Application to different industrial scenarios. Catal Today 2022;387:224–36.
https://doi.org/10.1016/j.cattod.2021.06.002.
[75] Xiao Z, Meng Q, Yuan Q, van Koningsbruggen PJ, Zheng Z, Zheng Y, et al. High-performance metal-base bifunctional catalysts (NixMgy-MMO) for aqueous phase reforming of methanol to hydrogen. Fuel 2023;350.
https://doi.org/10.1016/j.fuel.2023.128808.
[76] Xiong H, DeLaRiva A, Wang Y, Datye AK. Low-temperature aqueous-phase reforming of ethanol on bimetallic PdZn catalysts. Catal Sci Technol 2015;5:254–63. https://doi.org/10.1039/c4cy00914b.
[77] Roy B, Sullivan H, Leclerc CA. Effect of variable conditions on steam reforming and aqueous phase reforming of n-butanol over Ni/CeO2 and Ni/Al2O 3 catalysts. J Power Sources 2014;267:280–7. https://doi.org/10.1016/j.jpowsour.2014.05.090.
[78] Raso R, Abad E, García L, Ruiz J, Oliva M, Arauzo J. Renewable Hydrogen Production by Aqueous Phase Reforming of Pure/Refined Crude Glycerol over Ni/Al-Ca Catalysts. Molecules 2023;28.
https://doi.org/10.3390/molecules28186695.
[79] Pipitone G, Zoppi G, Frattini A, Bocchini S, Pirone R, Bensaid S. Aqueous phase reforming of sugar-based biorefinery streams: from the simplicity of model compounds to the complexity of real feeds. Catal Today 2020;345:267–79.
https://doi.org/10.1016/j.cattod.2019.09.031.
[80] Fasolini A, Cucciniello R, Paone E, Mauriello F, Tabanelli T. A short overview on the hydrogen production via aqueous phase reforming (APR) of cellulose, C6-C5 sugars and polyols. Catalysts 2019;9. https://doi.org/10.3390/catal9110917.
[81] Tokarev A V., Kirilin A V., Murzina E V., Eränen K, Kustov LM, Murzin DY, et al. The role of bio-ethanol in aqueous phase reforming to sustainable hydrogen. Int J Hydrogen Energy 2010;35:12642–9.
https://doi.org/10.1016/j.ijhydene.2010.07.118.
[82] Di Fraia A, Miliotti E, Rizzo AM, Zoppi G, Pipitone G, Pirone R, et al. Coupling hydrothermal liquefaction and aqueous phase reforming for integrated production

of biocrude and renewable H2. AIChE Journal 2023;69. https://doi.org/10.1002/aic.17652.
[83] Palo J, Reinikainen M, Rautiainen S, Pasanen AT, Baudouin D, Grénman H, et al. Aqueous-phase reforming of methanol, acetic acid, 4-methylcatechol, and phenol over supported nickel and platinum catalysts. Appl Catal A Gen 2025;699. https://doi.org/10.1016/j.apcata.2025.120172.
[84] Coronado I, Arandia A, Reinikainen M, Karinen R, Puurunen RL, Lehtonen J. Kinetic modelling of the aqueous-phase reforming of fischer-tropsch water over ceria-zirconia supported nickel-copper catalyst. Catalysts 2019;9. https://doi.org/10.3390/catal9110936.
[85] Justicia J, Heras F, Moreno I, Baeza JA, Calvo L, Fermoso J, et al. Understanding the relationship between catalytic pyrolysis conditions and hydrogen production by aqueous phase reforming of the water-soluble fractions of bio-oils. Energy Convers Manag 2024;320. https://doi.org/10.1016/j.enconman.2024.118999.
[86] Justicia J, Baeza JA, Calvo L, Heras F, Gilarranz MA. Valorization to hydrogen of bio-oil aqueous fractions from lignocellulosic biomass pyrolysis by aqueous phase reforming over Pt/C catalyst. Chemical Engineering Journal 2023;477. https://doi.org/10.1016/j.cej.2023.146860.
[87] Oliveira AS, Baeza JA, Calvo L, Alonso-Morales N, Heras F, Rodriguez JJ, et al. Production of hydrogen from brewery wastewater by aqueous phase reforming with Pt/C catalysts. Appl Catal B 2019;245:367–75. https://doi.org/10.1016/j.apcatb.2018.12.061.
[88] Pipitone G, Pirone R, Bensaid S. Aqueous Phase Reforming of Dairy Wastewater for Hydrogen Production: An Experimental and Energetic Assessment. Sustainability (Switzerland) 2024;16. https://doi.org/10.3390/su16051743.
[89] Saenz de Miera B, Oliveira AS, Baeza JA, Calvo L, Rodriguez JJ, Gilarranz MA. Treatment and valorisation of fruit juice wastewater by aqueous phase reforming: Effect of pH, organic load and salinity. J Clean Prod 2020;252. https://doi.org/10.1016/j.jclepro.2019.119849.
[90] Oliveira AS, Baeza JA, Calvo L, Gilarranz MA. Aqueous phase reforming of starch wastewater over Pt and Pt-based bimetallic catalysts for green hydrogen production. Chemical Engineering Journal 2023;460. https://doi.org/10.1016/j.cej.2023.141770.
[91] Bu Q, Wang J, Chen Y, Tao J, Kumar A, Yan B, et al. Aqueous-Phase Reforming of Biogas Slurry over MOF-Derived α-MoO3 Catalyst for Producing Renewable Hydrogen: Effect of Fermenting Time. Molecules 2024;29. https://doi.org/10.3390/molecules29235565.
[92] Joshi AN, Vaidya PD. Hydrogen Production by Aqueous Phase Reforming of Synthetic Sewage Using Pt/C Catalyst: Effect of Reaction Parameters and Pre-Treatment Strategies. Waste Biomass Valorization 2024;15:805–19. https://doi.org/10.1007/s12649-023-02187-4.
[93] Aho A, Alvear M, Ahola J, Kangas J, Tanskanen J, Simakova I, et al. Aqueous phase reforming of birch and pine hemicellulose hydrolysates. Bioresour Technol 2022;348. https://doi.org/10.1016/j.biortech.2022.126809.
[94] Tanksale A, Beltramini JN, Lu GQ. Reaction Mechanisms for Renewable Hydrogen from Liquid Phase Reforming of Sugar Compounds. vol. 14. 2006.
[95] Wen G, Xu Y, Xu Z, Tian Z. Direct conversion of cellulose into hydrogen by aqueous-phase reforming process. Catal Commun 2010;11:522–6. https://doi.org/10.1016/j.catcom.2009.12.008.
[96] Zoppi G, Tito E, Bianco I, Pipitone G, Pirone R, Bensaid S. Life cycle assessment of the biofuel production from lignocellulosic biomass in a hydrothermal liquefaction – aqueous phase reforming integrated biorefinery. Renew Energy 2023;206:375–85. https://doi.org/10.1016/j.renene.2023.02.011.
[97] Tito E, Zoppi G, Pipitone G, Miliotti E, Fraia A Di, Rizzo AM, et al. Conceptual design and techno-economic assessment of coupled hydrothermal liquefaction and

aqueous phase reforming of lignocellulosic residues. J Environ Chem Eng 2023;11. https://doi.org/10.1016/j.jece.2022.109076.
[98] Panisko E, Wietsma T, Lemmon T, Albrecht K, Howe D. Characterization of the aqueous fractions from hydrotreatment and hydrothermal liquefaction of lignocellulosic feedstocks. Biomass Bioenergy 2015;74:162–71. https://doi.org/10.1016/j.biombioe.2015.01.011.
[99] Pola L, Collado S, Wörner M, Hornung U, Díaz M. Valorisation of the residual aqueous phase from hydrothermally liquefied black liquor by persulphate-based advanced oxidation. Chemosphere 2023;339. https://doi.org/10.1016/j.chemosphere.2023.139737.
[100] Ashrafi O, Yerushalmi L, Haghighat F. Wastewater treatment in the pulp-and-paper industry: A review of treatment processes and the associated greenhouse gas emission. J Environ Manage 2015;158:146–57. https://doi.org/10.1016/j.jenvman.2015.05.010.
[101] Esmaeeli A, Sarrafzadeh MH, Zeighami S, Kalantar M, Bariki SG, Fallahi A, et al. A Comprehensive Review on Pulp and Paper Industries Wastewater Treatment Advances. Ind Eng Chem Res 2023;62:8119–45. https://doi.org/10.1021/acs.iecr.2c04393.
[102] Esmaeeli A, Sarrafzadeh MH, Zeighami S, Kalantar M, Bariki SG, Fallahi A, et al. A Comprehensive Review on Pulp and Paper Industries Wastewater Treatment Advances. Ind Eng Chem Res 2023;62:8119–45. https://doi.org/10.1021/ACS.IECR.2C04393.
[103] Oliveira AS, Aho A, Baeza JA, Calvo L, Simakova IL, Gilarranz MA, et al. Enhanced H2 production in the aqueous-phase reforming of maltose by feedstock pre-hydrogenation. Appl Catal B 2021;281. https://doi.org/10.1016/j.apcatb.2020.119469.
[104] Buta JG, Tefera ZT, Alemea MT. Ru on N-doped ordered mesoporous carbon support for conversion of glucose to sorbitol via in-situ generated hydrogen species: A greener approach. Renew Energy 2025;240:122225. https://doi.org/10.1016/J.RENENE.2024.122225.
[105] Dagar S, Singh SK, Gupta MK. Economics of advanced technologies for wastewater treatment: Evidence from pulp and paper industry. Front Environ Sci 2022;10. https://doi.org/10.3389/fenvs.2022.960639.
[106] Miklas V, Touš M, Miklasová M, Máša V, Horňák D. Winery Wastewater Treatment Technologies: Current Trends and Future Perspective. Chem Eng Trans 2022;94:847–52. https://doi.org/10.3303/CET2294141.
[107] Jorge N, Teixeira AR, Gomes A, Peres JA, Lucas MS. Winery Wastewater: Challenges and Perspectives †. Engineering Proceedings 2023;56. https://doi.org/10.3390/ASEC2023-15968.
[108] Chen G yi, Li W qing, Chen H, Yan B bei. Progress in the aqueous-phase reforming of different biomass-derived alcohols for hydrogen production. Journal of Zhejiang University: Science A 2015;16:491–506. https://doi.org/10.1631/jzus.A1500023.
[109] Nozawa T, Mizukoshi Y, Yoshida A, Naito S. Aqueous phase reforming of ethanol and acetic acid over TiO2 supported Ru catalysts. Appl Catal B 2014;146:221–6. https://doi.org/10.1016/j.apcatb.2013.06.017.
[110] Zhao Z, Zhang L, Tan Q, Yang F, Faria J, Resasco D. Synergistic bimetallic Ru–Pt catalysts for the low-temperature aqueous phase reforming of ethanol. AIChE Journal 2019;65:151–60. https://doi.org/10.1002/aic.16430.
[111] Xiong H, DeLaRiva A, Wang Y, Datye AK. Low-temperature aqueous-phase reforming of ethanol on bimetallic PdZn catalysts. Catal Sci Technol 2015;5:254–63. https://doi.org/10.1039/c4cy00914b.
[112] International organization of vine and wine OIV. World Wine Production Outlook. 2024.
[113] Bustamante MA, Paredes C, Moral R, Moreno-Caselles J, Pérez-Espinosa A, Pérez-Murcia MD. Uses of winery and distillery effluents in agriculture:

Characterisation of nutrient and hazardous components. Water Science and Technology 2005;51:145–51. https://doi.org/10.2166/wst.2005.0018.
[114] Presidente della Repubblica. 238/2016: Disciplina organica della coltivazione della vite e della produzione e del commercio del vino. 2016.
[115] Repubblica Italiana. Disciplina organica della coltivazione della vite e della produzione e del commercio del vino, LEGGE 12 dicembre 2016, n. 238 n.d. https://www.normattiva.it/uri-res/N2Ls?urn:nir:stato:legge:2016;238 (accessed September 6, 2025).
[116] Howell CL, Myburgh PA, Lategan EL, Hoffman JE. Seasonal Variation in Composition of Winery Wastewater in the Breede River Valley with Respect to Classical Water Quality Parameters. South African Journal of Enology and Viticulture 2016;37:31–8. https://doi.org/10.21548/37-1-756.
[117] Becker S, Bouzdine-Chameeva T, Jaegler A. The carbon neutrality principle: A case study in the French spirits sector. J Clean Prod 2020;274. https://doi.org/10.1016/j.jclepro.2020.122739.
[118] Melchiors E, Freire FB. Winery Wastewater Treatment: a Systematic Review of Traditional and Emerging Technologies and Their Efficiencies. Environmental Processes 2023;10. https://doi.org/10.1007/s40710-023-00657-4.
[119] Vlotman DE, Key D, Bladergroen BJ. Technological Advances in Winery Wastewater Treatment: A Comprehensive Review. South African Journal of Enology and Viticulture 2022;43:58–80. https://doi.org/10.21548/43-1-4931.
[120] Ioannou LA, Puma GL, Fatta-Kassinos D. Treatment of winery wastewater by physicochemical, biological and advanced processes: A review. J Hazard Mater 2015;286:343–68. https://doi.org/10.1016/j.jhazmat.2014.12.043.
[121] Mulidzi AR. Winery and distillery wastewater treatment by constructed wetland with shorter retention time. Water Science and Technology 2010;61:2611–5. https://doi.org/10.2166/wst.2010.206.
[122] Pipitone G, Zoppi G, Bocchini S, Rizzo AM, Chiaramonti D, Pirone R, et al. Aqueous phase reforming of the residual waters derived from lignin-rich hydrothermal liquefaction: investigation of representative organic compounds and actual biorefinery streams. Catal Today 2020;345:237–50. https://doi.org/10.1016/j.cattod.2019.09.040.
[123] Carrillo AJ, Navarrete L, Laqdiem M, Balaguer M, Serra JM. Boosting methane partial oxidation on ceria through exsolution of robust Ru nanoparticles. Mater Adv 2021;2:2924–34. https://doi.org/10.1039/d1ma00044f.
[124] Huang R, Lim C, Jang MG, Hwang JY, Han JW. Exsolved metal-boosted active perovskite oxide catalyst for stable water gas shift reaction. J Catal 2021;400:148–59. https://doi.org/10.1016/j.jcat.2021.05.029.
[125] Pipitone G, Zoppi G, Pirone R, Bensaid S. Sustainable aviation fuel production using in-situ hydrogen supply via aqueous phase reforming: A techno-economic and life-cycle greenhouse gas emissions assessment. J Clean Prod 2023;418. https://doi.org/10.1016/j.jclepro.2023.138141.
[126] Fasolini A, Cucciniello R, Paone E, Mauriello F, Tabanelli T. A short overview on the hydrogen production via aqueous phase reforming (APR) of cellulose, C6-C5 sugars and polyols. Catalysts 2019;9. https://doi.org/10.3390/catal9110917.
[127] Wen G, Xu Y, Xu Z, Tian Z. Direct conversion of cellulose into hydrogen by aqueous-phase reforming process. Catal Commun 2010;11:522–6. https://doi.org/10.1016/j.catcom.2009.12.008.
[128] Gómez-Camacho CE, Ruggeri B. Energy Sustainability Analysis (ESA) of energy-producing processes: A case study on distributed H2 production. Sustainability (Switzerland) 2019;11. https://doi.org/10.3390/su11184911.
[129] Fraterrigo Garofalo S, Demichelis F, Peletti V, Picco L, Tommasi T, Fino D. Comparative study of polyphenol extraction using physical techniques and water as a solvent: a sustainable approach for the valorization of apple pomace.

Environmental Science and Pollution Research 2024:1–14. https://doi.org/10.1007/S11356-024-34637-4/TABLES/6.
[130] Maggio P. Pechini. Method of preparing lead and alkaline earth titanates and niobates and coating method using the same to form a capacitor, 1963.
[131] Dimesso L. Pechini Processes: An Alternate Approach of the Sol–Gel Method, Preparation, Properties, and Applications. Handbook of Sol-Gel Science and Technology, Springer International Publishing; 2016, p. 1–22. https://doi.org/10.1007/978-3-319-19454-7_123-1.
[132] Rizzetto A, Piumetti M, Pirone R, Sartoretti E, Bensaid S. Study of ceria-composite materials for high-temperature CO2 capture and their ruthenium functionalization for methane production. Catal Today 2024;429:114478. https://doi.org/10.1016/J.CATTOD.2023.114478.
[133] Skinner WSJ, Calì E, Bonis AK, Kerherve G, Kousi K, Payne DJ. New opportunities for tailored nanoparticle catalysts through exsolution from inherently disordered defect fluorite-type oxides. J Mater Chem A Mater 2025;13:6451–68. https://doi.org/10.1039/d4ta06854h.
[134] Brunauer S, Emmett PH, Teller E. Adsorption of Gases in Multimolecular Layers. The Journal of the American Chemical Society 1938;60.
[135] Irvinq Langmuir B. The adsorption of gases on plane surfaces of glass, mica and platinum. J Am Chem Soc 1918;60.
[136] Barrett EP, Joyner LG, Halenda Vol PP, -RnAtn Apj R, Vn-Rn Atn Ac RA. The Determination of Pore Volume and Area Distributions in Porous Substances. I. Computations from Nitrogen Isotherms. The Journal of the American Chemical Society 1951;73.
[137] Di Addario M, Malavè ACL, Sanfilippo S, Fino D, Ruggeri B. Evaluation of sustainable useful index (SUI) by fuzzy approach for energy producing processes. Chemical Engineering Research and Design 2016;107:153–66. https://doi.org/10.1016/J.CHERD.2015.11.006.
[138] Ruggeri B, Gómez-Camacho CE. N.Georgescu-Roegen's production model for EROI evaluation. Case study: Electrolytic H2 production using solar energy. Energy Convers Manag 2023;283:116915. https://doi.org/10.1016/J.ENCONMAN.2023.116915.
[139] Towler GP., Sinnott RK. Chemical engineering design : principles, practice and economics of plant and process design. Butterworth-Heinemann is an imprint of Elsevier; 2022.
[140] Pipitone G, Zoppi G, Pirone R, Bensaid S. Sustainable aviation fuel production using in-situ hydrogen supply via aqueous phase reforming: A techno-economic and life-cycle greenhouse gas emissions assessment. J Clean Prod 2023;418. https://doi.org/10.1016/j.jclepro.2023.138141.
[141] Sladkovskiy DA, Godina LI, Semikin K V., Sladkovskaya E V., Smirnova DA, Murzin DY. Process design and techno-economical analysis of hydrogen production by aqueous phase reforming of sorbitol. Chemical Engineering Research and Design 2018;134:104–16. https://doi.org/10.1016/j.cherd.2018.03.041.
[142] Jiménez-Benítez A, Ruiz-Martínez A, Ferrer J, Ribes J, Rogalla F, Robles A. Life cycle costing of AnMBR technology for urban wastewater treatment: A case study based on a demo-scale AnMBR system. J Environ Chem Eng 2023;11. https://doi.org/10.1016/j.jece.2023.110267.
[143] Italian Republic. Legislative Decree No. 152 of 3 April 2006 on Environmental Regulations (Environmental Code) 2006. https://www.normattiva.it/uri-res/N2Ls?urn:nir:stato:decreto.legislativo:2006-04-03;152 (accessed October 10, 2025).
[144] European Parliament and the Council. Directive - EU - 2024/1203 - Protection of the environment through criminal law and replacing Directives 2008/99/EC and 2009/123/EC 2024 2024. https://eur-lex.europa.eu/eli/dir/2024/1203/oj/eng (accessed October 13, 2025).

[145] Pajares EM, Valero LG, Sánchez IMR. Cost of Urban Wastewater Treatment and Ecotaxes: Evidence from Municipalities in Southern Europe. Water 2019, Vol 11, Page 423 2019;11:423. https://doi.org/10.3390/W11030423.
[146] Khodabandehloo M, Larimi A, Khorasheh F. Comparative process modeling and techno-economic evaluation of renewable hydrogen production by glycerol reforming in aqueous and gaseous phases. Energy Convers Manag 2020;225. https://doi.org/10.1016/j.enconman.2020.113483.
[147] León M, Silva J, Carrasco S, Barrientos N. Design, Cost Estimation and Sensitivity Analysis for a Production Process of Activated Carbon from Waste Nutshells by Physical Activation. Processes 2020, Vol 8, Page 945 2020;8:945. https://doi.org/10.3390/PR8080945.
[148] Yang L, Hao C, Chai Y. Life Cycle Assessment of Commercial Delivery Trucks: Diesel, Plug-In Electric, and Battery-Swap Electric. Sustainability 2018, Vol 10, Page 4547 2018;10:4547. https://doi.org/10.3390/SU10124547.
[149] CONFLAVORO PMI F-C. CONTRATTO COLLETTIVO NAZIONALE DI LAVORO: Addetti all'Industria Metalmeccanica privata e alla Installazione Impianti 2024. https://file.conflavoro.it/pdf/ccnl/ccnl_metalmeccanico_industria_conflavoro.pdf (accessed October 14, 2025).
[150] William Townsend, Grant Faber. AssessCCUS Capital Equipment Cost Database 2021. https://assessccus.globalco2initiative.org/tea/databases/ (accessed October 14, 2025).
[151] European Central Bank. Official Interest Rates n.d. https://www.ecb.europa.eu/stats/policy_and_exchange_rates/key_ecb_interest_rates/html/index.en.html (accessed October 14, 2025).
[152] Eurostat. Annual inflation stable at 2.2% in the euro area 2025. https://ec.europa.eu/eurostat/web/products-euro-indicators/w/2-19052025-ap (accessed October 13, 2025).
[153] Economic indicators: Chemical engineering plant cost index (CEPCI); Marshall & swift equipment cost index. Chemical Engineering 2012.
[154] Chemical Engineering. The Chemical Engineering Plant Cost Index® n.d. https://www.chemengonline.com/pci-home/ (accessed October 14, 2025).
[155] Green, Don W, Southard, Marylee Z. Perry's Chemical Engineers' Handbook. n.d.
[156] The Italian Regulatory Authority for Energy Networks and Environment (ARERA). Annual report on the state of services and regulatory activities carried out during 2023. 2024.
[157] International Organization for Standardization (ISO). Environmental Management—Life Cycle Assessment—Principles and Framework (ISO 14040:2006). International Organization for Standardization: Geneva, Switzerland 2006. https://www.iso.org/standard/37456.html (accessed October 14, 2025).
[158] International Organization for Standardization (ISO). Environmental Management—Life Cycle Assessment—Requirements an Guidelines (ISO 14044:2006). ISO: Geneva, Switzerland 2006. https://www.iso.org/standard/38498.html (accessed October 14, 2025).
[159] Weidema B P, Bauer C, Hischier R, Mutel C, Nemecek T, Reinhard J, et al. Overview and methodology. Data quality guideline for the ecoinvent database version 3. Ecoinvent Report 1(v3). 2013.
[160] Mutel C. Brightway: An open source framework for Life Cycle Assessment. The Journal of Open Source Software 2017;2:236. https://doi.org/10.21105/JOSS.00236.
[161] ZAMPORI L, PANT R. Suggestions for Updating the Product Environmental Footprint (PEF) Method. JRC Publications Repository 2019. https://doi.org/10.2760/424613.
[162] Crenna E, Secchi M, Benini L, Sala S. Global environmental impacts: data sources and methodological choices for calculating normalisation factors for LCA.

INTERNATIONAL JOURNAL OF LIFE CYCLE ASSESSMENT 2019;24:1851–77. https://doi.org/10.1007/S11367-019-01604-Y.
[163] SALA S, CERUTTI A, PANT R. Development of a weighting approach for the Environmental Footprint 2017. https://doi.org/10.2760/945290.
[164] Patel K, Patel N, Vaghamshi N, Shah K, Duggirala SM, Dudhagara P. Trends and strategies in the effluent treatment of pulp and paper industries: A review highlighting reactor options. Curr Res Microb Sci 2021;2. https://doi.org/10.1016/j.crmicr.2021.100077.
[165] Kamali M, Khodaparast Z. Review on recent developments on pulp and paper mill wastewater treatment. Ecotoxicol Environ Saf 2015;114:326–42. https://doi.org/10.1016/j.ecoenv.2014.05.005.
[166] Patel K, Patel N, Vaghamshi N, Shah K, Duggirala SM, Dudhagara P. Trends and strategies in the effluent treatment of pulp and paper industries: A review highlighting reactor options. Curr Res Microb Sci 2021;2. https://doi.org/10.1016/j.crmicr.2021.100077.
[167] Pro Gest Group. Sustainability Report - 2023. 2023.
[168] Luo N, Fu X, Cao F, Xiao T, Edwards PP. Glycerol aqueous phase reforming for hydrogen generation over Pt catalyst - Effect of catalyst composition and reaction conditions. Fuel 2008;87:3483–9. https://doi.org/10.1016/j.fuel.2008.06.021.
[169] John W. Dolan. Avoiding Refractive Index Detector Problems 2012. https://www.chromatographyonline.com/view/avoiding-refractive-index-detector-problems-0?utm_source=chatgpt.com (accessed September 9, 2025).
[170] Körner P, Jung D, Kruse A. Influence of the pH Value on the Hydrothermal Degradation of Fructose. ChemistryOpen 2019;8:1121–32. https://doi.org/10.1002/open.201900225.
[171] Boga DA, Liu F, Bruijnincx PCA, Weckhuysen BM. Aqueous-phase reforming of crude glycerol: effect of impurities on hydrogen production. Catal Sci Technol 2016;6:134–43. https://doi.org/10.1039/c4cy01711k.
[172] Enrico Bonari, Laura Ercoli, Nicola Silvestri. Acque reflue derivanti da attività di vinificazione 2008.
[173] Noemi Bevilacqua, Massimo Morassut, Maria Cecilia Serra, Francesca Cecchini. Determinazione dell'impronta carbonica dei sottoprodotti della vinificazione e loro valenza biologica 217AD. https://doi.org/10.14672/ida.v4i3.1142.
[174] Policastro G, Giugliano M, Luongo V, Napolitano R, Fabbricino M. Enhancing photo fermentative hydrogen production using ethanol rich dark fermentation effluents. Int J Hydrogen Energy 2022;47:117–26. https://doi.org/10.1016/j.ijhydene.2021.10.028.
[175] Andreottola G, Foladori P, Ziglio G. Biological treatment of winery wastewater: An overview. Water Science and Technology 2009;60:1117–25. https://doi.org/10.2166/wst.2009.551.
[176] Mader AE, Holtman GA, Welz PJ. Treatment wetlands and phyto-technologies for remediation of winery effluent: Challenges and opportunities. Science of the Total Environment 2022;807. https://doi.org/10.1016/j.scitotenv.2021.150544.
[177] Ragauskas AJ, Williams CK, Davison BH, Britovsek G, Cairney J, Eckert CA, et al. The path forward for biofuels and biomaterials. Science (1979) 2006;311:484–9. https://doi.org/10.1126/science.1114736.
[178] Nozawa T, Yoshida A, Hikichi S, Naito S. Effects of Re addition upon aqueous phase reforming of ethanol over TiO2 supported Rh and Ir catalysts. Int J Hydrogen Energy 2015;40:4129–40. https://doi.org/10.1016/j.ijhydene.2015.01.152.
[179] Xiao Z, Meng Q, Yuan Q, van Koningsbruggen PJ, Zheng Z, Zheng Y, et al. High-performance metal-base bifunctional catalysts (NixMgy-MMO) for aqueous phase reforming of methanol to hydrogen. Fuel 2023;350. https://doi.org/10.1016/j.fuel.2023.128808.
[180] Joshi AN, Vaidya PD. Hydrogen Production by Aqueous Phase Reforming of Synthetic Sewage Using Pt/C Catalyst: Effect of Reaction Parameters and Pre-

Treatment Strategies. Waste Biomass Valorization 2024;15:805–19. https://doi.org/10.1007/s12649-023-02187-4.
[181] Phatak AA, Koryabkina N, Rai S, Ratts JL, Ruettinger W, Farrauto RJ, et al. Kinetics of the water-gas shift reaction on Pt catalysts supported on alumina and ceria. Catal Today 2007;123:224–34. https://doi.org/10.1016/j.cattod.2007.02.031.
[182] Roy B, Sullivan H, Leclerc CA. Effect of variable conditions on steam reforming and aqueous phase reforming of n-butanol over Ni/CeO2 and Ni/Al2O 3 catalysts. J Power Sources 2014;267:280–7. https://doi.org/10.1016/j.jpowsour.2014.05.090.
[183] Leng S, Shen T, Li S, Wang H, Barghi S, Wu D, et al. Aqueous-Phase Reforming of Methanol for Hydrogen Production on Nitrogen-Doped Ceria: The Effect of the Doping Method. ACS Sustain Chem Eng 2025;13:8078–92. https://doi.org/10.1021/acssuschemeng.5c02140.
[184] Zhang YC, Li Z, Zhang L, Pan L, Zhang X, Wang L, et al. Role of oxygen vacancies in photocatalytic water oxidation on ceria oxide: Experiment and DFT studies. Appl Catal B 2018;224:101–8. https://doi.org/10.1016/j.apcatb.2017.10.049.
[185] Hirai T, Ikenaga NO, Miyake T, Suzuki T. Production of hydrogen by steam reforming of glycerin on ruthenium catalyst. Energy and Fuels 2005;19:1761–2. https://doi.org/10.1021/ef050121q.
[186] Dubey M, Wadhwa S, Mathur A, Kumar R. Progress in mesoporous ceria: A review on synthesis strategies and catalytic applications. Applied Surface Science Advances 2022;12. https://doi.org/10.1016/j.apsadv.2022.100340.
[187] Carrillo AJ, Navarrete L, Laqdiem M, Balaguer M, Serra JM. Boosting methane partial oxidation on ceria through exsolution of robust Ru nanoparticles. Mater Adv 2021;2:2924–34. https://doi.org/10.1039/d1ma00044f.
[188] Guo J, Cai R, Cali E, Wilson GE, Kerherve G, Haigh SJ, et al. Low-Temperature Exsolution of Ni–Ru Bimetallic Nanoparticles from A-Site Deficient Double Perovskites. Small 2022;18. https://doi.org/10.1002/smll.202107020.
[189] Naeem MA, Abdala PM, Armutlulu A, Kim SM, Fedorov A, Müller CR. Exsolution of Metallic Ru Nanoparticles from Defective, Fluorite-Type Solid Solutions Sm2Ru xCe2- xO7 to Impart Stability on Dry Reforming Catalysts. ACS Catal 2020;10:1923–37. https://doi.org/10.1021/acscatal.9b04555.
[190] López-Rodríguez S, Davó-Quiñonero A, Bailón-García E, Lozano-Castelló D, Bueno-López A. Effect of Ru loading on Ru/CeO2 catalysts for CO2 methanation. Molecular Catalysis 2021;515. https://doi.org/10.1016/j.mcat.2021.111911.
[191] Naeem MA, Abdala PM, Armutlulu A, Kim SM, Fedorov A, Müller CR. Exsolution of Metallic Ru Nanoparticles from Defective, Fluorite-Type Solid Solutions Sm2Ru xCe2- xO7 to Impart Stability on Dry Reforming Catalysts. ACS Catal 2020;10:1923–37. https://doi.org/10.1021/acscatal.9b04555.
[192] Kolpakova V, Ospanov K, Kuldeyev E, Andraka D. Clarification of Biologically Treated Wastewater in a Clarifier with Suspended Sludge Layer 2021. https://doi.org/10.3390/w13182486.
[193] Yang H, Jin S, He Y, Liu Y. Experimental study on flame temperature distribution and pollutant emission characteristics of CH4 mixed with CO2/N2/H2 combustion. Int J Hydrogen Energy 2024;71:750–62. https://doi.org/10.1016/J.IJHYDENE.2024.05.255.
[194] Nordio M, Wassie SA, Van Sint Annaland M, Pacheco Tanaka DA, Viviente Sole JL, Gallucci F. Techno-economic evaluation on a hybrid technology for low hydrogen concentration separation and purification from natural gas grid. Int J Hydrogen Energy 2021;46:23417–35. https://doi.org/10.1016/J.IJHYDENE.2020.05.009.
[195] Salkuyeh YK, Saville BA, Maclean HL. Techno-economic analysis and life cycle assessment of hydrogen production from natural gas using current and emerging technologies. Int J Hydrogen Energy 2017. https://doi.org/10.1016/j.ijhydene.2017.05.219.

[196] Di Addario M, Malavè ACL, Sanfilippo S, Fino D, Ruggeri B. Evaluation of sustainable useful index (SUI) by fuzzy approach for energy producing processes. Chemical Engineering Research & Design 2016;107:153–66. https://doi.org/10.1016/J.CHERD.2015.11.006.
[197] Tribe MA, Alpine RLW. Scale economies and the "0.6 rule." Engineering Costs and Production Economics 1986;10:271–8. https://doi.org/10.1016/S0167-188X(86)80025-8.
[198] Environmental Protection Agency U, Heat C, Partnership P. Catalog of CHP Technologies, Full Report, September 2017 2017.
[199] Sayed-Ahmed H, Toldy I, Lappalainen M, Himanen O, Bajamundi C, Santasalo-Aarnio A. Strategies and challenges for reducing green hydrogen cost: Operation mode and revenue streams. Renewable and Sustainable Energy Reviews 2025;223. https://doi.org/10.1016/j.rser.2025.116065.
[200] Hubert M, Peterson D, Miller E, Vickers J, Mow DOE R, Klembara M, et al. Clean Hydrogen Production Cost Scenarios with PEM Electrolyzer Technology 2022.
[201] Zhao Z, Zhang L, Tan Q, Yang F, Faria J, Resasco D. Synergistic bimetallic Ru–Pt catalysts for the low-temperature aqueous phase reforming of ethanol. AIChE Journal 2019;65:151–60. https://doi.org/10.1002/AIC.16430.
[202] El-Khateeb M, Hassan GK, El-Liethy MA, El-Khatib KM, Abdel-Shafy HI, Hu A, et al. Sustainable municipal wastewater treatment using an innovative integrated compact unit: microbial communities, parasite removal, and techno-economic analysis. Ann Microbiol 2023;73:1–16. https://doi.org/10.1186/S13213-023-01739-2/TABLES/3.
[203] Foret B, Chirdon WM, Hernandez R, Fortela DLB, Revellame E, Gang D, et al. A Techno-Economic Analysis of Integrating an Urban Biorefinery Process Within a Wastewater Treatment Plant to Produce Sustainable Wood Adhesives. Sustainability 2025, Vol 17, Page 6679 2025;17:6679. https://doi.org/10.3390/SU17156679.
[204] Le-Boulch D, Morisset V, Jobard Z, Burguburu A, Czyrnek-Delêtre MM. Life cycle assessment of nuclear power in France: EDF case study. EPJ Nuclear Sciences & Technologies 2024;10:8. https://doi.org/10.1051/EPJN/2024005.
[205] International Energy Agency (IEA). Countries & Regions 2025. https://www.iea.org/countries/switzerland/energy-mix (accessed October 15, 2025).
[206] Valente A, Iribarren D, Dufour J. Harmonised life-cycle global warming impact of renewable hydrogen. J Clean Prod 2017;149:762–72. https://doi.org/10.1016/J.JCLEPRO.2017.02.163.
[207] Critical raw materials - Internal Market, Industry, Entrepreneurship and SMEs n.d. https://single-market-economy.ec.europa.eu/sectors/raw-materials/areas-specific-interest/critical-raw-materials_en (accessed October 15, 2025).
[208] Roy B, Leclerc CA. Study of preparation method and oxidization/reduction effect on the performance of nickel-cerium oxide catalysts for aqueous-phase reforming of ethanol. J Power Sources 2015;299:114–24. https://doi.org/10.1016/J.JPOWSOUR.2015.08.069.